THE INFLUENCE OF NANOSCALE SIZE CONFINEMENT ON THE PHASE BEHAVIOR OF MOLECULAR ORGANIC CRYSTALS

A DISSERTATION
SUBMITTED TO THE FACULTY OF THE GRADUATE SCHOOL
OF THE UNIVERSITY OF MINNESOTA
BY

Benjamin Dale Hamilton

IN PARTIAL FULFILLMENT OF THE REQUIREMENTS
FOR THE DEGREE OF
DOCTOR OF PHILOSOPHY

Michael D. Ward, Marc A. Hillmyer, Advisors

June 2009

Acknowledgements

Studying in the CEMS department of the University of Minnesota was a goal I developed during my junior year as an undergraduate. Many educators helped me get here, but without the mentoring of professors Hugh Hillhouse and Doraiswami Ramkrishna at Purdue University, I may have never had this opportunity. When graduate school began, I was blown away. It was terrifying and thrilling, and I was honored to study in the presence of such skillful peers and professors. I still feel that way, and think I always shall. For that feeling, I have to thank my classmates and my teachers.

My advisors were obviously central players in my graduate school experience. They have been educators, coaches, friends, and arch-nemeses. I have deep appreciation the time and resources they have invested in my education. Mike and Marc have distinct personalities and teaching styles, yet have equally high expectations. It has been a pleasure to study under them both. Indeed, I consider myself fortunate to have participated in a program that condones coadvised research. I am going to miss working with them, but they will both remain inspirations to me as I proceed with my career.

I also would like to thank Barbara Schwartz and Jöen Synder-O'Neil. They were my teachers outside of school, and provided me with the tools I needed to manage my mental and physical health. Their tutelage helped transform performance anxiety into a renewed love for science. My perfectionism transformed into passion and excitement. Barbara and Jöen have touched my life, and I consider them dear friends.

I owe a very special thanks to my wife, Kim. She has compassionately endured both the best and the worst behaviors that a graduate student husband might manifest. Her grace and patience astound me, and she is continuous source of strength. I am certain my studies would have been neither as pleasant nor as successful without her presence. As I have been told and completely agree, "Kim is the best decision you will ever make."

Lastly, I wish to thank God. Despite my persistent skepticism, I find myself hard pressed to question the existence of such a being when my life has been blessed with the people and opportunities like those mentioned here.

Abstract

This thesis details the evolution of the crystallization of molecular organic compounds under nanoconfinement. Within the confines of nanoporous matrices, crystals are limited to sizes comparable to their critical sizes, where their unfavorable surface energy outweighs their favorable volume energy. The central contribution of this thesis is the crystallization of glycine within nanoporous matrices. Namely, crystallization of glycine by evaporation of aqueous solutions in nanometer-scale channels of controlled-pore glass (CPG) powders and porous polystyrene-poly(dimethyl acrylamide) (p-PS-PDMA) monoliths, the latter prepared by etching polylactide (PLA) from aligned PS-PDMA-PLA triblock copolymers, preferentially results in exclusive formation of the β polymorph, which is not observed during crystallization in bulk form under identical conditions. X-ray diffraction (XRD) reveals that the dimensions of the embedded crystals are commensurate with the pore diameter of the matrix. β-glycine persists for at least one year in CPG and p-PS-PDMA with pore diameters less than 24 nm, but it transforms slowly to α-glycine over several days when confined within 55 nm CPG. Moreover, variable temperature XRD reveals that β-glycine nanocrystals embedded within CPG are stable at temperatures at which bulk β-glycine ordinarily transforms to the α form in the bulk. XRD and differential scanning calorimetry (DSC) reveal the melting of glycine nanocrystals within CPG below the temperature at which bulk glycine melts with concomitant decomposition. The melting point depression conforms to the Gibb-Thompson equation, with the melting points decreasing with decreasing pore size. This behavior permits an estimation of the melting temperature of bulk β-glycine, which cannot be measured directly owing to its metastable nature. Collectively, these results demonstrate size-dependent polymorphism for glycine and the ability to examine certain thermal properties under nanoscale confinement that cannot be obtained in bulk form. The observation of β-glycine at nanometer-scale dimensions suggests that glycine crystallization likely involves formation of β nuclei followed by their transformation to the other more stable forms as crystal size increases, in accord with Ostwald's rule of stages. When embedded in p-PS-PDMA, the nanocrystals also adopt preferred orientations with their fast-growth axes aligned parallel with the pore direction. When grown from aqueous solutions alone, the nanocrystals were oriented with their [010] and [0-10] axes, the native fast growth directions of the (+) and (-) enantiomorphs of β-glycine, respectively, aligned parallel with the pore direction. In contrast, crystallization in the presence of racemic mixtures of chiral auxiliaries known to inhibit growth along the [010] and [0-10] directions of the enantiomorphs produced β-glycine nanocrystals with their <001> axes nearly parallel to the pore direction. Enantiopure auxiliaries that inhibit crystallization along the native fast growth direction of only one of the enantiomorphs allow the other enantiomorph to grow with the <010> axis parallel to the cylinder. Collectively, these results demonstrate that crystal growth occurs such that the fast-growing direction, which can be altered by adding chiral auxiliaries, is parallel to the pore direction. This behavior can be attributed to a competition between differently aligned crystals due to critical size effects, the minimization of the surface energy of specific crystal planes, and a more effective reduction of the excess free energy associated with supersaturated conditions when the crystal grows with its fast-growth axis unimpeded by pore walls. These observations suggest that the β-glycine nanocrystals form by homogeneous nucleation, with minimal influence of the pore walls on orientation. Collectively, these results suggest new routes for controlling crystallization outcomes and new studies on the exploration of crystal properties on the nanometer length scale.

Table of Contents

List of Tables

List of Figures

Chapter 1: Crystallization

Crystals surround us in nature and technology, yet are taken for granted in daily life. The processes by which crystals form, known collectively as crystallization, are often complicated and difficult to control. In particular, polymorphism – the ability molecules possess to adopt multiple crystalline forms – presents one of the greatest challenges to designing reliable crystallization protocols. Each crystal form, also known as a polymorph, can exhibit a unique set of physical properties. Thus, polymorphs influence the performance of crystal-dependent products despite containing the same molecules. Consequentially, polymorphism is of great importance to any sector that relies on crystalline materials. This is underscored in the pharmaceutical industry, where polymorphism is heavily monitored by the Food and Drug Administration (FDA) and regulated in patent law.[1] Collectively, hundreds of millions, perhaps even billions of dollars have been spent and lost over polymorph-related issues. Despite decades of literature existing on the subject, no definitive method of controlling polymorphism exists, and so research into the causes and control of polymorphism continues today.

This thesis research was performed to further understanding of polymorphism and related phenomena, particularly during the early stages of crystal nucleation and growth. The remainder

of this chapter introduces crystallization with emphasis on molecular organic crystals, that is, crystals composed of organic molecules.

1-1: Crystal Nucleation Theory

The classic theory of nucleation was developed Gibbs,[2] Volmer,[3] and others to describe the process by which a sphere of liquid condenses from a vapor. Unlike liquids and vapors, treated in the theory as isotropic bodies with no internal structure, crystals exhibit both anisotropy and structure. Despite this difference, Gibbs extended classic nucleation theory to solids crystallizing from melts or supersaturated solutions. The theory approximates a crystal as a small sphere growing out of an endless pool of homogeneous and disordered source material. When this process involves only the crystal and its source material, it is known as homogeneous nucleation. Classic nucleation theory posits that crystal growth occurs by a single-addition mechanism, where a small cluster of molecules known as a nucleus grows by one particle at a time (Figure 1-1). The formation of the nucleus is accompanied by a free energy change, ΔG_{cryst} (Equation 1.1), that is the sum of a favorable volume contribution ($-\Delta\mu \bullet N$) and an unfavorable surface contribution ($\gamma \bullet A$). The volume free energy is the sum of the change in chemical potential, $\Delta\mu$, of each of N molecules as they transition from the source material to the crystal. The surface free energy results from the creation an interface between the two phases with an interfacial energy, γ, and surface area, A (Equation 1.1).[4,i]

i . A thorough thermodynamic derivation of the equations governing classic nucleation theory is provided in Appendix A.

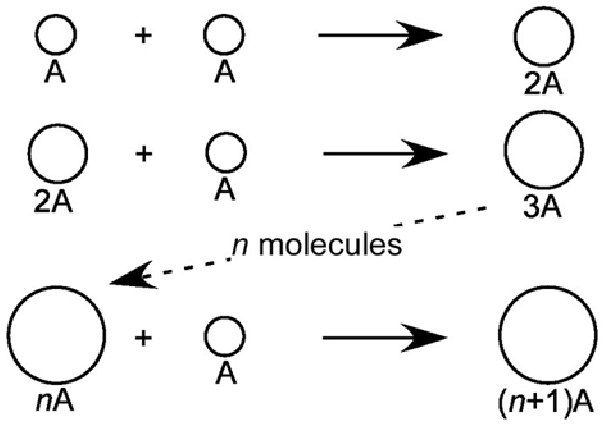

Figure 1-1. Growth by single addition. One molecule A adds to another molecule A to form a two molecule nucleus, 2A. Growth continues by the addition of a single molecule A at a time.

$$\Delta G_{cryst} = -\Delta\mu \cdot N + \gamma \cdot A \qquad 1.1$$

The N particles of the spherical nucleus can be described in terms of the volume of the sphere, with radius r, and the molecular volume, v. Likewise, the Gibbs energy associated with the interface formation can be described in terms of the surface area of the sphere (Equation 1.2, Figure 1-2). The change in chemical potential of the particles that join the nucleus may be rewritten according to thermodynamics for solutions, where a describes the activity of the particle prior to escaping the supersaturated solution (or supercooled melt) and a^* describes the activity of a particle in a saturated solution (or melt at the melting temperature) (Equation 1.3). T is absolute temperature and **k** is the Boltzmann constant. In the limit of near infinite dilution the activities a and a^* can be approximated respectively by the concentrations c and c^*, the ratio of which is the supersaturation, S (Equation 1.4). Alternate definitions for $\Delta\mu$ exist for discussions of other nucleation phenomenon (Table 1-1).

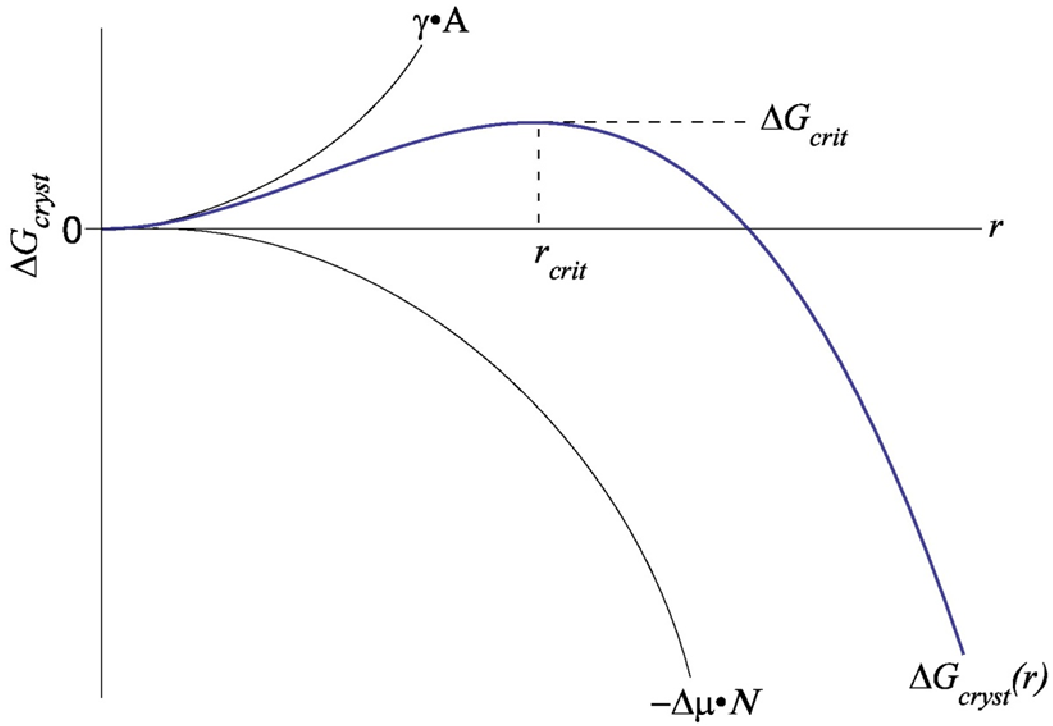

Figure 1-2. Illustration of the free energy (ΔG_{cryst}) profile of a growing crystal nucleus as a function of crystal radius, r. The energy profile results from the sum of the energetic benefit associated with a species changing phases, $-\Delta\mu \bullet N$, and the penalty associated with forming an interface between the original and crystalline phase, $\gamma \bullet A$. The profile goes through a maximum, ΔG_{crit}, for crystals of size r_{crit}. Crystals smaller than r_{crit} are expected to dissolve spontaneously, however, crystals larger than r_{crit} are expected to grow spontaneously. The formation of these crystals is discussed in the text.

$$\Delta G_{cryst} = -\frac{4/3\pi r^3}{v}\Delta\mu + 4\pi r^2\gamma \qquad 1.2$$

$$\Delta G_{cryst} = -\frac{4/3\pi r^3}{v}\mathbf{k}T\ln\left(a/a_*\right) + 4\pi r^2\gamma \qquad 1.3$$

$$\Delta G_{cryst} = -\frac{4/3\pi r^3}{v}\mathbf{k}T\ln\left(S\right) + 4\pi r^2\gamma \qquad 1.4$$

Table 1-1. Expressions for $\Delta\mu$, Equation 1.2, for different nucleation events. All of these expressions are contingent on the assumptions that the systems are ideal and that the entropies and enthalpies of transitions are independent of temperature. The temperatures T_i (i = transition type) are the bulk thermodynamic transition temperatures, while T are the size-dependent transition temperatures. The ΔH_i are the enthalpies of the transitions.

Nucleation Event	$\Delta\mu$	**Alternate** $\Delta\mu$
Vapor condensation into a liquid (vap) or solid (sub)	$\mathbf{k}T\ln\left(p/p_0\right)$	$\dfrac{\Delta H_{vap/sub}\left(T_{vap/sub}-T\right)}{T_{vap/sub}}$
Crystallization from solution	$\mathbf{k}T\ln\left(c/c_0\right)$	$\dfrac{\Delta H_{sol}\left(T_{sol}-T\right)}{T_{sol}}$
Bubble nucleation in liquid	$-\mathbf{k}T\ln\left(p/p_0\right)$	$-\dfrac{\Delta H_{vap}\left(T_b-T\right)}{T_b}$
Crystallization fom melt	-	$\dfrac{\Delta H^{fus}\left(T_m-T\right)}{T_m}$

Equation 1.4 describes a competition between the energetic benefit gained for particles forming a new phase (e.g., a crystal) when driven by supersaturation and the energetic penalty paid for forming an interface (e.g., the surface of the crystal) between the new and old phase. The energetic profile of a growing crystal nucleus is a function of crystal size, and is parameterized by the radius, *r*. Notably, this size-dependent profile passes through a maximum free energy, which can be determined along with the corresponding size when $d\Delta G_{cryst}/dr = 0$ (Equation 1.5). Nuclei smaller than the size corresponding to this maximum dissolve spontaneously, owing to increasing crystal free energy with increasing crystal size, however, nuclei larger than this size grow spontaneously. For these reasons, the size and corresponding maximum free energy are the critical radius, r_{crit} (Equation 1.6), and the critical energy, ΔG_{crit} (Equation 1.7), respectively. The free energy maximum, ΔG_{crit}, is tantamount to the energetic barrier to spontaneous crystal growth.

$$\frac{d\Delta G_{cryst}}{dr} = 0 = -\frac{4\pi r_{crit}^2}{v}\mathbf{k}T\ln(S) + 8\pi r_{crit}\gamma \quad 1.5$$

$$r_{crit} = \frac{2v\gamma}{\mathbf{k}T\ln(S)} \quad 1.6$$

$$\Delta G_{crit} = \frac{4\pi\gamma r_{crit}^2}{3} \quad 1.7$$

Equation 1.6 describes the dependence of r_{crit} on supersaturation. For crystallization from melts, the critical radius is instead dependent on supercooling (Equation 1.8). In this equation, γ is the surface energy of the nucleus, M *i*s the molar mass of the compound, T_m is the melting temperature, $\Delta\underline{H}^{fus}$ is the molar heat of fusion, T is the supercooled temperature, and ρ is the crystal density.

$$r_{crit} = \frac{2\gamma M T_m}{\Delta\underline{H}^{fus}\rho(T_m - T)} \quad 1.8$$

Classic nucleation theory assumes that a supersaturated solution or supercooled melt undergoes statistical fluctuations in concentration due to molecular motion, resulting in areas of transient high and low supersaturation within the solution. Within the areas of high supersaturation, the free energy of the solute may drive the formation of crystal nuclei, and if the energy is sufficient to create nuclei of radius larger than r_{crit}, spontaneous crystal growth occurs. The rate at which nucleation occurs, J, with units of nuclei formed per time per volume, is highly dependent on γ, T, and S, and is typically described by an Arrhenius relation (Equation 1.9). The use of the Arrhenius relationship for this purpose requires the assumption that nuclei form by the single addition mechanism described above. Substituting equation 1.7 into 1.9 yields the Arrhenius expression for classic nucleation (Equation 1.10). Early attempts to measure J for liquids nucleating from vapor facilitated the estimation of J_0 when J, γ, ν, and S were known and

J_0 was assumed to be constant with respect to supersaturation. These reports revealed J_0 to be approximately 10^{25} nuclei/cm^3 s.[5] The J_0 for a condensing gas was also calculated to be approximately 10^{30} nuclei/cm^3 s using classic nucleation theory and the Kinetic-Molecular Theory of Gases.[6]

$$J = J_0 \exp(-\Delta G_{crit} / \mathbf{k}T) \tag{1.9}$$

$$J = J_0 \exp\left(\frac{16\pi\gamma^3 v^2}{3\mathbf{k}^3 T^3 \ln^2(S)} \right) \tag{1.10}$$

The presence of foreign substances in supersaturated solutions can serve to lower the energetic barrier to nucleation, and in many cases, reports of homogeneous nucleation were later revealed to proceed by a heterogeneous route. The influence of a surface on a nucleating phase depends on the contact angle, sometimes called the wetting angle, which forms between the surface and nucleating phase when nucleation occurs at the surface. This influence is expressed mathematically by the Young Equation (Equation 1.11 Figure 1-3).The contact angle, θ, results from static equilibrium driven by the interfacial tensions between the nucleating phase and the surrounding fluid, γ_{nl}, the surface and the fluid, γ_{sl}, and the nucleating phase and the surface, γ_{ns}.

$$\gamma_{sl} = \gamma_{ns} + \gamma_{nl} \cos\theta \tag{1.11}$$

Classic nucleation theory describes the influence of γ on the energetic penalty paid for forming the interface between a crystal and its surroundings. From this description, it is clear that any effect that might serve to lower the surface energy of the nucleating phase would also lower the barrier to nucleation, ΔG_{crit}. The effect of contact angle on the critical energy is described as a function, $\phi(\theta)$, that modifies ΔG_{crit} to produce a critical energy for heterogeneous nucleation,

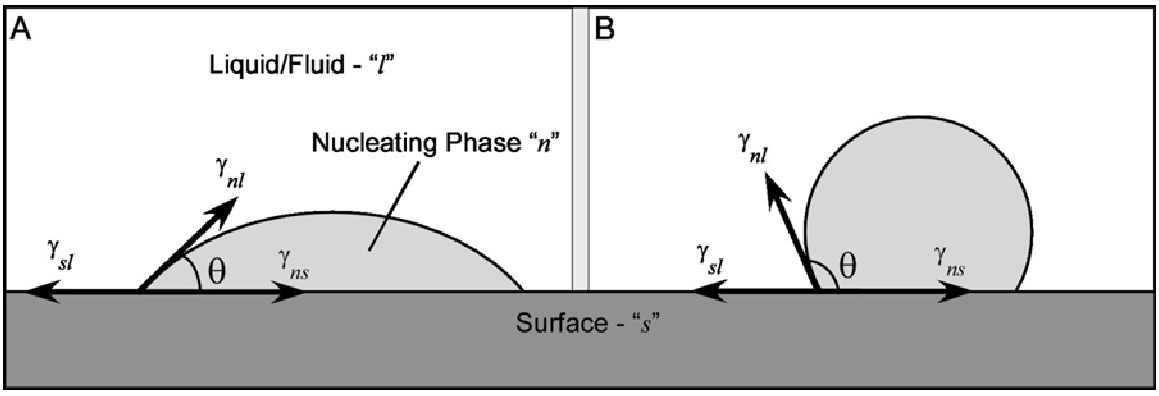

Figure 1-3. Illustration of the static equilibrium described by the Young equation. Three interfacial tensions, γ_{sl}, γ_{ns}, and $\gamma_{nl,}$ are balanced by the contact angle θ between the nucleating phase and the surface. (A) The case of good wetting, where $\theta < 180°$. (B) The case of poor wetting, where $\theta > 180°$.

$\Delta G'_{crit}$ (Equations 1.12, 1.13).[3] Any surface that permits wetting by the nucleating phase ($0° < \theta < 180°$) will reduce the energetic barrier to nucleation relative to the homogeneous route, whereas if the nucleating phase does not wet the surface at all ($\theta = 180°$), the result is consistent with homogeneous nucleation. In the limit of perfect wetting ($\theta = 0°$), the energetic barrier to nucleation is zero and no nuclei need to form for a crystal to grow, which is the case when seed crystals are added to a supersaturated solution.[7]

$$\Delta G'_{crit} = \phi(\theta)\Delta G_{crit} \qquad 1.12$$

$$\phi(\theta) = \frac{1}{4}(2+\cos\theta)(1-\cos\theta)^2 \qquad 1.13$$

Classic nucleation theory suffers from several deficiencies owing to the assumptions made in its development: (i) the theory assumes that thermodynamics is applicable for systems with only tens of particles, and that the macroscopic quantities such as γ and $\Delta\mu$ remain unchanged on the nanometer length scale. Thermodynamics is derived for a continuum, not for discrete particles, and nuclei of sizes on the order of one nanometer do not satisfy the continuum criteria, therefore thermodynamics cannot be assumed *a priori* to be applicable to crystal nuclei; (ii) real crystals

are neither spherical nor isotropic, and the addition of new particles to the nucleus depends on both the new particle configuration and location of attachment, resulting in the chemical potential $\Delta\mu$ having no clear definition even though one is assumed for the classic theory; (iii) the classic theory assumes *a priori* that a nucleus grows by single addition of molecules at the surface of a crystal; however, it does not account for the possibility of the crystallization of aggregates of pre-crystalline molecules, the combination of multiple nuclei into one crystal, or a multiple-step nucleation process that involves transient intermediate structures; (iv) in the cases of the formation of a crystalline solid from vapor, melt, or solution, there is a change of symmetry unaccounted for by the classic theory that occurs when the molecules pack into crystals. Furthermore, the classic description of nucleation neglects statistical mechanics, and this does not account for the contributions of particle translational and rotational states towards the nucleus free energy. As a result, thermodynamic aspects of the phase transformation are missing from the classic theory; (v) the kinetics of classic nucleation theory are dependent on the system exhibiting a slowly changing, near-equilibrium state, and a nucleation mechanism that passes through the structure of lowest free energy. In reality, systems rarely achieve such a state during crystallization; rather, the nucleation rate depends on the probability of the formation of a structure and not the free energy. Evidence of the flaws in classic nucleation kinetics appears in the pre-exponential factor – predicted to be approximately 10^{30} nuclei/cm^3 for nucleation of liquids from vapors – which varied between 10 to 10^4 nuclei/cm^3 s in later experimental measurements for crystallization from aqueous solutions.[4] This difference is noteworthy because reports on the nucleation rates of crystals employed the larger value for many years, leading to drastic overestimates of the nucleation rate of crystals. Despite these issues, classic nucleation theory remains a useful tool for understanding crystal growth phenomenon. Since the conception of the theory, scientists have reformulated it several times.[4,5,8] The outdated analytical models for

crystal growth, however, have replacements in simulations employing density functional theory,[9] statistical mechanics,[9] molecular dynamics,[10] Monte Carlo methods,[11] and various growth models.[12]

1-2: The Critical Size

Measurement of the critical size of crystal nuclei presents a significant challenge, primarily due to the difficulty researchers face in ensuring that nuclei form solely by homogeneous nucleation. Early attempts to measure crystal nuclei size resulted in estimates of nuclei sizes ranging from ten,[13] to one thousand,[14] to one million molecules.[15] Notably, the researchers in each of these cases ignored the degree of supersaturation, which can have a powerful impact on the critical size.

Recent reports describe attempts to measure critical size by fitting kinetic data to the classic theory and calculating r_{crit}. Boomadevi *et al*.[16] studied the growth of urea crystals from methanol solutions over a small range of low supersaturation values and temperatures. They reported critical radii ranging from 1.5 – 7.3 Å, corresponding to 0.2 – 22 molecules per nuclei. Additional work by other groups that employed the same technique generated critical size measurements of 3.5 – 9.6 Å (0.7 – 14 molecules) for potassium tetraborate tetrahydrate in water[17] and 15 – 32 Å (50 – 490 molecules) for bis glycine sodium nitrate.[18] In all of these examples the critical size decreases rapidly with increasing supersaturation, however, the small size of some of the nuclei reported, such as those containing less than one molecule per nucleus, suggests that this method does not always provide physically reasonable results. This failure is likely due to deficiencies in the assumptions used to develop classic nucleation theory.

The critical size of ice nuclei has been explored by a number of routes, including grazing-incidence X-ray diffraction, electron diffraction, and molecular dynamics simulations.[19] The diffraction studies suggest ice nuclei exhibit critical sizes no larger than 30 - 45 Å (500 - 1200 molecules), whereas the molecular dynamics simulations suggest the ice nuclei form in unstable 30 - 50 molecule groups, with the critical size ($d\Delta G_{cryst}/dr = 0$) corresponding to nuclei containing 150 molecules, and stable nuclei ($\Delta G_{cryst} < 0$) containing 500 molecules.[20] The experimental and simulated results for the critical size of ice are in good agreement, and are likely more accurate than those described previously as they are not based upon classic nucleation theory.

The growth of crystalline monolayers of bis(ethylenedithiolo)tetrathiafulvalene triiodide, $(ET)_2I_3$, on the basal plane of highly oriented pyrolytic graphite (HOPG) also exhibited critical size-like behaviors. Initial reports of the growth of $(ET)_2I_3$ on HOPG revealed that the $(ET)_2I_3$ formed monolayers that were epitaxially matched to the crystalline graphite surface.[21] A subsequent study examined the growth of $(ET)_2I_3$ in circular pits etched into the HOPG surface.[22] Formation of the monolayers near the edges of these pits was perturbed, and the rate of pit filling was inversely proportional to the size of the pit. Remarkably, in pits with diameters of less than 100 nm, the formation of $(ET)_2I_3$ monolayers was suppressed completely.

Only direct measurement of the critical size can provide concrete evidence on the nucleus size. Yau and Velikov[23] achieved the direct visualization of the nucleation of the protein apoferritin with atomic force microscopy (AFM). The large size of the apoferritin molecules facilitated their imaging via AFM, which revealed the assembly of the molecules into raft-shaped structures tens of nanometers long (20 – 50 molecules) and 1 – 2 molecules thick. The raft-shaped crystals grew from chain-like aggregates of molecules that the authors assert form in solution before settling on the AFM substrate. Notably, the authors observed that these molecular chains tended to dissolve on their own if they did not combine into the raft shaped crystals, leading them to speculate that

the chains of molecules were prenuclear aggregates. Notably, the report by Yau highlights that crystal nuclei are not spherical and can form in a multi-step process, which conflicts with the assumptions made for classic nucleation theory. In general, critical nuclei contain between 10-10^5 molecules, depending on the conditions of their formation, and exhibit sizes ranging from a few angstrom to tens of nanometers.[1]

1-3: Crystal Growth

Upon surpassing the critical size required for spontaneous growth, a crystal nucleus begins maturation towards its corresponding bulk crystal form. Researchers debate the process by which a crystal matures, and many crystal growth theories exist.[4] Gibbs[2] suggested the earliest theory of crystal growth as an extension his theory that a droplet with minimized surface free energy is most stable.[7] According to this theory, known as the surface energy model of crystal growth, the growth of a crystal, which is composed of faces with different surface energies, proceeds to minimize the total surface energy of the crystal. This leads to increased growth perpendicular to high-energy faces, while low energy faces tend to dominate the crystal. Furthermore, the theory suggests an ideal crystal in supersaturated conditions would adopt an equilibrium shape dictated by these surface energies. Wulff[24] proposed a construction that demonstrated that the surface energy model should hold true, and suggested that the growth perpendicular to the crystal faces occurs at rates proportional to the surface energy. Later mathematical proofs confirmed that the Wulff construction produced crystal shapes with absolute minimum surface energy.[25]

In practice, the competition of growth between crystal faces can result in faces exhibiting fast outward growth disappearing from the crystal (Figure 1-4). Furthermore, despite the assertions that crystals adopt equilibrium shapes, real crystals almost never appear the same because the

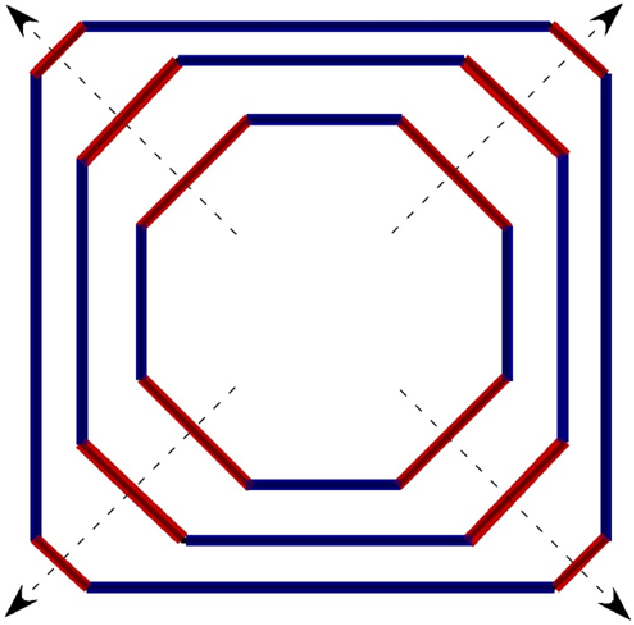

Figure 1-4. As a crystal grows outward, high-energy faces (red) tend to become smaller, owing to rapid growth perpendicular to those surfaces. Consequentially, the low energy faces (blue) dominate the shape of the crystal, and in many cases, the high energy faces vanish, forming corners.

crystal growth environment is constantly changing and so crystal growth is never at equilibrium. Additionally, the surface energy model does not provide a robust kinetic description for crystal growth, and very little quantitative data exists to support the minimal surface energy postulate. Despite these considerations, the surface-energy model for crystal growth is qualitatively useful in understanding and predicting crystal growth behaviors. Additionally, in further attempts to reduce the total surface energy of a system, small crystals tend to dissolve in favor of their material migrating to larger, more stable crystals. This process, known as Ostwald Ripening,[26] has been widely documented.[7] Newer growth theories, such as the adsorption layer theory, kinematic theory, diffusion-reaction theory, and others attempt to overcome the limitations of the surface energy model. Those theories are beyond the scope of this thesis, but are well documented elsewhere.[4]

The morphologies, or shapes, of crystals fit into categories known as habits (Figure 1-5). As mentioned above, the surface energy model for crystal growth predicts that growth perpendicular to a crystal face is proportional to the surface energy of that face; therefore, it is conceivable that an external influence capable of altering the surface energy of a particular crystal face may alter the crystal growth in certain directions. This ultimately alters the crystal habit. Consequentially, crystal habit can be influenced by interactions between crystal faces and solvents and impurities, or by manipulating crystallization rates, supersaturation, temperatures, and other environmental factors.[7] Controlling crystal habit is of great importance in the industrial sector, where crystals exhibiting certain habits are more prone to caking, other habits have a poor appearance, and others still are difficult to package or handle. It comes as no surprise, then, that the manipulation of crystallization factors has led to a vast array of techniques to assist in the control crystal habit.

The use of impurities, referred to as additives or auxiliaries when their presence is included deliberately in a crystallization environment, is the habit-controlling technique highlighted in this thesis. Most auxiliaries are chosen empirically, by trial-and-error. Thousands of reports on the effects of impurities on the growth of crystals exist in the literature,[1,7] however, the elegant example of the suppression of benzamide growth in along one of [100] (the *a* crystal axis), [010] (the *b* crystal axis), or [001] (the *c* crystal axis) by carefully selected *tailor-made* auxiliaries demonstrates the power of impurities on crystallization.[27] The phrase tailor-made is somewhat of a misnomer, as few of these additives are synthesized specifically for the purpose of habit modification. Rather, tailor-made crystallization auxiliaries are selected for their structural compatibility with some aspect of the crystal (instead of being chosen empirically). This is the case with the crystallization of benzamide, where the selection and use of benzoic acid, *o*-toluamide, and *p*-toluamide as crystallization auxiliaries selectively suppress the growth of benzamide crystals along the *b*, *a*, and *c* crystal axes, respectively.

Figure 1-5. (Left) Idealized examples of some of the many habits observed in crystals, including needles (formally: "acicular"), plates (formally: "tabular" or "lamellar"), cubes, and octahedra. (Middle and Right) Photographs of minerals exhibiting various natural habits. All photographs used in this figure are public domain. Source: http://en.wikipedia.org/wiki/Crystal_habit Last accessed: 2 April, 2009.

1-4: Polymorphism

Polymorphism, the ability of molecules to adopt multiple crystalline forms, was once thought to be a rare phenomenon, but is now known to be common.[1,28] The importance of polymorphism is underscored by efforts in the pharmaceutical sector, where polymorph discovery and characterization are essential for evaluating the bioavailability and shelf stability of pharmaceutical compounds, establishing patent protection for new crystal forms, complying with regulations that mandate polymorph characterization, and achieving reproducible crystallization outcomes.[29] The pervasiveness of polymorphism has inspired comments such as that by McCrone, "…every compound has different polymorphic forms and that, in general, the number of forms known for a given compound is proportional to the time and money spent in research on

that compound."[30] Two examples of polymorphs fit the strict definition above: (i) packing polymorphs, where molecules pack into different crystals in distinct molecular arrangements, and (ii) conformational polymorphs, where molecules pack into different crystals in the same packing arrangement with distinct molecular conformations. Several other solids present parallels to polymorphism but do not fit the strict definition. Most thorough treatises on polymorphism, such as the works of Threlfall,[31] Vippagunta *et al.*,[32] Bernstein,[1] or Brittain,[33] discuss one or more of these parallels in detail. The first examples are solvates, which contain the crystallizing molecules of interest and solvent molecules from the surroundings. Solvates containing water are referred to as hydrates, and are frequently mistaken for traditional polymorphs. Amorphous solids, although noncrystalline, are included as a parallel because many of the methods used to generate polymorphs also generate amorphous solids. Furthermore, amorphous solids are preferable to crystalline solids in many applications, therefore the pursuit of a stable amorphous phase parallels the study of polymorphism. Chiral crystals, which can form from achiral as well as chiral compounds, are called enantiomorphs. Furthermore, mixtures of two opposite enantiomorphs consisting of enantiopure chiral molecules are called conglomerates, and crystals formed from racemic mixtures of chiral molecules are called racemates. Non-racemic crystals composed of opposite enantiomers are treated as solid solutions. The separation of racemic mixtures of conglomerate crystals is a widely-studied field,[34] but the separation of racemate crystals into their corresponding conglomerates is challenging and approached as though the crystals were polymorphs. Additional examples of solids that exhibit properties related to polymorphism exist,[1] but are not mentioned here for brevity.

The thermodynamics of classic nucleation theory describes the total free energy of a crystal as being a combination of its surface and volume free energies. Two or more polymorphs, each with a unique internal structure and external surfaces, have different free energies. The prevalence of

one polymorph over another was described by Etter[35] as resulting from a complex equilibrium between competing nuclei - which resemble their mature crystalline forms - and disordered molecules (Figure 1-6), where eventually one or more nuclei achieve critical size and grow spontaneously, thereby adopting a polymorphic form and driving equilibrium in the direction of that growing polymorph. Experimental evidence for the competition between nuclei has been reported,[36,37] lending credence to the Etter postulate.

The relative stability of two polymorphs depends on their free energies, with the form having the lowest being the most stable. Thermodynamics dictates that the polymorph with the highest energy should transform to the form with the lowest energy over time. The Gibbs Free Energy (Equation 1.14: G is free energy, S is entropy, H is enthalpy, and T is temperature) of the polymorphs can be used to describe how the different forms relate to one another at different temperatures. The enthalpy and free energy of crystal formation are measurable quantities, and so graphs - denoted here as E/T diagrams - of the free energies and enthalpies as a function of temperature illustrate the thermotropic relationship between two polymorphs

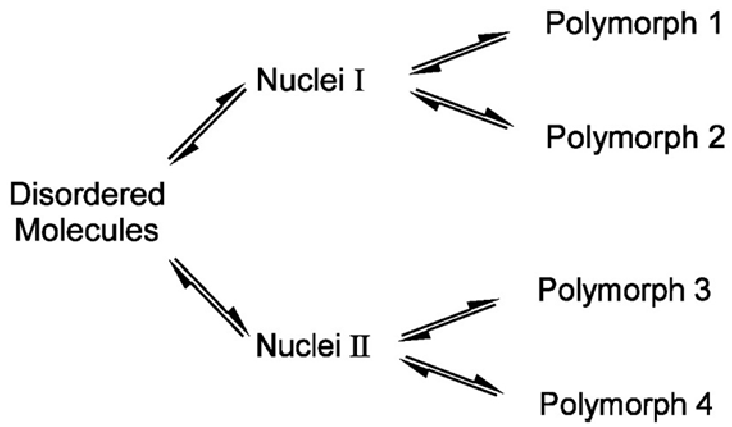

Figure 1-6. Scheme illustrating the equilibrium between competing crystal nuclei and their mature polymorphic forms.

(Figure 1-7).[ii] These plots do not provide any kinetic information about the phase changes. Two possible relationships exist between any two polymorphs and their melt. The first relationship, enantiotropism, arises when one polymorph transforms to another as temperature increases, and ultimately gives way to the melt (Figure 1-7A). The second relationship, called monotropism, arises when one polymorph is thermodynamically preferred over all temperatures until that polymorph melts (Figure 1-7B).

$$G = H - T \cdot S \tag{1.14}$$

Etter's model of competing nuclei suggests that a kinetic preference for the nuclei of a metastable polymorph may result in the thermodynamically stable form never appearing, because it only grows from a kinetically unfavored nucleus. Classic nucleation theory, with the concepts of critical size and the kinetics established by Volmer[3] (Equation 1.10), provides insight into the competition between polymorphs. Consider a case where a metastable polymorph, with a lower ΔG_{crit} compared with the more stable form, nucleates faster and appear first. Depending on the kinetic barrier to transformation to the more stable form, the metastable polymorph could persist for seconds, days, or even indefinitely. This example highlights the struggle between thermodynamic and kinetic dominance on crystallization, a problem evident from experimental results before the formulation classic nucleation. In an attempt to describe the appearance of these cases, Ostwald[38] suggested his Rule of Stages, "when leaving a metastable state, a given chemical system does not seek out the most stable state, rather the nearest metastable one that can be reached without loss of free energy".[39] Rephrased, polymorph transitions occur between the

[ii] Due to the ease of controlling pressure and temperature in experimental conditions, Pressure-Temperature (P/T) phase diagrams that describe ranges of polymorph appearance are also produced. These diagrams also reveal enantiotropic and monotropic behavior, but over a much wider range of conditions than the E/T diagrams, albeit without enthalpy or free energy information.

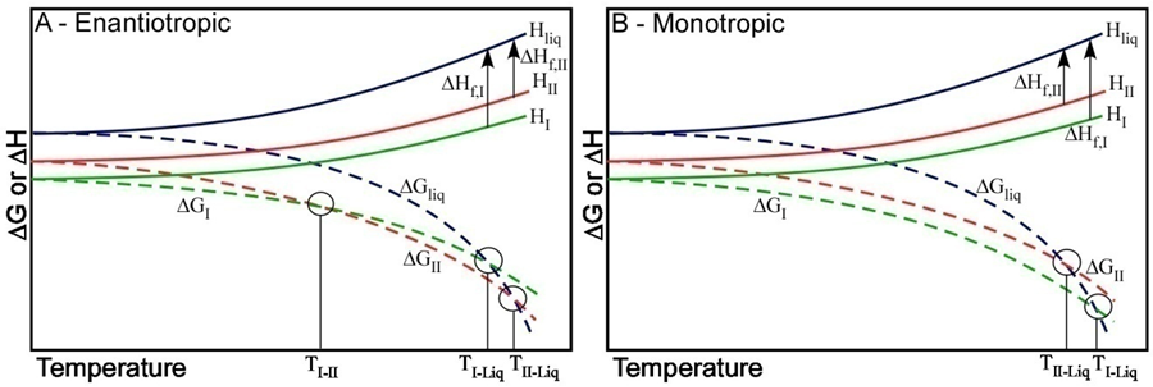

Figure 1-7. Energy/Temperature diagrams for two hypothetical substances, where the energies on either diagram are relative to an arbitrary standard. The substance on the right (A) exhibits an enantiotropic polymorph system, where polymorph I is most stable (lowest ΔG) until a transition temperature $T_{I\text{-}II}$, thereafter polymorph II is preferred. Eventually a temperature is reached where the polymorphs melt. The substance on the right (B) exhibits a monotropic system, where polymorph I is most stable over the entire temperature range prior to its melting. Transition temperatures between polymorphs and the melt are noted as $T_{x\text{-}y}$, where x and y are the corresponding form or melt. The heats of formation, $\Delta H_{f,x}$, of a given polymorph x are also apparent on the graphs.

forms with the lowest activation barriers. The complicated interplay of kinetics and thermodynamics that are observed in studies of polymorphism have resulted in a wide variety of examples that support and conflict with the Rule of Stages. Attempts to validate the Rule of Stages with the kinetics of classic nucleation revealed that Ostwald's assertion is not so simple in practice, and the rates of nucleation of two phases can intersect multiple times over a range of supersaturations. Notably, the intersection of the nucleation rates suggests conditions where two (or more) forms could nucleate simultaneously;[40] this phenomenon of concomitant polymorph growth has been reported for a number of systems.[41] Despite these deviations from the Rule of Stages, however, sufficient examples of successively crystallizing polymorphs exist to justify using the Rule of Stages as a guideline for understanding polymorph transitions.[1,7,33]

1-5: Polymorph Properties and Control

Polymorphs of a compound can manifest substantially different bulk physical properties, which can profoundly influence the behavior of a material dependent on the crystals. Consequently, the study and control of polymorphism is of great importance to sectors that harness crystal properties. This is most evident in pharmaceuticals.[1, 33] Both active pharmaceutical ingredients and formulation excipients can be crystalline, and the crystal forms adopted impact the rate of dissolution, solubility, stability, and aggregation behavior of the final product. According to Bernstein,[1] the dissolution properties and solubility of a compound are the greatest factors considered when selecting a crystalline form for the formulation of a drug. Furthermore, the control of the bioavailability of a compound, which is related to its dissolution rate and solubility, is also critical to the success of a pharmaceutical solid. For these reasons, many dosage forms incorporate amorphous solids and solvates as well. Polymorph stability is also crucial to the success of a formulation. In some cases, the inclusions of unstable polymorphs in formulations are intentional, and a polymorph transition is important to the product function. In other cases, polymorph transitions are undesired. The most dramatic examples of undesired polymorph transitions are those where a well-characterized polymorph vanishes or a new polymorph nucleates irreversibly.[42] For the pharmaceutical industry in particular, the legal, regulatory, and financial repercussions of an unexpected polymorph transitions can be severe.

Many dyes and explosives exhibit polymorphism, and in many cases the polymorphs impact the color (dyes) and stability (explosives) of the compounds.[1] As a result, researchers thoroughly characterize the polymorphism of these materials to ensure product function. Notably, the study of the impact of crystal structure on the electrical conductivity, magnetism, and other properties of materials has resulted in a keen interest in structure-property relationships.[1] Engineering

crystalline materials that exhibit specific electrical or magnetic properties from organic compounds presents a substantial challenge owing to significantly differences in behaviors exhibited by polymorphs. The study of structure-property relationships, however, has revealed many experimental strategies for obtaining polymorphs with specific properties.[43]

The primary methods employed to control polymorphism are similar to those used to control habit, which is unsurprising due to the codependence of habit and polymorphism on crystal structure. Polymorph selectivity is frequently achieved by growing crystals via sublimation, cooling of molten material, vapor diffusion or by evaporation of solvents. Additional routes to generating polymorphs include manipulating solvent systems, solubility, pH, temperature and thermal treatment, mechanical processing, and additives.[44] Crystallization on the cleaved surfaces of other crystals also induces selectivity,[45,46,47] and the use of tailor-made auxiliaries in controlling crystal habit by inhibiting the growth of specific crystal faces has parallels in polymorph control.[48] Recent reports detail the use of polymer heteronuclei as additives for controlling polymorphism.[49,50] The rate of crystallization can impact polymorph selectivity, and many of the methods mentioned above are used crystallize different polymorphs in near-thermodynamic or kinetic conditions.

Recently, the structure-property relationships of crystals and their formation have received substantial attention,[51,52] with a keen interest in understanding nucleation at the pre-crystalline aggregate stage in an effort to develop control strategies for nucleation.[53] These and related studies have provided insight into the control of crystal habit and polymorphism, both of which were traditionally empirical sciences. Structure-property relationships will remain a central theme throughout this thesis.

1-6: Examples of Polymorphism

While numerous examples of polymorphism exist in the literature, several well-known examples illustrate the general problem of polymorphism in academia and industry. The polymorphism of 5-methyl-2-[(2-nitrophenyl)amino]-3-thiophenecarbonitrile, known as ROY for the rich red, orange, and yellow colors of its various crystal forms (Figure 1-8), is one such case. ROY is a precursor to the antipsychotic drug olanzapine,[54] and adopts at least ten polymorphs (Figure 1-8, Table 1-2).[55] The many forms of ROY have been crystallized by a variety of methods, including fast crystallization, cooling of molten material, solution-mediated transformation,[56] epitaxy on single-crystal substrates,[47] crystallization under nanoconfinement,[57] and cross-nucleation on other ROY polymorphs.[58,59] Notably, most of the polymorphs of ROY are quite stable at ambient conditions, with several lasting indefinitely while others last from days to weeks. This characteristic of ROY, which is not ubiquitous among polymorphic systems, has allowed seven of the ROY polymorphs to be solved by X-ray crystallography and permitted detailed probing of the transformations between the various polymorphs. Furthermore, the conformational polymorphism that leads to the vibrant colors of the ROY polymorphs is one example of a structure-property relationship.[60]

Glycine is the simplest amino acid, a common excipient in pharmaceutical formulations, and is of interest in the study of the origin of life in the solar system. Glycine adopts three forms at ambient conditions, each of which exhibits well-defined habits and hydrogen bonding schemes, and two more at high pressures.[61] The most common polymorph of glycine, denoted as α,[62] is metastable and obtained by slow evaporation of water from aqueous glycine solutions, however, it is slow to transform to the most thermodynamically stable form, denoted as γ,[63] most likely

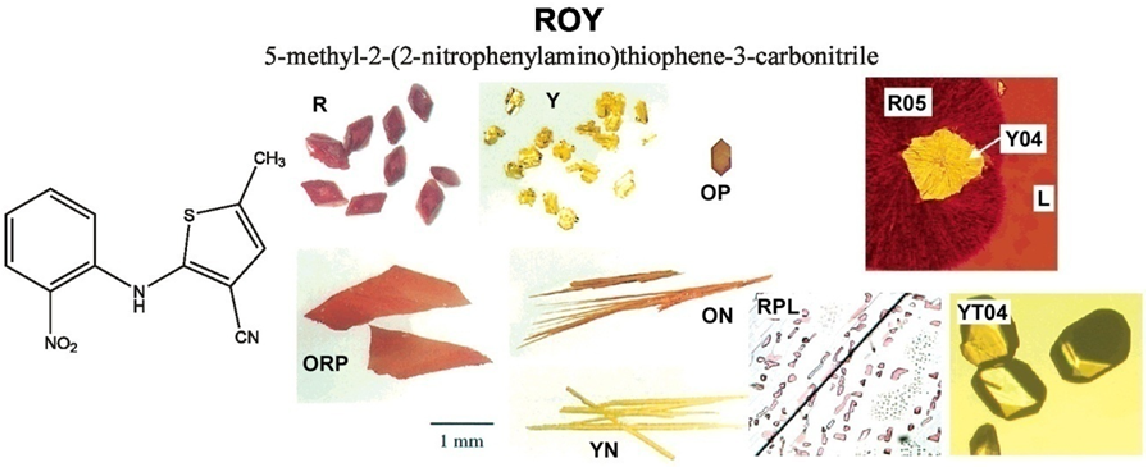

Figure 1-8. The molecular structure and photographs of the ten known polymorphs of 5-methyl-2-(2-nitrophenylamino)thiophene-3-carbonitrile, also known as ROY. The polymorphs are identified by abbreviation in Table 1-2, except for the phase labeled L, which is the red melt of ROY. The photographs are reproduced and modified from references 56, **Error! Bookmark not defined.**52, 58, and 59; used with permission. Copyrights, American Chemical Society, 2000, 2001, 2005, 2005.

Table 1-2. Polymorphs of ROY. Reproduced with permission from reference 58. Copyright American Chemical Society, 2005.

name	description	space group	mp, ºC	year reported
Y	yellow prism	$P2_1/n$	109.8	1995
R	red prism	$P1$	106.2	1995
ON	orange needle	$P2_1/c$	114.8	1995
OP	orange plate	$P2_1/n$	112.7	2000
YN	yellow needle	P-1	99	2000
ORP	orange-red plate	*Pbca*	97.4	2000
RPL	red plate	*a*	*b*	2001
Y04	yellow (2004)	*a*	*b*	2005
YT04	yellow prism	$P2_1/n$	106.9	2005
R05	red (2005)	*a*	*b*	2005

(a) structure not yet solved. (b) polymorph transition before melting

owing to substantial differences in molecular packing between the two forms (Figure 1-9). γ-glycine is formed by evaporation of water from acidic or basic aqueous solutions. The crystal structure of α-glycine consists of sheets of hydrogen bonded head-to-head dimers of glycine molecules, related to each other by inversion. This results in crystals that are nonpolar. In contrast, the γ-glycine structure consists of hydrogen bonded helices of glycine molecules. The

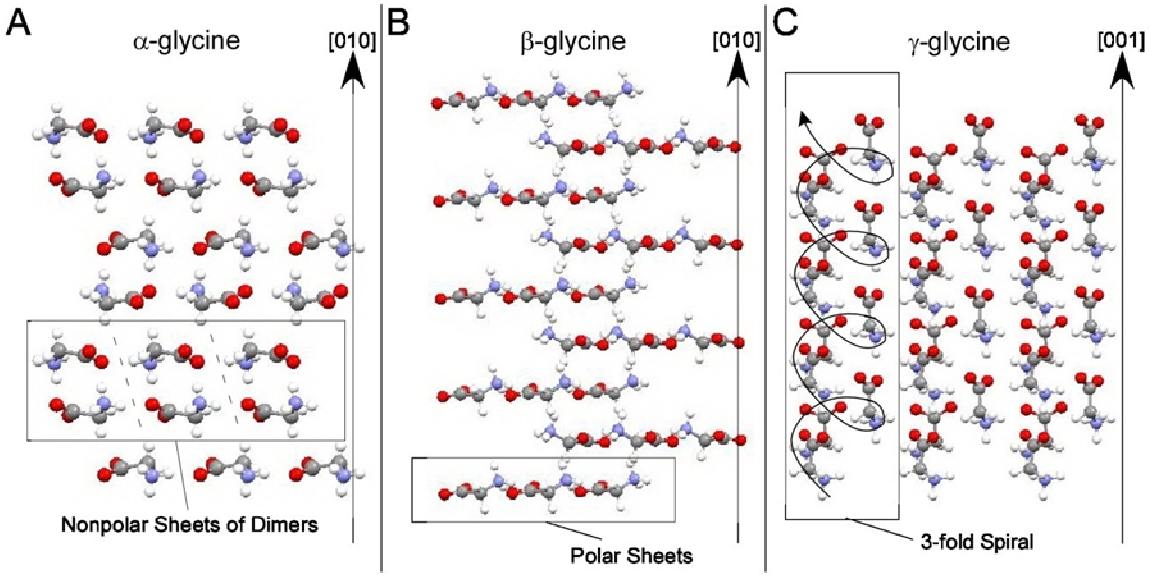

Figure 1-9. Comparison of the crystal structures of the (A) α, (B) β, and (C) γ polymorphs of glycine. Each polymorphs has a characteristic structure feature that is used to describe its structure. (A) α-glycine, which is readily crystallized from water, is composed of stacked sheets of head-to-head dimers, which are related to each other by inversion. As a result, α-glycine is nonpolar. (B) β-glycine, the least stable form, is composed of stacked sheets of molecules whose carboxyl moieties are exposed in the [010] direction and alkyl hydrogens pointed in the [0-10] direction. This packing results in β-glycine being polar. β-glycine converts readily to α-glycine in ambient conditions. (C) γ-glycine, the most stable form, is composed of densely packed 3-fold helices (spirals) of glycine molecules and is polar. Comparison between the three structures clearly reveals that γ-glycine is substantially different than α and β. Consequentially, α-glycine converts to γ-glycine very slowly.

most metastable ambient form of glycine, denoted as β,[64] is typically crystallized by rapidly decreasing the solubility of glycine in water, normally by adding alcohol to aqueous glycine solutions. This form rapidly transforms to α upon contact with humid air. The structure of β-glycine consists of hydrogen bonded molecular sheets, such as those observed in α-glycine, however, the β-glycine sheets are polar. The rapid transformation of β- to α-glycine is understandable, particularly when compared with the substantial structural differences between γ- and α-glycine, due to the small modification required to transform the β structure into the α structure. The thermal and temporal stability of glycine polymorphs are well studied,[65] and

glycine has been studied for the verification of pre-nuclei aggregates. For several years, glycine was suspected to exist as dimers in aqueous solution, owing to the formation of the favored α-glycine polymorph from hydrogen bonded cyclic glycine dimer units.[66] No evidence was reported, however, suggesting the existence of these dimers in undersaturated conditions. Indeed, a recent report revealed that the observation of glycine dimers was due to supersaturated conditions prior to crystallization, and that the association of glycine molecules into dimers in *undersaturated* solutions was unpreferred compared to glycine molecules existing as monomers in solution.[67] Glycine has also been a model system for the exploration of the effects of tailor-made auxiliaries on polymorphism and crystal habit. Recently, researchers employed specific tailor-made auxiliaries consisting of other amino acids to selectively crystallize each of the three main polymorphs of glycine, as well as selectively grow particular enantiomorphs of the chiral β-glycine.[68] Glycine will be a centerpiece in subsequent thesis chapters, owing to the wealth of literature on its polymorphic forms.

Two illustrative examples of polymorphism from the pharmaceutical sector that have had significant impact on the popular view of polymorphism include ranitidine hydrochloride (GlaxoSmithKline's Zantac) and ritonavir (Abbot's Norvir).[1] GSK patented the first form of ranitidine hydrochloride (RHCl) and a second form nucleated unexpectedly during scale-up several years later. The company patented the second form and shifted their entire RHCl production to produce it. The second form exhibited a needle habit, making it easier to process than the first form, which exhibited a plate habit. When the patent protection on the first form expired, the generic drug company Novopharm attempted to prepare the first form for the market, but only produced the second form. When Novopharm attempted to bring their drug to market, GSK sued the company for infringing upon its patents. Other litigations arose involving RHCl for similar issues, which ranged from discovery and recognition of polymorphic forms, to the roles of

the environment on polymorph selectivity, to polymorph stability, seeding, and polymorph purity. Abbot sold ritonavir for two years before a second polymorph formed unexpectedly. The second form had significantly lower bioavailability and solubility than the first, and eventually seeded the entirety of Abbot's ritonavir production, preventing production of the first form. As a result, Abbot removed ritonavir from the market for a year while they reformulated the drug to make use of the new polymorph. The capital loss incurred by Abbot over the mishap totaled over $500 million. These two cases of new and disappearing polymorphs are not isolated, and many other reports exist of similar behaviors in other systems.[1,33,42]

1-7: Concluding Remarks

Collectively, these reports highlight the challenges surrounding polymorphism, and discuss a number of methods by which polymorphism is controlled. Classic nucleation, however, suggests an additional method for controlling polymorphism. The concept of the critical size suggests that polymorph control may be achieved by intervening in the crystallization process on a corresponding length scale. For example, if a crystal exhibits two polymorphic forms, one form may grow selectively if limited to sizes below the critical size of the competing form. Alternatively, the energetic profile of two competing polymorphs may intersect, suggesting a length scale where a normally metastable polymorph (Form A) becomes thermodynamically preferred (Figure 1-10). Furthermore, it is possible in theory to suppress crystallization altogether if nuclei cannot achieve a favorable negative free energy.

To achieve the size constraints necessary for size-dependent polymorph control, crystallization reactors are needed that simultaneously permit crystal growth within them while confining the crystals to nanometer length scales. Chapter 2, Properties of Ultrasmall Crystals, reviews

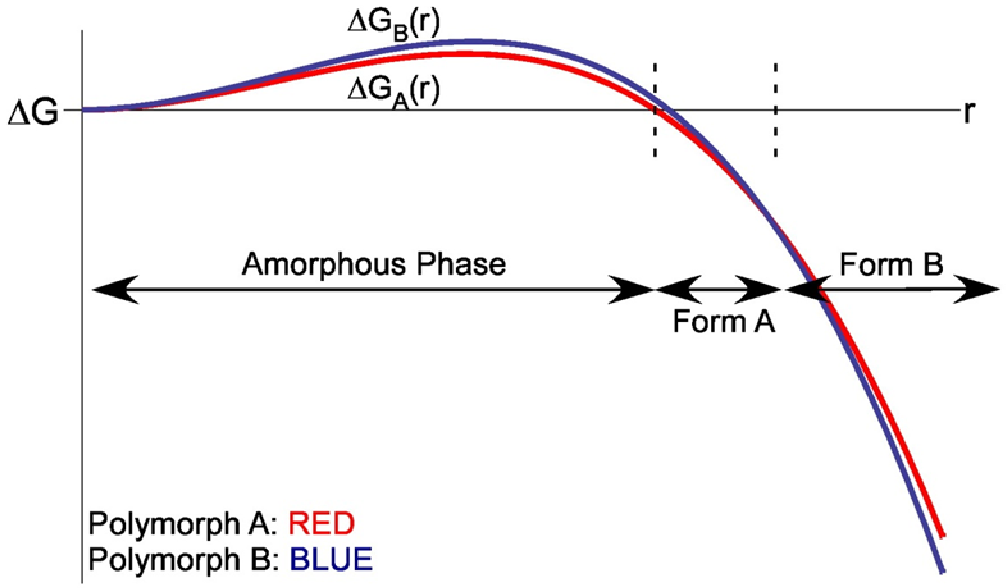

Figure 1-10. Illustration of the energetic profiles of two competing nuclei, Form A, and Form B, over a range of characteristic lengths. Crystallization of form B, which is thermodynamically stable bulk form in this illustration, may be suppressed if sufficient size constraints can be placed upon the growing nuclei. If the size confinement is sufficiently small, the crystallization of both forms may be suppressed in favor of an amorphous phase. This suppression would be expected to occur at any length scale where crystal nuclei are not permitted to achieve $\Delta G < 0$, which includes dimensions in excess of the critical size.

crystallization within a number of these crystallization reactors and discusses the crystallization of select organic molecules in detail. Chapter 3 discusses the phase behavior of glycine crystals embedded in nanoporous matrices. Chapter 4 discusses the orientation of the glycine crystals within ordered porous polymer monoliths. This thesis concludes with suggestions for future work, including preliminary results for the preparation of a new porous material, developed from block copolymers, with ordered pores and chiral moieties lining the pore walls.

1-8: References

1. Bernstein, J. *Polymorphism in Molecular Crystals*; Clarendon Press: Oxford, 2002.
2. Gibbs, J. W. *Collected Works, Vol. 1, Thermodynamics*; Yale University Press: New Haven, 1948.
3. Volmer, M. *Kinetic Der Phasenbildung*; Steinkoff: Dresden, 1939.
4. Nyvlt, J.; Sohnel, O. Matuchova, M. Broul, M. *The Kinetics of Industrial Crystallization*; Academia: Prague, 1985.
5 . Markov, I. V. *Crystal Growth for Beginners*; World Scientific: London, 2003.
6. Nielsen, A. E. *Kinetics of Precipitation*; Pergamon Press: New York, 1964.
7. Mullin, J.W. *Crystallization*; Elsevier Butterworth-Heinemann: London, 2001.
8. Ring, T. A. Nano-sized cluster nucleation. *Adv. Coll. Int. Sci.* **2001**, *91*, 473-499.
9. Oxtoby, D. W. Nucleation of First-Order Phase Transitions. *Acc. Chem. Res.***1998**, *31*, 91-97.
10. Vlieg, E.; Deij, M.; Kaminski, D.; Meekes, H.; van Knckevort, W. Towards an atomic-scale understanding of crystal growth in solution. *Faraday Disc.* **2007**, *136*, 57-69.
11. ten Wolde, P. R.; Ruiz-Montero, M. J.; Frenkel, D. Numerical calculation of the rate of crystal nucleation in a Lennard-Jones system at moderate undercooling. *J. Chem. Phys.* **1996**, *104*, 9932-9947.
12. Lan, C.W. Recent progress of crystal growth modeling and growth control. *Chem. Eng. Sci.* **2004**, *59*, 1437-1457.
13. Garten, V. A.; Head, R. B. Crystalloluminescence and the nature of the critical nucleus. *Phil. Mag.* **1966**, *14*, 1243-1253.
14. Otpushchennikov, N. F. Determination of the size of the elementary crystal nucleus from acoustic measurement. *Soviet Phys. Cryst.***1962**, *7*, 237-240.
15. Adamski, T. Commination of crystal nucleation by a precipitation method. *Nature* **1963**, *197*, 894.
16. Boomdevi, S.; Dhanasekaran, R.; Ramasamy, P. Investigations on Nucleation and Growth Kinetics of Urea Crystals from Methanol. *Cryst. Res. Technol.* **2002**, *37*, 159-168.
17. Sahin, O.; Dolas, H.; Demir, H. Determination of nucleation kinetics of potassium tetraborate tetrahydrate. *Cryst. Res. Technol.***2007**, *42*, 766-772.
18. Selvaraju, K.; Kirubavathi, K.; Vijayan, N.; Kumararaman, S. Investigations on the nucleation kinetics of bis glycine sodium nitrate. *J Cryst. Growth* **2008**, *310*, 2859-2862.
19. Weissbuch, I.; Lahav, M.; Leiserowitz, L. Toward Stereochemical Control, Monitoring, and Understanding Crystal Nucleation. *Cryst. Growth Des.* **2003**, *3*, 125-150.
20. Matsumoto, M.; Saito, S.; Ohmine, I. Molecular dynamics simulation of the ice nucleation and growth process leading to water freezing. *Nature*, **2002**, *416*, 409-413.

21. (a) Last, J. A.; Hillier, A. C.; Hooks, D. E.; Maxson, J. B. Epitaxially-Driven Assembly of Crystalline Molecular Films on Ordered Substrates. *Chem. Mater.* **1998**, *10*, 422-437. (b) Hillier, A. C.; Maxson, J. B.; Ward, M. D. Electrocrystallization of an Ordered Organic Monolayer: Selective Epitaxial Growth of b-$(ET)_2I_3$ on Graphite. *Chem. Mater.* **1994**, *6*, 2222-2226.
22. Hooks, D. E.; Yip, C. M.; Ward, M. D. Nanoconfined Electrochemical Nucleation of Crystalline Molecular Monolayers on Graphite Substrates. *J. Phys. Chem. B* **1998**, *102*, 9958-9965.
23. Yau, S.-T.; Vekilov, P. G. Quasi-planar nucleus structure in apoferritin crystallization. *Nature* **2000**, *466*, 494-497.
24. Wulff, G. Zur Frage der Geschwindigkeit des Wachstums unter Auflosung der Kristallfiachen. *Z. Krist.* **1901**, *34*, 449-530.
25. (a)Dinghas, A. Über einen geometrischen Satzs von Wulff für die Gleichgewichtsform von Kristallen. *Z. Krist.* **1944**, *105*, 304-314. (b) Johnson, C. A.; Chakerian, G. D. On the Proof and Uniqueness of Wulff's Construction of the Shape of Minimum Surface Free Energy. *J. Math. Phys.* **1965**, *6*, 1403-1404.
26. Ostwald, W. *Lehrbuch der Allgemeinen Chemie*; Leipzig, Germany, 1896. Vol. 8, Part 1.
27. Berkovitch-Yellin, Z.; Addadi, L.; Idelson, M. Lahav, M.; Leiserowitz, L. Controlled modification of crystal habit by 'tailor made' impurities: application to benzamide. *Angewandt Chemie Supplement* **1982**, 1336-1345.
28. Buerger, M. J.; Bloom, M. C. Crystal polymorphism. *Z. Kristallogr.* **1937**, *96*, 182-200.
29. (a) Byrn, S. R.; Pfeiffer, R.; Ganey, M.; Hoiberg, C.; Poochikian, G. Pharmaceutical Solids: A Strategic Apporach to Regulatory Considerations. *Pharm. Res.* **1995**, *12*, 945–954. (b) Rodrigeuz-Hornedo, N.; Murphy, D. Significance of Controlling Crystallization Mechanisms and Kinetics in Pharmaceutical Systems. *J. Pharm. Sci.* **1999**, *88*, 651–660.
30. McCrone, W. C. Polymorphism. In *Physics and chemistry of the organic solid state;* Fox, D.; Labes, M. M.; Weissberger, A. Eds.; Wiley Interscience: New York, 1965. Vol. 2.
31. Threlfall, T. L. Analysis of Organic Polymorphs – A Review. *Analyst* **1995**, *120*, 2435-2460.
32. Vippagunta, S. R.; Brittain, H. G.; Grant, D. J. W. Crystalline solids. *Adv. Drug Delivery Rev.* **2001**, *48*, 3-26.
33. Brittain, H.G. *Polymorphism in Pharmaceutical Solids*; New York: Marcel Decker, 1999.
34. Collet, A.; Brienn, M.-J.; Jacques, J. Optical Resolution by Direct Crystallization of Enantiomer Mixtures. *Chem. Rev.* **1980**, *80*, 215-230.
35. Etter, M. C. Hydrogen bonds as design elements in organic chemistry. *J. Phys. Chem.* **1991**, *95*, 4601-4610.

36. (a) Petit, S.; Coquerel, G.; Hartman, P. Nucleation and crystal growth of molecular solvates with several conformations both in solution and in solid state; application to some hydrated copper(II) sulfoxinates. *J. Cryst. Growth* **1994**, *137*, 585-594. (b) Grandeury, A.; Condamine, E.; Hilfert, L.; Gouhier, G.; Petit, S.; Coquerel, G. Chiral Discrimination in Host-Guest Supramolecular Complexes. Understanding Enantioselectivty and Solid Solution Behaviors by Using Spectroscopic Methods and Chemical Sensors. *J. Phys. Chem. B* **2007**, *111*, 7017-7026.
37. (a) Näther, C.; Bock, H.; Claridge, R. F. C. Solvent-shared radical ion pairs [pyrene$^-$Na$^+$O(C_2H_5)$_2$]inf: ESR evidence for two different aggregates in solution, room temperature crystallization, and structural proof of another polymorphic modification. *Helv. Chim. Acta* **1996**, *79*, 84-91. (b) Näther, C.; Nagel, N.; Bock, H.; Seitz, W.; Halvas, Z. Structural, kinetic and thermodynamic aspects of the conformational dimorphism of diethyl 3,6-dibromo-2,5-dihydroxyterephthalate. *Acta Crystallogr. B* **1996**, *52*, 697-706.
38. Ostwald, W. F. Studies on formation and transformation of solid materials. *Z. Phys. Chem.* **1897**, *22*, 289-330.
39. Ciechanowicz, M.; Skapski, A. C.; Troughton, P. G. H. The crystal structure of the orthorhombic form of hydridodicarbonylbis(triphenylphosphine)-iridium(I): successful location of the hydride hydrogen atom from x-ray data. *Acta Crystallgr.* B **1976**, *32*, 1673-1680.
40. Davey, R. J. General discussion. *Faraday Discuss.* **1993**, *95*, 160-162.
41. Bernstein, J.; Davey, R. J.; Henck, J.-O. Concomitant polymorphs. *Angew. Chem. Int. Ed.* **1999**, *38*, 3440-3461.
42. Dunitz, J. D.; Bernstein, J. Disappearing Polymorphs. *Acc. Chem. Res.* **1995**, *28*, 193-200.
43. Bernstein, J. Crystal growth, polymorphism and structure-property relationships in organic crystals. *J. Phys. D.* **1993**, *26*, B66-B76.
44. Guillory, J. K. Generation of Polymorphs, Hydrates, Solvates, and Amorphous Solids, in *Polymorphism in Pharmaceutical Solids*; Brittain, H. G., Ed.; New York: Marcel Dekker, 1999. p. 183-226.
45. (a) Carter, P. W.; Ward, M. D. Topographically Directed Nucleation of Organic Crystals on Molecular Single-Crystal Substrates. *J. Am. Chem. Soc.* **1993**, *115*, 11521-11535. (b) Carter, P. W.; Ward, M. D. Directing Polymorph Selectivity During Nucleation of Anthranilic Acid on Molecular Substrates. *J. Am. Chem. Soc.* **1994**, *116*, 769-770.
46. Bonafede, S. J.; Ward, M. D. Selective Nucleation and Growth of an Organic Polymorph by Ledge-Directed Epitaxy on a Molecular Crystal Substrate. *J. Am. Chem. Soc.* **1995**, *117*, 7853-7861.
47. Mitchell, C. A.; Yu, L.; Ward, M. D. Selective Nucleation and Discovery of Organic Polymorphs through Epitaxy with Single Crystal Substrates. *J. Am. Chem. Soc.* **2001**, *123*, 19830-10839.

48. Weissbuch, I.; Addadi, L.; Lahav, M.; Leiserowitz, L. Molecular recognition at crystal interfaces. *Science* **1991**, *253*, 637-645.

49. Lang, M.; Grzesiak, A. L.; Matzger, A. J. The use of Polymer Heteronuclei for Crystalline Polymorph Selection. *J. Am. Chem. Soc.* **2002**, *124*, 14834-14835.

50. Price, C.; Grzesiak, A. L.; Matzger, A. J. Crystalline Polymorph Selection and Discovery with Polymer Heteronuclei. *J. Am. Chem. Soc.* **2005**, *127*, 5512-5517.

51. Davey, R. J.; Allen, K.; Blagden, N.; Cross, W. I.; Lieberman, H. F.; Quayle, M. J.; Righini, S.; Seton, L.; Tiddy, G. J. T. Crystal engineering – nucleation, the key step. *CrystEngComm* **2002**, *4*, 257-264.

52. Weissbuch, I.; Lahav, M.; Leiserowitz, L. Toward Stereochemical Control, Monitoring, and Understanding of Crystal Nucleation. *Cryst. Growth Des.* **2003**, *3*, 125-150.

53. Chiarella, R. A.; Gillon, A. L.; Burton, R. C.; Davey, R. J.; Sadiq, G.; Auffret, A.; Cioffi, M.; Hunter, C. A. The nucleation of inosine: the impact of solution chemistry on the appearance of polymorphic and hydrated crystal forms.

54. Lilly Industries Limited, Kingsclere Road, Basingstoke Hants RG21 2XA, U.K. Eur. Pat. 0 454 436 A1, Bulletin 91/44, Oct 30, 1991.

55. Yu, L. Survival of the fittest polymorph: how fast nucleater can lose to fast grower. *Cryst. Eng. Comm.* **2007**, *9*, 847-851.

56. Yu, L.; Stephenson, G. A.; Mitchell, C. A.; Bunnel, C. A.; Snorek, S. V.; Bowyer, J. J.; Borchardt, T. B.; Stowell, J. G.; Byrn, S. R. Thermochemistry and Conformational Polymorphism of a Hexamorphic Crystal System. *J. Am. Chem. Soc.* **2000**, *122*, 585-591.

57. Ha, J.-M.; Wolf, J. H.; Hillmyer, M. A.; Ward, M. D. Polymorph Selectivity under Nanoscopic Confinement. *J. Am. Chem. Soc.* **2004**, *126*, 3382-3383.

58. Chen, S.; Xi, H.; Yu, L. Cross-Nucleation between ROY Polymorphs. *J. Am. Chem. Soc.* **2005**, *127*, 17439-17444.

59. Chen, S.; Guzei, I. A.; Yu, L. New Polymorphs of ROY and New Record for Coexisting Polymorphs of Solved Structures. *J. Am. Chem. Soc.* **2005**, *127*, 9881-9885.

60. Yu, L. Color Changes Caused by Conformation Polymorphism: Optical-Crystallography, Single-Crystal Spectroscopy, and Computation Chemistry. *J. Phys. Chem. A* **2002**, *106*,544-550.

61. Dawson, A.; Allan, D. R.; Belmonte, S. A.; Clark, S. J.; David, W. I. F.; McGregor, P. A.; Parsons, S.; Pulham, C. R.; Sawyer, L. Effect of High Pressure on the Crystal Structures of Polymorphs of Glycine. *Cryst. Growth Des.* **2005**, *5*, 1415–1427.

62. Marsh, R. E. Refinement of the crystal structure of glycine. *Acta Crystallogr.* **1958**, *11*, 654–663.

63. Iitaka, Y. The crystal structure of γ-glycine. *Acta Crystallogr.* **1961**, *14*, 1–10.

64. Iitaka, Y. The crystal structure of β-glycine. *Acta Crystallogr.* **1960**, *13*, 35–45.

65. Boldyreva, E. V.; Drebushchak, V. A.; Drebushchak, T. N.; Paukov, I. E.; Kovalevskava, Y. A.; Shutova, E. S. Poylmorphism of Glycine. Thermodynamic Aspects. Part I. Relative stability of the polymorphs. *J. Therm. Anal. Calorim.* **2003**, *73*, 409–418; and Boldyreva, E. V.; Drebushchak, V. A.; Drebushchak, T. N.; Paukov, I. E.; Kovalevskava, Y. A.; Shutova, E. S. Polymorphism of Glycine. Thermodynamic Aspects. Part II. Polymorphic Transitions. *J. Therm. Anal. Calorim.* **2003**, *73*, 419–428.

66 . Weissbuch, I.; Torbeev, V. Yu.; Leiserowitz, L.; Lahav, M. Solvent Effect on Crystal Polymorphism: Why Addition of Methanol or Ethanol to Aqueous Solutions Induces the Precipitation of the Least Stable b-Form of Glycine. *Ange. Chem. Int. Ed.* **2005**, *44*, 3226-3229.

67. Huang, J.; Stringfellow, T. C.; Yu, L. Glycine Exists Mainly as Monomers, Not Dimers, in Superstaturated Aqueous Solutions: Implications for Understanding Its Crystallization and Polymorphism. *J. Am. Chem. Soc.* **2008**, *130*, 13973-13980.

68. Torbeev, V. Yu.; Shavit, E.; Weissbuch, I.; Leiserowitz, L.; Lahav, M. Control of Crystal Polymorphism by Tuning the Structure of Auxiliary Molecules as Nucleation Inhibitors. The β-Polymorph of Glycine Grown in Aqueous Solutions. *Cryst. Growth Des.* **2005**, *5*, 2190-2196.

Chapter 2: Properties of Ultrasmall Crystals

Chapter 1 discussed the fundamentals of crystallization, with an emphasis on the polymorphism of molecular organic crystals. Classic nucleation theory suggests that the relative stabilities between polymorphs can switch for crystals of sufficiently small size, particularly on length scales corresponding to the sizes of the crystal critical nuclei. One possible method for influencing crystal growth on these length scales is by crystallizing compounds within the nanometer-scale channels of porous materials. The study of crystallization within nanopores was motivated by Thomson (a.k.a. Lord Kelvin)[1] and Gibbs[2], who postulated that thermodynamic properties such as vapor pressure and melting point change for solids of decreasing size. This chapter reviews the dependence of melting point, polymorphism, and other properties on crystal size.

2-1: Size Dependent Properties of Condensed Phases

Scientists have studied the phase transitions of compounds embedded in porous materials for decades.[3] The physical constraints imposed by the pores limit the size of nucleating phases, increasing the surface-to-volume ratio of the embedded compound compared with larger

particles. This increase is implicated in altering several physical properties. For example, Thomson[1] modified the Young-Laplace equation (Equation 2.1, frequently simplified to Equation 2.2),[4] which describes the capillary pressure difference across an interface between two static fluids, to predict the effect of small droplet size on vapor pressure (Equation 2.3).

$$\Delta p = \gamma \nabla g \hat{n} \tag{2.1}$$

$$\Delta p = 2\gamma / r \tag{2.2}$$

$$RT \ln\left(p / p_0 \right) = 2M\gamma / \rho r \tag{2.3}$$

In Equation 2.1 and 2.2, Δp is the capillary pressure across the interface, γ is the surface tension, $\hat{n}$ is the unit vector normal to the interface, and r is the radius of curvature of the interface. In Equation 2.3, r is the radius of curvature of the droplet, ρ is the droplet density, γ is the surface tension of the interface between the droplet and its surroundings, M is the molecular mass of the compound comprising the droplet, p is the size-dependent vapor pressure, p_0 is the bulk vapor pressure – i.e. for a surface with infinite curvature, R is the universal gas constant, and T is absolute temperature. Thomson's result, now known as the Kelvin Equation,[i] revealed that the equilibrium between a condensed phase and its vapor were dependent on the curvature between them. The Kelvin equation predicts that vapor pressure increases as particle size decreases. Gibbs[2] derived an equivalent relation for the effect of curvature on the equilibrium of any pure

i. The author would like to draw attention to naming discrepancies in textbooks for the various equations discussed in this chapter. For example, equation 2.3 is called the "Kelvin Equation" in Hiemenz, P. C; Rajagopalan, R. *Principles of Colloid and Surface Chemistry*. Marcel Dekker: New York, 1997, but is called the "Gibbs-Thomson Equation" in Mullin, J. W. *Crystallization*. Butterworth-Heinemann: London, 2001. The name "Gibbs-Thomson equation", however, traditionally refers to equation 2.4.

substance with its surroundings. These works motivated additional explorations of the influence of size on equilibrium, resulting in relationships between particle size and vapor pressure,[5] solubility,[6] and melting temperature (Table 2-1).[6,7] Notably, Defay *et al.* derived the thermodynamic relationship between particle size and melting point that is now known as the Gibbs-Thomson Equation (Equation 2.4).[8,9]

$$\frac{T_{m,bulk} - T_m(r)}{T_{m,bulk}} = -\frac{2M}{\Delta \underline{H}^{fus} \rho r} \gamma_{nl} \cos\theta \qquad 2.4$$

The definitions of M, ρ, and r are the same as in the Kelvin Equation (Equation 2.3). γ_{nl} is the surface tension (interfacial energy) between the condensed phase and the fluid surrounding it (see the Young Equation, Chapter 1, Equation 1.11), θ is the interfacial angle between the condensed phase and any surface it may have nucleated upon, $\Delta \underline{H}^{fus}$ is the molar heat of fusion of the

Table 2-1. Expressions for the left hand side of the Kelvin equation, Equation 2.3, for different nucleation events. All of these expressions are contingent on the assumptions that the systems are ideal and that the entropies and enthalpies of transitions are independent of temperature. The temperatures T_i (i = transition type) are the bulk thermodynamic transition temperatures, while T are the size-dependent temperatures. $\Delta \underline{H}_i$ are the molar enthalpies of the transitions, written as positive numbers.

Nucleation Event	Left side of Equation 2.3	Alternate Expression
Vapor condensation into a liquid (vap) or solid (sub)	$RT\ln(p/p_0)$	$\frac{\Delta \underline{H}_{vap/sub}(T_{vap/sub} - T)}{T_{vap/sub}}$
Crystallization from solution	$RT\ln(c/c_0)$	$\frac{\Delta \underline{H}_{sol}(T_{sol} - T)}{T_{sol}}$
Bubble nucleation in liquid	$-RT\ln(p/p_0)$	$-\frac{\Delta \underline{H}_{vap}(T_b - T)}{T_b}$
Crystallization from melt	-	$\frac{\Delta \underline{H}^{fus}(T_m - T)}{T_m}$

bulk condensed phase, $T_m(r)$ is the melting temperature of the condensed phase of radius r, and $T_{m,bulk}$ is the melting temperature of the condensed phase in the bulk (as $r \rightarrow \infty$). The Gibbs-Thomson equation predicts a linear relationship between the change in melting point, $T_{m,bulk}$-$T_m(r)$, and the inverse particle size, $1/r$, but only if the other parameters are not size dependent. The θ term in Equation 2.4 is generally assumed to be $\theta = 180°$. Substituting that into Equation 2.4 results in the most widely used form of the Gibbs-Thomson Equation (Equation 2.5).

$$\frac{T_{m,bulk} - T_m(r)}{T_{m,bulk}} = \frac{2M\gamma_{nl}}{\Delta\underline{H}^{fus}\rho r} \qquad 2.5$$

The $\theta = 180°$ assumption is valid for homogeneous nuclei that do not wet the surface (Figure 2.1), however, it is used almost ubiquitously in the literature, even when imperfect wetting between a melting particle and a surface is expected. The Gibbs-Thomson equation can also be combined with the Young equation (Chapter 1 - Equation 1.11) to generate a form that also encompasses the dependence of the melting point on the interfaces between the particle, surrounding fluid, and substrate (Equation 2.6). Researchers only recently invoked this form of the relation to explain experimentally observed melting point behaviors.[10]

$$\frac{T_{m,bulk} - T_m(r)}{T_{m,bulk}} = \frac{2M(\gamma_{ns} - \gamma_{sl})}{\Delta\underline{H}^{fus}\rho r} \qquad 2.6$$

Much like the equations governing classic nucleation theory, the Kelvin and Gibbs-Thomson equations were derived for liquid droplets in equilibrium with their vapors. Only later were they extended to solids. Consequently, there are a number of assumptions in these models to address: (i) both equations assume that the bulk physical properties of a compound - γ, $\Delta\underline{H}^{fus}$, and ρ - remain constant with decreasing size; (ii) they also assume that γ is isotropic over the entire surface, which is particularly unlikely for a multi-faceted anisotropic crystal; (iii) the vapor

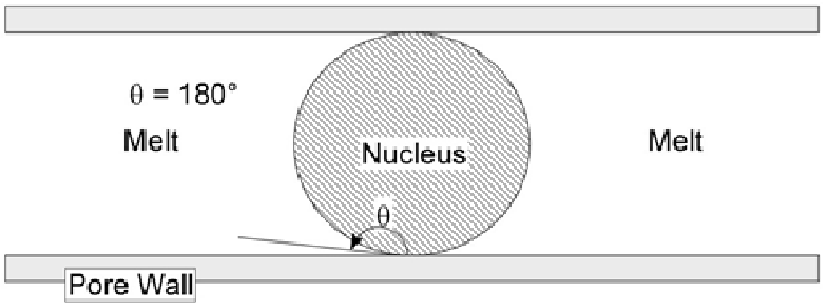

Figure 2.1. Schematic of a nucleus forming from the melt within a pore, where the nucleus does not wet the pore wall ($\theta = 180°$).

pressure of a small particle according to the Kelvin Equation is equivalent to the Laplace pressure across an interface in a capillary tube, which is only valid for a liquid droplet. Additional stresses in a crystal due to the anisotropy, rigidity, and high degree of molecular order cause dramatic deviations in vapor pressure predictions for crystals;[11] (iv) it is also notable that, while the Gibbs-Thomson equation is clearly stated for melting behavior, there are no corresponding analytic theories that associate solid-state transition temperatures such as amorphous-to-crystalline or polymorph transitions with decreasing pore size. This is in part because the non-melting transitions - freezing, vitrification, polymorph transitions and the like - are all prone to expressing kinetic barriers to change. In particular, glass transitions are kinetic phenomenon, although there is some discussion of the possibility of a thermodynamically mandated glass transition.[12] These barriers frustrate attempts to identify the thermodynamic behaviors of compounds under confinement. Consequentially, the effect of size confinement on melting point is studied far more widely than any other size-dependent phase transition.

2-2: Studies of Ultrasmall Crystals

Most early studies on the melting point depression of compounds embedded in porous solids were performed using porous siliceous materials, owing primarily to their availability. Reports

detailing the melting point depression of ice, benzene, naphthalene, and other organic molecules embedded in silica gel revealed substantial depression – by as much as 40 K – relative to the bulk solids. In addition to the depression, researchers noticed blurring of the melt transition, with reported temperature ranges as broad as 50 K.[13] Iodine absorbed on silica gel also exhibited melting point depression.[14] These early reports documented melting behavior in only one pore size of silica because materials with narrow pore size distributions and sufficiently small pore sizes were not available until later.[9] As a result, no single report examined the $1/r$ dependence of melting temperature. Nevertheless, these reports implicated small crystal size and large surface-to-volume ratios as the causes of the observed depressions.[15]

Eventually, glass fabrication techniques produced porous glasses with controlled pore sizes. The manufacture of glasses by sol-gel[16] processes resulted in porous materials after drying, whereas Vycor and controlled-pore glass (CPG) resulted upon etching the boron-rich phase from microphase-separated borosilicate glass.[17] All of these materials provided significant improvements in pore size availability and size distribution compared with earlier silica gels, thus facilitating testing of the Gibbs-Thomson equation.

Researchers revisited the melting point depression of ice within pores a number of times since the early work of the 1930's. Calorimetric studies in the 1960's suggested that 1-2 monolayers of water absorbed strongly to the walls of porous silica glasses. These layers did not freeze upon cooling the samples. Furthermore, $\Delta\underline{H}^{fus}$ was reported to decrease with decreasing thicknesses of absorbed water.[18,19] One author noted that in addition to monolayers adhering to the silica walls, additional water would not crystallize unless a minimum number of monolayers was present (~4 total).[19] A subsequent calorimetric study of ice embedded in CPG with pore diameters of 2 – 250 nm revealed that the Gibbs-Thomson equation described the melting temperature of ice reasonably well. The report suggested that aside from approximately three monolayers of water

bound tightly to the silica surface, the rest of the water in the pores acted like bulk water molecules under no influence from the silica walls.[20] The study also suggested that the $\Delta\underline{H}^{fus}$ was constant despite decreasing crystal size, which disagreed with the earlier studies. A more recent report detailing the size-dependence of T_m and $\Delta\underline{H}^{fus}$ for ice embedded in silica glasses revealed that melting depression of ice adhered to the Gibbs-Thomson equation except for samples of the smallest pore sizes (~ 1 nm in diameter).[21] This study noted that $\Delta\underline{H}^{fus}$ of the ice crystals decreased linearly with increasing $1/r$, and notably, $\Delta\underline{H}^{fus}$ decreased linearly with decreasing T_m. These authors, like those before them, noted a small number of water monolayers (~ 0.5 nm thickness) adhered tightly to the silica surface that did not crystallize; additionally, they noted that water in excess of these monolayers did not crystallize unless a sufficient number of them were present (~ 1.5 nm thick). The authors noted this in-between range as "puzzling", but overlooked the possibility that these additional water layers did not crystallize because they had not achieved sufficient size to have favorable crystal free energies, and instead favored an amorphous phase (see Chapter 1, Section 1.7). The critical diameter estimates for ice were approximately 3 - 4.5 nm,[22] larger than the thicknesses mentioned above. This discrepancy between critical size and thickness could be attributable to the energetically favorable interactions between the water and the silica pore wall it had wetted. In other words, the wetting angle between the ice crystals and the silica-absorbed water layer was less than 180° (Equation 2.4). The decrease of T_m with decerasing pore size suggests that $90° < \theta < 180°$, which is the wetting angle range consistent with melting point depression in Equation 2.4. A study of the melting and freezing of water in the pores of mesoporous silicates MCM-41[23] and SBA-15[24] revealed melting point depression coinciding with a slightly modified form of the Gibbs-Thomson equation.[25] Collectively, these studies highlight that the Gibbs-Thomson equation reasonably describes the dependence of

crystal size on melting temperature. None of the examples above except one[20] reported a constant $\Delta\underline{H}^{fus}$, contradicting the assumption of constancy in the Gibbs-Thomson equation. Nonetheless, the linearity between ΔT_m and $1/r$ was evident.

The melting and freezing behaviors of small particles of a number of metals, including lead, tin, bismuth,[26] gold,[27] in environments outside of porous matrices exhibit size dependence. In some cases, the temperature dependence on crystal size was dramatic, such as with the 500 K depression observed for the melting point of 5 nm gold particles.[27] A calorimetric study of iridium embedded in CPG with pore diameters ranging from 6 to 141 nm revealed agreement between iridium melting point depression and the Gibbs-Thomson equation.[28] Additionally, the authors noted a 66% reduction in $\Delta\underline{H}^{fus}$ for iridium crystals embedded in the smallest pore sizes compared with bulk crystals. A study on the melting behavior of iridium[29] and lead[30] nanoparticles on aluminum substrates revealed that the T_m of both metals *increased* with decreasing particle size when the materials were prepared with crystals epitaxially matched with the aluminum, but decreased when the crystals were randomly oriented with respect to the aluminum. The Gibbs-Thomson equation (Equation 2.4) accomodates the possibility of $T_m(r) > T_{m,bulk}$ only when $\theta < 90°$, that is, when the crystal nucleus favorably wets the surface. Other examples of the increasing of melting temperatures, also known as super-heating, exist in reviews on melting and freezing behaviors.[31] A non-calorimetric study of the melting and freezing of gallium embedded in porous glass revealed depression for the crystals in nanoconfinement that did not abide by the Gibbs-Thomson equation.[32] The authors speculated at some length as to why this was so, citing that the melting points of gallium were dependent on both pore geometry and sample thermal history. A reexamination of the thermotropic behavior of gallium in CPG or other porous media by

differential scanning calorimetry (DSC) and X-ray diffraction (XRD) may reveal more details about the complex phase behavior alluded to by this study.

Jackson and McKenna examined the melting of organic compounds embedded in 4 – 73 nm CPG.[9] The CPG beads were silanated to allow nonpolar organic liquids to wet the otherwise hydrophilic pores. The compounds examined were benzene, cyclohexane, chlorobenzene, naphthalene, heptanes, *cis*-decalin, and *trans*-decalin. The authors noted linear dependence of T_m on $1/r$, as expected from the Gibbs-Thomson equation, as well as a reduction in $\Delta\underline{H}^{fus}$ with decreasing pore size. The possible presence of an uncrystallizing liquid layer around the crystal was implicated in the reduction of $\Delta\underline{H}^{fus}$, because nuclei of various sizes surrounded by a shell of amorphous material with a fixed thickness would be more liquid-like for smaller nuclei, resulting in the observed depression of $\Delta\underline{H}^{fus}$. The authors noted that the presence of such a layer would likely cause deviation from the linear dependence of $\Delta\underline{H}^{fus}$ on $1/r$ for small pore sizes, particularly because the r^2 dependence of the surface area would cause the depression to be most pronounced for the smallest nuclei. The authors also suggested that the large surface-to-volume ratio of crystals of decreasing size could play a role in reducing $\Delta\underline{H}^{fus}$, citing previous studies on the melting of metals that revealed smearing of the melt transition as particle size decreased.[31] This smearing is believed to be due to the disperse nature of the solid-liquid interface, which could influence properties such as $\Delta\underline{H}^{fus}$ for small particles. The smearing effect was also observed in the studies of water,[13] but was not adequately explained at the time. A later report[10] addressed the smearing of the melt transition as due primarily to the distribution of pore sizes in the porous materials.

Rault *et al.*[21] examined the linear relationship between $\Delta\underline{H}^{fus}$ and T_m for the organic compounds studied by Jackson and McKenna.[9] Their report suggested that unlike water in CPG pores,

chlorobenzene did not manifest an uncrystallized layer between the solid and the modified silica walls. The remainder of the solvents examined by Jackson and McKenna, however, exhibited noncrystallizing solvent layers ranging from ~0.6 to 1.5 nm thick. The theory discussed by the authors suggested that the layer thicknesses below which no crystallization was observed should be between ~1.5 to 3 nm for the compounds. The authors did not note that these thicknesses might be a measure of the critical size of the solvent crystals. It is unclear whether the uncrystallizing layer contributes to that critical size. If so, the report reveals critical thickness estimates of 1.5 - 3 nm. If not, the report reveals critical thickness ranges of 0.9 – 1.5 nm.

Jackson and McKenna[33] also examined the effect of decreasing pore size on the crystallization and glassification of *o*-terphenyl and benzyl alcohol within 4 – 73 nm CPG. Both compounds formed crystals in the 73 nm CPG, but *o*-terphenyl formed only glasses in smaller pores (25 nm was the next largest pore size examined). Estimation of the critical nucleus size of *o*-terphenyl from classic nucleation theory (Equation 1.8) revealed r_{crit} ~ 3.1 nm. The suppression of *o*-terphenyl crystallization in pores > $2r_{crit}$ indicated the glass was kinetically stabilized. Benzyl alcohol did not crystallize when embedded within 4 nm CPG. Estimates of its critical size revealed r_{crit} ~ 2.5 nm. Notably, the pore size of 4 nm < $2r_{crit}$, suggesting size-dependent thermodynamic stabilization of the amorphous phase (Chapter 1, Section 1.7). As an aside, a different study revealed the suppression of crystallization in ultrasmall pores for lead embedded in carbon nanotubes.[34] Within 8.5 nm and larger CPG, benzyl alcohol formed glasses unless crystals were also absorbed on the CPG exterior, in which case the exterior crystals induced nucleation of the compound within the pores. This is a clear example of the amorphous phase being kinetically stabilized in pore sizes > $2r_{crit}$. Notably, the glass transition temperature (T_g) of both compounds decreased linearly with increasing inverse pore size, analogous to the size dependence of melting temperature captured by the Gibbs-Thomson equation. Collectively, these

results revealed that crystallization could be suppressed in favor of amorphous phases by both kinetic and thermodynamic means, although the authors did not directly implicate thermodynamics in the suppression of T_g.

Reviews on the effects of size confinement on T_m and T_g were written by Christenson[35] and Alcoutlabi and McKenna.[36] The Alcoutlabi[36] review focused primarily on the effects of size on the glass transition, but also treated many examples of melting point depression in porous solids, particularly CPG and Vycor. The authors noted that most of the melting behavior studied in previous work adhered to the Gibbs-Thomson relation for all but the smallest pores. Interestingly, they make no mention of the possibility of critical size effects or suppression of crystallization in favor of an amorphous phase as an explanation for that behavior. They do note, however, that the relationship of ΔT_m vs. $1/r$ is linear despite frequent reports of $\Delta \underline{H}^{fus}$ changing with decreasing crystal size, but they do not offer a theoretical justification for that observation. The concept of super-heating was discussed in the review, with comparison made between the melting of benzene crystals embedded in CPG, SBA-15, and activated carbon fibers (ACF).[37] Benzene embedded in silanated CPG and SBA-15 exhibited melting point depression with decreasing crystal size (Figure 2-2). Furthermore, the melting point depressions were different between the porous materials. Benzene exhibited melting point elevation (super-heating) when embedded in ACF. This elevation did not adhere to the Gibbs-Thomson relation. The assumption of $\theta = 180^o$ in the Gibbs-Thomson equation precludes any melting point dependence on porous matrix. If that was a realistic assumption, however, the size-dependence of the melting temperature of benzene should be the same in CPG, SBA-15, and ACF.[ii] None of the reports discussed in the review

ii. The $\theta = 180^o$ assumption also precludes the possibility of melting point elevation, such as that observed for benzene in ACF[37] and lead and iridium on aluminum.[29,30] By definition, all of the quantities in equation 2.4 except cos θ are positive. Thus, $(T_{m,bulk} - T_m(d)) < 0$ if $\cos(\theta) < 0$, or $90^o < \theta < 180^o$.

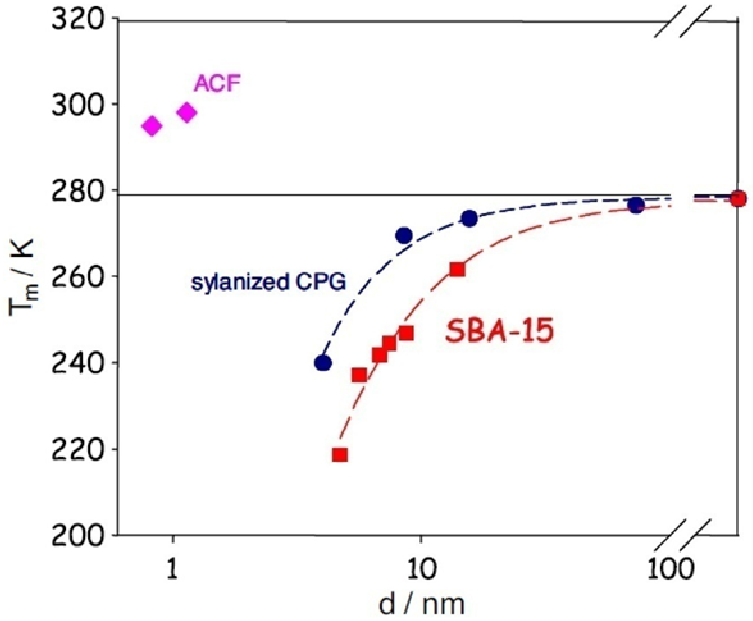

Figure 2-2 The melting temperature of benzene confined in different pores of diameter *d*: in activated carbon fibers (ACF, pink diamonds), in controlled pore glasses (CPG, blue circles), grafted at the surface with trimethylsilyl groups (in SBA-15, red squares) without treatment. Melting point depression in CPG and SBA-15 is well-described by the Gibbs-Thomson equation (Equation 2.5). Reproduced from reference 36. Used with permission.

revisited the $\theta = 180^{o}$ assumption in the Gibbs-Thomson equation, despite the clear dependence of ΔT_m on porous material. Monte Carlo simulations of crystals melting in porous silica and graphite revealed that the strength of the interaction between the pore wall and the fluid could drive the melting point to increase or decrease with decreasing pore size.[38]

Systematic analysis of the supercooling of liquid oxygen embedded within porous sol-gel and Vycor glasses of different pore sizes (ranging from 4 – 40 nm) revealed a strong dependence of freezing point on pore size.[39] Furthermore, once solid, the oxygen exhibited solid-state transitions between three allotropes (allotropes are polymorphs of pure atomic substances) - amorphous oxygen, γ-oxygen and β-oxygen - at temperatures that were also pore size dependent. Notably,

the relationship between the transition temperature, $\Delta T_{\gamma \rightarrow \beta}$, and inverse pore size, $1/r$, was linear. Although the authors did not mention it, this suggests that solid-state transitions such as enantiotropic polymorph transitions might obey relationships similar to the Gibbs-Thomson equation. Furthermore, the study implies that polymorph transitions might be controlled with size confinement.

In 2004, Ha et al.[40] reported the crystallization of polymorphic compounds under nanoconfinement. The authors crystallized anthranilic acid (AA), which adopts three polymorphs in the bulk state, within the pores of 7.5 nm, 24 nm and 55 nm CPG. The compound exhibited size dependent polymorph selectivity, with III-AA present in the 55 nm pores and on the surfaces of nonporous glass beads; a mixture of II- and III-AA formed in the 24 nm pores, and II-AA formed exclusively in the 7.5 nm pores. The II form, which was not thermodynamically favored, remained unchanged in the pores for more than one month at room temperature. The authors attributed this stability to suppression of the bulk-stable forms near their critical sizes, i.e. critical size effects. The polymorph selectivity might also be attributed to the II-AA form having a favorable free energy within the smallest pores (Chapter 1, Section 1.7). This report is a clear example of size dependent polymorph selectivity within CPG.

Emulating the reports by Ha et al.,[40] a pair of manuscripts in 2007 and 2008 detailed the polymorphism[41] and amorphous phase stabilization[42] of the pharmaceutical molecule acetaminophen in the pores of CPG. Acetaminophen, a polymorphic compound with three forms, exhibited melting point depression consistent with the Gibbs-Thomson equation. The authors estimated the critical size of acetaminophen nuclei to be ~3.6 nm using the slope of Gibbs-Thomson equation. Within the smallest pore sizes examined, ~4.6 nm diameter, all crystallization was suppressed in favor of an amorphous phase. The authors suggest that this is due to either critical size effects or a kinetic stabilization of the amorphous phase, and note that determining

whether amorphous acetaminophen is the equilibrium phase in the 4.6 nm pores is very difficult. For pores of 22 nm, 42 nm, and 60 nm, the metastable form III of acetaminophen was present exclusively. Mixtures of II- and III-acetaminophen formed within 103 nm CPG. The authors suppressed the crystallization of these forms by rapid quenching of molten acetaminophen, resulting in the amorphous phase that recrystallized slowly over time. The glass transition temperature decreased with decreasing pore size and broadened significantly for 4.6 nm CPG, indicating that the acetaminophen exhibited layers of molecules that interacted strongly with the silica walls. The authors noted that experimental parameters such as combination of pore size, crystal-pore wall interactions, and pore topology could be tailored for specific applications, such as the stabilization of pharmaceutical compounds.

2-3: Crystallization in Nanoporous Polymer Monoliths

The 2004 work of Ha et al.[40] also detailed the crystallization of ROY (5-methyl-2-[(2-nitrophenyl)-amino]-3-thiophenecarbonitrile) within the nanometer-diameter cylinder pores of porous polycyclohexylethylene (p-PCHE) monoliths. These monoliths, which are one example in a family of related porous materials,[43,44,45] are produced by etching the shear-aligned polylactide (PLA) cylinders from ordered PCHE-PLA diblock copolymers. Unlike many of the siliceous porous materials such as CPG, the resulting monoliths possess pores that are aligned and uniform in diameter (Figure 2-3). Furthermore, compared with silicates exhibiting well-ordered porosity such as SBA-15 and MCM-41, which typically exist as powders, the p-PCHE monoliths are macroscopic. The synthesis procedure allows for the facile generation of monoliths with a range of pore sizes, however, the monoliths are limited to applications below their glass transition temperatures, above which the monolith pores collapse. For the study of embedded ROY, Ha et al. employed p-PCHE monoliths with 20 nm and 30 nm diameter pores. Within the larger pore

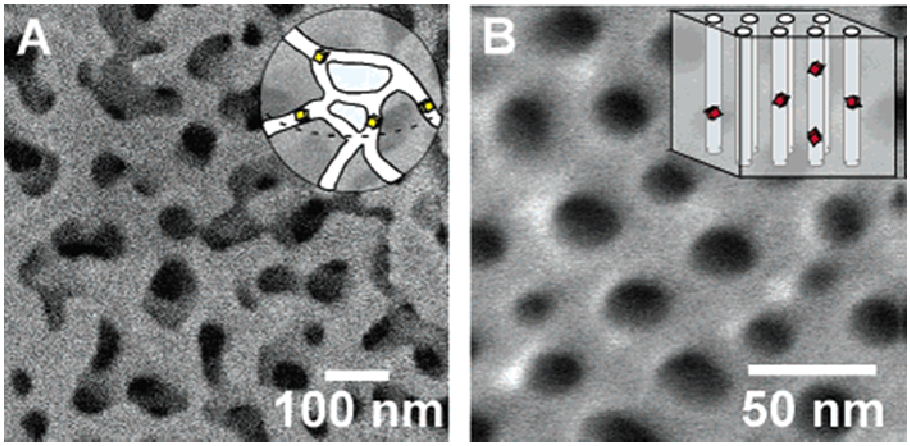

Figure 2-3. Scanning electron micrographs of (A) commercially available controlled porous glass (CPG) with a pore diameter (d = 55 nm) and (B) porous PCHE monolith with a hexagonal array of cylindrical pores (d = 30 nm). (Insets) Schematic representations of nanocrystals grown in the pores. From Reference 40, used with permission. Copyright American Chemical Society, 2004.

size, ROY crystallized as the Y form, which is the designation for yellow prisms. The authors identified the polymorph by comparing experimental XRD reflections with those expected for Y-ROY crystals. Heating the samples above the melting temperature of ROY (but below the T_g of PCHE) and then cooling resulted in the crystallization of R-ROY within the pores, as indicated by DSC measurements (Figure 2-4A). XRD with a 2-D detector permitted analysis of the orientation of the R-ROY within the pores, and revealed the nanocrystals to align with the (111) crystal plane perpendicular to the pore direction (Figure 2-4B). Within the 20 nm pores, crystallization of ROY was suppressed in favor of the red amorphous phase, *a*-ROY. As with the polymorph selectivity noted for anthranilic acid in CPG, the authors attributed this suppression to critical size effects. Based on the large pore size (20 nm) compared with the critical size estimates given in Chapter 1 and in this chapter ($2r_{crit}$ < 8 nm), it seems unlikely that Y-ROY was suppressed due to critical size effects. Instead, it is more likely that the suppression is due to either the kinetic stabilization of the amorphous phase or the suppression of crystallization due to Y-ROY of 20 nm having $\Delta G_{cryst} > 0$.

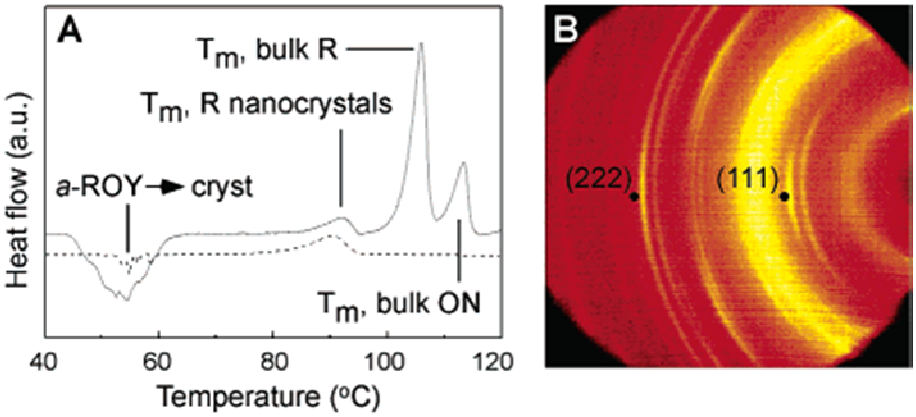

Figure 2-4. (A) DSC of an unwashed (solid line) and washed (dashed line) *p*-PCHE monolith impregnated with ROY (from pyridine) that has been subjected to heating at 120 ℃ and cooled to -25 ℃ (5 ℃/min in both directions). (B) 2-D diffraction pattern of an aligned monolith containing only R nanocrystals. Preferred orientation of R nanocrystals is in the azimuthal intensity maxima exhibited by the reflections. For clarity, only the (111) and (222) reflections are denoted here. From Reference 40, used with permission. Copyright American Chemical Society, 2004.

Ha et al. also studied the melting behaviors of R-methyl adipic acid (RMAA) and 2,2,3,3,4,4-hexafluoropentane-1,6-diol (HFPD) in CPG and porous polystyrene monoliths (p-PS).[10] The melting temperature dependence on pore size adhered to the 1/r dependence of the Gibbs-Thomson equation, and $\Delta \underline{H}^{fus}$ decreased linearly with increasing inverse pore size. The authors noted, however, that the temperature depression of HFPD was also strongly dependent on the porous matrix. Namely, γ_{nl} (Equation 2.5) varied with porous material, and the slope of ΔT_m vs. $1/r$ was dramatically different for HFPD embedded in CPG or p-PS (Figure 2-5). Reexamination of the classic form of the Gibbs-Thomson equation (Equation 2.5) revealed that the $\theta = 180^o$ assumption was not reasonable. The authors emphasized that despite the importance of $\cos \theta$ and the dependence of $\Delta \underline{H}^{fus}$ on crystal size, the melting point depression was still linear with $1/r$. Alcoutlabi and McKenna noted this concomitantly in their review.[36] This linearity, Ha et

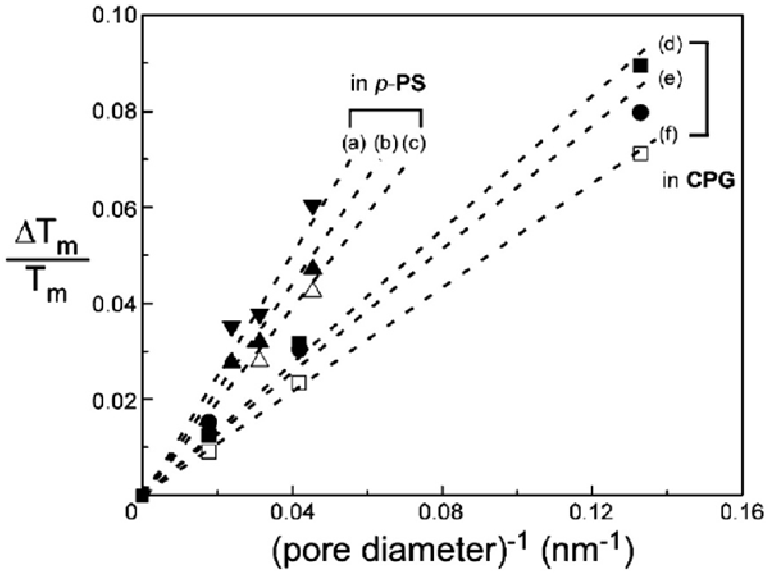

Figure 2-5. Dependence of the normalized melting point depression, Tm/Tm, on the channel diameter for (a, ▼) R-MAA in p-PS, imbibed from methanol, (b, ▲) HFPD in p-PS, (c,) HFPD in p-PS, imbibed from melt, (d,) HFPD in CPG, imbibed from methanol, (e,) R-MAA in CPG, imbibed from methanol, and (f,) HFPD in CPG imbibed from melt. The slopes are larger for the p-PS monoliths. The data for HFPD reveal that the effect of the porous matrix outweighs the differences arising from the method used to introduce the HFPD to the channels (melt or methanol solutions). The dashed lines represent the best fit to each data set, including a point added at $\Delta T_m/T_m = 0$, $1/d = 0$, that corresponds to the bulk melting temperature. From Reference 10. Used with permission. Copyright American Chemical Society, 2005.

al. argued, must be due to a fortuitous compensation of the change in $\Delta \underline{H}^{fus}$ by a change in $\gamma_{nl}\cos\theta$ (or more appropriately, $\gamma_{ns} - \gamma_{sl}$).

Collectively, the above reports reveal a variety of size-dependent crystal properties - polymorph selectivity, melting point depression, stabilization of amorphous phases, and suppression of crystallization. The dependence of these properties on decreasing crystal size is not fully understood. Reexamination of the classic assumptions of the Gibbs-Thomson equation, for example, has revealed that the walls of the porous materials influence the behaviors of embedded nanocrystals, and that the traditional assumption of $\theta = 180^o$ is not realistic for all materials. The above reports have revealed a number of ways to explore systematically the

aforementioned properties in nanoconfinement. The remainder of this chapter is focused on such an examination – the polymorphism and thermotropic properties of several organic compounds embedded in CPG and p-PCHE monoliths, and the subsequent examination of nanocrystal orientation within p-PCHE.

2-4: Polymorphism and Thermotropic Properties of Dicarboxylic Acids and Coumarin under Nanoscale Confinement.

Described herein is the crystallization of select α,ω-dicarboxylic acids and coumarin in the nanometer-scale pores of CPG beads and porous poly(cyclohexylethylene) (p-PCHE) monoliths, the latter prepared by etching the hexagonally packed polylactide (PLA) cylinders from shear-aligned PCHE-PLA diblock copolymers.[43] The confined nanocrystals display size-dependent melting point depression, polymorph stability crossovers, and transitions from enantiotropic phase behavior in the bulk to monotropic behavior under nanoconfinement. Furthermore, crystallization confined to these nanopores produced heretofore unknown polymorphs, demonstrating the impact of nanoconfinement on crystallization while suggesting a new route to the discovery of new polymorphs. Dr. Jeong-Myeong Ha performed the experimental work and presented the original discussion of the results as part of his Ph.D. thesis.[46] The results are discussed here in their entirety because this author contributed to the final discussion.[47]

2-4.1: Crystallization under nanoscale confinement

Controlled pore glass (CPG), a borate-silicate composite glass from which the borate phase is leached to produce a silica glass bead with a random pore network, was obtained commercially with pore sizes of 7.5 nm (± 6%), 24 nm (± 4.3%), and 55 nm (± 3.1%). Nonporous glass (NPG),

used as a control, was obtained as glass beads with diameters less than 106 μm. Companion studies were performed in porous poly(cyclohexylethylene) (p-PCHE) monoliths, which were prepared by chemically etching the hexagonally packed cylindrical polylactide (PLA) domains from shear-aligned PLA-PCHE diblock copolymers.[43] The cylindrical pores that result are uniformly spaced and have more uniform pore diameters than the pores of CPG. Scanning electron microscopy (SEM) of the etched monoliths revealed a hexagonal array of cylindrical pores with 30 nm diameters oriented parallel to the direction of diblock alignment (Figure 2-3). Monoliths also were prepared with 14 nm and 40 nm pore diameters. The uniform alignment of p-PCHE pores in each monolith permits characterization of the orientation of embedded nanocrystals with respect to the pore direction by 2D X-ray microdiffraction (μ-XRD). Conversely, the random CPG beads and pores were not amenable to crystal orientation analysis.

Pimelic acid, glutaric acid, suberic acid, and coumarin were crystallized within the pores of CPG beads and p-PCHE monoliths by either (*i*) immersion of the porous matrix in a saturated methanol solution of the compound, allowing infiltration of the solution into the pores through capillary action, followed by evaporation of the methanol solvent from the pores or (*ii*) immersion of the porous matrix in the melt of the compound, allowing infiltration of the melt into the pores through capillary action, followed by cooling the resulting composite. Whereas the loading of nanocrystals grown from methanol solutions was sufficient for detection by μ-XRD, crystallization from the infiltrated melts produced substantially higher loading, which was particularly useful for accurate determination of thermal properties by differential scanning calorimetry (DSC). The p-PCHE monoliths, however, soften and exhibit pore collapse at the glass

transition temperature of T_g ~ 136 °C.[iii] Consequently, only compounds with melting points (T_m) below the T_g (pimelic acid, glutaric acid, coumarin) can be embedded within p-PCHE from the melt (T_m = 106.5, 99, and 72 °C for pimelic acid, glutaric acid, and coumarin, respectively). Conversely, compounds with melting points above the T_g (suberic acid) must by introduced to the pores of p-PCHE by infiltration of methanol solutions (T_m = 143 °C for suberic acid). The pore loading of suberic acid was maximized by using methanol solutions saturated with the compound at 50 °C. After crystallization of the imbibed melt or solution, and prior to further sample characterization, the external surfaces of the monoliths were swabbed with a soft, methanol-dampened paper towel to remove any residual compound. The CPG beads were washed briefly with methanol prior to subsequent characterization of the embedded nanocrystals.

2-4.2: Glutaric acid

Two polymorphs, α and β, have been reported for glutaric acid ($HOOC(CH_2)_3COOH$, denoted here as C5).[iv] The single crystal structure of β-C5 has been reported previously, [48] but until this investigation only the space group and unit cell parameters of α-C5 were known.[49] Powder X-ray diffraction (PXRD) revealed that C5 obtained commercially was β-C5, which persisted indefinitely under ambient conditions. DSC and variable temperature PXRD revealed that β-C5 transformed upon heating to α-C5 at 76 °C ($\Delta\underline{H}_{\beta\rightarrow\alpha}$ = 2.34 ± 0.06 kJ/mol; Figure 2-6A,B). The α-C5 crystals melted at 99 °C ($\Delta\underline{H}_{\alpha\rightarrow melt}$ = 21.3 ± 0.6 kJ/mol), consistent with enantiotropic phase

iii. The T_g of p-PCHE varies slightly between samples. The T_g listed here is approximate, based on values measured for the the p-PCHE monoliths employed. See reference 43.

iv. (a) α-C5: Monoclinic, *C*2/*c*, *a* = 25.623, *b* = 4.9196, *c* = 9.9164, β = 94.079, Z = 8, D_c = 1.408, *T* = 173 K, R = 3.92 %. Full details are provided in supporting information. (b) β-C5:[50] Monoclinic, *C*2/*c* *a* = 12.968, *b* = 4.8296, *c* = 9.982, β = 96.872, Z = 4, D_c = 1.414, *T* = 293 K.

behavior in the bulk. Recrystallization of the C5 melt, which occurred between 80 °C and 95 °C, produced α-C5 ($\Delta \underline{H}_{melt \rightarrow \alpha}$ = 20.7 ± 0.4 kJ/mol), which transformed to β-C5 within one hour at room temperature.

Crystallization of C5 by evaporation of methanol from a 30% w/w methanol solution in 7.5, 23, and 55 nm CPG produced mixtures of α-C5 and β-C5, with β-C5 predominant (Figure 2-7A). Embedded α-C5 nanocrystals were observed exclusively in a small percentage of the samples, however. Both α-C5 and β-C5 nanocrystals were stable indefinitely at room temperature when confined within CPG. Cooling of embedded melts, produced by melting the embedded C5 above 100 °C ($T_{m,bulk}$ = 99 °C), produced α-C5 exclusively. These embedded α-C5 nanocrystals were stable indefinitely (at least months) at room temperature with no measurable transformation to β-C5, in contrast to the behavior observed for bulk α crystals, *indicating clearly a size-dependent polymorph stability crossover*.

DSC scans of the β-C5 nanocrystals formed initially in CPG by methanol evaporation revealed two endothermic events during heating (at 1, 5, and 20 °C/min), each shifting to lower temperatures with decreasing pore size (Figure 2-8). Variable temperature PXRD of the nanocrystals embedded in CPG revealed that β-C5 completely disappeared at the first DSC peak (86 °C, 82 °C, and 71 °C for 55, 23, and 7.5 nm CPG, respectively. Figure 2-9), with concomitant appearance of α-C5, which then disappeared at the second DSC peak. The second thermal signature, which corresponds to the α→melt transition, reveals monotonic melting point depression due to diminishing crystal size (T_m = 93 °C, 86 °C, and 74 °C in 55 nm, 23 nm, and 7.5 nm CPG, respectively). The temperatures of the first endotherm in 55 and 23 nm CPG are higher than the corresponding bulk value of 76 °C. Subsequent cooling scans revealed an exothermic event at T = 75, 70, and 44 °C for 55, 23, and 7.5 nm CPG, respectively, attributable to

crystallization of α-C5. A heating scan performed immediately upon reaching room temperature revealed only one endothermic peak at a temperature near that of the second endothermic peak in the initial scan, attributable (by PXRD) to melting of embedded α-C5 nanocrystals that were produced exclusively by cooling of the embedded melt.

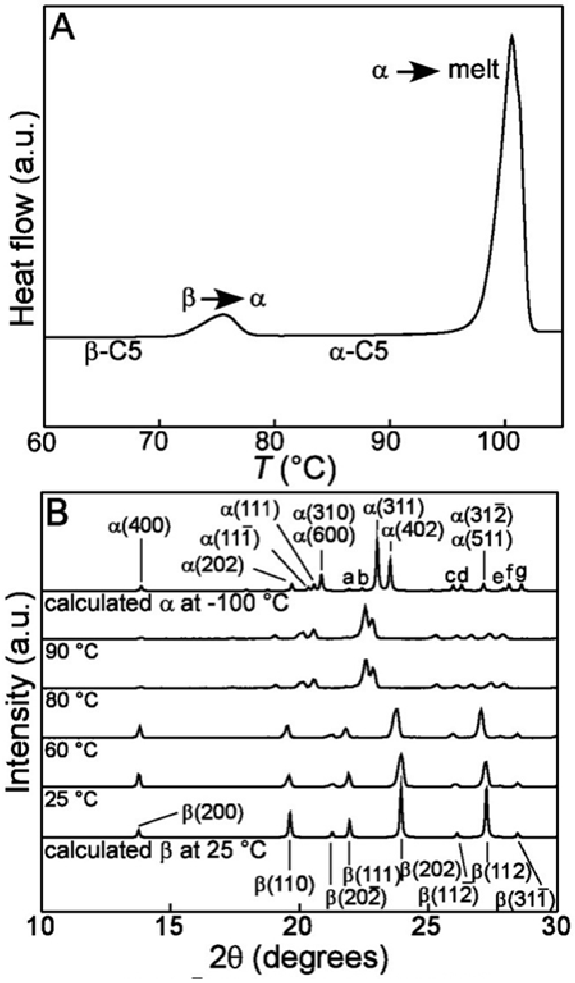

Figure 2-6. (A) A portion of a DSC scan collected from 25 ℃ to 110 ℃ for C5 obtained commercially. The first endotherm corresponds to the $\beta \rightarrow \alpha$ transition ($\Delta \underline{H}_{\beta \rightarrow \alpha}$ = 2.34 ± 0.06 kJ/mol) and the second to the $\alpha \rightarrow$melt transition ($\Delta \underline{H}_{\alpha \rightarrow melt}$ = 21.3 ± 0.6 kJ/mol). (B) PXRD of C5 crystals that confirm the $\beta \rightarrow \alpha$ transition upon heating. Key for labeled peaks in (B): a: α(40-2); b: α(31-1); c: α(112); d: α(51-1); e: α(800); f: α(312); g: α(602). Because the single crystal structure for α-C5 was collected at 100 ℃, the diffraction peaks attributed to α-C5 acquired at 80 ℃ were shifted slightly to lower 2 θ values owing to thermal expansion).

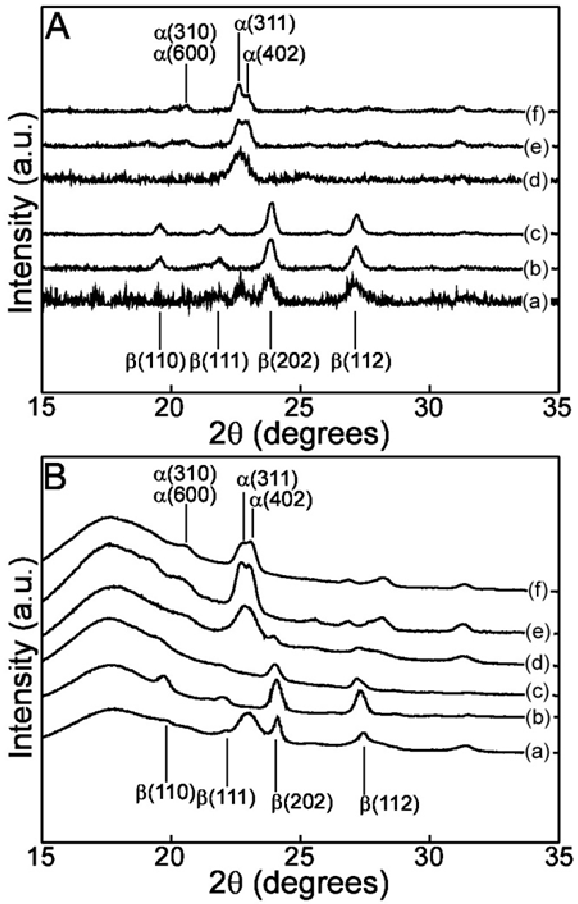

Figure 2-7. (A) PXRD for C5 nanocrystals, grown by evaporation of imbibed methanol solutions, in (a) 7.5 nm, (b) 23 nm, and (c) 55 nm CPG, and after crystallization from the melt of these nanocrystals in (d) 7.5 nm, (e) 23 nm, and (f) 55 nm CPG. (B) PXRD for C5 nanocrystals, grown by evaporation of imbibed methanol solutions, in (a) 14 nm, (b) 30 nm, and (c) 40 nm p-PCHE, and after crystallization from the melt of these nanocrystals in (d) 14 nm, (e) 30 nm, and (f) 40 nm p-PCHE.

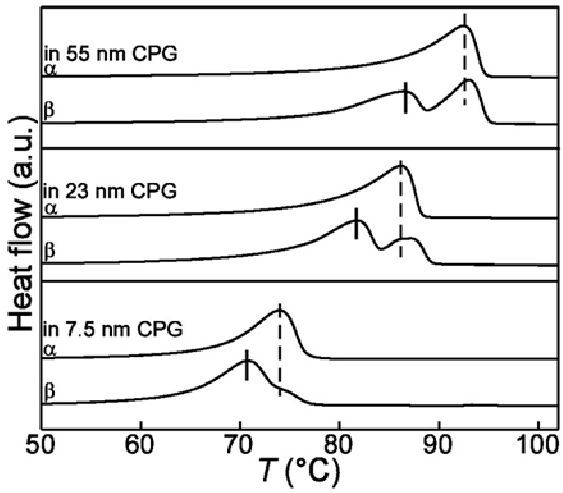

Figure 2-8. DSC heating scans, acquired with 5 ℃/min scan rates, illustrating the thermal behavior of C5 nanocrystals embedded in the three pore sizes of CPG. The two sets of data provided for each pore size correspond to DSC of (lower) the β-C5 nanocrystals formed upon evaporation of methanol from 30% (wt. % C5) methanol solutions imbibed by the CPG, and (upper) the α-C5 nanocrystals formed upon melting and recrystallizing the embedded nanocrystals. The vertical dashed lines indicate the melting of α-C5 nanocrystals, and the vertical solid lines indicate the β→α transformation. The DSC traces do not exhibit a signature associated with melting of bulk C5 (T_m = 99 ℃), indicating that the entirety of the C5 contents was located within the pores.

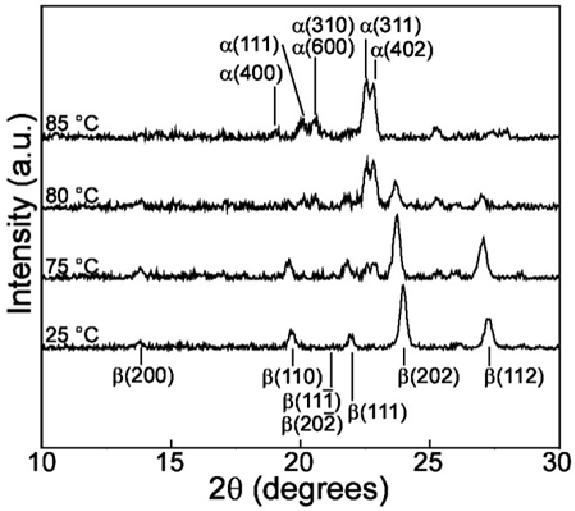

Figure 2-9. Variable temperature PXRD patterns of C5 nanocrystals embedded in 55-nm-CPG illustrating the transition from β-C5 to α-C5 upon heating.

The molar enthalpies for the β→α and α→melt transitions of bulk C5 crystals are $\Delta\underline{H}_{\beta\rightarrow\alpha,bulk}$ = 2.34 ± 0.06 kJ/mol and $\Delta\underline{H}_{\alpha\rightarrow melt,bulk}$ = 21.3 ± 0.6 kJ/mol, a ratio of 1:9. Surprisingly, for β-C5 embedded in 7.5 nm CPG (initially formed by methanol evaporation) this is reversed, such that the ratio of the heat flow of the two endotherms (first:second) was 9:1. This disparity between the bulk and nanoconfined forms diminishes with increasing CPG pore size: (first):(second) = 4.5:1 for 23 nm, 1:2.5 for 55 nm. Collectively, these observations suggest that the β→α transformation is suppressed by confinement and the first endotherm observed in CPG is actually due to a β→melt transition, which would be expected to yield a significantly higher molar enthalpy than the β→α phase transition. The observation of a remnant α→melt signature (the second peak) suggests partial (exothermic) crystallization of α-C5 from the β melt on the time scale of the DSC measurement, which would partially offset the endothermic heat flow for the β→α phase transformation. The melt→α crystallization temperatures ($T_{melt\rightarrow\alpha}$) observed in the reverse cooling scans are lower than the $T_{\beta\rightarrow melt}$, which accounts for the absence of any significant α crystallization from the β melt during the heating scan. *Collectively, these results reveal an unusual size-dependent change in the phase behavior, from enantiotropic to monotropic*, wherein the temperature for the melting of β nanocrystals is lower than that of the β→α transition when confined in nanometer-scale cavities. This implies that $T_{\beta\rightarrow\alpha}$ is not reduced with decreasing pore size to the same degree as $T_{\beta\rightarrow melt}$. It should also be noted, however, that this behavior also might reflect a "kinetic" monotropism, wherein the rate of the β→α transition is slow on the DSC time scale, possibly due to a negligible number of defects in nanosized crystals preventing the change.

The relationship between melting temperature and the size of crystals embedded in CPG and p-PCHE pores has been explained by the Gibbs-Thomson equation (Equation 2.4).[10] Many reports have assumed an absence of contact between the nanocrystals and channel walls, which is

tantamount to θ = 180º and affords the simplified version equation (Equation 2.5). If $\Delta\underline{H}^{fus}$, ρ and γ_{nl} are assumed to be independent of crystal size the Gibbs-Thomson equation predicts a linear relationship between ΔT_m and $1/d$, the latter presumed to be equal to the channel diameter.[v]

The $\Delta\underline{H}^{fus}$ of α-C5 nanocrystals embedded in CPG, measured from the single melting endotherm evident in the DSC scan of the samples reheated after recrystallizing C5 from the embedded melt (no β-C5 detected by PXRD), decreased monotonically with decreasing pore size (Figure 2-10A).[vi] A least squares fit of $T_{\alpha\rightarrow melt}$ vs. $1/d$ for both α-C5 and β-C5 was reasonably linear (Figure 2-10B) despite the decreasing values of $\Delta\underline{H}^{fus}$ with decreasing pore size. This has been explained by equation 2.6, which is obtained by substitution of $\gamma_{nl}\cos\theta$ with γ_{sl}-γ_{ns} according to the Young equation (See Chapter 1, Equation 1.11). The surface energies of the embedded nanocrystals are expected to approach that of their corresponding liquid with decreasing crystal size, thereby reducing the magnitude of γ_{sl}-γ_{ns}. The linearity of the data in Figure 2-B has been explained by a diminishing γ_{sl}-γ_{ns} (and therefore cos θ) term that offsets the decreasing $\Delta\underline{H}^{fus}$ with decreasing pore size. Extrapolation to $1/d = 0$ (i.e. infinite pore size) afforded a $T_{\alpha\rightarrow melt,(bulk)}$ = 95 ºC and a (hypothetical) $T_{\beta\rightarrow melt,(bulk)}$ = 88 ºC. The lower value of $T_{\beta\rightarrow melt,(bulk)}$ is consistent with the enantiotropic character of bulk C5.

C5 nanocrystals grown in 14, 30 and 40 nm p-PCHE by evaporation from imbibed methanol solutions produced a mixture of α-C5 and β-C5 in 14 nm p-PCHE, but only β-C5 in 30 and 40

v. We note, however, that $\Delta\underline{H}^{fus}$ can decrease with decreasing crystal size for organic crystals confined in CPG and porous polymer monoliths. See references 9,10,and 13.

vi. $\Delta\underline{H}^{fus}$ (55 nm) = 18.0 ± 1.6 kJ/mol, $\Delta\underline{H}^{fus}$ (23 nm) = 16.7 ± 1.0 kJ/mol, and $\Delta\underline{H}^{fus}$ (7.5 nm) = 9.9 ± 0.9 kJ/mol

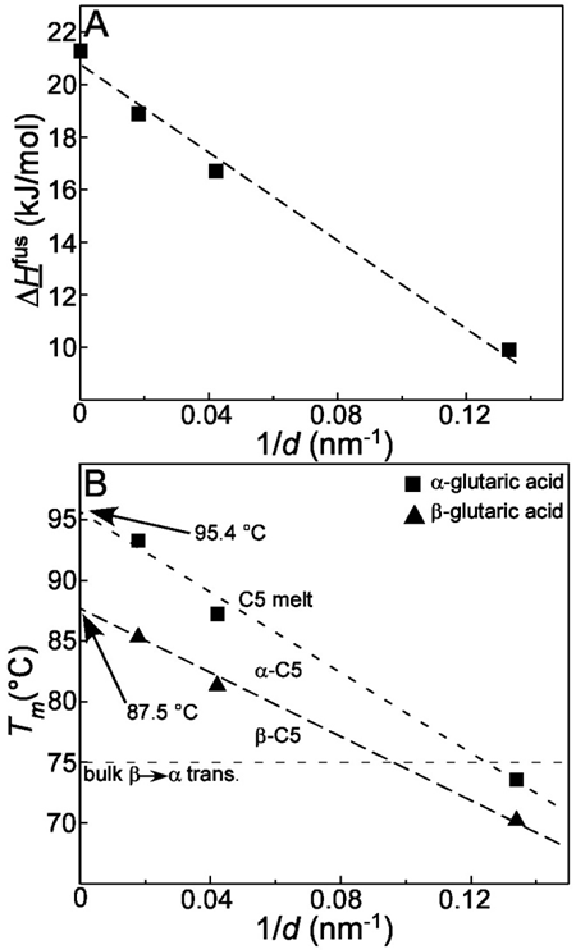

Figure 2-10. (A) Molar enthalpies of fusion, $\Delta\underline{H}^{fus}$, of α-C5 embedded in CPG pores of various diameters *d*. (B) Melting temperatures, T_m, of α- and β-C5 nanocrystals embedded in CPG pores of various diameters, *d*, with the bulk melting temperatures extrapolated from a linear fit of T_m vs. 1/*d*. The bulk β→α transition is indicated by the horizontal dashed line, and regions of α-, β-, and melt C5 within the CPG nanopores are denoted by phase.

nm p-PCHE. The sizes of the nanocrystals, determined from the full width at half maximum (fwhm) of selected peaks and the Scherrer equation,[vii] were consistent with the pore diameters.[viii]

vii.The dimensions of the embedded nanocrystals can be estimated by the Scherrer equation, $d = K\lambda/(B_c \cos\theta)$, where *d* is the crystal diameter, *K* is the Scherrer constant (usually assumed to be 0.9), λ is the X-ray wavelength, B_c is the corrected peak width at the fwhm such that $B_c = (B_{obs}^2 - B_{inst}^2)^{1/2}$, where B_{obs} is the observed peak width at the fwhm and B_{inst} is the instrumental peak broadening. θ is the Bragg angle. See Cullity, B. D. *Elements of X-ray Diffraction*; Addison-Wesley: Reading, MA, 1978. Klug, H.

After five months, a mixture of α-C5 and β-C5 was observed in 30-nm p-PCHE (Figure 2-11). Melting and recrystallization of C5 nanocrystals in p-PCHE afforded α-C5 exclusively in all three pore sizes, and α-C5 persisted indefinitely when embedded. Exclusive formation of α-C5 also was observed when C5 was imbibed initially from the melt. These results argue that, as in CPG, α-C5 is thermodynamically favored at these nanoscale dimensions, opposite to the bulk behavior. This also indicates that β-C5 is a kinetic product when crystallized by evaporation of imbibed methanol solutions. Collectively, the behavior of C5 in CPG and p-PCHE illustrates size-dependent polymorph stability with α-C5, which is metastable in the bulk, becoming more stable at ultrasmall pore sizes.

2-4.3: Pimelic Acid

Three polymorphs, denoted α, β, and γ, have been reported for pimelic acid ($HOOC(CH_2)_5COOH$, denoted here as C7). The crystal structures of α-C7 and β-C7 are known,[50,51] but γ-C7 has been identified only by thermal analysis; its single crystal structure and powder X-ray diffraction (PXRD) pattern have not been reported. Bulk crystals of C7 obtained commercially were identified as β-C7 by comparison with the PXRD pattern expected from its single crystal structure. β-C7 was stable indefinitely at room temperature. DSC measurements revealed an endothermic event at 74 ºC upon heating (Figure 2-12A) due to a β→α transition, as

---

P.; Alexander, L. E. *X-Ray Diffraction Procedures for Polycrystalline and Amorphous Materials*; Wiley: New York, 1974.

viii. The α(402) reflection was used to determine diagnose the α-C5 crystal size in the 14 nm p-PCHE and 30 nm p-PCHE because the nanocrystal orientation within the pores suggested the α(402) plane was perpendicular to the pore walls and would give the best estimate of nanocrystal size. The β(202) was used to determine the β-C5 crystal size in all three pore sizes of p-PCHE for the same reason.

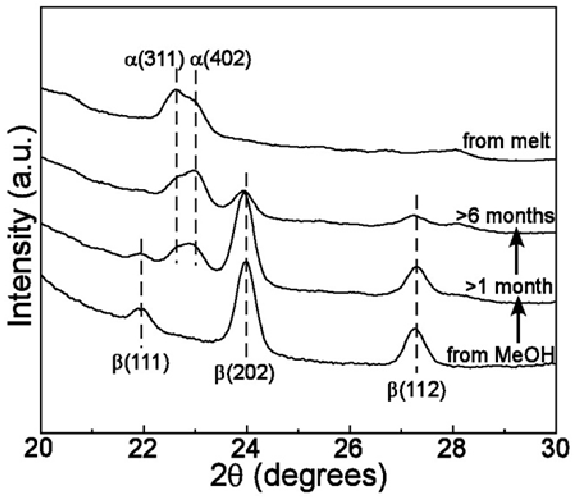

Figure 2-11. Illustrative PXRD data for C5 nanocrystals embedded in 30nm p-PCHE after evaporation of the methanol solvent from an imbibed 30% (w/w) methanol solution. The β-C5 nanocrystals transformed to a mixture of α-C5 and β-C5 under ambient conditions. The upper diffraction pattern was obtained after melting the embedded β-C5 nanocrystals and then cooling to room temperature.

determined by variable temperature PXRD. The Bragg peaks corresponding to the (102) and (121) reflections of α-C7 (2θ = 23.0º and 26.7º, respectively) disappeared at 99 ºC, accompanied by the appearance of two new peaks at 2θ = 21.9° and 25.7° (Figure 2-12B). DSC revealed an endothermic event at the same temperature corresponding to the α→γ transition, as reported previously.[52,53,54] Although the (002), (020), (021), (120) and (12-1) peaks originally attributed to α-C7 appear to persist at 99 ºC, the disappearance of the (102) and (121) peaks argues these are simply γ-C7 that overlap with the original α peaks. Upon further heating γ-C7 melts at 106.5 ºC.

The molar enthalpies for the phase transitions, measured by DSC, were $\Delta\underline{H}_{\beta\rightarrow\alpha}$ = 1.49 ± 0.03 kJ/mol and $\Delta\underline{H}_{\alpha\rightarrow\gamma}$ = 1.31 ± 0.03 kJ/mol. These values were significantly smaller than that determined for melting of the γ phase, $\Delta\underline{H}_{\gamma\rightarrow\text{melt}}$ = 28.4 ± 0.3 kJ/mol, as expected, and they compare well with those reported in the literature ($\Delta\underline{H}_{\beta\rightarrow\alpha}$ = 1.41 ± 0.07 kJ/mol, $\Delta\underline{H}_{\alpha\rightarrow\gamma}$ =1.31±0.03 kJ/mol, $\Delta\underline{H}_{\gamma\rightarrow\text{melt}}$ = 28.4 ± 0.3 kJ/mol).[52,53,54] Cooling the bulk melt

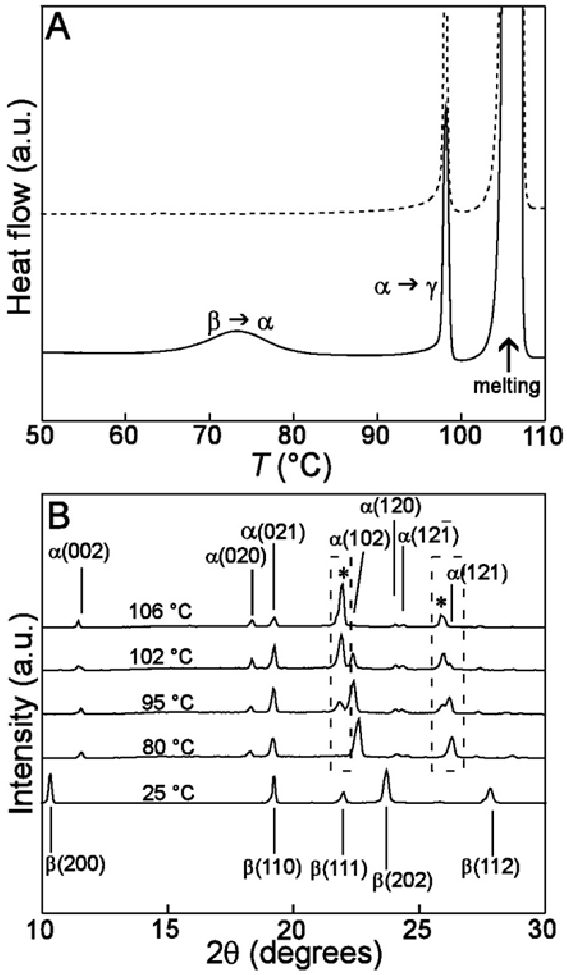

Figure 2-12. (A) DSC data collected for bulk pimelic acid (C7) during the first heating ramp (solid) and during a second heating ramp (dashed) after cooling from the melt at 5 ℃/min. The first ramp reveals the β→α, α→γ, and γ→melt transitions. The second ramp reveals the α→γ and γ→melt transitions, but no β→α transition. The cooling traces (not shown) revealed two exothermic events corresponding to the melt→γ and γ→α transitions. (B) Variable temperature powder XRD patterns of C7. The asterisk symbol (∗) denotes Bragg reflections of the γ-form.

from above 106.5 ºC at 5 ºC/min revealed a γ→α transition by DSC and PXRD, but no subsequent α→β transition, indicating that the β form does not crystallize from the melt over short time scales (~10 min.). Indeed, DSC data revealed that β-C7 did not appear until after at least one hour at room temperature. The α-C7 crystals obtained by cooling the melt transformed back to γ-C7 upon heating with no detectable formation of β-C7.

PXRD of C7 nanocrystals grown in CPG (7.5, 23, or 55 nm pores) or p-PCHE (14 nm, 30 nm, or 40 nm) by evaporation of methanol from imbibed saturated methanol solutions (20 w/w% C7) revealed the formation of either α-C7 or β-C7 phase, with a majority of the samples (~60%) containing α-C7. Crystallization in p-PCHE, however, revealed the exclusive formation of α-C7 in all three pore sizes. This behavior contrasts with the observation of mixtures of α-C7 and β-C7, in varying ratios, upon evaporation of methanol from bulk solutions of C7 under ambient conditions. The crystal dimensions, as determined from the fwhm of the Bragg were consistent with the pore diameters.[ix]

C7 nanocrystals also were grown within the CPG and p-PCHE matrices by allowing the matrices to imbibe molten C7 (CPG only) or by melting C7 embedded in the pores by evaporation of imbibed methanol solution, followed by cooling to room temperature. C7 nanocrystals thus formed in 7.5 nm CPG exhibited Bragg peaks that could not be assigned to α-C7, β-C7, or γ-C7 (Figure 2-13A), with new reflections at 2θ = 13.6º, 19.6º, 21.9º, and 25.3º. These data are consistent with a new polymorph, denoted herein as δ-C7. In contrast, cooling of the embedded melt in 23 nm CPG produced either δ-C7 or α-C7, but not both simultaneously, and only α-C7 form was observed in 55 nm CPG. PXRD revealed that the δ-C7 nanocrystals embedded within the 7.5 and 23 nm CPG transformed partially to α within one month (although in one sample the β polymorph was observed instead without any α form). Crystallization from a

ix. Nanocrystal dimensions were estimated for δ-C7 using the peak at 2θ = 22° (for 7.5 nm CPG and all p-PCHE samples) and for α-C7 using the peak at 2θ = 23° (for 23 and 55 nm-CPG): 7.5 nm CPG: 13 nm, 23 nm CPG: 29 nm, 55 nm CPG: 41 nm, 14 nm p-PCHE: 12 nm, 30 nm p-PCHE: 22 nm, 40 nm p-PCHE: 25 nm. The fwhm resolution of the instrument was approximately 0.27° (2θ) over the 2θ range of 15°-35°, allowing for a maximum crystal size estimate of 30 nm by the Scherrer equation.

bulk melt in contact with nonporous glass beads (NPG) or an aluminum DSC pan afforded α-C7 (Figure 2-13A), with partial transformation of α-C7 to β-C7 within one hour.[x] This observation indicates that the formation of δ-C7 is a consequence of size confinement, not contact with the glass walls of the CPG pores.

PXRD of C7 nanocrystals grown in 14 nm and 30 nm p-PCHE by cooling of the confined melt (at 5 ºC/min) exhibited Bragg reflections consistent with exclusive formation of δ-C7, whereas crystallization within 40 nm p-PCHE revealed a mixture of α-C7 and δ-C7 (Figure 2-13B, see also Figure 2-14C). Crystals grown from a melt in contact with non-porous PCHE films produced α-C7 solely, confirming that the formation of δ-C7 in the p-PCHE monoliths was due to size confinement, not the p-PCHE pore walls. Like δ-C7 in 7.5 and 23 CPG, the δ-C7 embedded in 30 nm p-PCHE transformed partially to α-C7 within one month (Figure 2-14). The δ-C7 embedded in 14 nm p-PCHE, however, remained stable for more than one year. The different stabilities of δ-C7 in 14 nm p-PCHE and 7.5 nm CPG, in which δ-C7 transformed partially to α-C7, most likely reflects less uniformity of pore sizes and the existence of pore intersections in CPG, where C7 crystals can grow larger than 14 nm. Collectively, these results demonstrate that size confinement can produce new polymorphs that are not observed in the bulk. Moreover, these results demonstrate that *the stability ranking of the polymorphs changes with size*, with δ-C7 becoming more stable than α as crystal size decreases, in both CPG and p-PCHE.

x. XRD analysis indicated that α:β ratio in the mixture was approximately 60:40, as determined from the structure factors of the known pure crystal forms, signifying that α crystallizes from the melt and eventually transforms to β when in contact with a glass surface.

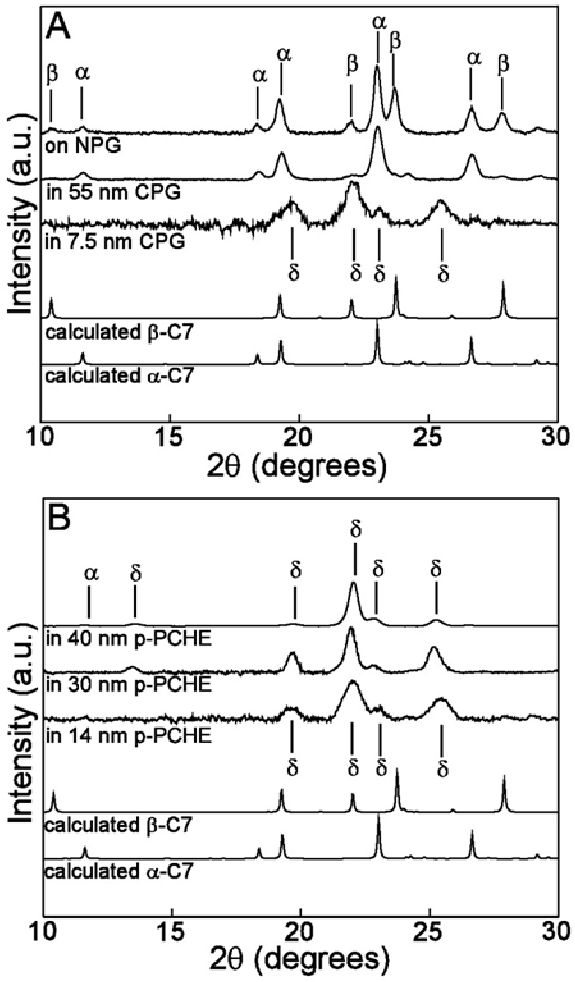

Figure 2-13. (A) PXRD from C7 nanocrystals grown from melts confined within CPG and nonporous glass beads (NPG). The δ-C7 polymorph crystallizes in 7.5 nm CPG. (B) PXRD from C7 nanocrystals grown from melts confined within p-PCHE. The δ-C7 polymorph crystallizes in all three pore sizes. Diffuse scattering from the amorphous CPG and p-PCHE matrices is subtracted for clarity in all data.

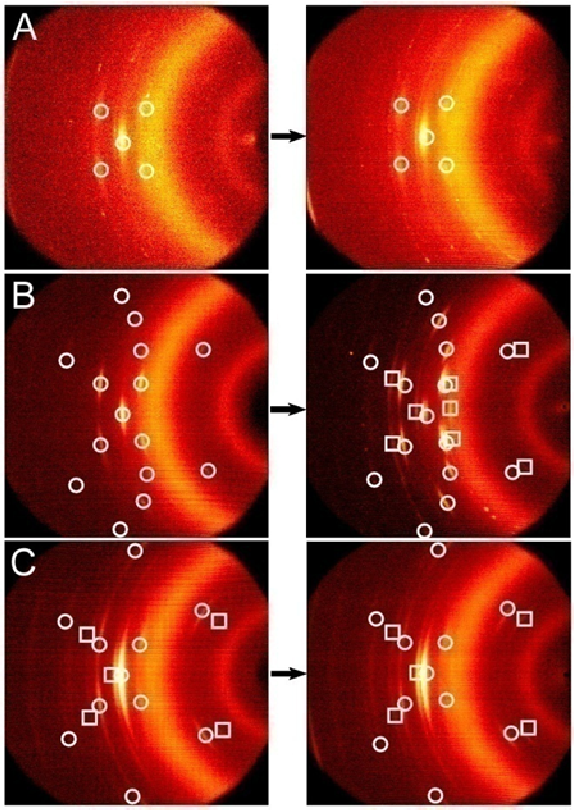

Figure 2-14. 2D μ-XRD data for δ-C7 embedded in (A) 14 nm p-PCHE, (B) 30 nm p-PCHE, and (C) 40 nm p-PCHE. The panels on the left side represent samples after one hour (left). The panels on the right represent the same samples after 12 months (right). The diffraction arcs are discontinuous, with localized bands of intensity that signify preferred orientation of the nanocrystals. The widths of these bands are characteristic of nanometer-sized crystals of δ-C7 and α-C7 nanocrystals, highlighted by circles and squares, respectively. The discrete diffraction spots with narrow line widths correspond to a few bulk α-C7 crystals on the external surface of the monolith. Collectively, these data indicate that the stability of δ-C7 toward transformation to α-C7 decreases with increasing pore size.

DSC and PXRD revealed that the δ-C7 nanocrystals in CPG persisted upon heating until melting, exhibiting melting temperatures that decreased monotonically with decreasing pore size (Figure 2-15A). A similar trend also was observed for δ-C7 nanocrystals in p-PCHE (Figure 2-15B).[xi] A fit of the T_m values for δ-C7 nanocrystals in CPG or p-PCHE according to equation 2.6 produced a y-intercept ($1/d = 0$, $d \approx \infty$) of 103 ºC (Figure 2-15C), corresponding to a (hypothetical) bulk melting temperature for δ-C7. This value, which is not measurable in bulk form, is less than the measured bulk melting point for T_m for γ-C7 (106.5 ºC), as expected for a phase that is metastable in the bulk.

2-4.4: Suberic acid

Only one polymorph has been reported for suberic acid ($HOOC(CH_2)_6COOH$, C8). This polymorph, denoted here as α, is stable at room temperature and has been characterized by single crystal X-ray diffraction.[55] DSC of bulk C8 revealed endothermic events at 134 ºC (9.18 ± 0.15 kJ/mol) and 143 ºC (30.1 ± 0.6 kJ/mol at 143 ºC) (Figure 2-16A). At room temperature, PXRD revealed diffraction peaks diagnostic of α-C8.[xii] These reflections vanished at 135 °C with concomitant appearance of new peaks at 2θ = 11.1°, 20.7°, 21.9°, and 23.3° (Figure 2-16B). Optical micrographs of the crystals collected over the same temperature range revealed that the transparent α-C8 crystals became opaque and fractured at 134 °C, followed by melting at 143 °C. Collectively, these data signal a transformation of α-C8 to a previously unreported polymorph, designated here as β-C8. Adequate crystals for single crystal diffraction could not be obtained,

xi. T_m(55 nm CPG) = 98.6 ± 0.1 ºC, T_m(23 nm CPG) = 92.2 ± 0.6 ºC, and T_m(7.5 nm CPG) = 74.5 ± 0.7 ºC. T_m(40 nm p-PCHE) = 97.1 ± 0.9 ºC, T_m(30 nm p-PCHE) = 94.1 ± 0.7 ºC, and T_m(14 nm p-PCHE) = 85.1 ± 1.2 ºC

xii. α(100) at 2θ = 10.0° , α(110) at 2θ = 20.2°, α(11-1) at 2θ = 21.5°, and α(20-2) at 2θ = 24.8°.

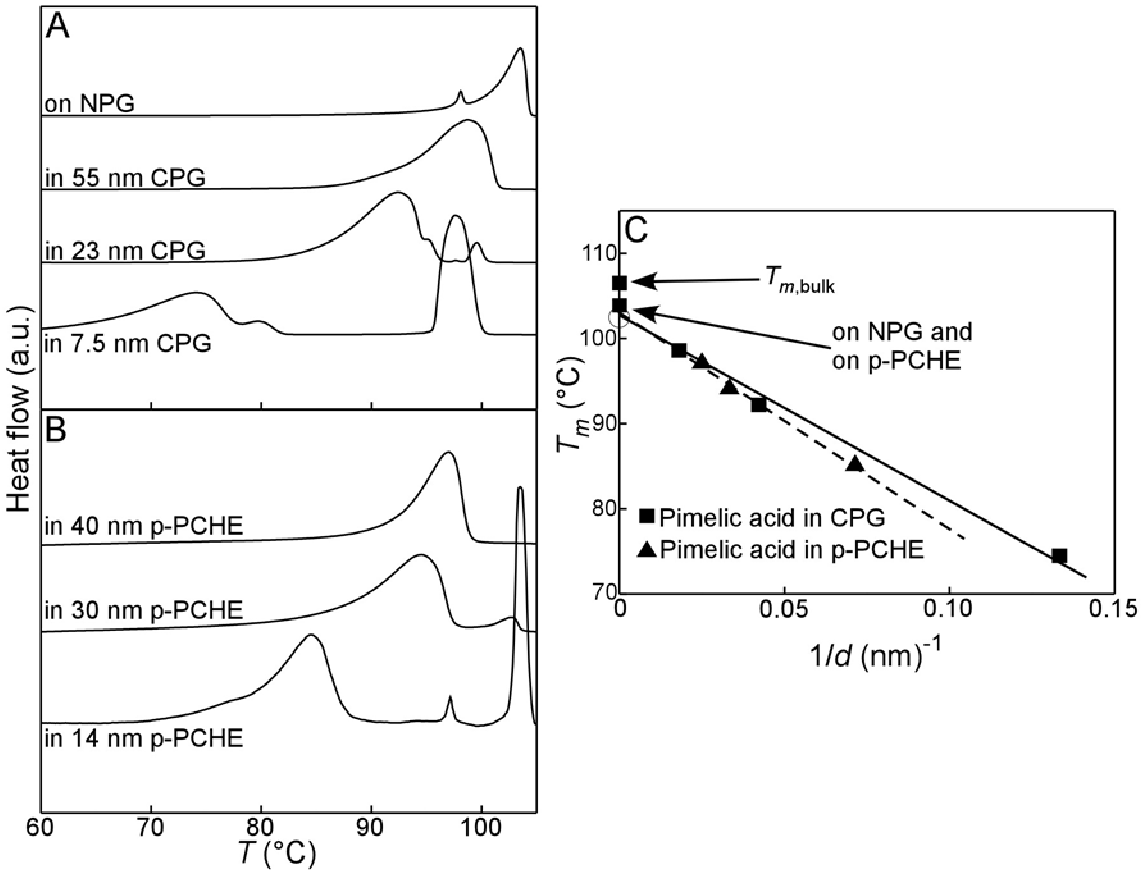

Figure 2-1. (A) The endothermic events observed by DSC upon heating for C7 crystals formed by cooling of melts confined in (A) CPG and (B) p-PCHE (7.5 nm CPG: 25.3 ± 1.7 kJ/mol; 23 nm CPG: 23.1 ± 1.3 kJ/mol; 55 nm CPG: 24.8 ± 1.1 kJ/mol). The cooling scans (not shown) for (A) and (B) each reveal a single exothermic event with a molar enthalpy equal in magnitude to the melting endotherms in the heating scans. Determination of the molar enthalpy of fusion for C7 in p-PCHE was precluded by difficulties in determining the mass of C7 embedded in the monoliths. (C) Dependence of the melting temperature, T_m, on the inverse of the pore diameter, *1/d*, for δ-C7 crystals in CPG (squares) and p-PCHE (triangles). The solid and dashed lines represent least squares fits of data for CPG and p-PCHE, respectively. Crystals embedded in 40 nm p-PCHE are a mixture of δ-C7 and α-C7. The empty circle represents an expected bulk melting temperature of δ-C7 crystals, obtained by extrapolating linear fits to the data.

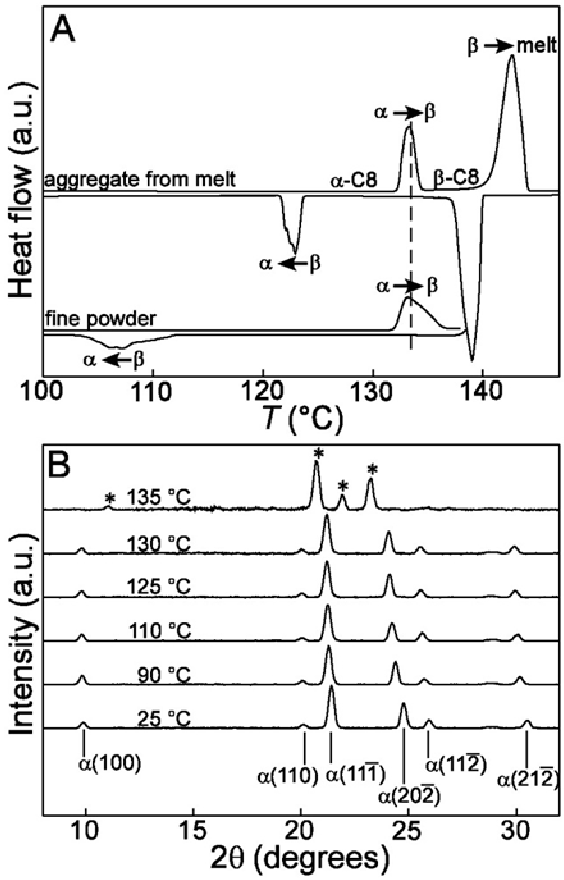

Figure 2-16. (A) DSC heating and cooling scans collected for C8 powder and C8 recrystallized from the molten powder. (B) Variable temperature PXRD data collected for C8, illustrating the transition from $\alpha \rightarrow \beta$ upon heating. Asterisked (*) reflections denote β-C8.

precluding assignment of the β-C8 peaks. The $\Delta\underline{H}_{\alpha\rightarrow\beta}$ (9.18 ± 0.15 kJ/mol) was substantially larger than that observed for similar in other dicarboxylic acids.[xiii] This transformation was reversible upon cooling for crystals grown from either methanol solutions or C8 melts (Figure 2-16A).

PXRD of C8 nanocrystals grown from 30 wt% methanol solutions in CPG revealed exclusive formation of α-C8. DSC revealed endothermic events corresponding to melting at 110 and 118 ºC for 7.5 nm CPG, 132 ºC for 23 nm CPG, and 137 ºC for 55 nm CPG, indicative of the influence of crystal size on melting point depression. The melting endotherm at 110 ºC for 7.5 nm CPG can be attributed to crystals embedded in the CPG pores whereas the endotherm at 118 ºC can be attributed to larger nanocrystals that exist in the larger voids formed by intersecting pores. PXRD revealed that the α-C8 crystals melted in 23 nm and 7.5 nm CPG without any transformation to β-C8 like that observed in the bulk (Figure 2-17A). In 55 nm CPG, however, PXRD revealed that the crystals transformed to β-C8 just prior to melting, which account for the shoulder observed by DSC at 134 ºC. These data reveal that confinement in nanopores depresses the melting point to a greater extent than the α→β transition temperature, resulting in a change from enantiotropic behavior to monotropic with decreasing crystal size. Crystallization of C8 from methanol in p-PCHE monoliths produced α-C8 exclusively, but the high melting temperature of C8, relative to the T_g of PCHE, precluded reliable examination of the thermotropic properties of the embedded nanocrystals.

Cooling of the embedded C8 melt at 5 °C/min produced exotherms due to recrystallization of β-C8 (by PXRD) at 99 °C for 7.5 nm CPG, 123 °C for 23 nm CPG, and 131 °C for 55 nm CPG,

xiii. Molar enthalpies and transition temperatures: $\Delta\underline{H}_{\beta\rightarrow\alpha,C3}$ = 1.86 ± 0.02 kJ/mol, 101 ºC; $\Delta\underline{H}_{\beta\rightarrow\alpha,C4}$ = 0.30 ± 0.02 kJ/mol, 152 ºC; $\Delta\underline{H}_{\beta\rightarrow\alpha,C5}$ = 2.34 ± 0.06 kJ/mol, 76 ºC; $\Delta\underline{H}_{\beta\rightarrow\alpha,C7}$ = 1.41 ± 0.07 kJ/mol, 74 ºC; $\Delta\underline{H}_{\alpha\rightarrow\gamma,C7}$= 1.30 ± 0.03 kJ/mol.

paralleling the melting point depression and signaling greater suppression of nucleation with decreasing pore size. Unlike bulk crystals, these confined β-C8 nanocrystals persisted indefinitely at room temperature. DSC of the β-C8 nanocrystals crystallized from the embedded melt in 55 nm CPG revealed a small endotherm at 62 ºC, followed by an exotherm spanning 80-100 ºC, which in turn was followed by two endothermic events, a shoulder at 134 ºC and a peak at 137 ºC (Figure 2-18A). Variable temperature PXRD revealed a β→α transition at 60 °C accompanying the first endotherm, but no noticeable changes over the range of 80-100 °C, which suggests crystallization of α-C8 from an amorphous phase that did not convert to β-C8 upon cooling in the previous scan. The endotherms at 134 °C and 137 °C were due to the α→β and β→melt transitions, as described above. The β-C8 nanocrystals in 23 nm CPG exhibited only a small endotherm at 60 °C (β→α) and a large endotherm at 132 °C (β→melt). The β-C8 nanocrystals in 7.5 nm CPG produced endotherms only at 110 °C and 120 °C, with no α-C8 detectable by PXRD prior to complete disappearance of the β-C8 nanocrystals by melting at 120 °C (the endotherms at 110 °C and 120 °C are consistent with β-C8 nanocrystals embedded in differently sized pores, as described above).

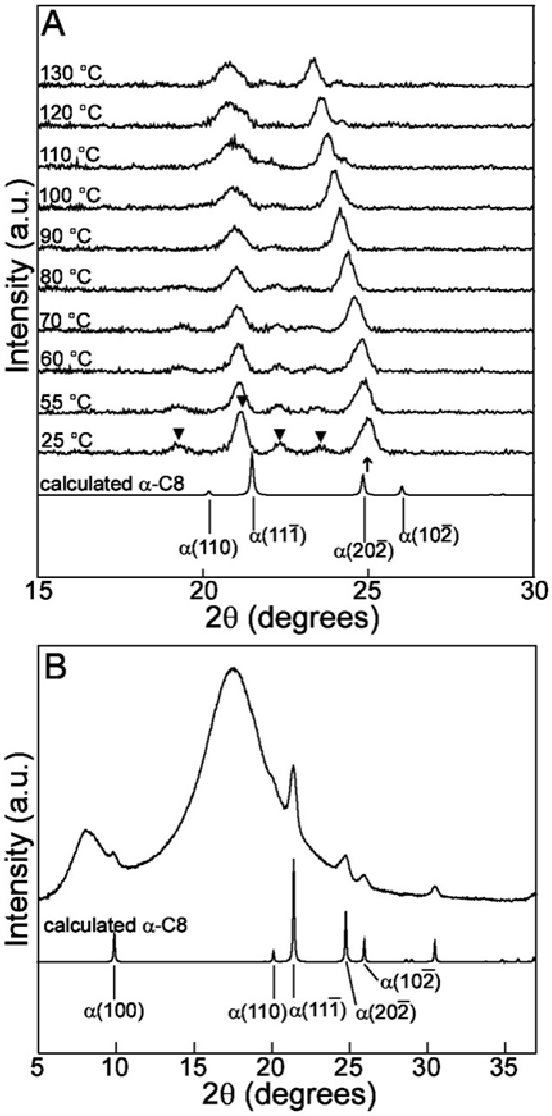

Figure 2-17. PXRD of C8 nanocrystals embedded in (A) 23 nm CPG obtained by cooling of an imbibed C8 melt and (B) 30 nm p-PCHE grown by evaporation of methanol from imbibed methanol solutions. For each plot, the bottom pattern is the calculated XRD pattern of α-C8. The reflections in (A) due to β-C8 and α-C8 were marked as '▼' and '↑', respectively. In (B), the reflections due to α-C8 are superimposed on two large, broad peaks due to amorphous scattering from the p-PCHE monoliths. No β-C8 was observed in the monoliths.

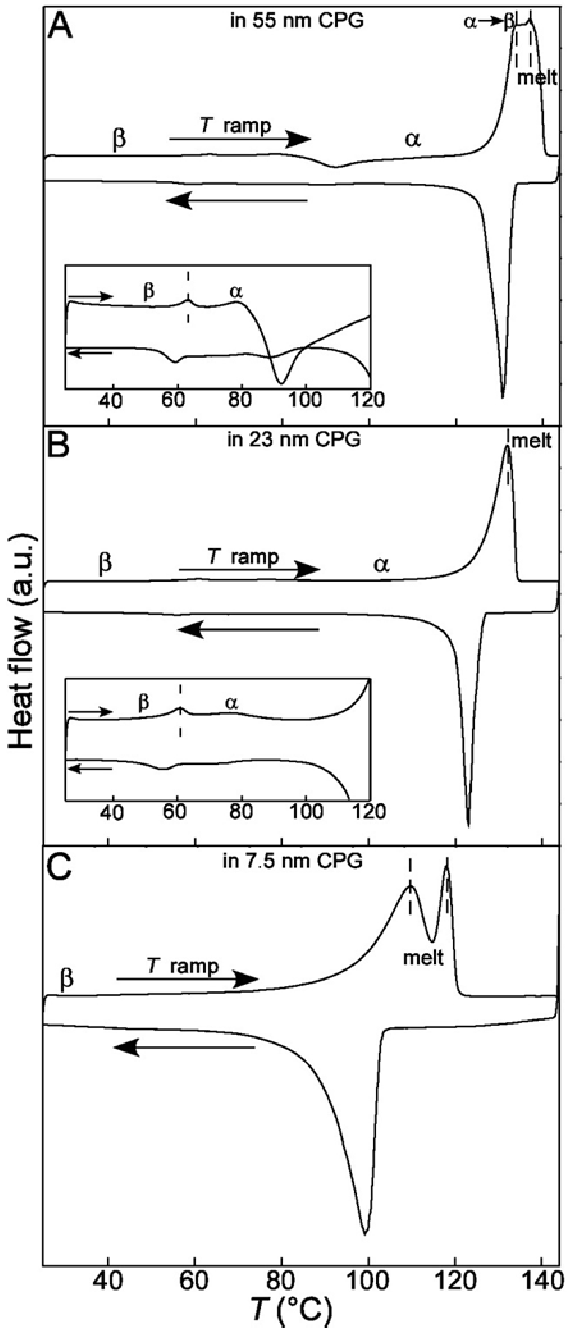

Figure 2-18. DSC of C8 crystallized from the melt embedded in (A) 55 nm CPG; inset: data expanded along y-axis; (B) 23 nm CPG; inset: data expanded along y-axis; (C) 7.5 nm CPG. Expanded DSC data for C8 nanocrystals embedded in 55 nm CPG and 23 nm CPG provided in the insets of (A) and (B), respectively.

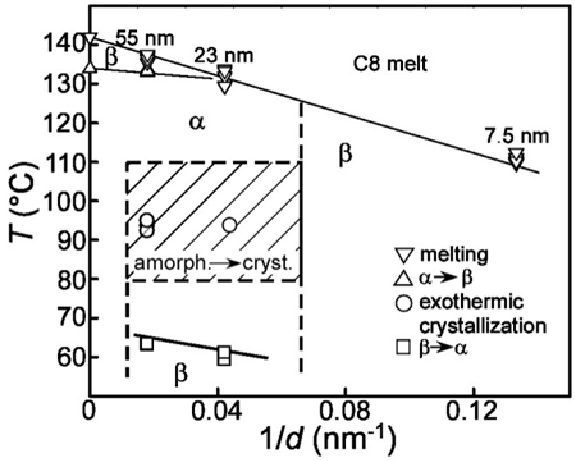

Figure 2-19 Phase diagram illustrating the phase boundaries for C8 nanocrystals in CPG obtained by cooling of an imbibed C8 melt. Replicate measurements are designated by additional symbols at each inverse pore size.

2-4.5: Coumarin

A common material found in plants, coumarin (1,2-benzopyrone) is used for its aromatic properties in products such as perfumes, and its derivatives are well-known laser dyes.[56] Coumarin crystals themselves are photochemically inert, but when mixed with photosensitizers can undergo topochemical reactions to produce photodimers. The crystallization of both coumarin and its photodimers have been investigated, [57,58,59] but only one crystal structure for coumarin, denoted here as α, has been reported. Single crystals of α-coumarin have been grown readily from ethyl ether and aqueous alcohol solutions. [60,61] We have observed that α-coumarin can be obtained by crystallization from ethyl acetate, acetonitrile, methanol and its melt (in aluminum DSC pans). DSC of coumarin that had crystallized on NPG revealed T_m = 71 ºC, in near agreement with the bulk value of 72 ºC. Bulk coumarin crystals also sublime at room temperature.

DSC revealed that nanocrystals of coumarin formed in CPG by cooling of an infiltrated melt to room temperature exhibited monotonic $\Delta\underline{H}^{fus}$ and T_m depression with decreasing pore size (Figure 2-20A and C),[xiv] reinforcing previous observations of size-dependent melting point depression and melting enthalpy. PXRD revealed that α-coumarin formed exclusively within the 55 nm CPG. In contrast, the diffraction peaks for the crystals embedded in 23 nm CPG were inconsistent with α-coumarin.[xv] Instead, this diffraction pattern signals a new polymorph of coumarin, denoted here as β-coumarin. The 7.5 nm CPG samples exhibited diffraction peaks that could be attributed to both polymorphs, although the β-form was clearly predominant (Figure 2-21A). Attempts in our laboratory to obtain a single crystal of β-coumarin suitable for crystallography were unsuccessful. Collectively, these results indicate that α-coumarin is more stable for crystal dimensions of 55 nm or greater whereas β-coumarin is more stable for crystal dimensions 23 nm or smaller.

xiv. T_m = 34 ºC (7.5 nm), 56 ºC (23 nm), and 67 ºC (55 nm). $\Delta\underline{H}^{fus}$ = 7.3 ± 0.8 kJ/mol (7.5 nm), 14.4 ± 0.5 kJ/mol (23 nm), and 16.6 ± 0.3 kJ/mol (55 nm). The melting enthalpy for was bulk coumarin was 17.2 ± 0.4 kJ/mol.

xv. Observed: 2θ = 12.4°, 15.6°, 16.4°, 17.6°, 19.3°, 21.6°, 24.2°, 25.0°, 26.4°, 28.0, and 29.2°. Expected for α-coumarin under ambient conditions: 2θ = 11.4°, 15.6°, 16.0°, 16.6°, 19.4°, 20.1°, 22.5°, 23.0°, 25.3°, 27.5°, 28.1°, and 29.8°.

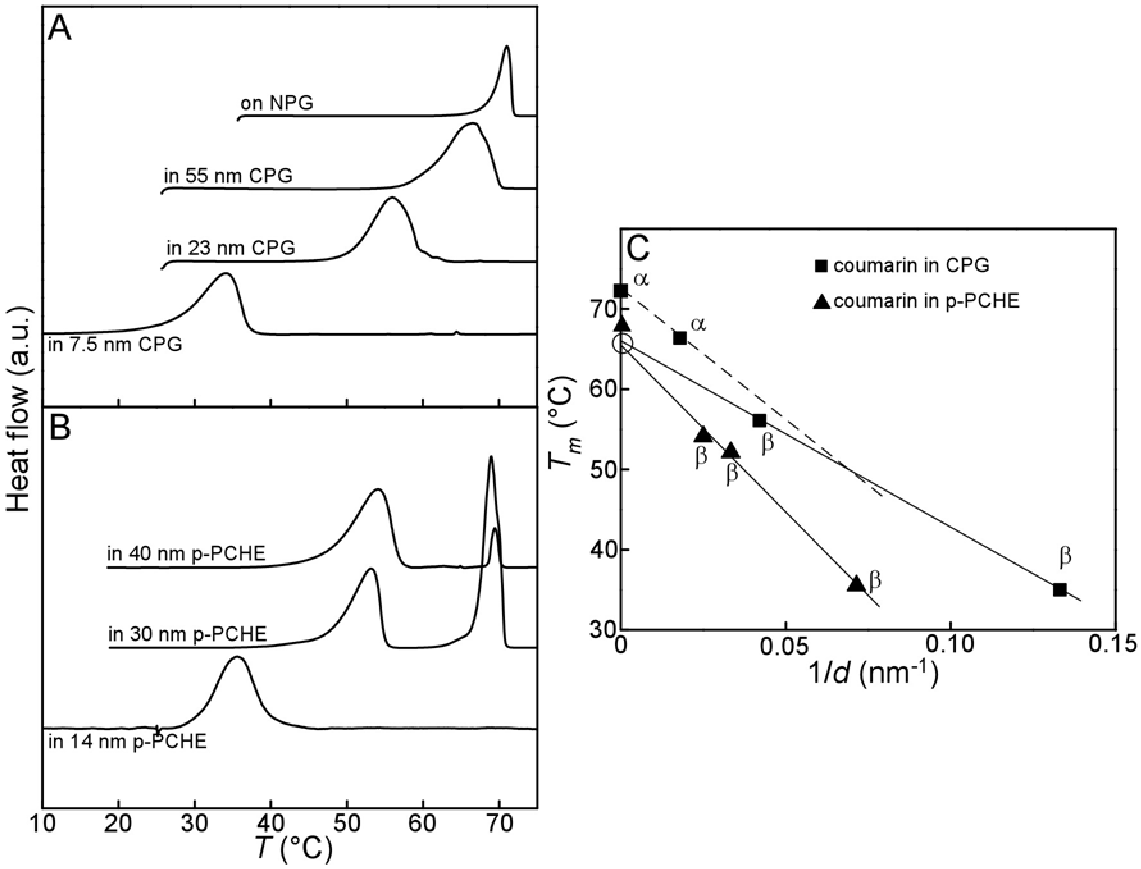

Figure 2-2. DSC of coumarin crystals embedded within (A) CPG and (B) p-PCHE, collected at a scan rate of 5 ℃/min. (C) Melting temperature of coumarin crystals embedded in CPG (■) and p-PCHE (▲). Solid lines represent the melting temperature of β-coumarin crystals embedded in CPG and p-PCHE whereas a dashed line represents that of α-coumarin nanocrystals embedded within CPG. The empty circle represents an expected bulk melting temperature of β-coumarin crystals, obtained by extrapolating linear fits to the data.

The melting point of coumarin ($T_{m,\text{bulk}}$ = 72 ºC) is below the T_g of the p-PCHE monoliths (T_g = 136 ºC), which allows infiltration of the pores by molten coumarin. PXRD of embedded nanocrystals formed upon cooling of the melt samples revealed diffraction peaks attributable to β-coumarin in 14 nm p-PCHE,[xvi] and a mixture of α- and β-coumarin in 30 nm and 40 nm p-

xvi. Analysis of the 2θ = 25.0° Bragg reflection fwhm by the Scherrer equation revealed crystal size estimates of 13 nm for 14 nm p-PCHE samples, 24 nm for 30 nm p-PCHE samples, and 22 nm for 40 nm p-PCHE samples.

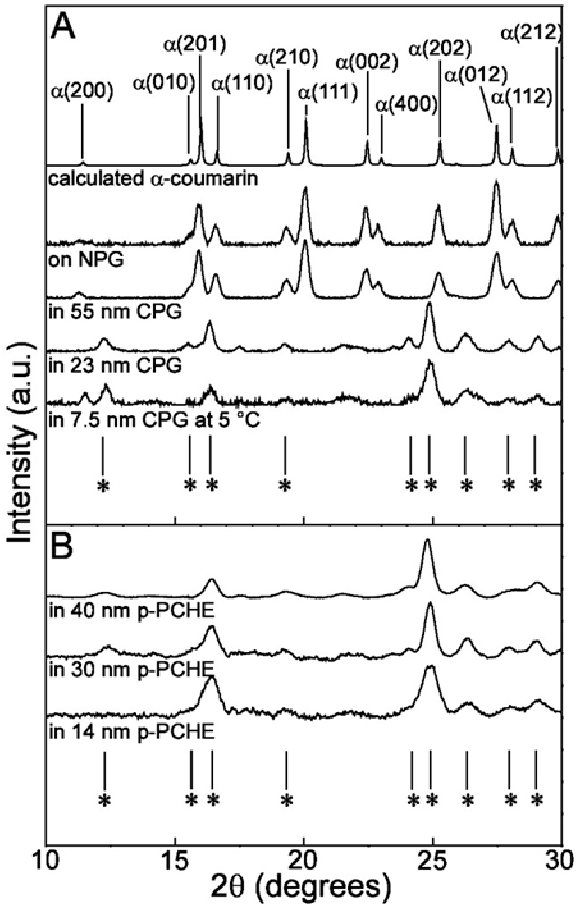

Figure 2-21. PXRD of coumarin crystals embedded in (A) CPG and (B) p-PCHE at room temperature for 55 nm, 23 nm CPG, and all p-PCHE. PXRD in 7.5 nm CPG was collected at 5 ºC owing to the melting point depression that resulted in partial melting at room temperature. Contributions from amorphous scattering from the CPG and p-PCHE were subtracted from the data. The asterisks denote the reflections for β-coumarin.

PCHE (Figure 2-21B). The β-coumarin nanocrystals in CPG and p-PCHE exhibited linear relationships between melting temperature and crystal size, as determined from DSC measurements (Figure 2-20). Extrapolation of the data for p-PCHE to $1/d = 0$ (bulk crystal size) suggested that the T_m of β-coumarin was approximately 65 ºC, which is lower than that of bulk α-coumarin (72 ºC) and consistent with β-coumarin being metastable in the bulk (Figure 2-20C).

2-4.6: Summary

The regulation of polymorphism is an issue of critical importance in many technologies, as underscored by challenges in the pharmaceutical sector, where polymorph screening and control are crucial aspects of drug development. The results described herein illustrate the influence of nanoscale confinement on polymorphism, with polymorph stability crossover observed in some compounds and a surprising shift from enantiotropic to monotropic behavior. Moreover, growth in the nanoscale pores affords polymorphs that heretofore have not been reported, suggesting a unique route to polymorph discovery. Collectively, these observations reflect the delicate balance between surface energy and volume free energy in the nanoscale size regime.

2-5: Preferred Orientation Behavior of Dicarboxylic Acid and Coumarin Crystals Under Nanoscale Confinement.

In the previous section, we discussed the polymorphism and thermotropic behaviors of crystals of several α,ω-alkanedicarboxylic acids (pimelic, suberic, and glutaric acids) and coumarin within the nanopores of porous poly(cyclohexylethylene) (p-PCHE) monoliths and controlled pore glass (CPG).[47] We exploited the size constraints imposed by the porous matrices to demonstrate for the first time the formation of previously unreported δ-pimelic acid and β-coumarin polymorphs and the transition of glutaric acid from an enantiotropic system to a monotropic system under size confinement. Whereas the pores of the CPG employed in that report were tortuous and had nonuniform pore diameters, the pores of the p-PCHE were well-ordered aligned nanocylinders with highly uniform pores (Figure 2-22), which facilitated the examination of the orientation of embedded nanocrystals relative to the pore direction. Herein, we describe the effects of confinement on the orientation of a series of α,ω-alkanedicarboxylic acid

nanocrystals and coumarin nanocrystals embedded in the one-dimensional pores of p-PCHE. The nanocrystals exhibit preferred orientations that reflect the heighted competition between surface and volume free energies for nanoscale crystals. Dr. Jeong-Myeong Ha performed the experimental work and presented the original discussion of the results as part of his Ph.D. thesis.[46] The results discussed herein are presented in their entirety because this author contributed to the final discussion.[62]

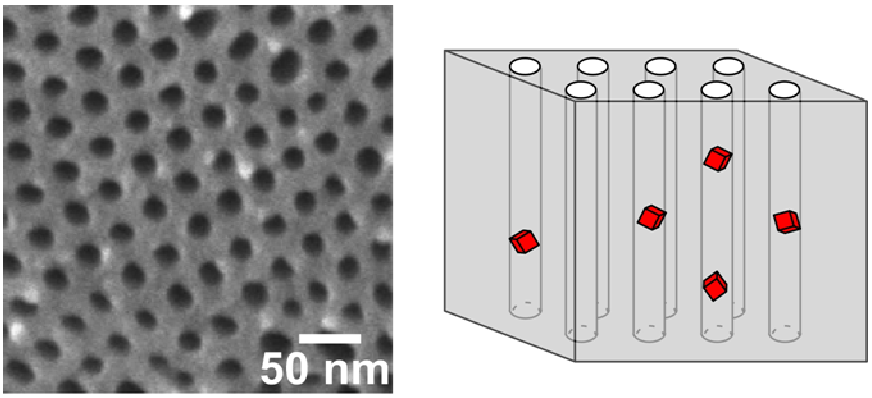

Figure 2-22. Scanning electron micrographs of a p-PCHE monolith with a hexagonal array of cylindrical pores (d ≈ 30 nm). (Right) Schematic representations of nanocrystals grown in the pores of the porous matrix. Figure adapted from reference 40. Copyright 2004 American Chemical Society. Used with Permission.

2-5.1: Sample Preparation

The p-PCHE monoliths were prepared by chemically etching the hexagonally packed cylindrical polylactide (PLA) domains from shear-aligned PCHE-PLA diblock copolymers.[43] Three sets of PCHE-PLA block copolymers, with different component weight fractions and molecular weights, were used to produce monoliths with three distinct pore diameters. Scanning electron microscopy (SEM) of etched monoliths prepared from the two sets of PCHE-PLA

diblock copolymers revealed hexagonal arrays of cylindrical pores with 14 nm, 30 nm, and 40 nm diameters oriented parallel to the direction of diblock alignment. The degree of the pore order was measured from small-angle X-ray scattering (SAXS) by the 2nd order orientation factor, F_2.[63] Only monoliths exhibiting $F_2 > 0.80$ were used in this study, as 0.80 was the minimum F_2 value for which nanocrystal orientation could be determined. Most monoliths exhibited $F_2 > 0.90$.

A series of α,ω-alkanedicarboxylic acids ($HO_2C(CH_2)_{n-2}CO_2H$, n = 2 - 15 we denote the diacids as C*n* herein) and coumarin (1,2-benzopyrone) were crystallized within the pores of p-PCHE monoliths by either immersing the porous matrices in a methanol solution of a single species or immersing the matrices in a melt of the species. Capillary action drew the liquids into the pores. The methanol-loaded samples were then dried under vacuum and the melt loaded samples cooled to room temperature to induce crystallization. The p-PCHE monoliths exhibit a glass transition temperature of 136 °C,[iii] above which the pores collapse. Thus, only the molecules exhibiting melting points below this glass transition (coumarin and C*n*; *n* = 5, 7, 9, 11, 13, 15) could be embedded within p-PCHE from the melt, although only C5 and C7 were loaded within the monoliths this way. Samples of C3, C9, C11 and C13 were prepared by imbibing methanol solutions within the pores, crystallizing the diacids by evaporation, and then melting and recrystallizing the embedded diacid material. This treatment was found to improve the quality of the nanocrystal orientation within the pores. Additionally, although the melting point of bulk C3 crystals is above the glass transition of the monoliths, C3 nanocrystals embedded within the pores from methanol solutions exhibit melting temperature depression sufficient to allow melting and recrystallization. The other diacids (C*n*; *n* = 2, 4, 6, 8, 10, 12, 14) were grown from imbibed methanol solutions. Nanocrystals of C5 and C7 were also crystallized within the p-PCHE from methanol solution in addition to crystallization from melt. Coumarin was embedded within the p-PCHE from the melt, although the material sublimed when treated this way. Attempts to grow

coumarin in the monoliths from methanol solutions failed because the vacuum drying step resulted in complete removal of the coumarin from the pores.

After crystallization, the exteriors of the p-PCHE matrices were swabbed with a soft, methanol-dampened paper towel to remove any external diacid or coumarin residue prior to characterization. The α,ω-alkanedicarboxylic acids consist of an alkyl backbone with carboxylic acids on the two terminal carbons. These compounds are available with a range of backbone lengths. The crystal structures for C2-C5 are dominated by three-dimensional hydrogen bonding schemes that result from the conformational limitations imposed by the small molecule size. In contrast, the larger dicarboxylic acids, C7-C15, adopt linear conformations with one-dimensional hydrogen bonding schemes. The acid groups of the molecules form head-to-head dimers, resulting in long chains of molecules packed parallel to one another. Notably, C7, C9, C11, and C13 all adopt the same space group (α-form: $P2_1/c$) and exhibit similar molecular packing.

The nanocrystals embedded in the aligned cylindrical nanopores of the p-PCHE monoliths were characterized by wide-angle X-ray microdiffraction (μ-XRD) using a 2D area detector. The 2D μ-XRD data were collected over the left quadrant ($45° \leq \delta \leq 135°$) of the full circle of Bragg reflections at values of $2.5° \leq 2\theta \leq 37.5°$. The μ-XRD data collected for each sample exhibited Bragg reflections consistent with the formation of crystals within the nanopores. Analysis of the peak widths by the Scherrer equation produced crystal size estimates comparable to the p-PCHE pore diameters.[xvii] The polymorph of the nanocrystals were determined by integrating the 2D μ-

xvii. Comparison of 1-D powder patterns generated from the 2-D μ-XRD data with patterns generated from the known dicarboxylic acid crystal structures allowed for polymorph identification. Analysis of the peak widths by the Scherrer equation (see: Cullity, B.D. Elements of X-ray Diffraction: Addison-Wesley: Reading, MA, 1978.) produced crystal size estimates consistent with the diameters of the p-PCHE pores.

XRD data to generate a 1D powder diffraction pattern, and comparing the positions (2θ) of the Bragg reflections on the 1D pattern to the positions of Bragg reflections in powder patterns generated from the known crystal structures of the molecules. The 2D Bragg reflections collected for C3, C5, C7, C9, C11, C13 and coumarin nanocrystals appeared as arcs with well-defined intensity maxima, located at specific azimuthal angles (*i.e.* δ). In contrast, the Bragg reflections collected for C2, C4, C6, C8, C10, C12, C14, and C15 nanocrystals appeared as broad arcs with no intensity maxima. The observation of intensity across a range of δ values rather than discrete points indicates that the nanocrystals adopt a statistical distribution of orientations. In the case of the arcs with clear intensity maxima, this distribution is about an average preferred orientation with respect to the cylinder axis. The reflections exhibiting no intensity maxima indicate that the orientations of the nanocrystals are random within the pores. Consequentially, the orientation behavior of only C3, C5, C7, C9, C11 and C13 were examined. The Bragg reflection arcs collected for nanocrystals of these species were sufficient for unambiguous identification of the nanocrystal orientation within the monolith pores.

The crystal orientations can be determined from the positions of the Bragg reflections ($h_2k_2l_2$), as given by the coordinates (2θ, δ) on the 2D detector (Figure 2), by calculating the angle (ϕ) between the Miller plane ($h_2k_2l_2$) and the Miller plane $(h_1k_1l_1)_\perp$ perpendicular to the pore direction (Equation 2.7). The identity of $(h_1k_1l_1)_\perp$ can be determined by trial-and-error, calculating the interplanar angles between ($h_2k_2l_2$) planes and trial values of $(h_1k_1l_1)_\perp$ until a self-consistent set of ϕ values that agrees with the data is obtained. The crystallographic direction parallel to pore direction can be defined as perpendicular to $(h_1k_1l_1)_\perp$.

$$\cos\phi = \cos\theta\cos\delta \qquad 2.7$$

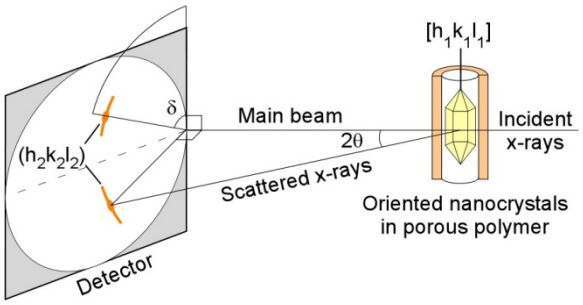

Figure 2-23. Configuration for diffraction using the μ-XRD, equipped with a 2D detector. The nanoporous monolith with embedded nanocrystals (depicted here as only a single cylinder) is held in a fixed orientation with respect to the detector, with the beam targeted at the right edge of the detector. Reflections from specific crystal planes produce diffraction spots on the 2D detector at coordinates of (2θ,δ), where 2θ is the Bragg diffraction angle and δ is the azimuthal angle on the detector that reflects the orientation of that plane with respect to δ = 0°, which coincides here with the pore axis (the normal setting for experiments described herein). Arcs of intensity (rather than discrete points) signify a distribution of orientations of the reflecting plane about the preferred orientation. Continuous bands of intensity signify a random distribution of orientations.

2-5.2: Glutaric Acid

Glutaric acid (C5) nanocrystals were embedded within 14 nm, 30 nm, and 40 nm p-PCHE monoliths from C5 melts and methanol solutions (30% weight C5). The 2D μ-XRD data collected for the nanocrystals embedded in the monoliths exhibited arc shaped Bragg reflections consistent with preferred crystal orientation within the pores (Figure 2-24). The polymorphs of the nanocrystals were identified by comparing the positions of the Bragg reflections (2θ) with the positions of reflections in powder patterns simulated from the known structures of α-C5 and β-C5, and reflections were assigned Miller indices from the indices of the corresponding peaks in the simulated pattern. The intensity maximum of each Bragg reflection arc was used to determine the azimuthal angle (δ) for that reflection. μ-XRD of nanocrystals grown from the melt within p-PCHE revealed the exclusive presence of α-C5 for all pore sizes. Likewise, α-C5 was the

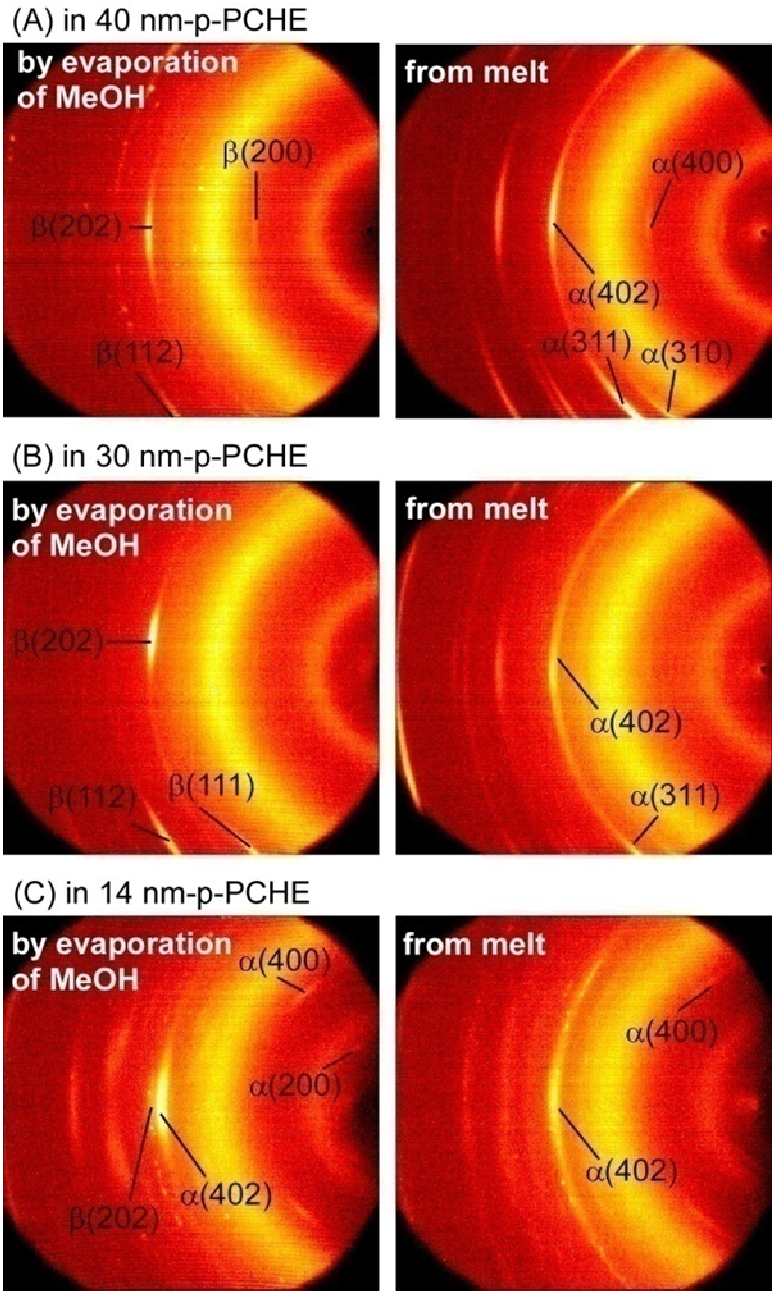

Figure 2-24. 2D-XRD images of C5 nanocrystals embedded in (A) 40 nm, (B) 30 nm, and (C) 14 nm p-PCHE. Images on the left correspond to crystals grown by evaporation of methanol from methanol solutions imbibed by the pores, and images on the right correspond to crystals grown by crystallizing molten C5.

exclusive polymorph observed when C5 crystals were grown from methanol solutions within 14 nm p-PCHE. Bragg reflections collected for C5 nanocrystals grown from methanol solutions within 30 and 40 nm p-PCHE, however, indicated that β-C5 was present in those samples instead of α-C5.

Diffraction from α-C5 nanocrystals embedded within 14 nm p-PCHE, regardless of whether the crystals were grown from melt or methanol solution, produced Bragg reflections with azimuthal positions suggesting these planes were consistent with the α(30-1) aligned perpendicular to the pore walls (Table 2-2). This is equivalent to having α[010] aligned parallel to the channel direction.[xviii] Examination of the single crystal structure for α-C5 reveals long chains of hydrogen bonded C5 molecules where neighboring chains subtend at an angle of 17°, with one chain coinciding with [1-1-2] and its neighbor coinciding with [11-2] (Figure 2-25A, B, and C). Notably, the α[010] bisects the [1-1-2] and [11-2], thus these directions form angles of 8.5° with respect to the channel direction. Examination of the α-C5 crystal structure reveals that there is no hydrogen bonding between chains. Furthermore, within each chain the size of the C5 molecules prevent the molecules from adopting linear conformations where the hydrogen bonds between molecules are parallel. Instead, the hydrogen bonds of the acid moieties protrude from all faces of the α-C5 unit cell, precluding the absolute determination of a dominant hydrogen bond direction. Attempts to corroborate the preferred orientation axis [010] with the native fast-growth axes of bulk α-C5 crystals were unsuccessful, because bulk α-C5 crystals adopt block-like habits with no clear fast-growth direction. The α-C5 nanocrystals grown from the melt within

xviii. Notably, the Bragg reflection arcs are symmetric about δ = 90° due to nanocrystals pointed towards opposite ends of the pores, and the distribution of those nanocrystals about the preferred orientation can cause the symmetric arcs to blend together and appear at δ = 90° when the true azimuthal angle for those reflections is near 90°.

Table 2-2. Measured and expected Bragg reflection parameters for α and β-C5 nanocrystals embedded within p-PCHE monoliths.

Reflection (hkl)	Measured 2θ (°)	Measured δ (°)[a]	Cos(θ)Cos(δ) (from measured)	φ (°) (from measured)[b]	Expected 2θ (°)	Expected φ (°)[c]	Expected δ (°)[a,b]
C5 in 14 nm p-PCHE from melt and methanol solutions					α(30-1)⊥pores		
α(400)	13.9	42, 138	0.74	42	13.9	40	39
α(202)	20.9	73, 107	0.29	73	20.9	73	72, 108
α(311)	23.0	90	0.00	90	23.0	83	83, 97
α(402)	23.5	90	0.00	90	23.5	89.5	89.5, 90.5
C5 in 30 and 40 nm p-PCHE from melt					α(010)⊥pores		
α(200)	6.9	90	0.00	90	6.9	90	90
α(400)	13.9	90	0.00	90	13.9	90	90
α(202)	20.9	35, 145	0.81	36	20.9	38	37, 143
α(402)	23.5	90	0.00	90	23.5	90	90
C5 in 30 and 40 nm p-PCHE from methanol solutions, orientation 1					β(010)⊥pores		
β(200)	13.8	90	0.00	90	13.7	90	90
β(202)	23.9	90	0.00	90	23.9	90	90
β(112)	27.3	46, 134	0.68	48	27.2	45	44, 136
C5 in 30 and 40 nm p-PCHE from methanol solutions, orientation 2					β(10-1)⊥pores		
β(200)	13.8	50, 130	0.64	50	13.7	43	43, 137
β(110)	19.6	78, 102	0.20	78	19.6	75	75, 105
β(111)	21.9	86, 94	0.07	86	21.9	81	85, 95
β(112)	27.3	73, 107	0.28	74	27.2	64	77, 103

[a]Reflections appearing as pairs of δ values symmetrically opposed across δ = 0° and 90° can be attributed to nanocrystals oriented in opposite directions within the pores. [b]Calculated using Eq. 2.7. [c]Calculated with (*hkl*) and the plane listed as perpendicular to the pores, denoted as $(hkl)_{\perp}$pores. Reflections that were observed but whose δ could not be measured, due to the peak maxima residing outside of the detector range, are not included in this table.

30 nm and 40 nm p-PCHE produced Bragg reflections with azimuthal angles markedly different from those observed for the reflections from α-C5 in 14 nm p-PCHE (Table 2-2). Analysis of these reflections using the trial-and-error method above revealed that the α(010) was perpendicular to the channel direction. Examination of the α-C5 crystal structure revealed that the C5 chains aligned along [1-1-2] and [11-2] are bisected by α(010) such that each forms an angle of 81.5° with that plane (Figure 2-25). Notably, this signifies a 90° change in nanocrystal orientation relative to the orientation determined for the nanocrystals embedded within 14 nm p-PCHE.

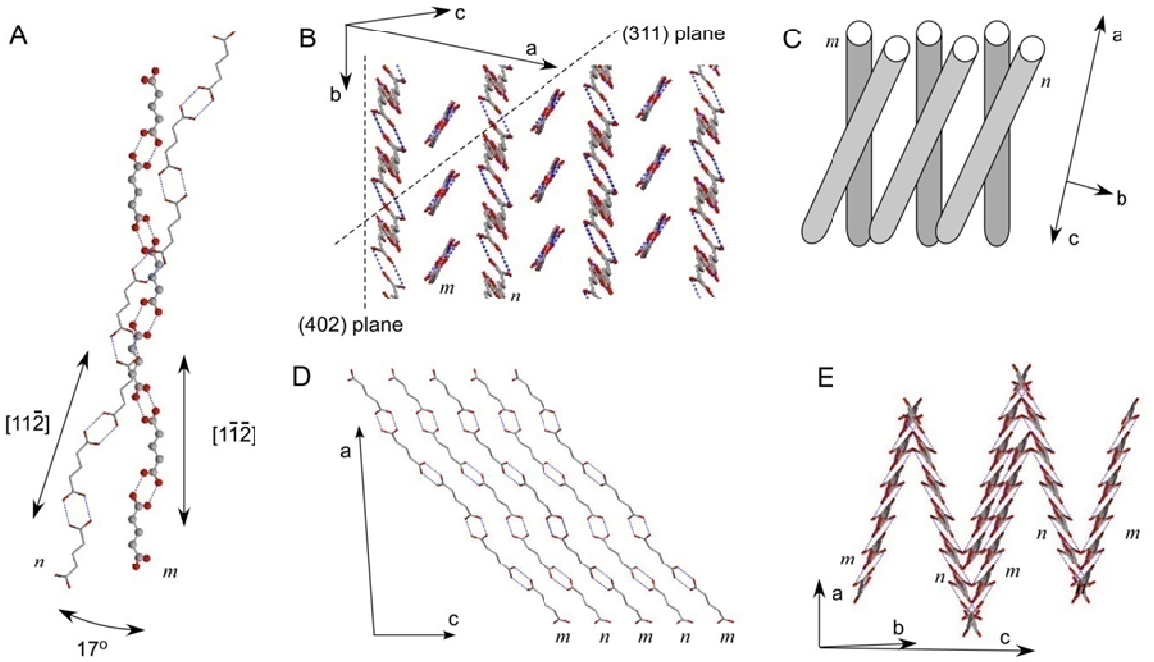

Figure 2-25. Single crystal structure of α-C5. (A) Illustration of the two hydrogen-bonded chains, *m* and *n*, which subtend an angle of 17°. (B) Illustration of the alternating (402) layers of the two chains. (C) Schematic representation of hydrogen-bonded chains. Illustration of (D) (010) plane and (E) (30-1) plane.

The observation of a preferred orientation argues against the instantaneous formation of randomly oriented nuclei that retain their initial orientation and grow uniformly. Instead, the observations are consistent with (*i*) a preferred orientation of the crystal nuclei at the early stages of crystallization due to the 1D anisotropy of the cylindrical nanopores; (*ii*) a continuous nucleation and growth process wherein nanocrystals with the direction parallel (or nearly parallel) to the pores are preferred because they can achieve critical size more readily than nuclei with other alignments. Such "misaligned" crystals would be prevented from achieving their natural habit, which reflects the balance between surface and volume free energies. As such, misaligned crystals would be less stable and more inclined to redissolve than those with their preferred growth axes aligned with the pores (via critical size effects or Ostwald ripening, see Chapter 1). The appearance of different preferred orientations for α-C5 in 14 nm p-PCHE compared with 30

and 40 nm p-PCHE (when imbibed from the melt) is probably a manifestation of the balance between surface and volume energies as well. Namely, the balance between surface and volume energy for nanocrystals embedded in 14 nm p-PCHE may be lowest for crystals that are aligned with α(30-1) perpendicular to the pore direction, whereas the ratio may be lowest for α-C5 embedded in 30 and 40 nm p-PCHE when the α(010) is perpendicular to the pore direction.

The predominant orientation for the β-C5 nanocrystals in 30 and 40 nm p-PCHE was with the β(010) normal to the pore direction (Table 2-2, Figure 2-26).[xix] In this orientation, chains of hydrogen bonded C5 molecules align perpendicular to the channel direction along β[10-1], with hydrogen bonds between chains parallel to the channel direction. In a small percentage of the samples of 30 nm and 40 nm p-PCHE, the β-C5 nanocrystals produced Bragg reflections consistent with the β(10-1) perpendicular to the pore direction (Table 2-2). This plane, in stark contrast to the β(010) plane, forms an 81° with the direction of hydrogen bonding, β[10-1]. Thus, nanocrystals aligned with the β(10-1) perpendicular to the pore direction have their chains of C5 molecules aligned nearly parallel to the pore wall. Both of the orientations adopted by β-C5 nanocrystals exhibit hydrogen bonding directions parallel to the pore walls, and the appearance of two orientations in the same pore sizes suggests that crystals of these orientations have comparable surface and volume energies.

xix.β-C5 nanocrystals were not observed within 14 nm p-PCHE owing to the influence of size confinement on polymorph selectivity (see Section 2-4), so the β-C5 orientations in the smallest pores could not be compared with the orientations in the 30 nm and 40 nm monoliths.

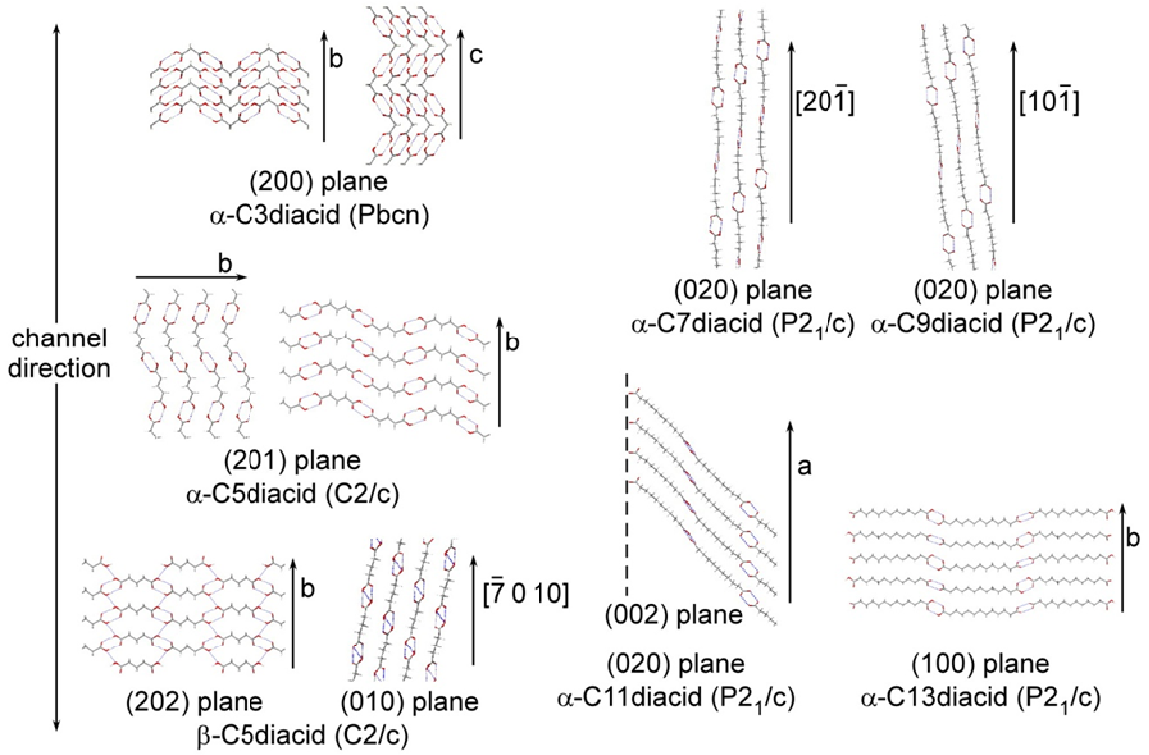

Figure 2-26. Orientation of dicarboxylic acids embedded in cylindrical pores of p-PCHE. Crystal orientations of α-C3diacid (Pbcn, $HOOCCH_2COOH$), α-C5diacid (C2/c, $HOOC(CH_2)_3COOH$), β-C5diacid (C2/c, $HOOC(CH_2)_3COOH$), α-C7diacid ($P2_1/c$, $HOOC(CH_2)_5COOH$), α-C9diacid ($P2_1/c$, $HOOC(CH_2)_7COOH$), α-C11diacid ($P2_1/c$, $HOOC(CH_2)_9COOH$), and α-C13diacid ($P2_1/c$, $HOOC(CH_2)_{11}COOH$) were observed.

2-5.3: Malonic Acid

Nanocrystals of malonic acid (C3) were grown within 30 nm and 40 nm p-PCHE monoliths from imbibed methanol solutions (30% wt. C3). As noted above, C3 could not be imbibed by the p-PCHE monoliths as a melt due to its melting temperature exceeding the glass transition temperature of the monoliths (136 °C). Bragg reflections (Figure 2-27A) collected for the C3 nanocrystals embedded within the 30 nm and 40 nm monoliths were consistent with diffraction from α-C3 nanocrystals with the α(010) perpendicular to the channel wall (Table 2-3, Figure 2-26). Notably, several of the reflections within the same samples also exhibited azimuthal intensity

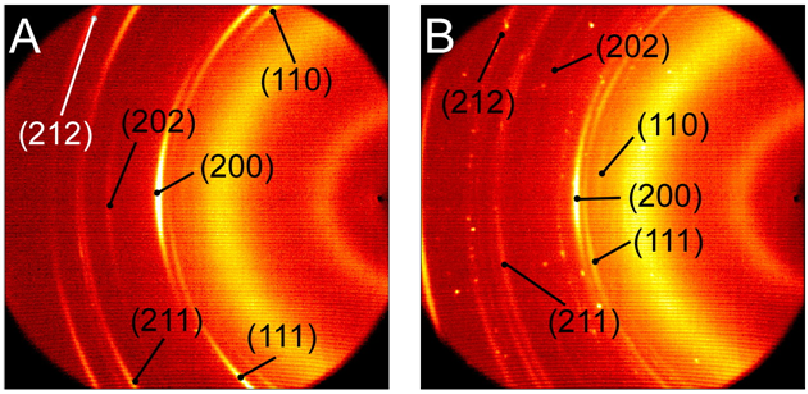

Figure 2-27. 2D μ-XRD data illustrating the Bragg reflections used to determine the orientation of α-C3 nanocrystals embedded in 30 nm p-PCHE. (A) α(010) and (B) α(001) planes are perpendicular pore walls, respectively.

Table 2-3. Measured and expected Bragg reflection parameters for α-C3 nanocrystals embedded within 30 and 40 nm p-PCHE monoliths.

Reflection (hkl)	Measured 2θ (°)	Measured δ (°)[a]	Cos(θ)Cos(δ) (from measured)	ϕ (°) (from measured)[b]	Expected 2θ (°)	Expected ϕ (°)[c]	Expected δ (°)[a,b]
C3 in 30 and 40 nm p-PCHE from methanol solutions, orientation 1					α(010)⊥pores		
α(110)	21.2	32, 148	0.83	34	21.1	33	33, 147
α(111)	22.5	34, 146	0.81	36	22.5	38	38, 142
α(200)	23.2	90	0.00	90	23.2	90	90
α(211)	30.3	51, 129	0.61	53	30.4	54	54, 126
α(113)	31.5	44, 136	0.69	46	31.5	56	56, 124
α(212)	33.3	56, 124	0.54	58	33.3	58	58, 122
C3 in 30 and 40 nm p-PCHE from methanol solutions, orientation 2					α(001)⊥pores		
α(110)	21.2	89	0.02	89	21.1	90	90
α(111)	22.5	71, 109	0.32	71	22.5	70	70, 110
α(200)	23.2	90	0.00	90	23.2	90	90
α(202)	28.0	58, 122	0.51	59	28.0	56	56, 124
α(211)	30.3	75, 105	0.25	76	30.4	75	75, 105
α(212)	33.3	64, 116	0.42	65	33.3	62	62, 118

[a]Reflections appearing as pairs of δ values symmetrically opposed across δ = 0° and 90° can be attributed to nanocrystals oriented in opposite directions within the pores. [b]Calculated using Eq. 2.7. [c]Calculated with (*hkl*) and the plane listed as perpendicular to the pores, denoted as $(hkl)_{\perp}$pores. Reflections that were observed but whose δ could not be measured, due to the peak maxima residing outside of the detector range, are not included in this table.

maxima consistent with the α(001) perpendicular to the pore direction (Table 2-3), which corresponds to a 90° degree rotation of the crystals within the pores. Examination of the α-C3 crystal structure reveals that hydrogen bonded C3 chains are parallel to α(001), but that the hydrogen bonds of each C3 molecule are antiparallel to the chain, forming angles of 32.9° with it. Consequentially, the hydrogen bond scheme in α-C3 is complex and three-dimensional, which is reflected in the block-like habits adopted by bulk α-C3 crystals. Notably, all of the samples examined produced Bragg reflections consistent with both orientations, arguing that α-C3 nanocrystals in these orientations maintain comparable surface and volume energies.

2-5.4: Pimelic Acid

Pimelic acid (C7) was embedded within the 14 nm, 30 nm, and 40 nm pores of p-PCHE by allowing methanol solutions of C7 (30% wt. C7) and C7 melt to penetrate the pores. After the C7 was crystallized, μ-XRD data revealed Bragg reflections consistent with α-C7 in 14 nm, 30 nm and 40 nm p-PCHE for crystals grown from methanol solution and α-C7 in 40 nm p-PCHE for crystals grown from the melt. Diffraction from C7 crystals grown from the melt within 14 nm p-PCHE produced Bragg reflections consistent with the δ-form, which we reported recently for the first time. The C7 nanocrystals grown from the melt within 30 nm p-PCHE adopted a mixture of the α- and δ- polymorphs (Figure 2-28). All of the Bragg reflections for the α and δ polymorphs in all samples were arcs suggesting preferred orientation of the C7 nanocrystals within the monolith pores, however, the assignment of Miller indices to the reflections owing to δ-C7 was prevented because there is no reported single crystal structure for this polymorph. This precluded the determination of the preferred orientation of the δ-C7 nanocrystals within the 14 nm and 30 nm p-PCHE. In contrast, the α-C7 crystals that formed within the pores exhibit a known crystal

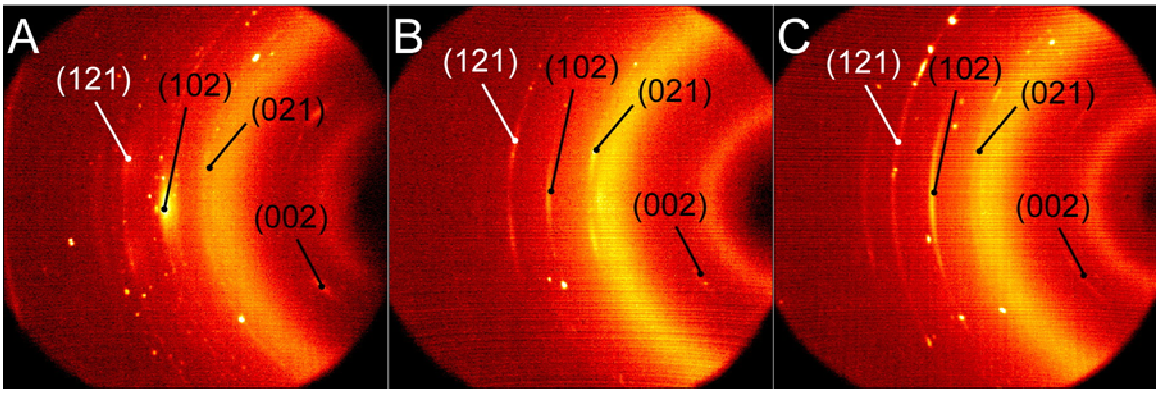

Figure 2-28. 2D data of α-C7 in (A) 14 nm, (B) 30 nm, and (C) 40 nm p-PCHE from methanol solutions.

structure, allowing for the assignment of Miller indices to its Bragg reflections and subsequent determination of the preferred orientation of the nanocrystals. Notably, diffraction from all of the α-C7 nanocrystals, regardless of pore size or crystallization method, produced Bragg reflections with azimuthal angles consistent with the alignment of the α(10-3) perpendicular to the pore direction (Table 2-4, Figure 2-26). Comparison of the preferred orientation with the crystal structure of α-C7 revealed that the [20-1] direction was parallel with the p-PCHE pore direction. The [20-1] direction coincides with the direction of the hydrogen-bonded chains of C7 molecules (Figure 2-29A), and the (10-3) plane intersects those hydrogen bonds.

Bulk crystals of α-C7 grown by slow evaporation of benzene, a nonpolar solvent expected to bind poorly to the carboxylic acid groups during crystal growth, exhibited a thin needle habit (Figure 2-29B) where the needle axis coincided with [20-1] direction. The needle axis is identical to preferred orientation axis of nanocrystals embedded in p-PCHE. The (10-3) faces of the [20-1] needles are vanishingly small, suggesting that these faces have high surface energies and that the observed crystal alignment minimized the overall surface energy of the nanocrystals. In contrast, bulk α-C7 crystals grown from the slow evaporation of methanol exhibited a plate-like block habit with a long axis along [010] and large (002) faces, which contain terminal polar carboxyl

Table 2-4. Measured and expected Bragg reflections for α-C7 nanocrystals embedded within 14, 30, and 40 nm p-PCHE monoliths from methanol solutions and within 30 and 40 nm p-PCHE monoliths from the melt. The α(10-3) was perpendicular to the pore direction.

Reflection (hkl)	Measured 2θ (°)	Measured δ (°)[a]	Cos(θ)Cos(δ) (from measured)	φ (°) (from measured)[b]	Expected 2θ (°)	Expected φ (°)[c]	Expected δ (°)[a,b]
α(002)	11.6	48, 132	0.67	48	11.6	52	52, 128
α(021)	19.3	78, 102	0.20	78	19.3	79	79, 111
α(102)	23.0	90	0.00	90	23.0	85	85, 95
α(121)	26.7	81, 99	0.15	81	26.7	78	78, 102

[a]Reflections appearing as pairs of δ values symmetrically opposed across δ = 0° and 90° can be attributed to nanocrystals oriented in opposite directions within the pores. [b]Calculated using Eq. 2.7. [c]Calculated with (*hkl*) and the plane listed as perpendicular to the pores, denoted as $(hkl)_{\perp}$pores. Reflections that were observed but whose δ could not be measured, due to the peak maxima residing outside of the detector range, are not included in this table.

groups on their surfaces (Figure 2-29C).[xx] In contrast to the environment created by benzene, the environment created by the methanol solvent would favor the formation of polar surfaces. Despite this preference, α-C7 nanocrystals grown in p-PCHE from methanol still adopted the [20-1] parallel to the pore walls. As such, the nanoscale pores physically constrain crystal growth so that the crystal face with the highest surface energy, (10-3), spans the narrowest dimension of the pore. Any tilt of this face relative to the pore direction would produce an increase of the surface area of this unfavorable plane, thereby increasing the total free energy of the crystal. The correspondence between the preferred orientation and bulk habit of α-C7 presents a clear example of preferred orientation that minimizes the competition between surface and volume energies.

xx. β-C7 crystals obtained by growth from methanol solution also exhibited a plate-like block habit with the large face coinciding with the (200) plane. This plane also has terminal polar carboxyl groups on the surface, as did the (002) plane of α-C7.

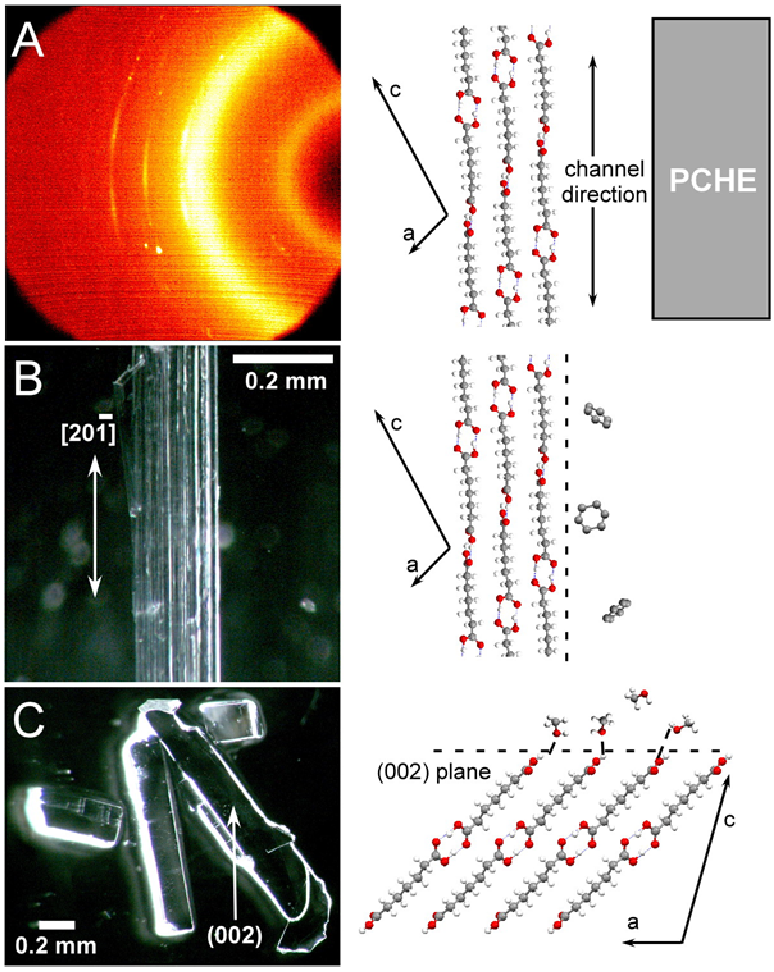

Figure 2-29. (A) 2D XRD data (left) collected for α-C7 nanocrystals embedded in 30 nm p-PCHE, and (right) a schematic illustrating the orientation of the nanocrystals relative to the pore walls. (B) Optical micrograph (left) of bulk α-C7 grown from benzene solutions, and (right) a schematic of the orientation and packing of C7 molecules in the α polymorph depicted in the micrograph, with benzene molecules indicating the locations where the benzene molecules likely interact most favorably with the crystal, thereby guiding the needle habit of the crystals by preventing C7 molecule addition along those directions. (C) Optical micrograph (left) of bulk α-C7 bulk crystals grown from methanol solutions, and (right) a schematic of the orientation of the C7 molecules in the crystals depicted in the micrograph and the interaction between the methanol solvent and the large (002) face of the crystals.

2-5.5: Azelaic, Undecanoic, and Brassaylic Acid

Azelaic Acid (C9), undecaneoic Acid (C11), and brassaylic Acid (C13) were crystallized within 30 nm and 40 nm p-PCHE from imbibed methanol solutions of individual species into the pores (30, 20, and 20% wt. for C9, C11, and C13, respectively). μ-XRD data collected after crystallization from methanol revealed circular Bragg reflections suggesting no preferred orientation. The samples were then heated above the diacid melting temperatures, and cooled to recrystallize the embedded material. Diffraction from the nanocrystals formed during this treatment produced Bragg reflection arcs consistent with oriented nanocrystals (Figure 2-30). The C9 nanocrystals produced Bragg reflections consistent with the α-polymorph with the α(10-6) plane perpendicular to the pore direction and α[10-1] parallel to the pore direction (Table 2-5, Figure 2-26). Examination of the single crystal structure of α-C9 reveals that this plane represent a rotation of the chains of hydrogen bonded C9 molecules by 6° (6° is the median and mode rotation of 16 samples; Mean = 8°; Standard deviation = 4°) compared with the pore direction (Figure 2-30, Figure 2-31). The C11 nanocrystals produced Bragg reflections consistent with the α-C11 polymorph and α(10-5) perpendicular to the pore wall with the [100] crystal direction parallel to the channel walls (Table 2-5, Figure 2-26). The C11 chains in these crystals form an angle of approximately 28° (7 samples; Median: 28°, Mode: 28°, Mean: 30°, Std. Dev: 7°) with the channel direction. The C13 nanocrystals produced reflections signifying the presence of the α-form with the α(010) perpendicular to and α[010] parallel to the pore direction (Table 2-5, Figure 2-26). Whereas C9 and C11 exhibited preferred orientations that vary slightly between samples, all samples of α-C13 in 30 nm and 40 nm exhibited one orientation with no variation. Within the oriented α-C13 nanocrystals, the chains of C13 molecules were perpendicular to the pore direction, forming angles of 90° with the pore walls.

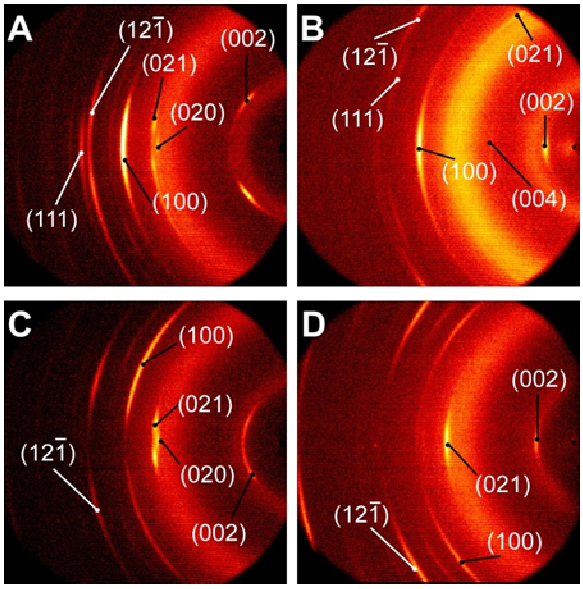

Figure 2-30. 2D μ-XRD data for (A) α-C9, (B) α-C13, and (C, D) α-C11 illustrating the Bragg reflections used to determine the orientation of the nanocrystals embedded within 30 nm and 40 nm p-PCHE.

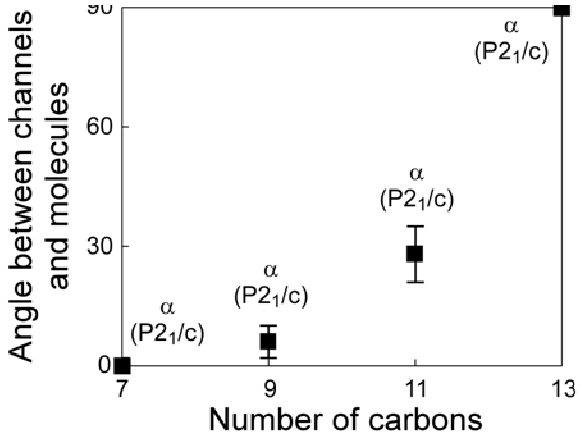

Figure 2-31. Angle between p-PCHE channels and hydrogen bonded chains of dicarboxylic acids.

The preferred orientation of C7, C9, C11, and C13 exhibit a progressive change in orientation that reflects the growing importance of nonpolar faces in determining the crystal surface energy. For C7 the preferred orientation is dominated by the hydrogen bonding direction, which coincides with the direction of fast growth for bulk α-C7 nanocrystals and minimization of the plane of

Table 2-5. Illustrative examples of measured and expected Bragg reflection parameters for α-C9, α-C11, and α-C13 nanocrystals embedded within 30, and 40 nm p-PCHE monoliths from methanol solutions, after subsequent melting and recrystallization within the pores.

Reflection (hkl)	Measured 2θ (°)	Measured δ (°)[a]	Cos(θ)Cos(δ) (from measured)	φ (°) (from measured)[b]	Expected 2θ (°)	Expected φ (°)[c]	Expected δ (°)[a,b]
C9 in 30 and 40 nm p-PCHE					α(10-6)⊥pores		
α(002)	9.4	51, 129	0.63	51	9.4	53	53, 127
α(020)	18.5	90	0.00	90	18.5	90	90
α(021)	19.1	83, 97	0.12	83	19.1	81	81, 99
α(100)	22.9	81, 99	0.15	81	22.9	84	84, 96
α(12-1)	27.1	77, 103	0.22	77	27.1	79	78, 102
α(111)	28.2	90	0.00	90	28.2	89	89, 91
C11 in 30 and 40 nm p-PCHE					α(10-4)⊥pores		
α(002)	7.8	90	0.00	90	7.9	88	88, 92
α(021)	19.0	90	0.00	90	19.0	89	89, 91
α(100)	22.8	48, 132	0.66	49	22.8	44	43, 137
α(12-1)	27.5	53, 127	0.58	54	27.5	53	53, 127
C13 in 30 and 40 nm p-PCHE					α(010)⊥pores		
α(002)	6.7	90	0.00	90	6.7	90	90
α(004)	13.4	90	0.00	90	13.4	90	90
α(021)	19.0	10, 170	0.97	14	19	10	9, 171
α(100)	22.6	90	0.00	90	22.6	90	90
α(111)	26.8	69, 111	0.35	70	26.8	70	69, 111
α(12-1)	27.7	48, 132	0.65	49	27.7	47	47, 133

[a]Reflections appearing as pairs of δ values symmetrically opposed across δ = 0° and 90° can be attributed to nanocrystals oriented in opposite directions within the pores. [b]Calculated using Eq. 2.7. [c]Calculated with (*hkl*) and the plane listed as perpendicular to the pores, denoted as $(hkl)_{\perp}$pores. Reflections that were observed but whose δ could not be measured, due to the peak maxima residing outside of the detector range, are not included in this table.

highest energy. As the chain length increases, however, the preferred orientation shifts towards the direction of hydrogen bonding pointing towards the pore walls. The surface energy argument for the selection of preferred orientation, used herein to explain the orientation behaviors of C3, C5, and C7 nanocrystals, suggests that the orientation shifts owe to the increasing importance of the nonpolar surfaces in determining the surface energies for the larger C*n* compounds.

2-5.6: **Coumarin**

Coumarin nanocrystals were grown within 14 nm, 30 nm and 40 nm p-PCHE from imbibed melts. Crystallization of coumarin from methanol solutions was not possible, as removal of the methanol under vacuum also sublimed the coumarin from the pores. Bragg reflections collected for the nanocrystals in 30 nm and 40 nm p-PCHE were consistent with either α-coumarin or with β-coumarin. Only β-coumarin was evident in 14 nm p-PCHE. All of the observed reflections were arcs consistent with nanocrystal orientation within the monolith pores, and the azimuthal angles of the Bragg reflections for α-coumarin were consistent with the α(010) aligned perpendicular to the pore direction (Figure 2-32, Table 2-6). This is equivalent to the crystallographic *b*-axis growing parallel to the pore walls. Unfortunately, the single crystal structure for β-coumarin has not been reported and we did not succeed in collecting it, precluding characterization of the β nanocrystal orientation within the monoliths. Bulk crystals of α-coumarin grown from cyclohexane solutions in our laboratory adopted needle habits with dimensions of approximately 10^3 μm x 10 μm. These crystals were too small to be used to determine the needle axis of α-coumarin, but our posit that crystals orient themselves to minimize their surface energies suggests that the fast growth axis, where the ends are vanishingly small, will be consistent with the axis aligned parallel to the pore walls for nanocrystals, [010]. Confirmation of this hypothesis would provide additional support for the posit that nanocrystals adopt preferred orientations such that their surface energies are minimized relative to their volume energies, but this cannot be tested until coumarin crystals of suitable size are obtained.

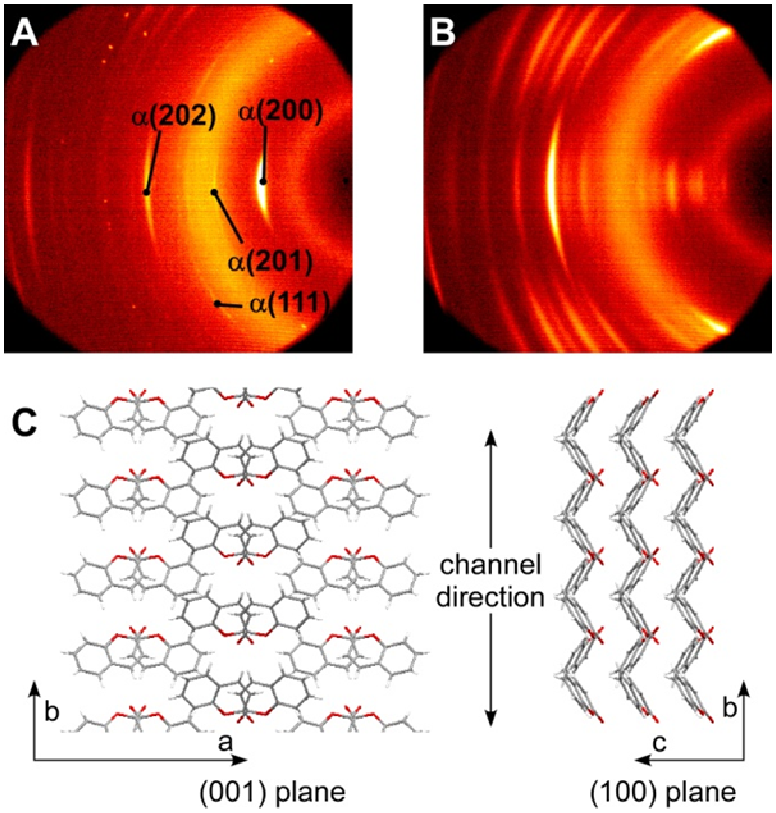

Figure 2-32. Preferred orientation of coumarin crystals embedded within p-PCHE. (A) Two dimensional XRD results of α-coumarin embedded within 40 nm p-PCHE. (B) Two dimensional XRD results of β-coumarin embedded within 40 nm p-PCHE. (C) Orientation of α-coumarin crystals embedded within p-PCHE along the cylindrical channel direction.

Table 2-6. Measured and expected Bragg reflection parameters for α-coumarin nanocrystals embedded within 30 and 40 nm p-PCHE monoliths from the melt. The α(010) crystal plane was preferentially aligned perpendicular to the pore direction.

Reflection (hkl)	Measured 2θ (°)	Measured δ (°)[a]	Cos(θ)Cos(δ) (from measured)	ϕ (°) (from measured)[b]	Expected 2θ (°)	Expected ϕ (°)[c]	Expected δ (°)[a,b]
α(200)	11.4	90	0.00	90	11.4	90	90
α(201)	16.0	90	0.00	90	16.0	90	90
α(202)	25.3	90	0.00	90	25.3	90	90

[a]Reflections appearing as pairs of δ values symmetrically opposed across δ = 0° and 90° can be attributed to nanocrystals oriented in opposite directions within the pores. [b]Calculated using Eq. 2.7. [c]Calculated with (*hkl*) and the plane listed as perpendicular to the pores, denoted as $(hkl)_{\perp}$pores. Reflections that were observed but whose δ could not be measured, due to the peak maxima residing outside of the detector range, are not included in this table.

2-5.7: Summary

Nanocrystals of select α,ω-carboxylic acids and coumarin adopt preferred orientations when confined to the well ordered pores of p-PCHE monoliths. The preferred orientations reflect a tendency for crystals to grow to minimize the competition between their surface and volume energies. We have reported herein that this competition may result in exclusive orientations, concomitant orientations, and orientations that appear to change as a function of crystal size. Notably, all of the orientation behaviors observed have parallels in polymorphism, which is probably a consequence of the reliance of polymorphs and these preferred orientations on the delicate balance of surface and volume energies for crystals. This suggests that examples of preferred orientations may arise that are kinetically stabilized or controlled by the factors (such as solvent, temperature, auxiliaries) that are used to control polymorphism.

2-6: Experimental Details for Sections 2-4 and 2-5

Materials. Controlled pore glass (CPG), a borate-silicate composite glass from which the borate phase is leached to produce a silica glass bead with a random pore network, was obtained from CPG, Inc. (Lincoln Park, New Jersey). The pore diameters denoted herein, 7.5 nm (± 6%), 24 nm (± 4.3%), and 55 nm (± 3.1%), were chosen because they were readily available from the vendor. At least 80% of the pore volume is within 10% of the prescribed pore size, and the remaining 20% of the pore volume is unspecified. The specific pore volume and internal surface areas reported by the vendor are 0.47 cm^3/g and 140.4 m^2/g for 7.5 nm CPG, 0.95 cm^3/g and 78.8 m^2/g for 24 nm CPG, and 1.6 cm^3/g and 59.4 m^2/g for 55 nm CPG, respectively. Nonporous glass (NPG), used as a control, was obtained as glass beads with diameters less than 106 μm (Sigma-Aldrich Inc., St. Louis, Missouri). Both CPG and NPG were washed with boiling nitric acid prior

to use, then washed with deionized water and dried for 12 hours under vacuum. The acid-washed CPG were stored under air in a desiccator. This treatment has little effect on the channel dimensions.[64]

C3, C4, C5, C6, C7, C8, C9, C10, C11, and C13 were purchased from Aldrich (Milwaukee, WI). C15 was purchased from TCI (Tokyo, Japan). Coumarin (1,2-benzopyrone) was purchased from Acros (Geel, Belgium). These chemicals were used without further purification. Oxalic acid (C2) was purchased from Fisher Scientific (Fair Lawn, NJ) as a dihydrate, which was dried at 130 °C for 3 hours to obtain pure oxalic acid and thereafter stored in a desiccator. p-PCHE monoliths were prepared by first pressing a powder of a PCHE-PLA diblock copolymer in a plaque mold at 200°C and 1000 psi for 10 minutes using a laboratory press, affording thin plaques of compressed polymer with poorly ordered PLA cylinders embedded in a PCHE matrix. These plaques were added to a channel die (3 mm wide × 60 mm long), heated to 200 °C, and compressed gently over the course of 1 hour to cause the polymer to flow toward the ends of the channels. Typical compression ratios for the polymer ranged from 6 to 15. This process resulted in the PLA cylinders within the PCHE aligning parallel to the channel direction and packing into an ordered hexagonal microstructure. The resulting aligned PCHE-PLA diblock copolymer monoliths were allowed to slowly cool for several hours before removal from the channel die. The PLA component was then etched by immersing the aligned diblock copolymer for 7 – 14 days in a 65 °C, 60:40 (volume) water/methanol solution containing 0.5 M NaOH. These etched p-PCHE monoliths were washed with a 60:40 water/methanol solution (no NaOH) and dried under vacuum for 12 hour. The p-PCHE monoliths and CPG beads were characterized by Scanning Electron Microscopy (JEOL 6500 and Hitachi S-900 FE-SEM, University of Minnesota), which permitted direct visualization of the channels at the monolith surface. The existence of internal porosity in p-PCHE was confirmed by SEM characterization of fractured monoliths. The channel

dimensions of the various p-PCHE monoliths were corroborated from the *d*-spacings measured by SAXS (Characterization facility, University of Minnesota) and the known volume fraction of PLA in the PCHE-PLA diblock copolymer.

Crystallization in Nanoporous Matrices. The p-PCHE monoliths and CPG beads were mixed with coumarin bulk crystals, heated above the coumarin T_m of 72 °C, and allowed to absorb the coumarin melt by capillary action for 3 minutes while heating in the DSC instrument. Cooling these nanoporous matrices below the melting point of coumarin resulted in coumarin nanocrystals embedded within the nanopores, as evident from Bragg peaks assignable to coumarin in XRD data collected on the matrices. The heating and cooling of the coumarin-matrix mixtures were performed within a differential scanning calorimeter at 5 °C/min of scan rate. Growth of the nanocrystals embedded in the nanoporous matrices was confirmed by the melting temperature depression of the nanocrystals and XRD data.

The p-PCHE monoliths or CPG beads were also immersed in methanol solutions containing a single dicarboxylic acid such as glutaric acid (C5) or pimelic acid (C7) in a 10 - 30% (w/w) concentration. Initially, the empty p-PCHE monoliths and CPG beads were opaque, but they became translucent within approximately 30 min when infiltrated by the methanol solution. After this treatment, the p-PCHE monoliths and CPG beads were removed from the solution and allowed to dry under ambient conditions for 3 hours to allow for crystallization within the channels as the imbibed methanol evaporated. Crystals of dicarboxylic acids present on the external surfaces of the p-PCHE monoliths were removed by carefully wiping the surfaces of the monolith with a damp cloth. The p-PCHE monoliths were then dried in a vacuum for 6 hours. The infiltrated CPG materials were not amenable to the same cleaning procedures. Therefore, they were simply dried in a vacuum for 6 hours after the ambient drying step. While the dicarboxylic acid nanocrystals embedded within the nanopores could be grown by the

evaporation of solvent, coumarin nanocrystals could not be grown by this method due to the ease of sublimation of coumarin under vacuum.

The p-PCHE monoliths were mixed with coumarin bulk crystals, heated above the coumarin melting temperature, 80 °C, and allowed to absorb the coumarin melt by capillary action for 3 minutes during Differential Scanning Calorimetry (DSC) experiments. Cooling these nanoporous matrices below the melting point of coumarin resulted in coumarin nanocrystals forming within the nanopores, as evident from Bragg peaks assignable to coumarin in XRD data collected for the matrices. The heating and cooling of the coumarin-matrix mixtures were performed within a differential scanning calorimeter at 5 °C/min of scan rate. Growth of the nanocrystals embedded in the nanoporous matrices was confirmed by the melting temperature depression of the nanocrystals and 2D XRD data. Bulk crystals of coumarin were grown by the slow evaporation of cyclohexane solutions and adopted the α polymorph, a needle-like habit, and dimensions of 10^3 μm x 10 μm. These crystals were too small for single crystal XRD experiments, precluding the determination of the crystallographic direction corresponding to the needle axis of the crystals.

Single crystals of α-C5 were obtained by melting the C5 solid between two glass plates and then cycling several times between 99 ºC and 100 ºC with 1 ºC/min cooling scans and 10 ºC/min heating scans. The temperatures of these scans were controlled with a LTS350 stage and TP94 controller (Linkam Scientific Instruments, Ltd., Surrey, UK). The crystal growth was monitored through an upper glass plate with an optical microscope. To prevent the bulk α-C5 crystals from transforming to the β-C5 before X-ray data collection, a single crystal of α-C5 was quickly mounted on a glass fiber, using mineral oil to hold the crystal in place. The fiber was attached to a sample holder on the goniometer head, which was then mounted on the goniometer of an X-ray diffractometer (Bruker-AXS). The sample was immediately cooled to -100 ºC, and Bragg

reflections were collected. The single crystal of α-C5 did not transform after more than 8 hours at -100 ºC.

Characterization. Wide-angle X-ray scattering microdiffraction (μ-XRD) was performed on a Bruker-AXS (Madison, Wisconsin) microdiffractometer, equipped with a 2D CCD detector, located in the University of Minnesota Characterization Facility. A 0.8 mm beam collimator was employed, and the full width at half maximum (fwhm) resolution of the instrument was determined by measuring the fwhm for both a single crystal LaB_6 wafer and a single crystal of highly oriented pyrolytic graphite (HOPG). The fwhm resolution of the instrument was approximately 0.27° (2θ) over the 2θ range of 15°–35°, allowing for a maximum crystal size estimate of 30 nm by the Scherrer equation.[vii] Variable temperature XRD was performed on the microdiffractometer using a heating stage connected to a calibrated Omega temperature controller and an Omega RTD-850 thermocouple (Omega, Inc., Stamford, Connecticut), ramping in 10 °C increments and collecting XRD data for 10 minutes at each increment. A succinic acid standard (T_m = 181 °C) was used to determine the instrument accuracy, and melting of the standard occurred at 170 °C, indicating the face of the sample stage was slightly hotter than the thermocouple during heating. Powder X-ray diffraction (PXRD) patterns were generated by integrating the 2D μ-XRD over azimuths of constant 2θ.

To determine the preferred orientation of crystals embedded in the p-PCHE, the monoliths were affixed at the end of a brass pin using a small amount of clay such that striations on the monolith surface, known to be parallel with the direction of the pores, were parallel with the brass pin. The brass pin was then inserted into a sample holder supplied by the manufacturer and then tightened with a small screw. This sample was then mounted on a four-circle Eulerian cradle such that the cylindrical pores were aligned parallel with the X-ray detector, and then the cradle was

adjusted via the instrument controls until the pores were aligned also parallel with the vertical centerline of the detector. A laser-video alignment system supplied by the manufacturer was used to determine whether the monolith was aligned with the beam, and the position of the brass pin was adjusted with small screws in the sample holder until the alignment system indicated the monolith was in the beam path. To verify the pores were aligned parallel with the vertical centerline of the detector, an initial set of X-ray data was collected and the azimuthal positions of the resulting Bragg reflections were observed. Proper alignment of the sample was evident when the reflections were symmetric about $\delta = 90°$, which verified that crystals pointed in opposite directions within the pores were also symmetric about $\delta = 90°$. This indicated the pores were parallel with the vertical center, and if the data suggested otherwise, the Eulerian cradle was adjusted with the instrument controls until the Bragg reflections from the monolith met this criteria. Data were collected in a forward scattering mode, initially with the monolith aligned parallel with the vertical center line of the detector ($\delta = 0°$) and the incident X-ray beam centered on the right edge of the detector (Figure 2-23). The sample-to-detector distance was 15 cm. Reflections were readily discerned at this sample-to-detector distance, although this configuration precluded data collection spanning the entire 360° azimuth. Instead, Bragg reflections were collected over the quadrant of the full-circle ranging from $2.5° \leq 2\theta \leq 37.5°$ and $45° \leq \delta \leq 135°$. These data were sufficient for the determination of the nanocrystal orientation within the pores.

Single Crystal X-ray Diffraction was performed on a Bruker-AXS (Madison, Wisconsin) diffractometer equipped with a CCD area detector and Oxford Cryostream Cooler, all located at the University of Minnesota X-ray Crystallography Laboratory. The diffraction data for the single crystal structure of α-C5 was collected at -100 ºC, and the structure was solved using SHELXS-97 (Bruker-AXS) and refined using SHELXL-97 (Bruker-AXS).

Differential scanning calorimetry (DSC) was performed on a Pyris-1 (Perkin-Elmer Inc., Wellesley, and Massachusetts) differential scanning calorimeter. Ice, gallium, and indium standards were used to calibrate the instrument and nitrogen was used as the purge gas. The scan rate for the samples was 5 °C/min unless otherwise noted. The molar enthalpy, $\Delta \underline{H}^{fus}$, corresponding to each phase transition were calculated from the DSC data by estimating the area under each endothermic peak (given in J) and dividing it by the total amount of C7 material (to give J/mol, or kJ/mol). Quantitative measurement of the molar enthalpies for the endothermic events for CPG-embedded nanocrystals formed by evaporation of methanol was precluded owing to the inherent imprecision of mass measurements at low mass loadings, however, nanocrystals loaded into the matrices as melts provided sufficient material for these measurements.

2-7: Concluding Remarks

Herein we discussed the evolution of crystallization under size confinement. The early predictions of the influence of particle size on phase behavior led to studies of the melting behavior of small crystals. These studies demonstrated that the size of a particle drastically influences its stability, particularly on the nanometer scale. Recent developments have revealed that size can also impact polymorph selectivity and stabilization, which was posited in Chapter 1. Furthermore, crystallization in nanoporous matrices with well-ordered pores allows the examination of crystal orientation within those pores. The preferred orientation adopted by the nanocrystals reflects the surface energy/volume energy competition that dominates polymorph selectivity and melting point depression. Despite these successes, however, the complex interplay between kinetics and thermodynamics in the phase behavior of nanoconfined materials is not fully understood. Consequentially, we will examine the polymorphism (Chapter 3) and

orientation (Chapter 4) of glycine in nanoconfinement. Glycine is a compound with rich, well-characterized, bulk polymorphism and thermotropic behavior. As discussed in Chapter 1, glycine is widely studied, and will serve as an enlightening model system for crystallization in nanoconfinement.

2-8: References

1. Thomson, W. On the equilibrium of vapour at a curved surface of liquid. *Phil. Mag.* **1871**, *42*, 448-452.
2. Gibbs, J. W. *Collected Works, Vol. 1, Thermodynamics*; Yale University Press: New Haven, 1948.
3. Many good reviews exist on this topic. For examples, see citations within references 9, 28, 36, and 35.
4. (a) Laplace, P. S. Traité de Mécanique Céleste; Supplement au Dixième Livre, Sur l'Action Capillaire. Courcier: Paris, 1806. (b) Young, T. Essay on the Cohesion of Fluids. *Phil. Trans.* **1805**, *xx*, 65-87.
5. Pawlow, P. The dependency of melting point on the surface energy of a solid body. *Z. Phys. Chem.* **1909**, *65*, 545-548.
6. Harbury, L. Solubility and Melting Point as Functions of Particle Size. 1. *J. Phys. Chem.* **1946**, *50*, 190-199.
7. (a) Kubelka-Prag, P. *Z. Elektrochem.* **1932**, *38*, 611. (b) Jackson, K. A.; Chalmers, B. Freezing of liquids in porous media with special reference to frost heave in soils. *J. Appl. Phys.* **1958**, *29*, 1178-1181.
8. Defay, R.; Prigogine, I. *Surface Tension and Adsoption*; Longmans: London, 1966.
9. Jackson, C. L.; McKenna, G. B. The melting behavior of organic materials confined in porous solids. *J. Chem. Phys.***1990**, *93*, 9002-9011.
10. Ha, J.-M.; Hillmyer, M. A.; Ward, M. D. Thermotropic Properties of Organic Nanocrystals Embedded in Ultrasmall Chambers. *J. Phys. Chem. B* **2005**, *109*, 1392-1399.
11. Frenkel, D.; Cacciuto, A. Stresses Inside Critical Nuclei. *J. Phys. Chem. B* **2005**, *109*, 6587-6594.
12. Tanaka, H. Possible resolution of the Kauzmann paradox in supercooled liquids. *Phys. Rev. E* **2003**, 011505, 1-8.
13. Patrick, W. A.; Kemper, W. A. Melting Temperatures of Compounds Adsorbed on Silica Gel. *J. Phys. Chem.* **1938**, *42*, 369-380.
14. Patrick, W. A; Land, W. E. A Study of the Influence of Capillarity on the Melting Point of Iodine. *J. Phys. Chem.* **1934**, *38*, 1201-1210.

15. Jackson, K. A.; Chalmers, B. Freezing of liquids in porous media with special reference to frost heave in soils. *J. Appl. Phys.* **1958**, *29*, 1178-1181.
16. Brinker, C. J.; Scherer, G. W. *Sol-Gel Science - The Physics and Chemistry of Sol-Gel Processing;* New York, Academic Press, 1990.
17. Haller, W. Rearrangement Kinetics of the Liquid-Liquid Immiscible Microphases in Alkali Borosilicate Melts. *J. Chem. Phys.* **1965**, *42*, 686-693.
18. (a) Litvan, G. G.; McIntosh, R. Phase Transitions of Water and Xenon Adsorbed In Porous Vycor Glass. *Can. J. Chem.* **1963**, *41*, 3095-3107. (b) Antoniou, A. A. Phase Transformations of Water in Porous Glass. *J. Phys. Chem.* **1964**, *68*, 2754-2763.
19. Litvan, G. G. Phase Transitions of Adsorbates. 1. Specific Heat and Dimensional Changes of the Porous Glass-Water System. *Can. J. Chem.* **1966**, *44*, 2617-2622.
20. Rennie, G. K.; Clifford, J. Melting of Ice in Porous Solids. *J. Chem. Soc. Faraday Trans. 1* **1997**, *73*, 680-689.
21. Rault, J.; Neffati, R.; Judeinstein, P. Melting of ice in porous glass: why water and solvents confined in small pores do not crystallize? *Eur. Phys. J. B* **2003**, *36*, 627-637.
22. Weissbuch, I.; Lahav, M.; Leiserowitz, L. Toward Stereochemical Control, Monitoring, and Understanding Crystal Nucleation. *Cryst. Growth Des.* **2003**, *3*, 125-150.
23. Beck, J.S.; Vartuli, J. C.; Roth, W. J., Leonowicz, M. E.; Kresge, C. T.; Schmitt, K. D.; Chu, C. T.-W.; Olson, D. H.; Sheppard, E. W.; McCullen, S. B.; Higgins, J. B.; Schlenker, J. L. A new family of mesoporous molecular-sieves prepared with liquid crystal templates. *J. Am. Chem. Soc.* **1992**, *114*, 10834-10843.
24. Zhao, D.; Feng, J.; Huo, Q.; Melosh, N.; Fredrickson, G. H.; Chmelka, B. F.; Stucky, G. D. Triblock Copolymer Synthesies of Mesoporous Silica with Periodic 50 to 300 Angstrom Pores. *Science*, **1998**, *279*, 548-552.
25. Schreiber, A.; Ketelsen, I.; Findenegg, G. H. Melting and freezing of water in ordered mesoporous silica materials. *Phys. Chem. Chem. Phys.* **2001**, *3*, 1185-1195.
26. Takagi, M. Electron-Diffractionstudy of Liquid-Solid Transition. *J. Phys. Soc. Jpn.* **1954**, *9*, 359-363. (in English)
27. Buffat, Ph.; Borel, J.-P. Size effect on the melting temperature of gold particles. *Phys. Rev. A.* **1976**, *13*, 2287-2298.
28. Unruh, K. M.; Huber, T. E.; Huber, C. A. Melting and freezing behavior of indium metal in porous glasses. *Phys. Rev. B* **1993**, *48*, 9021-9027.
29. Sheng, H. W.; Ren, G.; Peng, L. M.; Hu, Z. Q.; Lu, K. Epitaxial dependence of the melting behavior of In nanoparticles embedded in Al matrices. *J. Mater. Res.* **1997**, *12*, 119-123.

30. Sheng, H. W.; Ren, G. Peng, L. M.; Hu, Z. Q.; Lu, K. Superheating and melting-point depression of Pb nanoparticles embedded in Al matrices. *Phil. Mag. Lett.* **1996**, *73*, 179-186.
31. Bilgram, J. H. Dynamics at the solid-liquid transition. *Phys. Rep.* **153**, 1-89.
32. Borisov, B. F.; Charnaya, E. V.; Hoffmann, W. D.; Michel, D.; Shelyapin, A. V.; Kumzerov, Yu. A. Nuclear magnetic resonanoce and acoustic investigations of the melting-freezing phase transition of gallium in a porous glass. *J. Phys.: Condens. Matter* **1997**, *9*, 3377-3386.
33. Jackson, C. L.; McKenna, G. B. Vitrification and Crystallization of Organic Liquids Confined to Nanoscale Pores. *Chem. Mater.* **1996**, *8*, 2128-2137.
34. Prasad, R.; Lele, S. Stabilization of the amorphous phase inside carbon nanotubes: solidification in a constrained geometry. *Phil. Mag. Lett.* **1994**, *70*, 357-361.
35. Christenson, H.K. Confinement effects on freezing and melting. *J. Phys.: Condens. Matter* **2001**, *13*, R95-R133.
36. Alcoutlabi, M.; McKenna, G. B. Effects of confinement on material behavior at the nanometer size scale. *J. Phys.: Condens. Matter* **2005**, *17*, R461-R524.
37. Alba-Simionesco, C. Dosseh, G.; Dumont, E.; Frick, B.; Geil, B.; Morineau, D.; Teboul, V.; Xia, Y. Confinement of molecular liquids: consequences on thermodynamic, static, and dynamical properties of benzene and toluene. *Eur. Phys. J. E* **2003**, *12*, 19-28.
38. Radhakrishnan, R.; Gubbins, K. E.; Sliwinska-Bartkowiak, M. Effect of the fluid-wall interaction on freezing of confined fluids: Towad the development of a global phase diagram. *J. Chem. Phys.* **2000**, *112*, 11048 – 11057.
39. Awschalom, D. D.; Warnock, J. Supercooled liquids and solids in porous glass. *Phys. Rev. B* **1987**, *35*, 6779-6785.
40. Ha, J.-M.; Wolf, J. H.; Hillmyer, M. A.; Ward, M. D. Polymorph Selectivity under Nanoscopic Confinement. *J. Am. Chem. Soc.***2004**, *126*, 3382-3383.
41. Beiner, M.; Rengarajan, G. T.; Pankaj, S.; Enke, D.; Steinhart, M. Manipulating the Crystalline State of Pharmaceuticals by Nanoconfinement. *Nano Lett.* **2007**, *7*, 1381-1385.
42. Rengarajan, G. T.; Enke, D.; Steinhart, M.; Beiner, M. Stabilization of the amorphous state of pharmaceuticals in nanopores. *J. Mat. Chem.* **2008**, *18*, 2537-2539.
43. Wolf, J. H.; Hillmyer, M. A. Ordered Nanoporous Poly(cyclohexylethylene). *Langmuir* **2003**, *19*, 6553-6560.
44. (a) Zalusky, A. S. Olayo-Valles, R.; Taylor, C. J.; Hillmyer, M. A. Mesoporous Polystyrene Monoliths. *J. Am. Chem. Soc.* **2001**, *123*, 1519-1520. (b) Zalusky, A. S. Olayo-Valles, R.; Wolf, J. H.; Hillmyer, M. A. Ordered Nanoporous Polymers from Polystyrene-Polylactide Block Copolymers. *J. Am. Chem. Soc.* **2002**, *124*, 12761-12773. (c) Mao, H.; Hillmyer, M. A. Nanoporous Polystyrene by Chemical

Etching of Poly(ethylene oxide) from Ordered Block Copolymers. *Macromolecules* **2005**, *38*, 4038-4039.

45. (a) Rzayev, J.; Hillmyer, M. A. Nanoporous Polystyrene Containing Hydrophilic Pores from an ABC Triblock Copolymer Precursor. *Macromolecules* **2005**, *38*, 3-5. (b) Rzayev, J.; Hillmyer, M. A. Nanochannel Array Plastics with Tailored Surface Chemistry. *J. Am. Chem. Soc.* **2005**, *127*, 13373-13379.
46. Ha, J.-M. Crystallization and Thermotropic Properties of Organic Solids in Nanoscopic Reactors. Ph.D. Thesis, University of Minnesota, September 2006.
47. Ha, J.-M.; Hamilton, B. D.; Hillmyer, M. A.; Ward, M. D. Phase Behavior and Polymorphism of Organic Crystals Confined within Ultrasmall Chambers. *Manuscript in preparation* **2009**.
48. Four single crystal structures have been reported that describe the β-polymorph (CSD Refcodes: GLURAC, GLURAC02, GLURAC03, and GLURAC04) Morrison, J. D.; Robertson, J. M. *J. Chem. Soc.* **1949**, 1001. Although GLURAC02 was reported as a monoclinic III form, the reduced cell parameters are identical with those of the β-polymorph. Gopalan, R. S.; Kumaradhas, P.; Kulkami, G. U.; Rao, C. N. R. *J. Mol. Struct.* **2000**, *521*, 97. Thalladi, V. R.; Nusse, M.; Boese, R. *J. Am. Chem. Soc*. **2000**, *122*, 9227. GLURAC04 was chosen as the basis for XRD data analyzed in this study owing to its low R factor.
49. Dupre La Tour, F. *Compt. Rend.* **1932**, *194*, 622.
50. Thalladi, V. R.; Nisse, M.; Boese, R. The Melting Point Alteration in α,ω-Alkanedicarboxylic Acids. *J. Am. Chem. Soc.* **2000**, *122*, 9227-9236. (a) α-form: Monoclinic, $P2_1/c$, a = 5.648, b = 9.654, c = 16.022, β = 108.02°, T = 293 K. (b) β-form: Monoclinic, $C2/c$, a = 17.663, b = 4.789, c = 9.888, β = 105.61°, T = 293 K.
51. Kay, M. I.; Katz, L. The Crystal Structure of α-Pimelic Acid. *Acta Cryst.* **1958**, *11*, 289-294.
52. Steele, W. V.; Chirico, R. D.; Cowell, A. B.; Knipmeyer, S. E.; Nguyen, A. Thermodynamic Properties and Ideal-Gas Enthalpies of Formation for 1,4-Diisopropylbenzene, 1,2,4,5-Tetraisopropylbenzene, Cyclohexanone Oxime, Dimethyl Malonate, Glutaric Acid, and Pimelic Acid. *J. Chem. Eng. Data*, **2002**, *47*, 725-739.
53. Petropavlov, N. N.; Tsygankova, I. G.; Teslenko, L. A. Microcalorimetric investigation of polymorphic transitions in organic crystals. *Sov. Phys. Crystallogr.* **1988**, *33*, 853-855.
54. Cingolani, A.; Berchiesi, G. A DSC Study of phase transitions in aliphatic dicarboxylic acids. *J. Thermal Anal.* **1974**, *6*, 87-91.
55. Gao, Q.; Weber, H.-P.; Craven, B. M.; McMullan, R. K. Structure of suberic acid at 18.4, 75, and 123 K from neutron diffraction data. *Acta Cryst.* **1994**, *B50*, 695-703.

56. Haydon, S. C. Dye-Laser Fluorescence of 4-Methylumbelliferone and Related Coumarins. *Spectrosc. Lett.* **1975**, *8*, 815-892.
57. Meng, J.; Fu, D.; Yao, X.-K.; Wang, R.-J.; Matsuura, T. Solid-state photodimerization of coumarin in the presence of crystal lattice-controlling substance. *Tetrahedron* **1989**, *45*, 6979-6986.
58. Brett, T. J.; Alexander, J. M.; Clark, J. L.; Ross II, C. R.; Harbison, G. S.; Stezowsk, J. J. Chemical insight from crystallographic disorder: structural studies of a supramolecular β-cyclodextrin/coumarin photochemical system. *Chem. Commun.* **1999**, 1275-1276.
59. Moorthy, J. N.; Venkatesan, K.; Weiss, R. G. Photodimerization of coumarins in solid cyclodextrin inclusion complexes. *J. Org. Chem.* **1992**, *57*, 3292-3297.
60. α-coumarin: Gavuzzo, E.; Mazza, F. Determination of the molecular packing in the crystal of coumarin by means of potential-energy calculations. *Acta Cryst.* **1974**, *B30*, 1351-1357. Orthorhombic, *Pca*2_1, a = 15.466, b = 5.676, c = 7.917, Z = 4, D_c = 1.41, T = 293 K. This known polymorph of coumarin was assigned as α-form in our lab to tell it from a new polymorph.
61. Myasnikova, R. M.; Davydova, T. S.; Simonov, V. I. *Sov. Phys. Crystallogr.* **1974**, *18*, 454-456.
62. Ha, J.-M.; Hamilton, B. D.; Hillmyer, M. A.; Ward, M. D. *Manuscript in preparation* **2009**.
63. Sakurai, S.; Aida, S.; Okamoto, S.; Ono, T.; Imaizumi, K.; Nomura, S. Preferential Orientation of Lamellar Microdomains Induced by Uniaxial Stretching of Cross-Linked Polystyrene-block-polybutadiene-block-polystyrene Triblock Copolymer. *Macromolecules* **2001**, *34*, 3672-3678.
64. Sands, B. W.; Kim, Y. S.; Bass, J. L. Characterization of bonded-phase silica gels with different pore diameters. *J. Chromatogr.* **1986**, *360*, 353-369.

Chapter 3: Glycine Polymorphism in Nanoscale Crystallization Chambers[i]

Polymorphism, the ability of a material to exhibit multiple crystalline forms, can influence solid-state properties that depend on crystal structure and impact food,[1] dye,[2] and pharmaceutical applications.[3] The importance of polymorphism is underscored by efforts in the pharmaceutical sector, where polymorph discovery and characterization are essential for evaluating the bioavailability and shelf stability of pharmaceutical compounds, establishing patent protection for new crystal forms, complying with regulations that mandate polymorph characterization, and achieving reproducible crystallization outcomes.[4] Despite these efforts, however, reliable protocols for controlling crystallization and crystal properties, particularly polymorphism, remain a central challenge. As such, polymorph discovery and formation usually rely on the manipulation of conventional process variables such as solvent,[5] temperature,[6] additives,[7] and crystallization rate, and more recently, substrates[8] that regulate heterogeneous nucleation.

i. This work was reported in *Crystal Growth & Design* **2008**, *8*, 3368. Reproduced with permission. Copyright 2008, American Chemical Society.

Crystallization theory posits that mature crystals grow from crystal nuclei, which are generally accepted to have structures that resemble the mature crystalline forms and are believed to determine many crystal characteristics such as size, habit, and polymorph.[9] The growth of nuclei into mature crystals becomes favorable when they achieve critical size, at which the energetically favorable volume free energy begins to outweigh the energetically unfavorable surface energy.[10] Crystallization methods that permit control and intervention at the nucleation stage, combined with the characterization of crystals having dimensions near those expected for nuclei (typically nanometer scale), can provide new routes to regulating crystallization outcomes, including polymorphism.

The crystallization and thermotropic properties of nanometer-scale crystals have been studied by embedding crystalline solids, usually by imbibing melts or solutions, in nanometer-scale pores of controlled pore glass (CPG). These investigations have revealed that the high surface area-to-volume ratio of nanocrystals alters their thermotropic properties relative to their corresponding macroscopic forms, behavior that is evident from dramatic lowering of the melting points of organic compounds, metals, and ice when confined within nanometer-scale pores.[11,12,13,14] The role of nanoconfinement on the stability of amorphous states has also been explored.[15,16,17] We recently demonstrated similar behavior for organic crystals embedded in nanoscale cylindrical pores created in monoliths of shear-oriented block copolymers that had been chemically etched to remove the block comprising the cylinders. These studies revealed melting point depression for the embedded crystals comparable to that observed for the same compounds in CPG,[18] suppression of amorphous-to-crystalline phase transitions at very small pore sizes and size-dependent polymorph selectivity regulated by the diameter of the cylinders (10-70 nm),[19] and the discovery of new polymorphs.[20] The promise of this approach for regulating polymorphism and suppressing amorphous-to-crystalline phase transitions was further reinforced by the observation

of size-dependent polymorphism[21] and amorphous phase stabilization[22] for acetaminophen confined within the nanopores of CPG. Collectively, these investigations have revealed that the enthalpy of fusion decreases with crystal size and that the melting temperature depression can be influenced by crystal-wall interactions as well as crystal size. Glycine, the simplest amino acid, is used as an excipient for proteins[23] and pharmaceutical reagents,[24] and it has been implicated in the origin of life.[25] Glycine crystallizes in three polymorphic forms at ambient conditions[26] and two polymorphs at high pressures.[27] The three ambient forms of glycine are denoted as α, β, and γ: α-glycine is most common, readily crystallizing by cooling or evaporation of aqueous solutions;[28] γ is the most stable form at ambient conditions, crystallizing from aqueous solutions containing acetic acid;[29] β is metastable in the bulk state, obtained by mixing ethanol or methanol with aqueous glycine solutions. The β form of glycine readily transforms to the α form upon contact with humid air.[30] The polymorphic transitions for bulk glycine have been described in detail, and the relative stabilities of the three common polymorphs of bulk glycine at ambient conditions are $\gamma > \alpha > \beta$.[31] Glycine also exhibits a small but measurable vapor pressure, allowing for the determination of its enthalpy of sublimation,[32] but its melting is accompanied by decomposition, which has precluded determination of its bulk melting temperature and other thermochemical properties.[33,34] Glycine has been the subject of numerous studies, including examination of the mechanisms responsible for its nucleation and polymorphism,[35,36,37,38,39,40,41,42] but the polymorphism and thermotropic properties of nanoscale glycine crystals, which may resemble glycine nuclei during crystallization, have not been investigated.

Herein we describe the crystallization of β-glycine by evaporation of glycine solutions that have been imbibed by the hydrophilic nanometer-scale pores of CPG powder and porous polystyrene-poly(dimethyl acrylamide) (p-PS-PDMA) monoliths.[43] Whereas α-glycine is

observed during crystallization of bulk crystals under the same conditions and γ-glycine is the thermodynamically preferred form at ambient conditions, crystallization in the nanopores of CPG and p-PS-PDMA (Figure 3-1) resulted in the exclusive formation of the β polymorph. The β-glycine crystals were indefinitely stable when confined within pores having dimensions less than 24 nm, but they slowly transformed to α-glycine in 55 nm pores. These studies reinforce previous observations of size-dependent polymorphism while demonstrating that size confinement can enable determination of thermotropic properties that cannot be determined by direct measurements with bulk forms. The observation of β-glycine at dimensions comparable to the critical size expected for crystal nuclei suggests that glycine crystallization likely involves formation of β nuclei followed by their transformation to the other forms as crystal size increases, in accord with Ostwald's rule of stages.[44] Furthermore, these observations suggest that formulations based on nanosized crystals need to consider polymorph stability crossing as crystal size is reduced, particularly for applications where polymorphism is subject to regulatory standards.

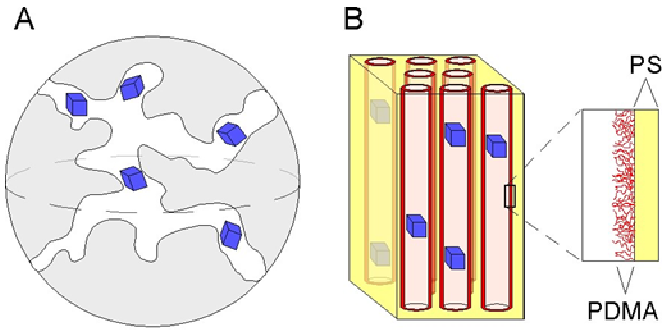

Figure 3-1. Schematic representations of (A) crystals embedded within CPG and (B) crystals embedded within the pores of p-PDMA-PS monoliths.

3-1: Experimental Procedures

Materials and Methods. All reagents and solvents were used as received unless otherwise noted. Glycine was purchased from Sigma- Aldrich, Inc. (St. Louis, Missouri). Aqueous glycine solutions were passed through a 0.45 μm poly(tetrafluoroethylene) syringe filter before use to remove any insoluble particulate matter. Controlled pore glass (CPG), a borate-silicate composite glass from which the borate phase is leached to produce a silica glass bead with a random pore network, was obtained from CPG, Inc. (Lincoln Park, New Jersey). The pore diameters denoted herein, 7.5 nm (± 6%), 24 nm (± 4.3%), and 55 nm (± 3.1%), were chosen because they were readily available from the vendor. At least 80% of the pore volume is within 10% of the prescribed pore size, and the remaining 20% of the pore volume is unspecified. The specific pore volume and internal surface areas reported by the vendor are 0.47 cm^3/g and 140.4 m^2/g for 7.5 nm CPG, 0.95 cm^3/g and 78.8 m^2/g for 24 nm CPG, and 1.6 cm^3/g and 59.4 m^2/g for 55 nm CPG, respectively. Nonporous glass (NPG), used as a control, was obtained as glass beads with diameters less than 106 μm (Sigma- Aldrich Inc., St. Louis, Missouri). Both CPG and NPG were washed with boiling nitric acid prior to use. Polylactide-poly(dimethyl acrylamide)-polystyrene (PLA-PDMA-PS) triblock copolymers and monoliths were prepared according to previously reported procedures,[43] with minor modifications as noted in Appendix B. PLA-PDMA-PS triblock copolymers were synthesized with volume fractions conducive to the formation of a hexagonally packed cylinder structure, which when shear oriented generated cylinders of PLA that were etched in base (1 M NaOH solution in 50:50 MeOH/H_2O) at 60 °C for 5 days to generate porous PS-PDMA (p-PS-PDMA) monoliths with cylindrical pores having 10 and 20 nm diameters. The p-PS-PDMA monoliths were dried under vacuum at room temperature for 3 h to remove residual water after postetch rinsing. In contrast to CPG, the cylindrical pores in the p-PS-

PDMA monoliths were well ordered, as confirmed by small-angle X-ray scattering. The interior lining of the pores was PDMA-rich and therefore hydrophilic, which permitted absorption of aqueous solutions.

Crystallization in Porous Matrices. CPG beads were immersed in aqueous solutions containing 5%, 11%, 18% glycine (weight percent). In each case the amount of solution was chosen to be approximately equal to the total pore volume of the CPG beads, based on the total mass of CPG and the specific pore volume quoted by the manufacturer. This procedure maximized glycine loading in the pores while minimizing residual glycine on the exterior surfaces of the CPG beads that otherwise may complicate diffraction analysis. Glycine crystallization within the pores was achieved either by evaporation of the water solvent at ambient conditions or by vacuum drying, with no discernible difference in crystallization outcome. Therefore, vacuum drying was used throughout for convenience. Glycine crystals within the CPG pores were evident from Bragg peaks assignable to glycine. The use of more highly concentrated glycine solutions and larger specific CPG pore volumes afforded greater peak intensities in the XRD data, consistent with larger amounts of crystalline glycine in the CPG beads. DSC and TGA data were collected after XRD analysis. Glycine crystallization on the surfaces of nonporous glass beads (NPG) were examined as a comparison with the CPG studies. NPG beads were wetted with a small amount of aqueous glycine solution, sufficient only to wet the beads for the NPG or cover the bottom of the vial, which was then stirred and allowed to dry at ambient conditions. XRD data typically revealed the presence of glycine crystals on the NPG surfaces within 24 h. For comparison, glycine crystals were visible on the walls of the glass vials within the same period.

The p-PS-PDMA monoliths (approximately 1 mm × 2 mm crosssection and 3 mm along the pore direction) were immersed in water for 2 h prior to imbibing glycine solutions. This

pretreatment was found necessary for consistent loading of glycine in the pores, as surmised from the Bragg peak intensity in the XRD. The monolith pieces were subsequently immersed in 15% glycine solution for 2 h, during which the glycine solution diffused into the pores of the monolith. After removal from solution, the outer surfaces of the monoliths were carefully wiped with a soft dampened tissue to remove any external glycine solution residue. The monoliths were then dried under vacuum at approximately 0.1 mmHg for 4 h. Further drying did not affect the crystallization outcome.

Characterization. Wide-angle X-ray scattering microdiffraction (μ-XRD) was performed on a Bruker AXS (Madison, Wisconsin) microdiffractometer, equipped with a 2D CCD detector, located in the University of Minnesota Characterization Facility. A 0.8 mm beam collimator was employed, and the full width at half-maximum (FWHM) resolution of the instrument was determined by measuring the fwhm for both a single crystal LaB_6 wafer and a single crystal of highly oriented pyrolytic graphite (HOPG). The fwhm resolution of the instrument was approximately 0.27° (2θ) over the 2θ range of 15°-35°, allowing for a maximum crystal size estimate of 30 nm by the Scherrer equation.[ii] Variable temperature XRD was performed using a heating stage connected to a calibrated Omega temperature controller and an Omega RTD-850 thermocouple (Omega, Inc., Stamford, Connecticut), ramping in 10 °C increments and collecting XRD data for 10 min at each increment. A succinic acid standard (T_m = 181 °C) was used to

ii. (a) The dimensions of the embedded nanocrystals can be estimated by the Scherrer equation, d) $K\lambda/(B_c \cos\theta)$, where d is the crystal diameter, K is the Scherrer constant (usually assumed to be 0.9), λ is the X-ray wavelength, Bc is the corrected peak width at the FWHM such that B_c) $(B_{obs}^2 - B_{inst}^2)^{1/2}$, where B_{obs} is the observed peak width at the FWHM and B_{inst} is the instrumental peak broadening. θ is the Bragg angle. See Cullity, B. D. *Elements of X-ray Diffraction*; Addison-Wesley: Reading, MA, 1978. (b) Klug, H. P.; Alexander, L. E. *X-Ray Diffraction Procedures for Polycrystalline and Amorphous Materials*; Wiley: New York, 1974.

determine the instrument accuracy, and melting of the standard occurred at 170 °C, indicating the face of the sample stage was slightly hotter than the thermocouple during heating.

Simulated X-ray powder patterns for α-, β-, and γ-glycine were generated using Mercury (Cambridge Crystallographic Data Center, Cambridge, United Kingdom, version 1.4.1) with crystallographic parameters obtained from the Cambridge Structural Database (Cambridge Crystallographic Data Center, Cambridge, United Kingdom). Differential scanning calorimetry (DSC) was performed on a Pyris-1 (Perkin-Elmer Inc., Wellesley, and Massachusetts) differential scanning calorimeter. An indium standard was used to calibrate the instrument and nitrogen was used as the purge gas. The scan rate for the samples was 5 °C/min. Enthalpies were calculated by integrating the areas under the peaks after defining a baseline. In cases wherein the enthalpies were small (less than 1 J/g sample) the variance in the calculated enthalpies approached 30%. Thermal gravimetric analysis (TGA) data were collected on a Perkin-Elmer Diamond TG/DTA (Perkin-Elmer Inc., Wellesley, Massachusetts), at a scan rate of 5 °C/min. The scan ranges were 25-240 °C for DSC and 25-500 °C for TGA. The decomposition point of bulk glycine also was measured with a melting point apparatus at a heating rate of 5 °C/min. Infrared spectroscopy (IR) was performed on a Nicolet Magna-IR 550 spectrometer, using samples prepared by pressing a mixture of CPG or bulk glycine with dry KBr.

3-2: Polymorph Identification

The influence of nanometer-scale confinement on the polymorphism and thermotropic properties of glycine was examined for crystals formed in controlled porous glass (CPG) beads, having nominal pore diameters of 7.5 nm, 24 nm, and 55 nm, or porous polystyrene-poly(dimethyl acrylamide) (p-PS-PDMA) monoliths with cylindrical pores, having 10 and 20 nm diameters, created by chemical etching of the PLA block of shear-oriented PS-PDMA-polylactide

(PLA) triblock copolymers. Related investigations in our laboratory examined the polymorphic and thermotropic behavior of organic crystals formed in CPG or porous poly(cyclohexylethylene) (PCHE) or poly(styrene) (PS) monoliths prepared from PCHE-PLA and PS-PLA diblock copolymers, respectively. In these cases, the organic compounds (i) were imbibed directly as melts and crystallized subsequently by cooling or (ii) were introduced by absorption of methanol solutions and subsequently crystallized by evaporation of the solvent.[19,20] The melting temperature of glycine (~236 °C) exceeds the glass transition temperature of PS ($T_g \approx 100$ °C) and PCHE ($T_g \approx 145$ °C),[45] at which the monolith matrix softens and the pores collapse, precluding introduction of glycine from its melt. Furthermore, glycine melting is accompanied by decomposition, which precludes imbibing of the melt by CPG. The solubility of glycine in methanol (0.002 g/g MeOH)[46] is insufficient for achieving a detectable amount of glycine (by XRD or DSC) in the pores by absorption of methanol solutions. The greater solubility of glycine in water (0.234 g/g H2O)[47] ensures that a detectable amount of glycine can be embedded following evaporation of solutions absorbed into CPG pores, but the pores of the p-PCHE and p-PS monoliths are not sufficiently hydrophilic to absorb water. The p-PS-PDMA monoliths used herein, however, readily absorb aqueous glycine solutions as the interior lining of the pores is PDMA-rich and hence hydrophilic. Therefore, glycine was crystallized in the pores of CPG and p-PS-PDMA by absorption of aqueous solutions of glycine followed by vacuum drying to remove water from the pores. The mass of glycine in the CPG and p-PS-PDMA pores was calculated using the concentration of glycine solution filling the pores and the total pore volume available to the solution. In the case of CPG, the actual mass of material within the pores after drying was approximately 50% higher than expected based on glycine alone, suggesting that water remained

trapped in the pores. Infrared spectroscopy of glycine-loaded CPG beads confirmed traces of water within the samples after vacuum drying.[iii]

The embedded nanocrystals were characterized with wide-angle X-ray microdiffraction (μ-XRD) using a 2D area detector. The CPG beads and their pores are randomly oriented and thus are not amenable to crystal orientation analysis. Consequently, the Bragg peaks for glycine embedded within CPG appear as continuous arcs on the 2D detector (Figure 3-2A), consistent with an overall random orientation of the glycine crystals. The locations of the arcs along the horizon or conversion of the 2D data by azimuthal integration to a 1D powder pattern revealed peaks at $2\theta = 17.9°$, 23.8°, 28.4°, 31.1°, and 33.8°. Comparison of the 1D powder pattern with those expected from the single crystal structures of α-, β-, and γ-glycine[28–30] revealed the exclusive formation of β-glycine for all pore sizes, with no detectable amounts of the other two forms (Figure 3-3, p.114). The most intense diffraction peaks corresponded to β(001), β(110), and β(020), which were superimposed on a broad peak due to diffuse scattering from the amorphous CPG matrix. In contrast, glycine crystals grown on the surface of nonporous glass (NPG) beads or on the inner surfaces of glass vials by evaporation of the same glycine solutions revealed the exclusive presence of α-glycine.

iii. Traces of the carboxyl O-H stretch, alkane stretch and amine stretch were present exclusively for the glycine loaded CPG. Due to the small mass of glycine within the CPG pores and the instrumental limits on the amount of CPG in each IR sample, the glycine absorption peaks were weak.

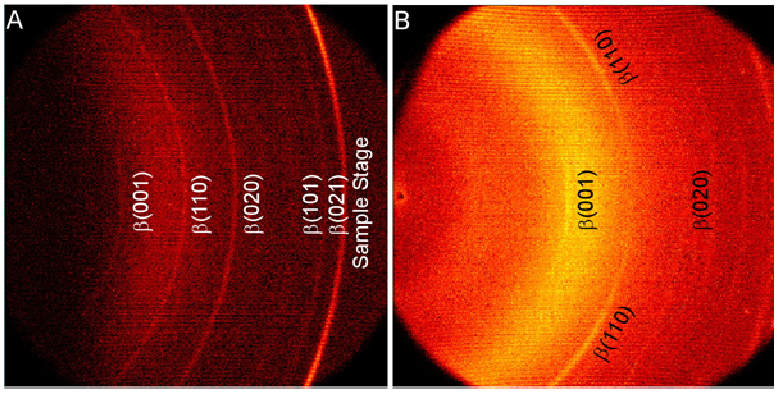

Figure 3-2. (A) 2D μ-XRD data for β glycine nanocrystals embedded within (A) 24 nm CPG and (B) 20 nm p-PS-PDMA. The Miller indices for the more prominent reflections appear to the right of their respective diffraction arcs.

The 2D μ-XRD data and the corresponding 1D powder pattern for glycine crystals formed in p-PS-PDMA also revealed the exclusive formation of β-glycine. The p-PS-PDMA mono-liths, typically cut into pieces having 3 mm lengths in the pore direction and 1 mm × 2 mm cross-sectional areas, were aligned with respect to the incident X-ray beam so that crystal orientation within the pores could be gleaned from the diffraction data.49 The β(001), β(110), β(020), β(101), and β(021) reflections were clearly evident for 20 nm p-PS-PDMA, although they were superimposed on diffuse scattering from the amorphous polymer matrix. Only the β(001), β(110), and β(020) reflections were evident for 10 nm p-PS-PDMA, as the small total pore volume of these samples contained less crystalline glycine, thus producing less intense reflections compared with the 20 nm monoliths. Unlike the CPG samples, examination of the 2D XRD data revealed discontinuous arcs for the more discernible lower index reflections (Figure 3-2B). This observation is consistent with a preferred orientation of the β-glycine nanocrystals within the aligned pores of the polymer monolith.[47]

The full widths at half-maximum (fwhm) of the β(001), β(110), and β(020) diffraction peaks indicated that the sizes of the embedded nanocrystals reflected the size confinement of the pores.

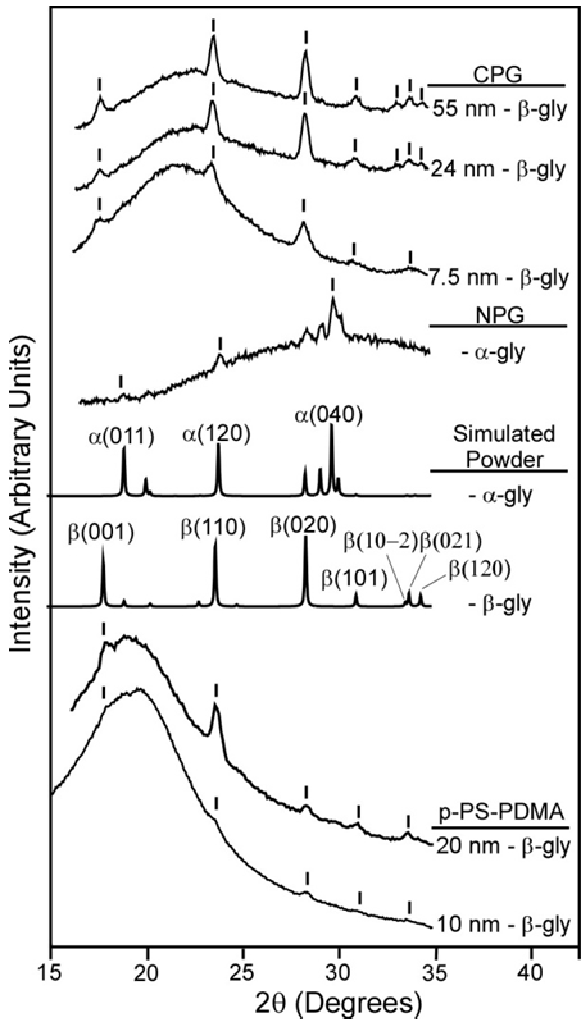

Figure 3-3. 1D XRD data for glycine nanocrystals embedded within CPG, glycine crystals grown on NPG, and glycine nanocrystals embedded within 20 nm and 10 nm p-PS-PDMA monoliths. The diffraction peaks are superimposed on diffuse scattering from the amorphous glass and polymer matrices in CPG and p-PS-PDMA, respectively. Comparison of the data with the simulated powder diffraction patterns, based on the known single crystal structures for α- and β-glycine, reveals the exclusive formation of β-glycine in the nanopores.

Using the Scherer equation,[45] the data indicate crystal sizes of 7 nm in 7.5 nm CPG, 22 nm in 24 nm CPG, and 30 nm in 55 nm CPG.[iv] The diffraction peak widths approached the instrumental limit of 30 nm in the case of the crystals formed in the 55 nm CPG and on NPG, preventing accurate size determination in these cases. Similar analyses for glycine nanocrystals embedded in p-PS-PDMA were consistent with crystal sizes of 9 nm in 10 nm p-PS-PDMA and 22 nm in 20 nm p-PS-PDMA.

3-3: Polymorph Stability

β-Glycine nanocrystals embedded within CPG and p-PSPDMA exhibited significantly increased temporal stability against transformation to other forms at ambient conditions compared with the bulk form, which is known to be metastable. Whereas bulk β-glycine readily transforms to the α form at ambient conditions, in our hands usually within minutes,[48] β-glycine nanocrystals embedded in 55 nm CPG changed to the α form only after 60 days (Table 3-1). Remarkably, β-glycine nanocrystals were indefinitely stable in 7.5 nm CPG, 24 nm CPG, 10 nm p-PS-PDMA, and 20 nm p-PS-PDMA, with no other phases present even after one year at ambient conditions.

Embedded β-glycine nanocrystals also were more stable against phase transitions at elevated temperatures compared with bulk β-glycine. Bulk β crystals are stable under anhydrous conditions up to 67 °C, at which transformation to the α form occurs within several minutes.[49] In

iv. In a small number (<10%) of the CPG and p-PS-PDMA samples one or two intense, discrete spots corresponding to α-glycine appeared in the 2D XRD data in addition to the β-glycine nanocrystal arcs. The diffraction peaks widths for these α-glycine crystals indicating crystal sizes larger than the maximum estimable size of 30 nm, suggesting that these α-glycine crystals were bulk crystals on the surfaces of the porous materials. The presence of these bulk crystals appeared to have no impact on the nanocrystal behavior.

Table 3-1. The polymorphs exhibited by glycine crystals grown at room temperature in CPG, NPG, and p-PS-PDMA, over various times and for various concentrations of imbibed glycine solution.

Matrix and pore diameter (nm)	Glycine solution concentration (% weight)	Polymorph after 4 hrs	Polymorph after 40 hrs	Polymorph after 60 days
7.5 nm CPG	6	β	β	β
	11	β	β	β
	18	β	β	β
24 nm CPG	6	β	β	β
	11	β	β	β
	18	β	β	β
55 nm CPG	6	β	β	α
	11	β	β	α
	18	β	β & α	α
NPG	11	α	α	α
10 nm p-PS-PDMA	15	β	β	β
20 nm p-PS-PDMA	15	β	β	β

contrast, μ-XRD analysis of β-glycine nanocrystals embedded in CPG (all pore sizes) at 80 °C and ambient humidity revealed no polymorph transitions at the conclusion of these measurements (3 h). Variable temperature μ-XRD performed while heating the CPG samples in 10 °C intervals, holding at each temperature for 10 min during data collection, revealed disappearance of β-glycine diffraction peaks at 160 °C for 7.5 nm CPG, 170 °C for 24 nm CPG, and 170 °C for 55 nm CPG (Figure 3-4). The temperature at which the β-glycine diffraction peaks disappeared is well below the temperature of bulk glycine decomposition (236 °C, as measured in our laboratory), which is not expected to be a size-dependent property. Bulk glycine decomposition, however, is accompanied by melting, as observed in our laboratory in melting point capillaries and reported previously.[33] This suggests that the disappearance of β-glycine in the CPG at temperatures less than 236 °C is due to melting without decomposition, made possible because of the melting point depression effects expected for the nanoscale crystal size.[11]

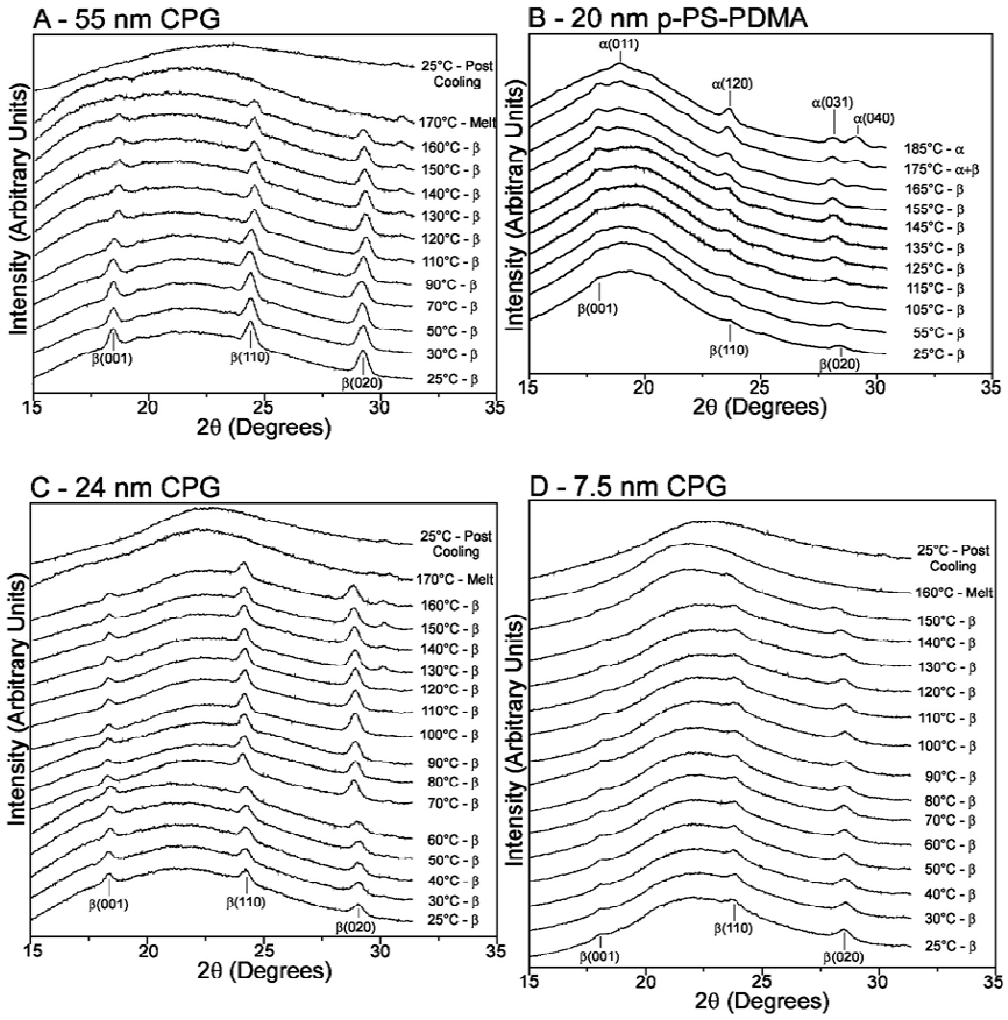

Figure 3-4. (A) 1D variable temperature XRD data of glycine nanocrystals embedded within 55 nm CPG. β-glycine is the exclusive polymorph for temperatures up to 160 ℃, but is no longer evident at 170 ℃ and does not return upon cooling. (B) 1D variable temperature XRD data of glycine nanocrystals embedded within 20 nm p-PS-PDMA. Although in this particular sample, the intensities of the diffraction peaks are not as intense as for nanocrystals embedded in CPG and some peaks assignable to α- and β-glycine from the data overlap, the eventual disappearance of a peak assignable to β(001) accompanied by the emergence of a peak assignable to α(040) reveal the $\beta \rightarrow \alpha$ transition. (C) 1D variable temperature XRD data for 24 nm and (D) 7.5 nm CPG, for which β-glycine reflections are no longer apparent at 170 ℃ and 160 ℃, respectively.

Immediately following the disappearance of the β-glycine diffraction peaks, the samples were allowed to cool to room temperature. Curiously, no diffraction peaks were observed for these samples at room temperature, signaling the absence of recrystallization and the possible formation of an amorphous phase from the melt. It is reasonable to suggest that this amorphous phase exists as a thin film due to solidification of the glycine melt that has wetted the highly polar pore walls, thus reducing the effective dimensions of the solid to a value below the critical size for nucleation.22 The thicknesses of such films can be estimated from the amount of embedded glycine and the internal surface area of the CPG beads, assuming uniform wetting of the surface: 0.4 nm in 7.5 nm CPG, 1.3 nm in 24 nm CPG, and 3.0 nm in 55 nm CPG.[v]

Variable temperature μ-XRD analysis of glycine nanocrystals embedded within 20 nm p-PS-PDMA, performed in the same manner as the CPG samples, revealed β-glycine as the exclusive polymorph until 170 °C, at which a mixture of α- and β-glycine nanocrystals was observed until complete conversion to α-glycine at 185 °C (the data reveal an increase in the intensity of the β(001) peak, suggesting an increase in the crystallinity of β-glycine with increasing temperature prior to the transition). This behavior differs from that observed for β-glycine nanocrystals in CPG, which appear to melt without conversion to α-glycine. Small angle X-ray scattering reveals that the pores of the p-PS-PDMA monoliths collapse at temperatures exceeding the glass transition temperature of PS ($T_g \approx 100$ °C). Nonetheless, the diffraction peak widths for the α-glycine crystal generated by the phase transformation were consistent with a crystal size of 16

v. For example, the expected amount of glycine embedded within 1 gram of 24 nm CPG with total pore volume 0.95 cm^3/g, using a 15% glycine solution (weight percent), is 0.167 g. Based on the surface area of the pores in 24 nm CPG (78.8 m^2/g) and the density of glycine (1.58 g/cm^3), the thickness of a uniform glycine layer on the pore walls would be 1.34 nm.

nm, effectively identical to the size of the original β-glycine nanocrystals. These observations suggest that upon heating above T_g the β-glycine nanocrystals become surrounded by the polymer matrix, instead of residing in open cylinders, eventually transforming to α-glycine crystals having the same size. The embedded α-glycine nanocrystals persisted upon cooling the monoliths to room temperature, identical to behavior observed for bulk glycine. The XRD peaks for the α-glycine nanocrystals in p-PS-PDMA vanished when heated to 236 °C, consistent with decomposition. These results indicate that the unique environment created by the collapse of the polymer monolith pores around the β-glycine crystals allows the formation of α-glycine, in stark contrast to the behavior observed in CPG. A plausible explanation for this behavior involves crystallization of α-glycine from a transient melt that has pooled within polymer voids formed by the collapse of the pores around the original β-glycine crystals. These voids, which would contain the melt rather than allowing it to form an amorphous thin film, as surmised for CPG, would have volumes that were sufficiently large for nucleation of α-glycine.

Thermogravimetric analysis (TGA) of bulk glycine revealed one mass loss event, with an apparent onset at approximately 200 °C and increasing rate of mass loss as the temperature approached 236 °C. As the temperature was raised further, the mass loss became more gradual until at 500 °C (the highest temperature of the measurement) a black residue with a mass equivalent to 20% of the original mass remained. This behavior is consistent with the known melting/decomposition behavior of glycine.[34] DSC analysis of bulk glycine revealed a single endothermic peak at 236 °C corresponding to the overlap of glycine melting and decomposition.[33]

Unlike bulk glycine, TGA measurements for glycine nanocrystals in CPG revealed onsets for mass loss at temperatures that decreased with decreasing pore size: 192 °C for 55 nm CPG, 185 °C for 24 nm CPG, and 170 °C for 7.5 nm CPG (Figure 3-5A, p. 114). The mass lost between

these onset temperatures and 236 °C also decreased with decreasing pore size, as expected for the smaller mass loadings attained in the smaller pore sizes.[vi] These losses corresponded to approximately 50% of the mass of glycine embedded in the CPG beads, equivalent to the extra mass attributed to trapped water, as surmised by weighing the CPG beads after evaporative crystallization (see above). The CPG beads became discolored (brownish or black) upon continued heating to 500 °C due to decomposition of the embedded glycine, after which the remaining mass within the pores was equivalent to approximately 25% of the initial mass of the glycine nanocrystals. DSC data revealed a single endothermic peak in each sample with an onset temperature that coincided with the onset temperature for the initial mass loss event observed by TGA (Figure 3-5B): 195 °C for 55 nm CPG, 185 °C for 24 nm CPG, and 175 °C for 7.5 nm CPG.[vii] The total enthalpy increased with pore size and with increasing amount of glycine embedded in the pores (Table 3-2).

vi. The respective absolute mass losses for the CPG samples were 2.2% for 7.5 nm CPG, 4.2% for 24 nm CPG, and 6.5% for 55 nm CPG.

vii. The DSC peak maxima occurred at 210 °C for 7.5 nm CPG, 219 °C for 24 nm CPG, and 229 °C for 55 nm CPG.

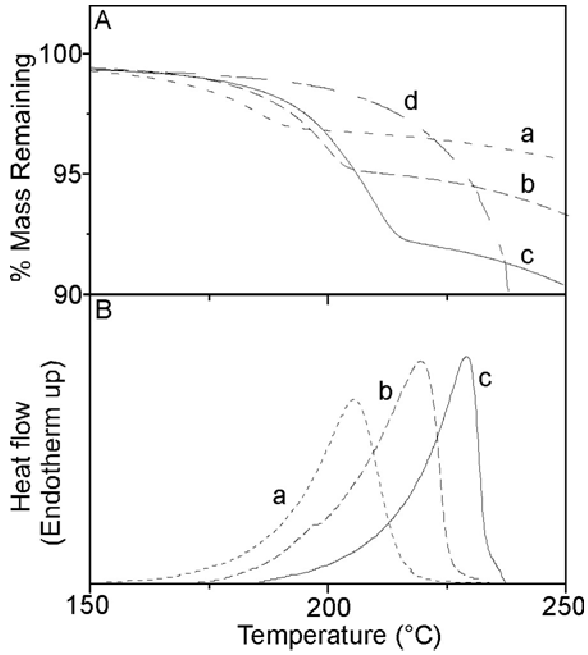

Figure 3-5. (A) TGA data for glycine nanocrystals embedded within (a) 7.5 nm CPG, (b) 24 nm CPG, (c) 55 nm CPG, and (d) bulk glycine crystals. (B) DSC data for glycine nanocrystals embedded within (a) 7.5 nm CPG, (b) 24 nm CPG, (c) 55 nm CPG. The onsets of the endothems coincide with the respective onsets of mass loss. The endotherm for bulk glycine (not shown) coincides with the TGA data.

Table 3-2. Calculation of heat of fusion for β-glycine embedded within CPG.

CPG pore diameter (nm)	Glycine Solution Concentration % (weight)	Expected Glycine (g/g CPG)	Expected Water (post-dry) (g/g CPG)	DSC Sample Mass (mg)	DSC Peak Enthalpy (mJ)	DSC Peak Enthalpy (J/g sample)	DSC Peak Enthalpy (J/g glycine)	Average Enthalpy (J/g glycine)	Std. Dev Enthalpy (J/g glycine)
7.5	6	0.03	0.01	2.1	11.0	5.2	210	326	105
	11	0.06	0.03	2.1	37.9	18.1	354		
	18	0.09	0.04	2.0	64.0	32.0	413		
24	6	0.06	0.03	1.1	26.1	23.7	437	503	101
	11	0.11	0.06	1.0	59.2	59.2	620		
	18	0.19	0.09	1.2	78.8	65.7	453		
55	6	0.10	0.05	1.4	64.9	46.4	545	586	36
	11	0.18	0.09	1.8	156.0	86.7	608		
	18	0.31	0.16	1.8	230.5	128.1	605		

Collectively, the TGA and DSC data suggest that embedded β-glycine nanocrystals trap small pockets of water within the CPG that escape only once the nanocrystals melt and wet the pore walls, thus opening passages to release the trapped water. The onset and peak temperatures did not depend on scan rate (compared at 1 °C/min and 5 °C/min), corroborating the assignment of the DSC peaks to melting rather than decomposition.[viii] Consequently, the onset of the mass loss due to the release of water surmised from TGA parallels the trend in melting point depression observed by DSC. We note that DSC analyses of CPG beads immersed in water and then vacuum dried revealed an endotherm due to water vaporization between 50-100 °C, far below the onset of the endotherm in the glycine embedded samples. Furthermore, TGA revealed a mass loss over the same range assigned to the loss of trapped water, with no further mass loss at higher temperatures. These measurements demonstrate that, in the absence of glycine, the CPG matrix does not retain water at elevated temperatures.

Based on the premise that the onset temperatures of the DSC peaks corresponded to the melting of β-glycine, their dependence on pore size was fitted to the conventional form of the Gibbs- Thompson equation (Equation 1), where (ΔT_m) is the melting point depression, $T_m(d)$ is the depressed melting temperature, T_m is the bulk melting temperature, $\gamma_{solid\text{-}melt}$ is the crystal-melt interfacial energy, ρ is the crystal density, $\Delta \underline{H}^{fus}$ is the crystal molar heat of fusion, M is molecular mass (g/mol), and d is the pore size.[ix]

---

viii. For example, the shape of the endotherms and their onset temperature (185 °C) were independent of scan rate (by comparing scans at 1 °C/ min and 5 °C/min) as was the peak temperature (219 °C @ 5 °C/min and 222 °C at 1 °C/min, within the error of measurement).

ix. (a) This form of the Gibbs-Thompson equation assumes constant density, constant heat of fusion, and a crystal-pore wall contact angle of 180°. The assumption of a 180° contact angle, however, may not always be valid. See (b) Scherer, G. W. *Cem. Concr. Res.* **1999**, *29*, 1347–1358, and ref 18.

$$\Delta T_m(d) = T_{m,bulk} - T_m(d) = \frac{4M\gamma_{solid-melt}}{\Delta \underline{H}^{fus}\rho d} T_{m,bulk} \quad (0.1)$$

The Gibbs-Thompson equation predicts a linear relationship between ΔT_m or $T_m(d)$ and pore size. Extrapolation of the linear fit to the y-intercept, which is tantamount to determining the melting temperature for bulk β-glycine ($d \approx \infty$), affords a bulk β-glycine melting temperature of 195 °C (± 4 °C) (Figure 3-6).[x] This melting temperature is not accessible through conventional bulk measurements owing to the facile bulk β-to-α transition at T = 67 °C. Although this bulk melting temperature is lower than that observed at 236 °C for α-glycine, it seems reasonable given that bulk β-glycine is less stable than α-glycine.

Evaluation of the enthalpy of the thermal processes associated with the contents of the CPG pores proved difficult. The mass of the beads after evaporation of the infiltrated solution suggested the presence of trapped water in addition to the β-glycine nanocrystals. Therefore, the measured endothermic heat flow may reflect contributions from vaporization of trapped water as well as glycine melting. The measured heat flow, however, was smaller than expected for these endothermic processes combined, suggesting an offsetting contribution from an exothermic process, possibly concomitant solidification of the presumed amorphous film.[xi] The convolution

---

x. The slope of the linear fit was -155 (± 44 °C/nm^{-1}). The error bars represent 1 esd based on the linear regression analysis of three data points for each pore size. This error in the melting point can be discerned readily by varying the slope of the fitted line within the limits imposed by all three pore sizes.

xi) For example, the DSC data for the 55 nm CPG beads containing embedded β-glycine nanocrystals, which were prepared by imbibing an 18% (weight percent) glycine solution, exhibited an endothermic peak corresponding to a total enthalpy of 0.128 kJ/g total sample (i.e. CPG beads plus contents). The contribution to the endothermic heat flow expected from the known enthalpy of water vaporization

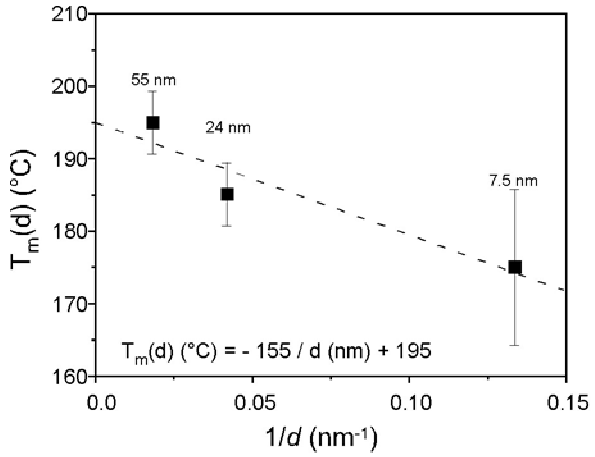

Figure 3-6. The melting temperature dependence on the inverse of the CPG pore diameter (*d*). Error bars represent one standard deviation of the plotted data.

of these multiple processes precludes an unambiguous determination of the enthalpy of $\Delta \underline{H}^{fus}$ for the embedded nanocrystals. Similarly, DSC measurements for glycine within 20 nm p-PS-PDMA (after pore collapse) revealed an endothermic event at 179 °C that coincided with the β-to-α transition observed by μ-XRD in this polymer matrix, but attempts to determine the enthalpy associated with this process were complicated by the onset of decomposition of the polymer matrix at these high temperatures.

($\Delta \hat{H}_{vap}$ = 2.28 kJ/g) and the amount of water presumed trapped within the pores is 0.210 kJ/g total sample. Endothermic glycine melting would be expected to add to this heat flow. As such, the measured heat flow is substantially less than expected based on the contents within the pores. This suggests an exothermic process that offsets the endothermic contributions, possibly the concomitant solidification of a higher melting amorphous phase. Based on the heat flow expected from the trapped water and the amount embedded glycine (0.21 g/g total sample) the exothermic enthalpy of solidification of the amorphous phase would need to be 30 kJ/mol greater than the melting enthalpy of β-glycine, which seems unreasonably large. This difference would be smaller if the measured heat flow contribution from trapped water was reduced due to a slow and gradual release of water, prior to the onset temperature, which may not be readily detectable.

3-4: Concluding Remarks

The regulation of crystallization outcomes, including polymorphism, is an issue of critical importance in many commercial technologies, and the elucidation of the principles relating nucleation, growth, and polymorphism is one of the grand challenges of organic solid state chemistry. The work described above demonstrates that an otherwise metastable form of a crystalline substance, in this case β-glycine, actually becomes the stable form when the crystal size is constrained to nanometer-scale dimensions. Furthermore, these nanoscale crystals exhibit melting point depression, which becomes more significant with decreasing crystal size. Although the melting point depression of nanoscale crystals in CPG and nanoporous polymer monoliths has been established previously, the size confinement of β-glycine reduces the melting point below the temperature at which melting occurs concomitant with decomposition. This permits determination of the actual melting temperature of β-glycine through the use of the Gibbs-Thomson relationship, an accepted standard for such measurements. Furthermore, the observation of β-glycine at dimensions comparable to the critical size expected for crystal nuclei suggests that glycine crystallization likely involves formation of β nuclei followed by their transformation to the other forms as crystal size increases. Most important, the dependence of polymorph stability on size suggests that caution must be exercised when preparing formulations containing nanoscale crystals for applications wherein the polymorph identity is crucial, for example, when preparing pharmaceutical compounds with the aim of increasing dissolution rates for increased bioavailability.

3-5: References

1. Loisel, C.; Keller, G.; Lecq, G.; Bourgaux, C.; Ollivon, M. Phase transitions and polymorphism of cocoa butter. *J. Am. Oil Chem. Soc.* **1998**, *75*, 425–439.
2. Yu, L.; Stephenson, G. A.; Mitchell, C. A.; Bunnell, C. A.; Snorek, S. V.; Bowyer, J. J.; Borchardt, T. B.; Stowell, J. G.; Byrn, S. R. Thermochemistry and Conformational Polymorphism of a Hexamorphic Crystal System. *J. Am. Chem. Soc.* **2000**, *122*, 585.
3. Chemburkar, S. R.; Bauer, J.; Deming, K.; Spiwek, H.; Patel, K.; Morris, J.; Henry, R.; Spanton, S.; Dziki, W.; Porter, W.; Quick, J.; Bauer, P.; Donaubauer, J.; Narayanan, B. A.; Soldani, M.; Riley, D.; McFarland, K. Dealing with the impact of ritonavir polymorphs on the late stages of bulk drug process development. *Org. Process Res. Dev.* **2000**, *4*, 413–417.
4. (a) *Polymorphism in Pharmaceutical Solids*; Brittain, J. G. , Ed.; Marcel Dekker: New York, 1999. (b) Byrn, S. R.; Pfeiffer, R.; Ganey, M.; Hoiberg, C.; Poochikian, G. Pharmaceutical Solids: A Strategic Apporach to Regulatory Considerations. *Pharm. Res.* **1995**, *12*, 945–954. (c) Rodrigeuz-Hornedo, N.; Murphy, D. Significance of Controlling Crystallization Mechanisms and Kinetics in Pharmaceutical Systems. *J. Pharm. Sci.* **1999**, *88*, 651–660.
5. Khoshkhoo, S.; Anwar, J. Crystallization of polymorphs: the effects of solvent. *J. Phys. D: Appl. Phys.* **1993**, *26*, B90–B93.
6. Kitamura, M. Controlling factor of polymorphism in crystallization. *J. Cryst. Growth* **2002**, *237-239*, 2205–2214.
7. Davey, R. J.; Blagden, N.; Potts, G. D.; Docherty, R. Polymorphism in Molecular Crystals: Stabilization of a Metastable Form by Conformational Mimicry. *J. Am. Chem. Soc.* **1997**, *119*, 1767–1772.
8. (a) Last, J. A.; Hooks, D. E.; Hillier, A. C.; Ward, M. D. The Physiochemical Origins of Coincident Epitaxy in Molecular Overlayers: Lattice Modeling vs Potential Energy Calculations. *J. Phys. Chem. B* **1999**, *103*, 6723–6733. (b) Price, C. P.; Grzesiak, A. L.; Matzger, A. J. Crystalline Polymorph Selection and Discovery with Polymer Heteronuclei. *J. Am. Chem. Soc.* **2005**, *127*, 5512–5517. (c) Bonafede, S. J.; Ward, M. D. Selective nucleation and growth of an organic polymorph by ledge-directed epitaxy on a molecular crystal substrate. *J. Am. Chem. Soc.* **1995**, *117*, 7853–7861.
9. Bernstein, J. *Polymorphism in Molecular Crystals*; Oxford: New York, 2002.
10. Oxtoby, D. W. Nucleation of First-Order Phase Transitions. *Acc. Chem. Res.* **1998**, *31*, 91–97.

11. (a) Jackson, C. L.; McKenna, G. B. The melting behavior of organic materials confined in porous solids. *J. Chem. Phys.* **1990**, *93*, 9002–9011. (b) Patrick, W. A.; Kemper, W. A. Melting Temperatures of Compounds Adsorbed on Silica Gel. *J. Phys. Chem.* **1938**, *42*, 369–380.
12. (a) Borisov, B. F.; Charnaya, E. V.; Hoffmann, W. D.; Michel, D.; Shelyapin, A. V.; Kumzerov; Yu., A. A. Nuclear magnetic resonanoce and acoustic investigations of the melting-freezing phase transition of gallium in a porous glass. *J. Phys. Condens. Matter* **1997**, *9*, 3377–3386. (b) Buffat, Ph.; Borel, J.-P. Size effect on the melting temperature of gold particles. *Phys. Re*V. *A* **1976**, *13*, 2287–2298.
13. Reinnie, G. K.; Clifford, J. Melting of Ice in Porous Solids. *J.Chem. Soc., Faraday Trans. 1* **1977**, *73*, 680–689.
14. Christenson, H. K. Confinement effects on freezing and melting. *J. Phys.: Condens. Matter* **2001**, *13*, R95-R133.
15. Jackson, C. L.; McKenna, G. B. Vitrification and Crystallization of Organic Liquids Confined to Nanoscale Pores. *Chem. Mater.* **1996**, *8*, 2128–2137.
16. Ajayan, P. M.; Iijima, S. Capillarity-induced filling of carbon nanotubes. *Nature* **1993**, *361*, 333–334.
17. Prasad, R.; Lele, S. Stabilization of the amorphous phase inside carbon nanotubes: solidification in a constrained geometry. *Phil. Mag. Lett.* **1994**, *70*, 357–361.
18. Ha, J.-M.; Hillmyer, M. A.; Ward, M. D. Thermotropic Properties of Organic Nanocrystals Embedded in Ultrasmall Chambers. *J. Phys. Chem. B* **2005**, *109*, 1392–1399.
19. Ha, J.-M.; Wolf, J. H.; Hillmyer, M. A.; Ward, M. D. Polymorph Selectivity under Nanoscopic Confinement. *J. Am. Chem. Soc.* **2004**, *126*, 3382–3383.
20. Ha, J.-M. Crystallization and Thermotropic Properties of Organic Solids in Nanoscopic Reactors. Ph.D. Thesis, University of Minnesota, 2006.
21. Beiner, M.; Rengarajan, G. T.; Pankaj, S.; Enke, D.; Steinhart, M. Manipulating the Crystalline State of Pharmaceuticals by Nanoconfinement. *Nano Lett.* **2007**, *7*, 1381–1385.
22. Rengarajan, G. T.; Enke, D.; Beiner, M.; Steinhart, M. Stabilization of the amorphous state of pharmaceuticals in nanopores. *J. Mat. Chem.* **2008**, *18*, 2537–2539.
23. (a) Chang, B. S.; Reeder, G.; Carpenter, J. F. Development of a Stable Freeze-dried Formulation Recombinant Human Interleukin-1 Receptor Antagonist. *Pharm. Res.* **1996**, *13*, 243–249. (b) Bush, L.; Webb, C.; Bartlett, L.; Burnett, B. The formulation of recombinant factor IX. Stability, robustness and convenience. *Semin. Hematol.* **1998**, *35*, 18–21.
24. Nail, S. L.; Shan, J. *Pharm. Biotech.* **2002**, *14*, 281–360.
25. (a) Kuan, Y.-J.; Charnley, S. B.; Huang, H.-C.; Tseng, W.-L.; Kisiel, Z. Interstellar Glycine. *Astrophys. J.* **2003**, *593*, 848–867. (b) Snyder, L. E.; Lovas, F. J.; Hollis, J. M.; Friedel, D. N.; Jewell,

P. R.; Remijan, A.; Ilyushin, V. V.; Alekseev, E. A.; Dyubko, S. F. A Rigorous Attempt to Verify Interstellar Glycine. *Astrophys. J.* **2005**, *619*, 914– 930. (c) Elsila, J. E.; Dworkin, J. P.; Bernstein, M. P.; Martin, M. P.; Sandford, S. A. Mechanisms of Amino Acid Formation in Interstellar Ice Analogs. *Astrophys. J.* **2007**, *660*, 911–918.

26. (a) Albrecht, G.; Corey, R. B. The crystal structure of glycine. *J. Am. Chem. Soc.* **1939**, *61*, 1087–1103. (b) Marsh, R. E. A refinement of the crystal structure of glycine. *Acta Crystallogr.* **1958**, *11*, 654–663. (c) Destro, R.; Roversi, P.; Barzaghi, M.; Marsh, R. E. Experimental Charge Density of [alpha]-Glycine at 23 K. *J. Phys. Chem. A* **2000**, *104*, 1047–1054. (d) Jonsson, P.-G.; Kvick, Structure of protein and nucleic acid components. III Å. *Acta Crystallogr. B* **1972**, *28*, 1827–1833. (e) Power, L. F.; Turner, K. E.; Moore, F. H. The crystal and molecular structure of glycine by neutron diffraction – a comparison. *Acta Crystallogr. B* **1976**, *32*, 11–16. (f) Legros, J.-P.; Kvick, Å. Deformation electron density of glycine at 120 K. *Acta Crystallogr. B* **1980**, *36*, 3052–3059. (g) Boldyreva, E. V.; Drebushchak, T. N.; Shutova, E. S. *Z. Kristallogr.* **2003**, *218*, 366–376. (h) Pervolich, G. L.; Hansen, L. K.; Bauer.Brandl, A. The Polymorphism of Glycine. Thermochemical and structural aspects. *J. Therm. Anal. Calorim.* **2001**, *66*, 699–715.
27. Dawson, A.; Allan, D. R.; Belmonte, S. A.; Clark, S. J.; David, W. I. F.; McGregor, P. A.; Parsons, S.; Pulham, C. R.; Sawyer, L. Effects of High Pressure on the Crystal Structures of Polymorphs of Glycine. *Cryst. Growth Des.* **2005**, *5*, 1415–1427.
28. Marsh, R. E. A refinement of the crystal structure of glycine. *Acta Crystallogr.* **1958**, *11*, 654–663. α-glycine: $P2_1/c$, (*a*, *b*, *c*) = (5.1020, 11.9709, 5.4575 Å), β = 111.7°
29. Iitaka, Y. The Crystal Structure of γ-Glycine. *Acta Crystallogr.* **1961**, *14*, 1–10. γ-glycine: $P3_2$, (*a*, *b*, *c*) = (7.046, 7.046, 5.491 Å), γ = 120°
30. Iitaka, Y. The crystal structure of β-glycine. *Acta Crystallogr.* **1960**, *13*, 35–45. β-glycine: $P2_1$, (*a*, *b*, *c*) = (5.077, 6.268, 5.38 Å), β = 113.2°
31. (a) Boldyreva, E. V.; Drebushchak, V. A.; Drebushchak, T. N.; Paukov, I. E.; Kovalevskava, Y. A.; Shutova, E. S. Polymorphism of Glycine. Thermodynamic Aspects. Part I. Relative stability of the polymorphs. *J. Therm. Anal. Calorim.* **2003**, *73*, 409–418. (b) Boldyreva, E. V.; Drebushchak, V. A.; Drebushchak, T. N.; Paukov, I. E.; Kovalevskava, Y. A.; Shutova, E. S. Polymorphism of Glycine. Thermodynamic Aspects. Part II. Polymorphic transitions. *J. Therm. Anal. Calorim.* **2003**, *73*, 419–428. (c) Chongprasert, S.; Knopp, S. A.; Nail, S. L. *J. Pharm. Sci.* **2001**, *90*, 1720–1728.
32. (a) Takagi, S.; Chihara, H.; Seki, S. Vapor Pressure of Molecular Crystals. XIII. Vapor Pressure of α-Glycine Crystal. The Energy of Proton Transfer. *Bull. Chem. Soc. Jpn.* **1959**, *32*, 84–88. (b) deKruif, C. G.; Voogd, J.; Offringa, J. C. Enthalpies of sublimation and vapour pressures of 14 amino acids and

peptides. A. *J. Chem. Thermodyn.* **1979**, *11*, 651–656. (c) Raabe, G. *Z.* The Use of Quantum Chemical Semiempirical Methods to Calculate the Lattice Energies of Organic Molecular Crystals. Part I: The Three Polymorphs of Glycine. *Naturforsch.* **2000**, *55a*, 609–615.ro

33. (a) Rodante, F.; Marrosu, G.; Catalani, G. Thermal analysis of some α-amino acids with similar structures. *Thermochim. Acta* **1992**, *194*, 197–203. (b) Wesolowski, M.; Erecinska, J. Relation Between Chemical Structure of Amino Acids and their Thermal Decomposition. Analysis of the data by principal component analysis. *J. Therm. Anal. Calorm.* **2005**, *82*, 307–313.
34. Li, J.; Wang, Z.; Yan, X.; Hu, L.; Liu, Y.; Wang, C. Evaluate the pyrolysis pathway of glycine and glycylglycine by TG-FTIR. *J. Anal. Appl. Pyrolysis* **2007**, *80*, 247–253.
35. Torbeev, V. Y.; Shavit, E.; Weissbuch, I.; Leiserowitz, L.; Lahav, M. Control of Crystal Polymorphism by Tuning the Structure of Auxiliary Molecules as Nucleation Inhibitors. The β-Polymorph of Glycine Grown in Aqueous Solutions. *Cryst. Growth Des.* **2005**, *5*, 2190–2196.
36. Landau, E.; Meir; Grayer.Wolf, S.; Levanon, M.; Leiserowitz, L.; Lahav, M.; Sagiv, J. Stereochemcial studies in crystal nucleation. Oriented crystal growth of glycine at interfaces covered with Langmuir and Langmuir-Blodgett films of resolved α-amino acids. *J. Am. Chem. Soc.* **1989**, *111*, 1436–1445.
37. Lee, A. Y.; Lee, I. S.; Dette, S. S.; Boerner, J.; Myerson, A. S. Crystallization on Confined Engineered Surfaces: A Method to Control Crystal Size and Generate Different Polymorphs. *J. Am. Chem. Soc.* **2005**, *127*, 14982–14983.
38. Zaccaro, J.; Matic, J.; Myerson, A. S.; Garetz, B. A. Nonphotochemical, Laser-Induced Nucleation of Supersaturated Aqueous Glycine Produces Unexpected γ-Polymorph. *Cryst. Growth Des.* **2001**, *1*, 5–8.
39. Kang, J. F.; Zaccaro, J.; Ulman, A.; Myerson, A. Nucleation and growth of glycine crystal on self-assembled monolayers on gold. *Langmuir* **2000**, *16*, 3791–3796.
40. Chattopadhyay, S.; Erdemir, D.; Evans, J. M. B.; Ilavsky, J.; Amenitsch, H.; Segre, C. U.; Myerson, A. S. SAXS Study of the Nucleation of Glycine Crystals from a Supersaturated Solution. *Cryst. Growth Des.* **2005**, *5*, 523–527.
41. Lee, I. S.; Kim, K. T.; Lee, A. Y.; Myerson, A. S. Concomitant Crystallization of Glycine on Patterned Substrates: The Effect of pH on the Polymorphic Outcome. *Cryst. Growth Des.* **2008**, *8*, 108–113.
42. Sun, X.; Garetz, B. A.; Myerson, A. S. Supersaturation and Polarization Dependence of Polymorph Control in the Nonphotochemical Laser-Induced Nucleation (NPLIN) of Aqueous Glycine Solutions. *Cryst. Growth Des.* **2006**, *6*, 684–689.
43. (a) Rzayev, J.; Hillmyer, M. A. Nanoporous Polystyrene Containing Hydrophilic Pores from an ABC Triblock Copolymer Precursor. *Macromolecules* **2005**, *38*, 3–5. (b) Rzayev, J.; Hillmyer, M. A.

Nanochannel Array Plastics with Tailored Surface Chemistry. *J. Am. Chem. Soc.* **2005**, *127*, 13373–13379.

44. Ostwald, W. Z. Studies on formation and transformation of solid materials. *Z. Phys. Chem.* **1897**, *22*, 289–330.
45. Brandrup, J.; Immergut E. H.; Grulke E. A. ; Abe A.; Bloch R. *Polymer Handbook*, 4th ed.; John Wiley & Sons: New York, 1999.
46. Bouchard, A.; Hofland, G. W.; Witkamp, G.-J. Solubility of Glycine Polymorphs and Recrystallization of β-Glycine. *J. Chem. Eng. Data* **2007**, *52*, 1626–1629.
47. Hamilton, B. D.; Weissbuch, I.; Lahav, M.; Hillmyer, M. A.; Ward, M. D. Manipulating Crystal Orientation in Nanoscale Cylindrical Pores by Stereochemical Inhibition. *J. Am. Chem. Soc.* **2009**, *131*, 2588–2596.
48. Drebushchak, T. N.; Boldyreva, E. V.; Shutova, E. S. β-Glycine. *Acta Crystallogr.* **2002** *E58* o634–o636. Also ref 30.
49. Drebushchak, T. N.; Boldyreva, E. V.; Seryotkin; Yu, V.; Shutova, E. S. Crystal Structure Study of the Metastable β-Modification of Glycine and its Transformation into the α-Modification. *J. Struct. Chem.* **2002**, *43*, 835–842.

Chapter 4: Glycine Nanocrystal Orientation in Nanoporous Polymer Monoliths[i]

Crystal habit, the shape adopted by a crystal as it matures, is strongly influenced by the crystallization environment during nucleation and growth.[1] Solvents and additives can affect crystal habit by binding to specific crystal faces, which slows growth along the direction perpendicular to the adsorbing face while permitting unimpeded growth along other crystallographic directions. Additives designed to serve as crystallization regulators, sometimes referred to as crystallization auxiliaries, also can influence polymorphism,[2,3] the ability of molecules to adopt multiple crystalline forms. Certain crystallization auxiliaries, specifically amino acids, can inhibit growth of α-glycine crystals to the extent that the β-glycine form is generated.[4] Furthermore, whereas β-glycine generated by the addition of ethanol to an aqueous solution of glycine typically forms needles coinciding with the [010] direction,[5,6] resulting in

i. This work was reported in the *Journal of the American Chemcal Society* **2009**, *131,* 2420. Reproduced with permission. Copyright 2009, American Chemical Society.

vanishingly small (010) faces, evaporation of glycine solutions containing certain amino acid auxiliaries affords β-glycine crystals as plates with large (010) faces.

In Chapters 2 and 3, we discussed the crystallization of organic compounds in nanoscale pores of controlled porous glass (CPG) and aligned cylindrical pores of porous polymer monoliths fabricated from diblock and triblock polymers.[7,8,9] These investigations revealed that the sizes of the crystals embedded within the pores were comparable with the pore diameters and that polymorph selectivity during crystallization and polymorph stability rankings were affected by pore size. This behavior, which has been corroborated by others in studies of acetominophen crystallization in CPG,[10,11] can be attributed to the increasing importance of surface free energy compared with volume free energy as crystal size is reduced. Using X-ray microdiffraction, we also found that nanocrystals embedded in the porous polymer monoliths often exhibit preferred orientations with respect to the direction of the aligned pores.[7,8,9]

We demonstrated that glycine crystallization in the nanopores of CPG and porous polystyrene-poly(dimethyl acrylamide) monoliths (p-PS-PDMA) resulted in exclusive formation of the β polymorph under conditions that generate α-glycine when crystallization is performed in bulk.[12] The β-glycine nanocrystals embedded in either matrix were remarkably stable. In CPG this form persisted well above the bulk β→α phase transition temperature ($T_{\beta\rightarrow\alpha}$= 67 °C), melting near 180 °C. In p-PS-PDMA, the β-glycine nanocrystals converted to α-glycine only upon heating beyond the glass transition temperature of polystyrene ($T_g \approx 100$ °C). Numerous reports have described the crystallization of various materials within nanopores,[13] but only one system has addressed crystal alignment, finding that polymer crystals tend to grow with their fast-growth direction aligned parallel to the confining walls of one-dimensional pores (≈ 20 nm diameter) in porous alumina.[14] Herein we describe the effect of confinement on the orientation of β-glycine

nanocrystals grown in the one-dimensional pores of p-PS-PDMA and the role of crystallization auxiliaries on orientation. In the absence of auxiliaries, the β-glycine nanocrystals grow with their native fast-growth direction (i.e. the crystallographic *b* axis) parallel to the pore direction. The introduction of a racemic mixture of chiral auxiliaries known to block growth through enantioselective binding to the (010) faces, which are perpendicular to the native fast-growth direction, produces a different orientation, one that permits the crystal to grow unimpeded by both the pore walls and the auxiliaries. Interestingly, the *b*-axis is parallel to the pore axis when only one of the enantiopure chiral auxiliaries is present, confirming that a single enantiomer binds to the fast growing end of only one of the β-glycine enantiomorphs.

4-1: Monolith Preparation and Alignment

Nanoporous PS-PDMA monoliths were fabricated by chemical etching of the PLA block of shear oriented monolith of a PS-PDMA-PLA triblock polymer (PS = polystyrene; PDMA = poly(dimethyl acrylamide); PLA = poly(lactide))[15] prepared with volume fractions of $f_{PLA} = 0.30$, $f_{PDMA} = 0.13$, $f_{PS} = 0.57$. This composition was conducive to the formation of hexagonally-packed cylinders of PLA in the PS matrix, and etching produced aligned empty cylinders with hexagonal order in the PS matrix. Nuclear magnetic resonance (NMR) analysis confirmed ≥ 99% removal of the PLA with retention of the PDMA, which lined the interior walls of the pores. Scanning electron microscopy (SEM) of the etched monoliths revealed a hexagonal array of cylindrical pores with 20 nm diameters oriented parallel to the direction of triblock alignment (Figure 4-1A). The PDMA lining imparted a hydrophilic character to the cylinder walls, enabling penetration of aqueous solutions. Recently, we capitalized on this property by filling the cylindrical pores with an undersaturated aqueous glycine solution by immersion of the monolith in the solution.[12] After

removal from the solution in which the monolith was immersed, subsequent evaporation of the water from the cylindrical pores resulted in the formation of glycine nanocrystals confined within the nanopores, exclusively as the metastable β polymorph (Figure 4-1B). The selectivity for β-glycine was attributed to a size-dependent polymorph stability crossing, as only α-glycine is observed under the same conditions when crystallized in bulk.[16] The influence of size was corroborated by the selectivity for β-glycine in the nanopores of controlled porous glass (CPG), with β-glycine observed in pores sizes that ranged from 7.5 nm to 55 nm.

Unlike CPG, the uniformity of the nanopores in the p-PS-PDMA monoliths and their high degree of alignment presents an opportunity to explore in detail the influence of the anisotropic 1D environment of the nanopores on crystal growth. As reported previously, individual

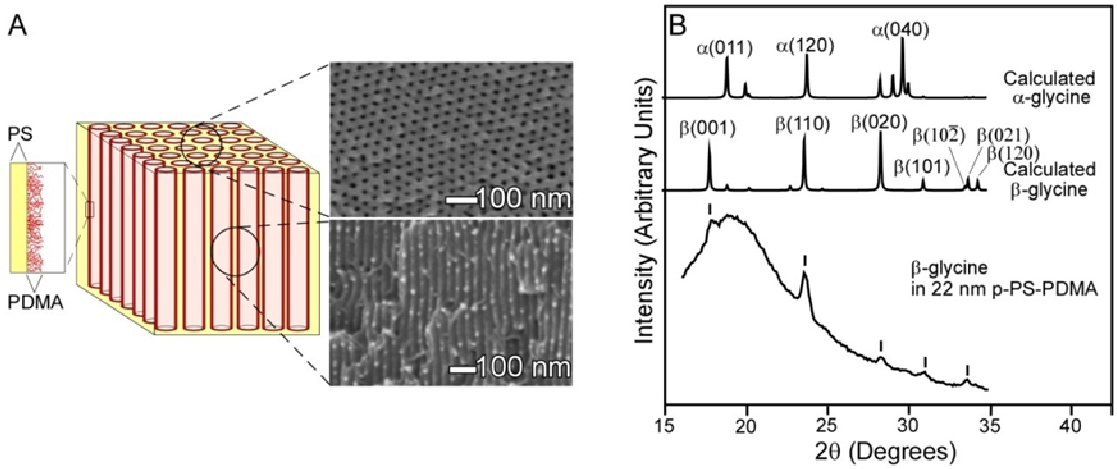

Figure 4-1. (A) Schematic representation (left) and SEM images (right) of a p-PS-PDMA monolith produced by chemical etching of PLA from shear-aligned p-PS-PDMA-PLA triblock copolymers. The SEM images are views parallel (top) and perpendicular (bottom) to the cylinder axes. The pores exhibit hexagonal order and diameters consistent with those determined by SAXS (22 ± 2 nm). The spherical features in the bottom SEM figure are attributed to plastic deformation of the PS matrix due to shear stresses occurring during fracture of the monolith. (B) 1D XRD data for β-glycine nanocrystals embedded within p-PS-PDMA monoliths with 22 nm pores. The diffraction peaks are superimposed on diffuse scattering from the amorphous polymer matrix. Comparison of the data with the simulated powder diffraction patterns, based on the known single crystal structures for α- and β-glycine, confirms the exclusive formation of β-glycine in the nanopores.

monoliths, with the pores in a fixed orientation, can be interrogated by X-ray microdiffraction, enabling determination of the correspondence between the nanocrystal and pore orientations.[7,8,9] The large number of pores in a 1 mm x 1 mm x 2 mm monolith ($> 10^9$) ensures that the number of crystals formed is sufficiently large that the X-ray data is effectively a powder pattern of the embedded crystals with random orientations about the pore axis while allowing determination of the crystal orientation with respect to the pore direction. Accurate determinations of nanocrystal orientation, however, requires that the alignment of the nanopores is sufficiently uniform. Prior to etching, small-angle X-ray scattering (SAXS) of the aligned triblocks revealed Bragg peaks consistent with hexagonally-packed PLA cylinders with diameters of 22 nm ± 2 nm, where the error corresponds to the pore diameters expected at $q^* \pm \sigma$ (σ = one standard deviation of the intensity distribution about q*). These cylinders are surrounded by a PDMA lining (approximately 1.7 nm thick, based on the PDMA volume fraction) and a PS matrix. The extent of cylinder orientation in the triblock monoliths, as given by the second order orientation factor F_2 (Equation 4.1), was determined from the 2-D SAXS data using the normalized orientation distribution function $P(\phi)$ (Equation 4.3), where ϕ is the azimuthal angle around a circle of constant q and $I(q^*,\phi)$ is the scattering intensity at the primary Bragg peak, q^*.[17] Typically, $F_2 \approx 0.92$ (Equation 4.3) for the PS-PDMA-PLA monoliths.[17,18,ii] Monoliths with F_2 values in the range $0.8 \leq F_2 \leq 0.9$ were obtained occasionally, but the apparent nanocrystal orientation measured by X-ray microdiffraction, which relies on uniform alignment of the pores, decreased with decreasing F_2. Monoliths with $F_2 < 0.8$ were completely unsuitable due to highly non-uniform

ii. Additional monoliths were obtained with the same nominal pore size and F_2 values between 0.8 and 0.9. The orientation of glycine nanocrystals embedded within these monoliths was evident in μ-XRD, but the degree of this orientation decreased as F_2 decreased. Below $F_2 \approx 0.8$, nanocrystal orientation was not observed.

orientation of the pores. Therefore, only monoliths with $F_2 \approx 0.92$ were used for chemical etching and subsequent investigations of nanocrystal orientation. SAXS measurements of the p-PS-PDMA monoliths obtained after chemical etching of the PLA block confirmed retention of the alignment, with $F_2 \approx 0.92$. The cylinder diameter inferred from the SAXS data is equivalent, within error, to the 20 nm diameter measured by SEM, which is reduced from the actual value by the platinum coating (Figure 4-1).

$$F_2 = 1 - 3\left\langle (\cos\phi)^2 \right\rangle \tag{4.1}$$

$$\left\langle (\cos\phi)^2 \right\rangle = \int_0^{\pi} (\cos\phi)^2 P(\phi) \sin\phi d\phi \tag{4.2}$$

$$P(\phi) = \frac{I(q^*,\ \phi) q^{*2}}{\int_0^{\pi} I(q^*,\ \phi) q^{*2} \sin\phi d\phi} \tag{4.3}$$

4-2: Crystallization of β-glycine nanocrystals.

The crystallization of β-glycine in the nanopores of p-PS-PDMA is particularly interesting because of the unique crystallographic characteristics of this polymorph and the influence of certain additives on its growth. Macroscopic β-glycine grows as needles (typically 500 μm long and 25 μm in diameter) from alcohol/water solutions,[6] crystallizing in the $P2_1$ space group with a = 5.077 Å, b = 6.268 Å, c = 5.38 Å, and β = 113.2°. The long axis of the needles coincides with the [010] direction of the crystal (b-axis). The $P2_1$ space group is chiral and β-glycine exists as two polar enantiomorphs, (+)-β and (-)-β. Because the crystals are polar, each enantiomorph is characterized by one end that grows more rapidly than the other. Previous attempts to assign the polarity of individual crystals via the Bijvoet method were unsuccessful owing to the weak anomalous scattering of the constituent atoms in glycine and the near-centrosymmetry of the

crystals;[5] therefore, the individual enantiomorphs were assigned according to the direction of the glycine C-H bonds: the enantiomorph with the C-H bonds protruding from the (010) face was defined as (+)-β, whereas the enantiomorph with the C-H bonds protruding from the (0-10) face was defined as (-)-β, as required by symmetry. The enantiomorphs were discerned experimentally by the effect of chiral amino acid additives on growth, wherein R-amino acids bound selectively to the (010) face of (+)-β and S-amino acids to the (0-10) face of (-)-β (Figure 4-2).[19,20] In each case, the additives significantly attenuated crystal growth by binding to the face at the fast-growing end. Based on the action of the chiral additives, the fast-growing end was assigned to the face with exposed C-H groups. That is, in the absence of additives (+)-β glycine grows rapidly along the +*b* direction, or [010], and (-)-β-glycine grows rapidly along the -*b* direction, or [0-10]. By extension, the addition of an R-amino acid will suppress the growth of (+)-β with no significant impact on the growth of (-)-β glycine, whereas the opposite will occur upon addition of an S-amino acid. In this respect, R- and S-Trp, R- and S-Phe, and R- and S-Met (Trp = tryptophan; Phe = phenylalanine; Met = methionine) were particularly effective growth inhibitors.

Glycine was crystallized within the aligned cylinders of the p-PS-PDMA monoliths by evaporating the water from the imbibed aqueous solutions. The exterior surfaces of the monoliths were subsequently swabbed with a damp cloth to remove any extraneous crystals or residue, which were evident from SEM images of some unswabbed monoliths. Some crystals were found to lay flat on the surface of the exposed cylindrical pores, whereas other crystals protruded from the pores (circled, Figure 4-3A). This crystal habit is unlike that observed on the sides of the unswabbed monoliths or on non-porous substrates, where α-glycine is observed. This suggests that these needles, which have the customary habit of β-glycine, grew out of the monolith during

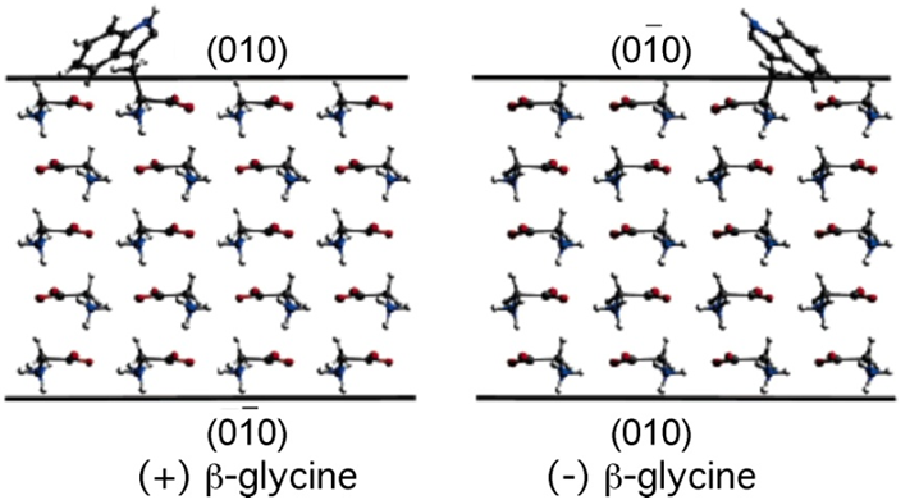

Figure 4-2. Molecular packing in the two enantiomorphs of β-glycine as viewed parallel to the (010) and (0-10) planes, depicted with a R-Trp and S-Trp binding to the (010) and (0-10) surfaces, respectively. Adapted from reference 5.

solvent evaporation from β-glycine nanocrystals embedded just beneath some of the pore entrances, then collapsed across the surface during handling. Based on the concentration of the glycine solution, the density of β-glycine, and complete filling of the pores, approximately 14% of the pore volume should be filled by crystals.[iii] The SEM images suggest that crystals emanate from roughly 1% of the pores exposed at the surface. Several of the monoliths were cooled in liquid nitrogen and cut with a razorblade at a depth of approximately 0.1 mm below the exposed porous surface. No crystals were evident in SEM images of newly exposed surfaces, which could reflect the small loading of glycine within the monolith. We note that similar difficulties were encountered in attempts to visualize cadmium sulfide particles embedded in nanoporous polystyrene monoliths.[21]

The nanocrystals embedded in the highly aligned cylindrical nanopores of the p-PS-PDMA monoliths were characterized by wide angle X-ray microdiffraction (μ-XRD) using a 2-D area

iii. Based on an aqueous 18% (w/w water) glycine solution and a glycine density of ρ = 1.16 g/mL.

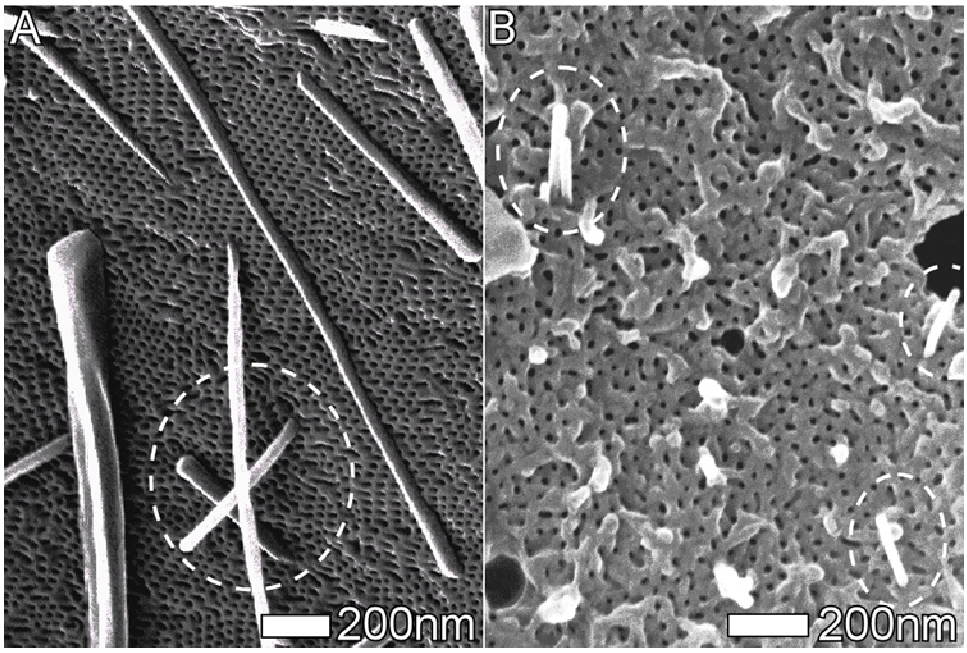

Figure 4-3. SEM images of β-glycine nanocrystals upon the outer surface of a p-PS-PDMA monolith after evaporation of an aqueous glycine solution containing (A) 18% glycine (w/w water) and (B) 18% glycine and 1.2% (w/w water) R,S-phenylalanine auxiliary prior to swabbing. The circled regions contain glycine nanocrystals protruding from the monolith pores. Long β-glycine needles laying flat on the monolith surface also are observed in (A). The bright irregular features in (B) are attributed to plastic deformation of the PS matrix during fracture of the monolith. The diameters of the crystals appear larger than the pore diameters, which likely reflects maturation of the crystals protruding from the pores as the aqueous glycine solution evaporates**.**

detector. These nanocrystals produced Bragg reflections at 2θ = 17.9°, 23.8°, 28.4°, 31.1°, and 33.8°, consistent with β-glycine, superimposed on background scattering due to the monolith (Figure 4-1B).[iv] The peak widths corresponded to crystal sizes commensurate with the 22 nm pore diameter. The 2-D μ-XRD data, which were collected as a full circle ($0° \leq \delta \leq 360°$) at

iv. Comparison of 1-D powder patterns generated from the 2-D μ-XRD data with patterns generated from the known glycine crystal structures indicated that β-glycine was the exclusive polymorph for ~90% of the samples; the remainder contained α-glycine. Analysis of the peak widths by the Scherrer Equation (See Cullity, B. D. *Elements of X-ray Diffraction*; Addison-Wesley: Reading, MA, 1978.) produced β-glycine crystal size estimates of 22 nm, consistent with the 22 nm pore diameter of the p-PS-PDMA.

values of $0° \leq 2\theta \leq 30°$, contained bright spots near the beam stop at azimuthal angles of $\delta = 90°$ and 270° (with δ measured from the top of the circle) caused by small-angle scattering from the monolith cylinders, which were aligned parallel to $\delta = 0°$. Although careful inspection of the 2D scattering pattern revealed $\beta(020)$ reflections at $\delta = 0°$ and 180° (Figure 4-4A), other reflections were difficult to detect among the background scattering. Additional reflections could be discerned, however, by increasing the sample-to-detector distance so that diffraction data was collected for only one quadrant of the full-circle at a time, specifically for the left ($45° \leq \delta \leq 135°$; Figure 4-4C,D) and top ($-45° \leq \delta \leq 45°$; Figure 4-4E,F) quadrants. Data collection for the two remaining quadrants was not necessary as these were simply mirror images of the left and top quadrants. This configuration permitted collection of Bragg reflections at values of $2.5° \leq 2\theta \leq 37.5°$. The reflections appeared as arcs with well-defined intensity maxima, located at specific azimuthal angles (*i.e.* δ). The observation of intensity across a range of δ values rather than discrete points indicates that the nanocrystals adopt a statistical distribution of orientations about an average preferred orientation (the intensity maximum) with respect to the cylinder axis. The (001), (110), and (020) reflections were sufficiently intense for accurate analysis of the intensity distribution with respect to δ, which revealed that 95% of the intensity was contained within $65° \leq \delta \leq 115°$, $43° \leq \delta \leq 67°$, and $-20° \leq \delta \leq 20°$, respectively.

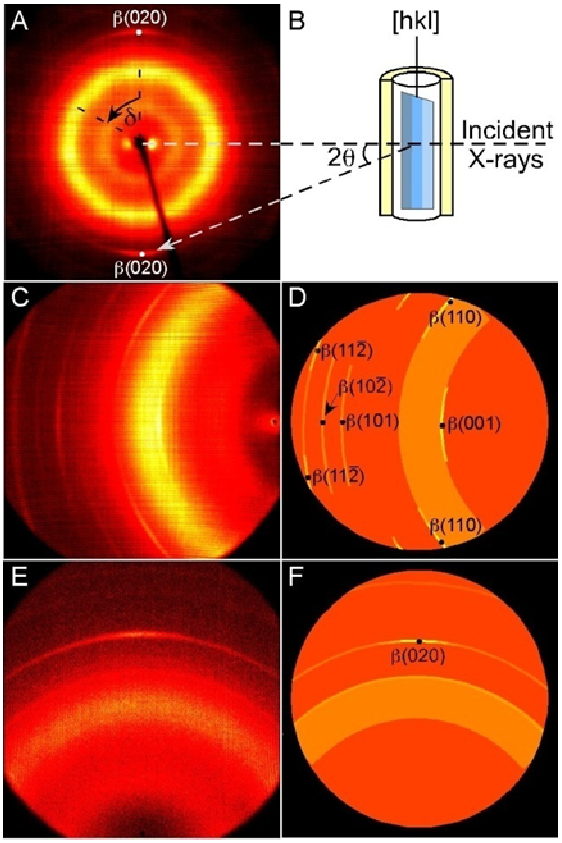

Figure 4-4. (A) Diffraction pattern observed on the 2D detector for β-glycine nanocrystals embedded in a 22-nm p-PS-PDMA monolith with its cylindrical pores parallel to the vertical axis at $\delta = 0$, as depicted in (B). (C) The left quadrant of the 2D detector ($45^o \leq \delta \leq 135^o$) revealing arcs of intensity due to Bragg reflections. (D) A schematic enhancing the reflection positions and locations of maximum intensity in (C) with the corresponding assignments. (E) The top quadrant of the 2D detector ($-45^o \leq \delta \leq 45^o$) with the monolith fixed in the same configuration and (F) A schematic enhancing the reflection positions and locations of maximum intensity in (E), with the corresponding assignments. The azimuthal angles (δ) of the Bragg reflections are consistent with preferential orientation of the {010} axis of β-glycine parallel to the pore direction. The schematics (D) and (F), which were constructed using the raw data as a guide, are intended to clarify the positions of the Bragg reflections and their assignments. The black dots denote the azimuthal angle corresponding to maximum intensity. Some reflections exhibit intensity maxima at two azimuthal angles, related by symmetry, corresponding to opposite orientations of the crystals in the monolith pores (see Table 1, below).

The orientation of the nanocrystals can be determined from the positions of the Bragg reflections ($h_2k_2l_2$), as given by the coordinates ($2\theta, \delta$) on the 2D detector, by calculating the angle (ϕ) between the Miller plane ($h_2k_2l_2$) and the Miller plane $(h_1k_1l_1)_\perp$ perpendicular to the pore direction (Equation 4.4). The identity of $(h_1k_1l_1)_\perp$ can be determined by trial-and-error, calculating the interplanar angles between ($h_2k_2l_2$) planes and trial values of $(h_1k_1l_1)_\perp$ until a self-consistent set of ϕ values that agrees with the data is obtained. The crystallographic direction parallel to pore direction can be defined as perpendicular to $(h_1k_1l_1)_\perp$. When applied to the scattering data in Figure 4-4C (Table 4-1), this analysis revealed unambiguously that the (020) planes were perpendicular to the cylinder axis. Given the monoclinic symmetry of β-glycine, whereby the [010] and (020) are perpendicular, the embedded nanocrystals are preferentially oriented with the [010] axis, *the native fast growth direction,* aligned with the pore direction.

The deduction of [010] as the crystallographic axis coinciding with the pore direction was corroborated by the diffraction pattern observed on the top quadrant, which exhibited an arc at $2\theta = 28.5°$, consistent with the (020) reflection. Crystals aligned with the (010) plane perpendicular to the pore-direction and parallel to the incident X-ray beam ordinarily would not produce Bragg reflections from any (*hkl*) when $h = 0$ and $l = 0$, as only forward scattering would be observed on the detector. Under this condition, however, (*hkl*) with only $h = 0$ or only $l = 0$ will produce Bragg reflections on the detector if they are allowed by symmetry. The observation of a (020) reflection at $2\theta = 28.5°$ suggests that a small fraction of the crystals (f_θ) are sufficiently tilted relative to the beam such that scattering from the (020) planes satisfies the Bragg condition upon reaching the detector. This can only occur for crystals tilted relative to the beam by $\theta = 14.25°$, because only for these crystals will the Bragg condition be satisfied for scattering from (020). Because these f_θ crystals have their (020) tilted relative to the beam by $\theta = 14.25°$, the measured θ

and δ values produce an apparent $\phi_{app} = \theta = 14.25°$ (Equation 4.4, Table 4-1). It is important to note that this ϕ_{app} is solely due to diffraction by the f_θ crystals and not crystals in the preferred orientation, which do not produce reflections because they do not meet the Bragg condition. The azimuthal spread of the (020) reflection containing 95% of the total intensity was $-20° \leq \delta \leq 20°$, indicating the angular distribution of these crystals about the beam axis. Because the pores have cylindrical symmetry, one would expect the δ spread to be comparable to $\theta = 14.25°$, the tilt observed for a measureable fraction of the crystals. The maximum of the azimuthal intensity is located at $\delta = 0°$, which argues that of the crystals described by f_θ, most are rotated about the beam axis by only a small amount. Analysis of the azimuthal intensity distribution reveals a Gaussian profile for the (020) reflections with 99% of the intensity confined within an angular spread of $-29° \leq \delta \leq 29°$, suggesting a range of crystal orientations comparable to the tilt of the f_θ crystals. Notably, crystals aligned with (020) in this range could achieve lengths as large 44 nm

Table 4-1. Measured and expected Bragg reflection parameters for β-glycine nanocrystals embedded within p-PS-PDMA monoliths, based on the [010] crystal axis coinciding with the cylindrical pores.

Reflection (hkl)	Measured 2θ (°)	Measured δ (°)[a]	$\cos(\theta)\cos(\delta)$ (from measured)	ϕ (°) (from measured)[b]	Expected 2θ (°)	Expected ϕ (°)[c]	Expected δ (°)[a,b]
(001)	17.9	90	0.00	90	17.9	90	90
(110)	23.8	55, 125	0.56	56	23.8	53	52, 128
(020)	28.5	0[d]	0.97	14[d]	28.5	0[d]	-[d]
(101)	31.1	90	0.00	90	31.1	90	90
(10-2)	33.7	90	0.00	90	33.7	90	90
(021)	33.8	30, 150	0.83	34	33.8	32	28, 152
(120)	34.4	30, 150	0.83	34	34.4	34	30, 150
(002)	33.6	90	0.00	90	36.3	90	90
(11-2)	36.6	70, 110	0.32	71	36.7	67	65, 115

[a]Reflections appearing as pairs of δ values symmetrically opposed across $\delta = 0°$ and 90° can be attributed to glycine nanocrystals oriented in opposite directions within the pores. [b]Calculated using Equation 4.4. [c]Calculated with (*hkl*) and (010) assuming [010] parallel with the pore direction. [d]ϕ (from measured) is the *apparent* angle between (*hkl*) and (010), the plane perpendicular to the pore direction. The (020) is perpendicular to [010], and only forward scattering would be expected from this plane, that is there would be no reflection for the (020). The crystals are not all perfectly aligned, however, and the small fraction of crystals oriented such that their (020) is tilted $(2\theta/2)\ \theta = 14.25°$ relative to the beam satisfy the Bragg condition. This leads to the appearance of the (020) reflection at $\delta = 0°$, which corresponds to an *apparent* $\phi = \theta = 14.25°$.

along <010>, the fast growth direction. Crystals outside this range would be smaller along this direction, which could prohibit crystals thus aligned from achieving critical size.

$$\Phi = \cos^{-1}\left(\cos\theta\cos\delta\right) \tag{4.4}$$

$$\delta = \cos^{-1}\left(\frac{\cos\Phi}{\cos\theta}\right) \tag{4.5}$$

The observation of a preferred orientation argues against the instantaneous formation of randomly oriented nuclei that retain their initial orientation and grow uniformly. Instead, the observations are consistent with (*i*) a preferred orientation of the crystal nuclei at the early stages of crystallization due to the 1D anisotropy of the cylindrical nanopores; (*ii*) a continuous nucleation and growth process wherein nanocrystals with the fast-growth direction parallel (or nearly parallel) to the pores are preferred because they can achieve critical size more readily than nuclei with other alignments in which growth along the fast-growth direction would be obstructed by the pore walls. Such "misaligned" crystals would be prevented from achieving their natural habit, which reflects the balance between surface and volume free energies. As such, misaligned crystals would be less stable and more inclined to redissolve than those with their fast-growth axis aligned with the pores; (*iii*) (010) and (0-10) faces of the two enantiomorphs are vanishingly small, suggesting that these faces have high surface energies and that the observed crystal alignment minimizes the overall surface energy of the nanocrystals. Examination of the crystal structure of β-glycine reveals multiple hydrogen bonds along <010>, <001>, and <100>. Notably, the [010] direction is characterized by the greatest number of hydrogen bonds, which is consistent with large surface energies for the (010) and (0-10) faces. As such, the nanoscale pores physically constrain crystal growth so that the crystal face with the highest surface energy spans the narrowest dimension of the pore. Any tilt of this face relative to the pore direction would produce

an increase of the surface area of this unfavorable plane, thereby increasing the total free energy of the crystal.

4-3: Stereochemical Control of Glycine Orientations

Racemic Trp alone, quasi-racemic Phe-Trp or Met-Trp, combinations of enantiopure Phe or Met with racemic Trp, combinations of racemic Phe or Met with enantiopure Trp, and combinations of racemic Phe or Met with racemic Trp dramatically suppress growth along the <010> of bulk β-glycine crystals, resulting in a substantial change in the habit of the crystals from needles to plates or prismatic blocks (Figure 4-5A, B)[5] due to binding of the chiral auxiliaries to the {010} faces.

This behavior prompted us to examine the effect of these auxiliaries on the growth characteristics of β-glycine nanocrystals embedded in the 1D cylinders of the p-PS-PDMA monoliths by infiltrating the monoliths with solutions containing both glycine and individual auxiliaries, in concentrations comparable to those used in the prior bulk experiments. β-Glycine was then crystallized in the monoliths as described above. SEM of the porous surface of the monoliths following this treatment revealed nanocrystals protruding from the cylindrical pores, as illustrated in Figure 3B for crystals grown in the presence of R,S-phenylalanine. Notably, these crystals were substantially smaller than those observed in the absence of the auxiliaries (Figure 4-3A), which mirrors the changes in crystal habit observed in the bulk due to suppression along <010>. We also note that glycine crystallization from bulk solutions (by evaporation) in the presence of racemic Phe or racemic Met results in the exclusive formation of the γ-glycine polymorph. Crystallization in the cylindrical nanopores of the PS-PDMA monoliths, however, only afforded the β polymorph, underscoring the influence of nanoconfinement on the crystallization outcome.

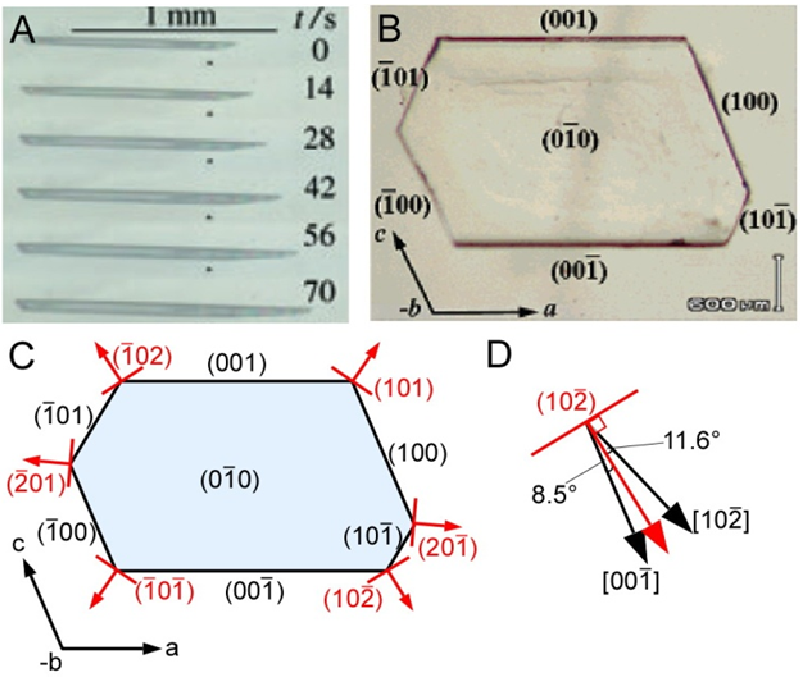

Figure 4-5. (A) Bulk β-glycine crystals retrieved at different times during evaporation of ethanol-water solutions containing glycine without chiral auxiliaries (adapted from reference 3). The long axes of the needles correspond to the <010> directions. (B) A bulk β-glycine crystal, grown by evaporation of an aqueous solution containing glycine and 0.3% R,S-Trp (w/w water; equivalent to 2% w/w glycine) exhibits a plate-like habit (adapted from reference 4). The crystal habit is illustrative of the habit for β-glycine crystals grown with Phe and Met auxiliaries. The large faces of the plate correspond to the {010} planes that result from the suppression of growth along <010> by the auxiliary. (C) Schematic representation of the β-glycine crystal in (B) illustrating the crystal faces (red) that have vanishingly small areas because of fast growth along directions (red arrows) perpendicular to their surface. Notably, X-ray diffraction reveals that the (10-2) plane is effectively perpendicular to the p-PS-PDMA monolith pore direction when glycine is crystallized in the presence of a racemic mixture of a chiral auxiliary (Met, Phe, Trp). (D) Illustration of the relationship between the (10-2) plane and the nearly perpendicular [00-1] and [10-2] directions.

The scattering patterns obtained for the embedded β-glycine nanocrystals grown in the presence of racemic mixtures of chiral auxiliaries (R,S-Phe, R,S-Met, R,S-Trp) differed significantly from those observed for β-glycine alone, signifying a change in the preferred orientation of the nanocrystals (Figure 4-6). The Bragg reflections were characterized by arcs of intensity, with the azimuthal spread comparable to that described above for β-glycine alone, with

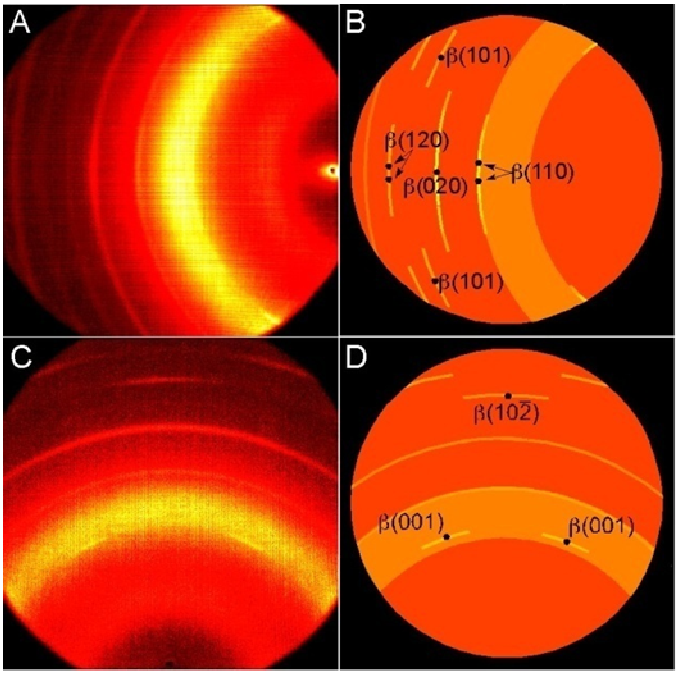

Figure 4-6. Diffraction patterns for β-glycine nanocrystals, grown by evaporation of aqueous solutions containing 18% glycine (w/w water) and 1.2% R,S-Phe (w/w water), embedded within the 22-nm cylindrical pores of a p-PS-PDMA monolith. Similar diffraction patterns are observed for β-glycine nanocrystals grown in the presence of R,S-Met and R,S-Trp. (A) The left quadrant of the 2D detector ($45^o \leq 2\theta \leq 135^o$) reveals arcs of intensity due to Bragg reflections. (B) A schematic enhancing the reflection positions and locations of maximum intensity in (A) with the corresponding assignments. (C) Top quadrant of the 2D detector ($-45^o \leq 2\theta \leq 45^o$) with the monolith fixed in the same configuration (D) A schematic enhancing the reflection positions and locations of maximum intensity in (A) with the corresponding assignments. The orientation of the Bragg reflections and monolith channels suggests the [00-1] directions of β-glycine grow nearly parallel to the pore direction. The schematics (B) and (D) were constructed using the raw data as a guide with the intent of clarifying the Bragg reflection assignments and positions in the raw data. The black dots denote the azimuthal angle corresponding to maximum intensity. Some reflections exhibit intensity maxima at two azimuthal angles, related by symmetry, corresponding to opposite orientations of the crystals in the monolith pores (see Table 3, below).

(001), (020), and (10-2) exhibiting measurable intensities over the ranges $20° \leq \delta \leq 40°$, $74° \leq \delta \leq 106°$, and $-16° \leq \delta \leq 16°$, respectively. Analysis of the scattering pattern revealed that the (10-2) plane was perpendicular to the cylindrical pore (Table 4-2). Under the monoclinic symmetry of β-glycine, the [10-5] direction is perpendicular to this plane and thus would coincide with the pore direction. The [001] axis and [10-2] directions, however, are nearly perpendicular to (10-2), at 8.5^{o} and 11.6^{o} from the plane normal, respectively. Moreover, the data reveal the {010} planes were now parallel to the cylinder direction, corresponding to the <010> directions perpendicular to the cylinder direction, a 90° "flip" compared with the orientation in the absence of auxiliaries. Combinations of a racemic mixture of a chiral auxiliary (R,S-Met or R,S-Phe) with an enantiopure or racemic mixture of Trp afforded similar results. In contrast, the scattering patterns obtained for the embedded β-glycine nanocrystals grown in the presence of enantiopure chiral auxiliaries (R- or S- Phe, Met, or Trp; Table 4-3), which should only impede the growth of one of the β-glycine enantiomorphs, were identical to those observed for β-glycine alone.

Examination of the crystal structure of β-glycine reveals multiple hydrogen bonds along <010>, <001>, and <100>. The interruption of growth along <010> by racemic auxiliaries would be expected to favor growth along other hydrogen-bonding directions, in this case <001>, which lies in {010} and is nearly perpendicular to (10-2). The (10-2) can be described as having a high surface energy because it truncates the <001> hydrogen bonds. This high surface energy would forecast a small area for this face and fast growth perpendicular to its surface so that the overall surface energy is minimized as the crystal volume expands. This is consistent with bulk β-glycine crystals grown in the presence of racemic mixtures of chiral auxiliaries, where the (10-2) face is vanishingly small, corresponding to a corner intersected by the (00-1) and (10-1) planes (Figure 4-5C). Therefore, this crystal alignment under confinement minimizes the overall surface energy

Table 4-2. The effect of chiral auxiliaries on the orientation of β-glycine nanocrystals embedded in p-PS-PDMA.

Auxiliary 1[a]	(% w/w water)	(% w/w gly)[b]	Auxiliary 2[a]	(% w/w water)	(% w/w gly)[b]	β-glycine crystal direction parallel to pore direction[c]
None	-	-	-	-	-	[010]
R- or S-Phe	1.2	8	-	-	-	[010]
R- or S-Met	1.2	8	-	-	-	[010]
R- or S-Trp	0.3	2	-	-	-	[010]
R,S-Met	0.6-1.2	4-8	-	-	-	[00-1]
R,S-Phe	0.6-1.2	4-8	-	-	-	[00-1]
R,S-Trp	0.3	2	-	-	-	[00-1]
R,S-Met	1.2	8	R,S-Trp	0.3	2	[00-1]
R,S-Met	1.2	8	R- or S- Trp	0.3	2	[00-1]
R,S-Phe	1.2	8	R,S-Trp	0.3	2	[00-1]
R,S-Phe	1.2	8	R- or S-Trp	0.3	2	[00-1]

[a]The auxiliary abbreviations are Phe (Phenylalanine), Met (Methionine), and Trp (Tryptophan). [b]The aqueous solutions contained 18% glycine (w/w water). [c]The glycine crystals grown from aqueous solutions containing glycine and racemic mixtures of amino acids resulted in crystals with (10-2) perpendicular to the pore direction, with [00-1], which was a strong hydrogen bonding direction in β-glycine and the fast-growth direction, nearly parallel to the pores (8.5° difference).

of the nanocrystals, apparently overcoming any favorable volume free energy due to growth along the <010> directions. As with the <010> alignment for crystallization without auxiliaries, the nanoscale pores physically constrain crystal growth so that the crystal face with the higher surface energy spans the narrowest dimension of the pore. Any tilt of this face relative to perpendicular to the pore direction results in an increase of the surface area of this unfavorable plane, thereby increasing the total free energy of the crystal, all other factors being equal. For β-glycine embedded within p-PS-PDMA, this attempt to minimize the surface area of (10-2) results in [10-5] aligned parallel to the pore direction and [001], the fast growth direction, aligned very nearly parallel to the pore direction (Figure 4-5D). *We also note that the observation of two different alignments for crystals grown in the absence and presence of auxiliaries argues that heterogeneous nucleation on the pore walls, involving a favorable interaction with a specific set of crystal planes of emerging nuclei, has little influence on the crystallization process.*

Table 4-3. The measured and expected δ values for glycine nanocrystals grown in the monoliths with R,S-phenylalanine auxiliaries. The (10-2) crystal plane was preferentially aligned perpendicular to the pore direction.

Reflection (hkl)	Measured 2θ (°)	Measured δ (°) [a]	Cos(θ)Cos(δ) (from measured)[b]	φ (°) (from measured)[b]	Expected 2θ (°)	Expected φ (°) [c]	Expected δ (°) [a,b]
(001)	17.9	30, 150	0.82	35	17.9	31.6	30, 150
(110)	23.8	90	0.00	90	23.8	83.2	83, 97
(020)	28.5	90	0.00	90	28.5	90	90
(101)	31.1	69, 121	0.31	72	31.0	66	65, 115
(10-2)	33.7	0[d]	0.83	17[d]	33.7	0[d]	-[d]
(021)	33.8	60, 120	0.42	65	33.8	62.8	61, 119
(120)	34.3	85, 95	0.07	86	34.4	85.3	85, 95
(12-1)	36.6	60, 120	0.42	65	36.3	58.8	57, 123
(11-2)	36.6	N/A[e]	-	-	36.7	23	14, 166

[a]Reflections appearing as pairs of δ values were caused by glycine nanocrystals oriented in opposite directions within the pores, where the symmetry between the crystal orientations resulted in reflections mirrored across δ = 0° and 90°. [b]Calculated using Equation 4.4. [c]Calculated from (hkl) and (10-2). The [001] is assumed to be the fast-growth direction and is nearly parallel to the pore direction. [d]φ (from measured) is the *apparent* angle between (hkl) and (10-2), the plane perpendicular to the pore direction. The (10-2) is parallel to the beam, and only forward scattering would be expected from this plane, that is, there would be no reflection expected for the (10-2). The crystals are not all perfectly aligned, however, and the small fraction of crystals oriented such that their (10-2) is tilted (2θ/2) θ = 16.85° relative to the beam satisfy the Bragg condition. This leads to the appearance of the (10-2) reflection at δ = 0°, which corresponds to an *apparent* φ = θ = 16.85°. [e]Reflection not observed in the data.

Collectively, these observations reveal a correspondence between the effect of chiral auxiliaries on the growth of bulk β-glycine and embedded β-glycine nanocrystals, and a connection between the fast growth direction of β-glycine nanocrystals and their orientation in the cylindrical pores. In the absence of auxiliaries the nanocrystals grow with their native fast growth direction, <010>, aligned with the cylindrical pore. This suggests that "misaligned" nuclei, with <010> axes inclined to the pore direction, are disfavored because their growth is obstructed by the pore walls, with fewer achieving critical size during crystallization compared with those with <010> aligned along the pore direction. The suppression of these misaligned nuclei would diminish as <010> approaches an alignment coinciding with the pore direction, which is consistent with the distribution of orientations evident from the arcs of intensity about central maxima for the Bragg reflections. The addition of racemic auxiliaries, however, alters the

relative kinetics of growth along the various crystallographic directions, suppressing growth along <010> such that growth along another crystallographic direction is preferred, in this case the <001>.

Notably, because β-glycine is chiral and exists as two enantiomorphs, an enantiopure chiral auxiliary binds selectively to a particular face of only one of the enantiomorphs, in this case the (010) of (+)-β or the (0-10) of (-)-β, depending on the handedness of the auxiliary.[v] Under these conditions, the enantiopure auxiliary will inhibit the growth of only one of the enantiomorphs, allowing the other to grow unimpeded with characteristics identical with those observed for in the absence of any stereochemical inhibitor. For example, S-Trp, S-Met, and S-Phe selectively inhibit growth along the [0-10] direction for (-)-β-glycine by binding to the (0-10) face.[4] Because growth of the (+)-β enantiomorph is not affected these crystals grow normally along the [010] direction, such that the (+)-β nanocrystals are oriented with [010] parallel to the pore direction (Figure 4-7).

4-4: Concluding Remarks

These results demonstrate that β-glycine crystals, which are favored under nanoscale confinement, adopt an orientation in which the fast-growth direction is aligned with the pore direction. The addition of a racemic mixture of chiral auxiliaries, which inhibits growth along the native fast-growth direction, generates a different orientation. These observations argue against heterogeneous nucleation wherein a particular crystal plane interacts favorably with the pore walls. Instead, the results suggest that the observed orientations are a consequence of critical size effects and surface energy considerations, wherein confinement favors growth orientations

[v] The range of orientations exhibited by the β-glycine nanocrystals embedded in p-PS-PDMA precluded the determination of their chirality from any of the 2-D μ-XRD data.

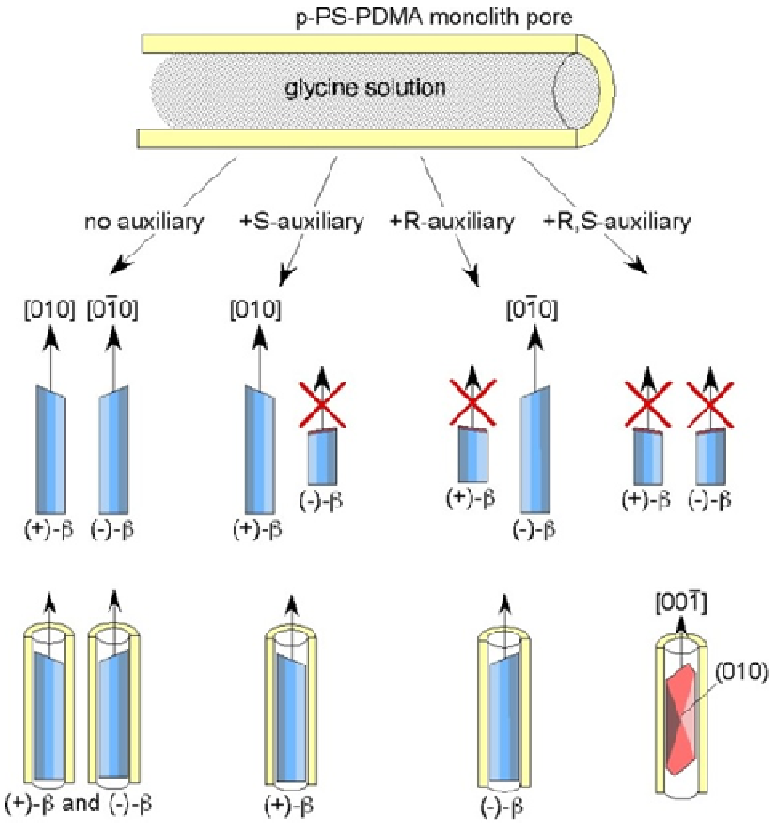

Figure 4-7. Preferred orientations adopted by β-glycine nanocrystals grown within p-PS-PDMA in the presence of no, enantiopure, and racemic mixtures of chiral auxiliaries.

that permit nuclei to achieve critical size more competitively when their fast-growth axis is unimpeded by pore walls and the area of the face with the highest surface energy is minimized when aligned perpendicular to the pore. Collectively, these observations illustrate the connection between bulk crystal habit and nanocrystal orientation under size confinement. The ability to manipulate the orientation of nanocrystals under extreme size confinement could provide new routes to composite materials while enabling exploration of the structure-property relationships at the nanoscale, for example, solid-state reactions occurring in organic nanocrystals with dimensions smaller than those reported previously.[22,23] It is also interesting to consider whether the formation of a non-centrosymmetric crystalline phase because of nanoconfinement - in this

case β-glycine, the simplest amino acid – suggests a role for this phenomenon in the genesis or amplification of biological homochirality in clay or mineral matrices.[24]

4-5: Experimental Procedures

4-5.1: Methods and Materials.

All reagents and solvents were used as received unless otherwise noted. Glycine was purchased from Sigma-Aldrich, Inc. (St. Louis, Missouri). Aqueous glycine solutions were passed through a 0.45 μm poly(tetrafluoroethylene) syringe filter before use to remove any insoluble particulate matter. Polylactide-poly(dimethyl acrylamide)-polystyrene (PLA-PDMA-PS) triblock polymers and monoliths were prepared according to procedures described in a previous report.[12] PLA-PDMA-PS triblocks were synthesized with volume fractions of $f_{PLA} = 0.30$, $f_{PDMA} = 0.13$, $f_{PS} = 0.57$, which were conducive to the formation of a hexagonally-packed cylinder structure. When shear oriented, these triblock copolymers generated cylinders of PLA, which were etched in base (1 M NaOH solution in 50:50 MeOH/H_2O) at 60 °C for 5 days to generate porous PS-PDMA (p-PS-PDMA) monoliths with cylindrical pores having 22 nm diameters. The p-PS-PDMA monoliths were dried under vacuum at room temperature for 3 hours to remove residual water after post-etch rinsing. The cylindrical pores in the p-PS-PDMA monoliths were well ordered, as confirmed by small angle X-ray scattering. The interior lining of the pores was PDMA-rich and therefore hydrophilic, which permitted infiltration of aqueous solutions.

4-5.2: Crystallization in Nanoporous Block Copolymers

The p-PS-PDMA monoliths (approximately 1 mm x 2 mm cross-section and 3 mm along the pore direction) were immersed in water for 2 hours prior to imbibing glycine solutions. This

pretreatment was found necessary for consistent loading of glycine in the pores, as surmised from the Bragg peak intensity in the XRD. The monolith pieces were subsequently immersed in 18% glycine solution for 2 hours, during which the glycine solution migrates into the pores of the monolith. After removal from solution, the outer surfaces of the monoliths were carefully swabbed with a soft dampened tissue to remove any external glycine solution residue. The monoliths were then dried under vacuum at approximately 0.1 mm Hg for 4 hours, although nanocrystals were detected by X-ray microdiffraction (see below) within 30 minutes. Further drying under vacuum did not affect the crystallization outcome, and allowing the monoliths to dry under ambient conditions afforded identical results but nanocrystals were not detected until after approximately 2 hours. Further crystallization was evident during the next hour of drying.

4-5.3: Characterization

Wide-angle X-ray scattering microdiffraction (μ-XRD) was performed on a Bruker AXS (Madison, Wisconsin) microdiffractometer equipped with a 2D Siemens multi-wire area detector and a 0.8 mm beam collimator. The full width at half maximum (FWHM) resolution of the instrument was determined by measuring the FWHM for both a single crystal LaB_6 wafer and a single crystal of highly oriented pyrolytic graphite (HOPG). The FWHM resolution of the instrument was approximately 0.27° (2θ) over the 2θ range of 15°–35°, allowing for a maximum crystal size estimate of 30 nm by the Scherrer equation. Simulated X-ray powder patterns for α, β, and γ-glycine were generated using Mercury (Cambridge Crystallographic Data Center, Cambridge, United Kingdom, version 1.4.1) with crystallographic parameters obtained from the Cambridge Structural Database (Cambridge Crystallographic Data Center, Cambridge, United Kingdom).

The monoliths were affixed at the end of a brass pin using a small amount of clay such that striations on the monolith surface, known to be parallel with the direction of the pores, were parallel with the brass pin. The brass pin was then inserted into a sample holder supplied by the manufacturer and then tightened with a small screw. This sample was then mounted on a four-circle Eulerian cradle such that the cylindrical pores were aligned parallel with the X-ray detector, and then the cradle was adjusted via the instrument controls until the pores were aligned also parallel with the vertical centerline of the detector. A laser-video alignment system supplied by the manufacturer was used to determine whether the monolith was aligned with the beam, and the position of the brass pin was adjusted with small screws in the sample holder until the alignment system indicated the monolith was in the beam path. To verify the pores were aligned parallel with the vertical centerline of the detector, an initial set of X-ray data was collected and the azimuthal positions of the resulting Bragg reflections were observed. Proper alignment of the sample was evident when the reflections were symmetric about $\delta = 90°$, which verified that crystals pointed in opposite directions within the pores were also symmetric about $\delta = 90°$. This indicated the pores were parallel with the vertical center, and if the data suggested otherwise, the Eulerian cradle was adjusted with the instrument controls until the Bragg reflections from the monolith met this criteria.

Data were collected in a forward scattering mode, initially with the monolith aligned parallel with the vertical center line of the detector ($\delta = 0°$) and the incident X-ray beam centered on the detector (Figure 4-8A). The sample-to-detector distance was 6 cm. In this configuration, Bragg reflections were collected over a full azimuthal circle ($0° \leq \delta \leq 360°$) with radius $0° \leq 2\theta \leq 30°$ (Figure 4-8A). Data also were collected at a sample-to-detector distance of 15 cm and the monolith positioned parallel to the right edge of the detector ($\delta = 0°$; Figure 4-8B). Many

reflections were more readily discerned at the longer sample-to-detector distance, although this configuration precluded data collection spanning the entire 360° azimuth. Instead, Bragg reflections were collected over the quadrant of the full-circle ranging from $2.5° \leq 2\theta \leq 37.5°$ and $45° \leq \delta \leq 135°$. Rotation of the monoliths counterclockwise about the δ-axis by 90°, such that $\delta = 0°$ was coincident with the horizon of the detector, allowed data collection ranging from $2.5° \leq 2\theta \leq 37.5°$ and $-45° \leq \delta \leq 45°$, which was equivalent to the top quadrant of the full circle. Data collection for the two remaining quadrants was not necessary as these are simply mirror images of the left and top quadrants.

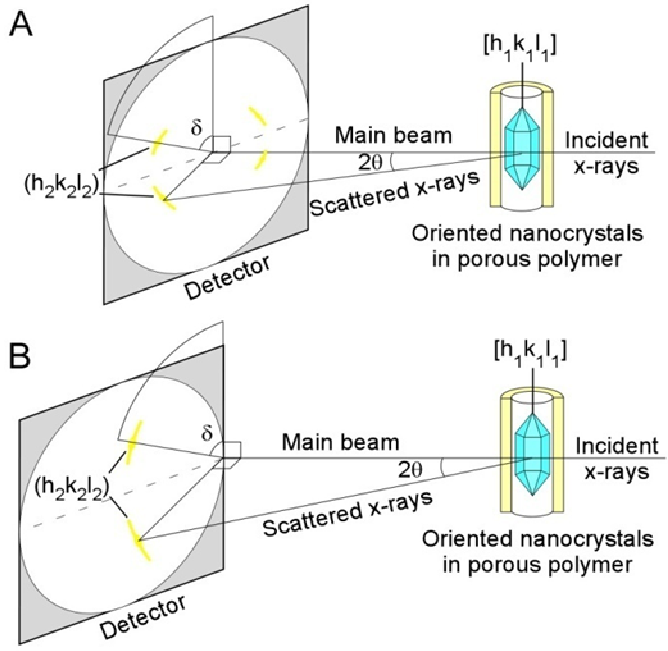

Figure 4-8. Configuration for diffraction using the μ-XRD, equipped with a 2D detector. The nanoporous monolith with embedded nanocrystals (depicted here as only a single cylinder) is held in a fixed orientation with respect to the detector, with the beam targeted at either the (A) center or (B) right edge of the detector. Reflections from specific crystal planes produce diffraction spots on the 2D detector at coordinates of $(2\theta,\delta)$, where 2θ is the Bragg diffraction angle and δ is the azimuthal angle on the detector that reflects the orientation of that plane with respect to $\delta = 0°$, which coincides here with the pore axis (the normal setting for experiments described herein). Arcs of intensity (rather than discrete points) signify a distribution of orientations of the reflecting plane about the preferred orientation.

4-6: References

1. Mullin, J W. *Crystallization*; Elsevier: Oxford, 2004.
2. Bernstein, J. *Polymorphism in Molecular Crystals*; Oxford: New York, 2002.
3. Weissbuch, I.; Leiserowitz L.; Lahav M. Tailor-Made and charge-transfer auxiliaries for the control of the crystal polymorphism of glycine. *Adv. Mater*. **1994** *6*, 952-956.
4. Torbeev, V. Yu.; Shavit, E.; Weissbuch, I.; Leiserowitz, L.; Lahav, M. Control of Crystal Polymorphism by Tuning the Structure of Auxiliary Molecules as Nucleation Inhibitors. The β-Polymorph of Glycine Grown in Aqueous Solutions. *Cryst. Growth. Des.* **2005**, *5*, 2190-2196.
5. Weissbuch, I.; Torbeev, V. Yu.; Leiserowitz, L.; Lahav, M. Solvent Effect on Crystal Polymorphism: Why Addition of Methanol or Ethanol to Aqueous Solutions Induces the Precipitation of the Least Stable β Form of Glycine. *Angew. Chem. Int. Ed. Engl*. **2005**, *44*, 3226-3229.
6. (a) Iitaka, Y. *Acta Crystallogr*. **1960**, *13*, 35-45. (b) Ferrari, E. S.; Davey, R. J.; Cross, W. I.; Gillon, A. L.; Towler, C. S. Crystallization in Polymorphic Systems: The Solution-Mediated Transformation of β to α Glycine. *Cryst. Growth Des.* **2003**, *3*, 53-60.
7. Ha, J.-M.; Wolf, J. H.; Hillmyer, M. A.; Ward, M. D. Polymorph Selectivity under Nanoscopic Confinement. *J. Am. Chem. Soc.* **2004**, *126*, 3382-3383.
8. Ha, J.-M.; Hillmyer, M. A.; Ward, M. D. Thermotropic Properties of Organic Nanocrystals Embedded in Ultrasmall Chambers. *J. Phys. Chem. B* **2005**, *109*, 1392-1399.
9. Ha, J.-M. Crystallization and Thermotropic Properties of Organic Solids in Nanoscopic Reactors. PhD Thesis, University of Minnesota, **2005**.
10. Beiner, M.; Rengarajan, G.T.; Pankaj, S.; Enke, D.; Steinhart, M. Manipulating the Crystalline State of Pharmaceuticals by Nanoconfinement. *Nano Lett.*, **2007**, *7*, 1381-1385.
11. Rengarajan, G.T.; Enke, D.; Steinhart, M.; Beiner, M. Stabilization of the amorphous state of pharmaceuticals in nanopores. *J. Mater. Chem*. **2008**, *18*, 2537-2539.
12. Hamilton, B. D.; Hillmyer, M. A.; Ward, M. D. Glycine Polymorphism in Nanoscale Crystallization Chambers. *Cryst. Growth Des.* **2008**, *8*, 3368-3375.
13. (a) Jackson, C. L.; McKenna, G. B. The melting behavior of organic materials confined in porous solids. *J. Chem. Phys.* **1990**, *93*, 9002-9011. (b) Ajayan, P. M.; Iijima, S. Capillarity-induced filling of carbon nanotubes. *Nature* **1993**, *361*, 333-334. (c) Prasad, R.; Lele, S. Stabilization of the amorphous phase inside carbon nanotubes: solidification in a constrained geometry. *Phil. Mag. Lett.* **1994**, *70*, 357–361. (d) Patrick, W. A.; Kemper, W. A. Melting Temperatures of Compounds Adsorbed on Silica Gel. *J. Phys. Chem.* **1938**, *42*, 369-380. (e) Borisov, B. F.; Charnaya, E. V.; Hoffmann, W. D.; Michel,

D.; Shelyapin, A. V.; Kumzerov, Yu. A. Nuclear magnetic resonance and acoustic investigations of the melting-freezing phase transition of gallium in a porous glass. *J. Phys.*: *Condens. Matter* **1997**, *9*, 3377-3386. (f) Buffat, Ph.; Borel, J.-P. Size effect on the melting temperature of gold particles. *Phys. Rev. A* **1976**, *13*, 2287-2298. (g) Reinnie, G. K.; Clifford, J. Melting of Ice in Porous Solids. *J. Chem. Soc., Faraday Trans. 1* **1977**, *73*, 680-689. (h) Christenson, H. K. Confinement effects on freezing and melting. *J. Phys: Condens. Matter* **2001**, *13*, R95-R133.

14. (a) Steinhart, M.; Göring, P.; Dernaika, H.; Prabhukara, M.; Gösele, U.; Hempel, Thurn-Albrecht, T. Coherent Kinetic Control over Crystal Orientation in Macroscopic Ensembles of Polymer Nanorods and Nanotubes. *Phys. Rev. Lett.* **2006**, *97*¸ 027801. (b) Steinhart, M.; Stephan S.; Wehrspohn, R.B.; Gosele, U.; Wendorff, J. H. Curvature-Directed Crystallization of Poly(vinylidene difluoride) in Nanotube Walls. *Macromolecules* **2003**, *36*, 3646-3651.
15. (a) Rzayev, J.; Hillmyer, M. A. Nanoporous Polystyrene Containing Hydrophilic Pores from an ABC Triblock Copolymer Precursor. *Macromolecules* **2005**, *38*, 3-5. (b) Rzayev, J.; Hillmyer, M. A. Nanochannel Array Plastics with Tailored Surface Chemistry. *J. Am. Chem. Soc.* **2005**, *127*, 13373-13379.
16. (a) Boldyreva, E. V.; Drebushchak, V. A.; Drebushchak, T. N.; Paukov, I. E.; Kovalevskava, Y. A.; Shutova, E. S. Polymorphism of Glycine. Thermodynamic Aspects. Part I. Relative stability of the polymorphs. *J. Therm. Anal. Calorim.* **2003**, *73*, 409-418. (b) Boldyreva, E. V.; Drebushchak, V. A.; Drebushchak, T. N.; Paukov, I. E.; Kovalevskava, Y. A.; Shutova, E. S. Polymorphism of Glycine. Thermodynamic Aspects. Part II. Polymorphic transitions. *J. Therm. Anal. Calorim.* **2003**, *73*, 419-428. (c) Chongprasert, S.; Knopp, S. A.; Nail, S. L. *J. Pharm. Sci.* **2001**, *90*, 1720-1728.
17. Sakurai, S; Aida, S.; Okamoto, S.; Ono, T.; Imaizumi, K.; Nomura S. Preferential Orientation of Lamellar Microdomains Induced by Uniaxial Stretching of Cross-Linked Polystyrene-block-polybutadiene-block-polystyrene Triblock Copolymer. *Macromolecules* **2001**, *34*, 3672-3678.
18. (a) Zalusky, A. S.; Olayo-Valles, R.; Taylor, C. J.; Hillmyer, M. A. Mesoporous Polystyrene Monoliths. *J. Am.Chem. Soc.* **2001**, *123*, 1519-1520. (b) Zalusky, A. S.; Olayo-Valles, R.; Wolf, J.H.; Hillmyer, M. A. Ordered Nanoporous Polymers from Polystrene-Polylactide Block Copolymers. *J. Am. Chem. Soc.* **2002**, *124*, 12761-12773. (c) deGennes, P. G.; Prost, J. *The Physics of Liquid Crystals*; Oxford University Press: New York, 1993.
19. Weissbuch, I.; Lahav, M.; Leiserowitz, L. Toward Stereochemical Control, Monitoring, and Understanding of Crystal Nucleation. *Cryst. Growth Des.* **2003**, *3*, 125-150.
20. Weissbuch, I., Leiserowitz, L.; Lahav, M. Direct assignment of the absolute configuration of molecules from crystal morphology. *Chirality* **2008**, *20*, 736-748.

21. Johnson, B. J. S.; Wolf, J. H.; Zalusky, A. S.; Hillmyer, M. A. Template Syntheses of Polypyrrole Nanowires and CdS Nanoparticles in Porous Polymer Monoliths. *Chem. Mater.* **2004**, *16*, 2909-2917.
22. Takahashi, S.; Miura, H.; Kasai, H.; Okada, S.; Oikawa, H.; Nakanishi, H. Single-Crystal-to-Single-Crystal Transformation of Diolefin Derivatives in Nanocrystals. *J. Am. Chem. Soc.* **2002**, *124*, 10944-10945.
23. Bucar, D.-K.; MacGillivray L. R. Preparation and Reactivity of Nanocrystalline Cocrystals Formed via Sonocrystallization. *J. Am. Chem. Soc.* **2007**, *129*, 32-33.
24. (a) Weissbuch, I.; Leiserowitz, L.; Lahav, M. Stochastic "Mirror Symmetry Breaking" via Self-Assembly Reactivity and Amplification of Chirality: Relevance to Abiotic Conditions. *Top. Curr. Chem*. **2005**, *259*, 123-165. (b) Castro-Puyana, M.; Salgado, A.; Hazen, R. M.; Crego, A. L.; Alegre, M. L. M. The first contribution of capillary electrophoresis to the study of abiotic origins of homochirality: Investigation of the enantioselective adsorption of 3-carboxy adipic acid on minerals. *Electrophoresis* **2008**, *29*, 1548-1555. (c) Hazen, R. M.; Sholl, D. S. Chiral selection on inorganic crystalline surfaces. *Nature Mat.* **2003**, *2*, 367-374. (d) Hazen, R. M.; Filley, T. R.; Goodfriend, G. A. Selective adsorption of l- and d-amino acids on calcite: Implications for biochemical homochirality. *Proc. Nat. Acad. Sci.* **2001**, *98*, 5487-5490.

Chapter 5: Future Work

5-1: The Effects of Size Confinement on Crystallization of Racemic Compounds

The effect of size confinement on the crystallization of racemic and enantiomorph crystals has yet to be explored. Most racemic crystals are centrosymmetric. The mirror image of a centrosymmetric unit cell can be mapped back onto the original cell. In contrast, single enantiomers prefer chiral crystal structures,[1] which cannot be mapped onto their mirror images. These distinct structural characteristics necessitates that racemates and enantiomorphs exhibit different physical properties, including melting temperature, solubility, and bioavailability.[2] Hence, controlling whether racemic molecules crystallize as racemates or enantiomorphs is greatly important to the pharmaceutical sector.[1] The property differences between chiral and centrosymmetric crystal structures are also evident for polymorphs of achiral molecules such as glycine, where the α-form is centrosymmetric (Space Group: $P2_1/c$) and the β-form is chiral (Space Group: $P2_1$) and each exhibits different stabilities and melting behaviors (See Chapter 3).

No general rule exists for predicting the relative stabilities or physical properties of racemic and enantiomorphic crystals of a compound. For example, a number of compounds crystallize spontaneously as conglomerates – mixtures of enantiomorphs of the chiral compound – even when the source material for the solid is a racemic mixture of chiral molecules. The separation of enantiomers from racemic mixtures is relatively straightforward for conglomerate systems, and a number of methods exist to perform such separations.[1,3] Contrarily, many racemic compounds form true racemates – crystals with both enantiomers in the unit cell. Separation of enantiomers is considerably more difficult for true racemates compared with conglomerates. In order to achieve these separations, the enantiomers from the true racemates are often derivatized in attempts to induce conglomerate crystallizations.[2] Alternative methods of controlling the crystallization of chiral compounds are analogous to those for controlling the polymorphism of achiral compounds.[4] The crystallization of glycine in the presence of chiral auxiliaries induced polymorph selectivity between centrosymmetric and chiral crystal forms.[5] The energy difference between conglomerates and true racemates is on the same order as the difference between traditional polymorphs (~1 kcal/mol).[6,7] This suggests that crystallization of racemic mixtures of chiral molecules under size confinement may generate new protocols for controlling the crystallization of racemates and conglomerates.

The classic description of chiral recognition - the Three Point Interaction model[8] - posits that an enantiomer molecule absorbs to a chiral surface by aligning its chiral center with the surface to minimize their interaction energy. Opposite enantiomers will manifest different interaction energies with a chiral surface (Figure 5-1). Consequentially, one of the two enantiomers will have a more favorable interaction with the surface, resulting in preferential absorption. This concept is applied extensively in chiral catalysis[8] and chromatography,[9] and can be harnessed to rationally design chiral surfaces.[8]

Frostman[10] suggested tailoring a surface with chiral molecules could provide a favorable nucleation site for one enantiomer of a conglomerate over the racemate (Figure 5-2), thereby

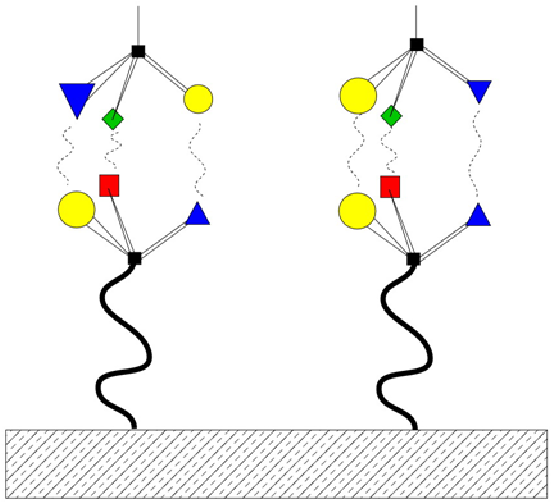

Figure 5-1. Illustration of the Three Point Interaction model for chiral recognition. If two enantiomers (top left, top right; interacting units are depicted by blue triangles, green diamonds, and yellow circles) come into proximity of a chiral surface (bottom; interacting units are depicted as blue triangles, red squares and yellow circles), the two enantiomers can not align their substituents with the same functional units on the surface. Different interaction energies result.

driving the separation of the enantiomers. The Osaka group[11] demonstrated that enantiomers of leucine selectively absorb to self-assembled monolayers of a leucine derivative with the same handedness. They noted from the crystal structures of racemic and enantiomorphic leucine that the crystals are composed of layers of single enantiomers (with alternating enantiomeric layers for the racemate), and the orientation of the enantiomers are different in the enantiomorphs and racemate. This difference, which owed to the orientation of the hydrophobic side chain of leucine, induced preference for the growth of one enantiomorph on the surface. The Osaka report clearly revealed that a chiral surface exhibits enantiomorphic selectivity. Notably, the results of this report indicate that crystallization in a nanoporous matrix with chiral pore walls – where the surface effects are greatly enhances – may result in enantiomorphic selectivity for achiral

molecules crystallizing in chiral space groups *or* conglomerate selectivity for racemic molecules that typically grow as racemates.

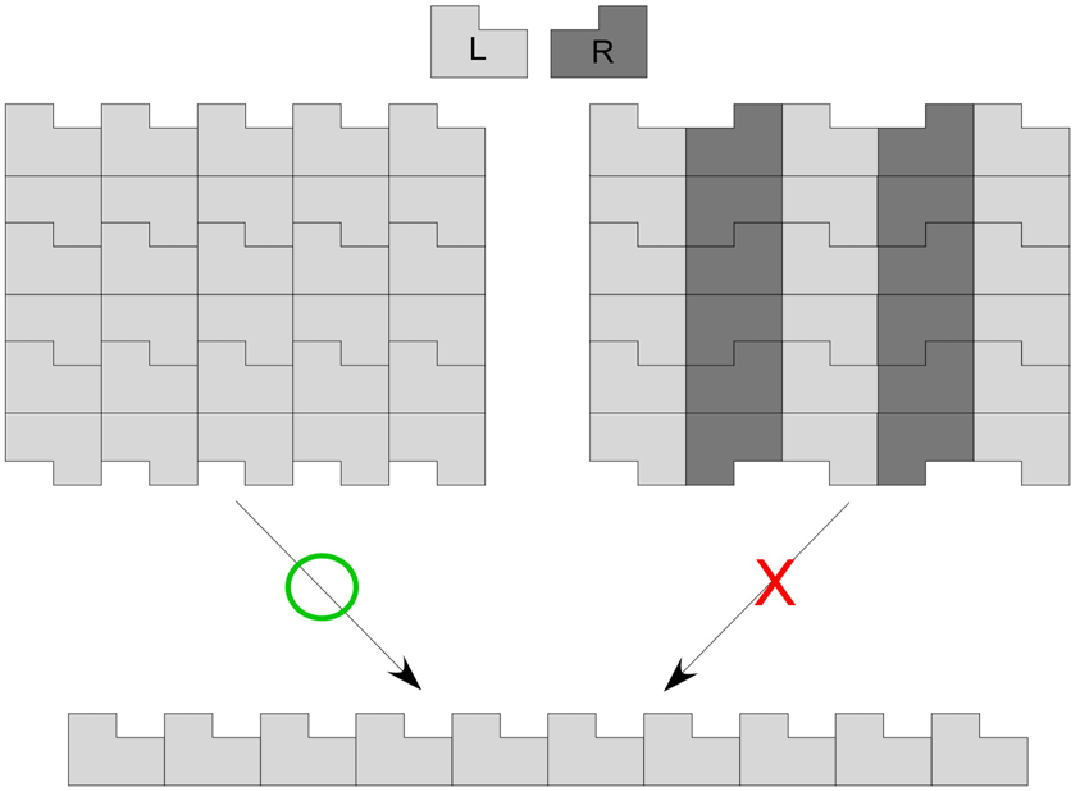

Figure 5-2. Illustration of the effect of a homochiral surface on the heterogeneous nucleation of crystals of a racemic compound. The surface is more compatible with one of the two conglomerates than with the racemate crystal, thus promoting the nucleation and formation of conglomerate crystals over the racemate. Adapted from Reference 10.

Possible routes for the preparation of porous materials with chiral pore wall functionality include (a) silanization of CPG[12] with a chiral silane (b) hydrolysis of p-PS-PDMA to p-PS-PAA (PAA = poly acrylic acid) followed by the EDAC (*N*-ethyl-*N*′-(3-dimethylaminopropyl)-carbodiimide) mediated coupling of a chiral amine to the PAA,[13] or (c) preparation of a new triblock copolymer, similar to PS-PDMA-PLA, that would replace the PDMA component with a chiral polymer. Route (c) holds significant promise, owing to the uniform pore size, pore

alignment, and inclusion of the chiral functionality during the triblock synthesis. Furthermore, a monolith with chiral pore walls could facilitate exploration in areas other than crystallization – such as membrane-based chiral separations or catalysis.

5-1.1: Preparation of Hydrophilic Polymer Monoliths With Chiral Pore Walls

Studies of the effects of *tailor made* auxiliaries on bulk crystallizations revealed that hydrogen bonds between the auxiliary and crystal surface serve as the linkage that promotes enantioselectivity. Fortuitously, a number of candidates for a replacement to PDMA exhibit hydrogen bonds. Our earlier experience with amino acids – of which glycine is the only achiral example – immediately implicated them as possible candidates for pore wall moieties. Notably, the second-simplest amino acid, alanine, is chiral, soluble in water (~18g/100 ml water)[i], and inexpensive. Furthermore, alanine has two hydrogen bonding groups - the amine and carboxyl units of the amino acid – that permit the reaction of one to achieve integration into a monomer while permitting the other to serve as a linkage to promote crystal-pore wall interactions.

The acrylamide derivative of L-alanine, *N*-acryloyl-L-alanine (NALA), was synthesized according to a previously reported procedure (Figure 5-3A).[14] An aqueous solution of L-alanine (10g in 100 ml H_2O) was cooled to ~2 ºC in an ice bath. Sodium hydroxide solution (25g) in water (75 ml) was added dropwise, which prevented the bath from warming. Acryloyl chloride (10 ml) was added dropwise and the solution was stirred for two hours, during which time the ice bath was permitted to warm to room temperature. After reaction, 12M HCl solution (100 ml) was added dropwise to acidify the solution, resulting in the precipitation of a white solid. The mixture was stirred for one hour at room temperature and subsequently extracted three times with ethyl

i. After glycine and alanine, the solubility of amino acids in water decreases rapidly. Their solubility in methanol is generally one fifth of that of water.

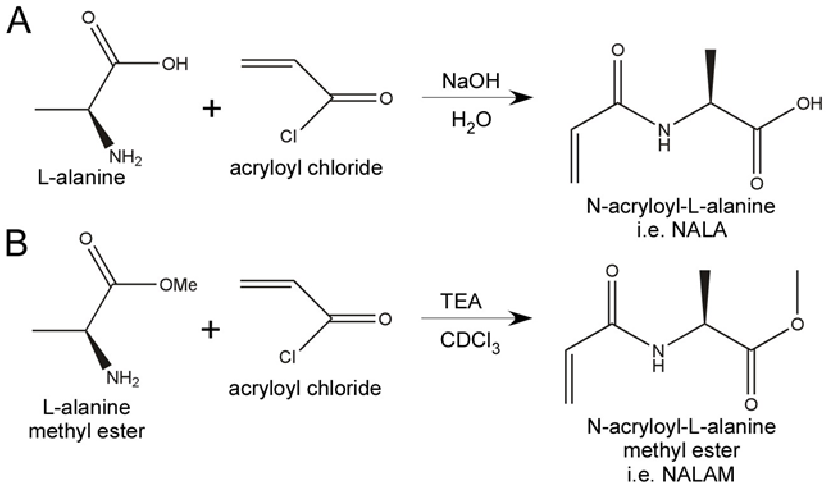

Figure 5-3. (A) Scheme depicting the synthesis of *N*-acryloyl-L-alanine, i.e. NALA. (B) Scheme depicting the synthesis of N-acryloyl-L-alanine methyl ester, i.e. NALAM.

acetate. The organic phases were collected and dried over magnesium sulfate. The solvent was removed under reduced pressure to afford the white powder product, *N*-acryloyl-L-alanine (5.8 g, 36% yield). ^{1}H NMR of the product revealed chemical shifts consistent with those reported in the literature (Figure 5-4).[14,15]

NALA (0.25 g) was homopolymerized in dimethyl formamide (DMF, 1ml) using Azoisobisbutyronitrile (AIBN, 2.5 mg) as an initiator and S-1-Dodecyl-S'-(α,α'-dimethyl-α''-acetic acid)trithiocarbonate[16] as a chain transfer agent (CTA, 11 mg). The concentration of NALA was approximately 1.7 M. After 60 minutes at 60 ºC, an ^{1}H NMR (in DMSO) was collected for the crude reaction mixture. Comparison of the integrated intensities for the monomer and polymer resonances suggested a conversion of 50%, corresponding to an M_n ~ 4 kg/mol for poly(*N*-acryloyl-L-alanine) (PALA). Attempts to redissolve the polymer in methylene chloride, chloroform, and THF failed, precluding analysis of the polymer by $CHCl_3$- or THF-eluent SEC. The polymer was precipitated in 50/50 ethyl acetate/pentane twice to remove unreacted monomer and solvent.

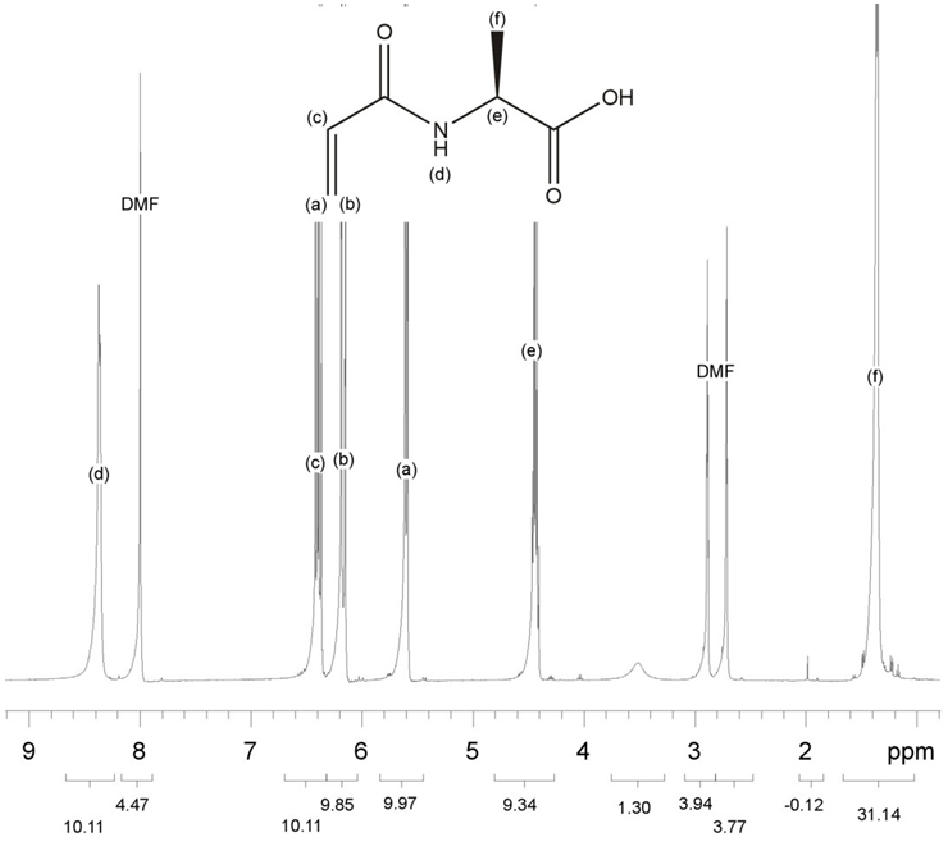

Figure 5-4. ^{1}H NMR spectra of *N*-acryloyl-L-alanine (NALA) in DMF solvent.

After successful synthesis of PALA homopolymer, NALA (1 g), PLA-CTA (1.5g), and AIBN (10 mg) were mixed in DMF (2 mL) and degassed with three freeze-pump-thaw cycles. The combination was stirred at 60 ºC for 2 hours, thereafter, the crude reaction mixture was sampled and interrogated by ^{1}H NMR (in deuterated DMSO). The spectrum revealed no resonances consistent with PALA, indicating that PALA was not added to the PLA-CTA macroinitiator. Spectra collected in deuterated DMSO, $CDCl_3$, and D_2O indicated the same result. The reaction product was precipitated in pentane and dried, and subsequent ^{1}H NMR and SEC revealed the product to be exclusively PLA-CTA. Several subsequent studies were performed with temperatures as high as 70 ºC and stir times as long as 24 hours, but analysis of those reactions

also indicated no polymerization of NALA. The cause of these failures was not established conclusively.

A second monomer was prepared by dissolving *N*-methyl-L-alanine (2g) into 100 mL of water.[17] Notably, the solubility of *N*-methyl-L-alanine was substantially less than that of L-alanine. The solution was cooled in an ice bath. Sodium Hydroxide solution (10 g in 25 mL H_2O) was added dropwise, followed by dropwise addition of acryloyl chloride (2 mL). The solution was stirred for 2 hours, and the bath was allowed to warm to room temperature. The reaction mixture was acidified with 12 N HCl (100 mL) and extracted three times with ethyl acetate, after which the organic phases were collected, dried over magnesium sulfate, and concentrated under reduced pressure. The product was a small quantity brown crystals (<10 mg), which could not be sequestered for subsequent analysis. Prior reports of the synthesis of *N*-acryloyl-*N*-methyl-L-alanine indicated yields of 40%. Additional syntheses of this monomer were performed following the reported procedure exactly, but yields in excess of a trace amount of brown crystals were not obtained.

Attempts to prepare a third monomer, *N*-acryloyl-L-alanine methyl ester (NALAM), in water with acryloyl chloride and NaOH (as per the synthesis of NALA, above) resulted in hydrolysis of the ester, producing >99% NALA according to ^{1}H NMR spectra. The sequestered NALA was esterified to NALAM by adding trimethylsilyldiazomethane dropwise to a THF/methanol solution of the monomer.[14] The resulting NALAM compound, however, required purification by column chromatography, which increased the appeal of pursuing other direct synthesis methods. One such method was the synthesis of NALAM in water from L-alanine methyl ester hydrochloride and acryloyl chloride, with sodium bicarbonate as replacement for sodium hydroxide.[15] This followed the same procedure as the synthesis of NALA, but the result was a very low yield (~0.25% by mass) of an oil residue, despite the original report[15] indicating yields

of 90%. The yields obtained in our laboratory were too low for the polymerization NALAM on a scale necessary for monolith preparation.

The synthesis of NALAM was also performed by dissolving L-alanine methyl ester hydrochloride (25 g) in chloroform (200 mL), chilling the solution in an ice bath, then adding triethyl amine (25 mL) and acryloyl chloride (14.5 mL) dropwise over two hours (Figure 5-3B). The solution was stirred for another two hours, and allowed to return to room temperature. Subsequently, the solution was washed once with water, twice with 5% HCl solution, and once with brine. The organic phases were collected and dried over magnesium sulfate. The solvent was removed under reduced pressure, which produced a clear oil (11g; ~32% yield). ^{1}H NMR revealed chemical shifts consistent with those reported in the literature (Figure 5-5).[15] The hydrolyzed byproduct, *N*-methyl-L-alanine, was present (~15% mole), but the NALAM was used with this impurity. The product oil was stored in the refrigerator at ~0 ºC to prevent polymerization, and did not auto polymerize after two weeks at this temperature.

NALAM (0.5 mL) was mixed with AIBN (5 mg) in DMF (0.5 mL). The mixture was sealed in an airtight reaction vessel and evacuated by three freeze-pump-thaw cycles. The mixture was heated to 60 ºC and stirred. At 30 minutes and 45 minutes, aliquots were removed. A small portion of each aliquot was placed directly into an NMR tube and diluted with $CDCl_3$. The chemical shifts at δ = 5.55, 6.15, and 6.2, each of which corresponded to one of the alkene protons on the monomer, were still present, and the integrated intensities of the NMR peaks were normalized so each of these shifts was approximately one. Several broad peaks had appeared near $\delta \sim 2$, which suggests the formation of the alkyl backbone of the polymer chain. The chemical shifts of the monomer peak at δ = 3.75, corresponding to the methyl ester protons, had broadened.

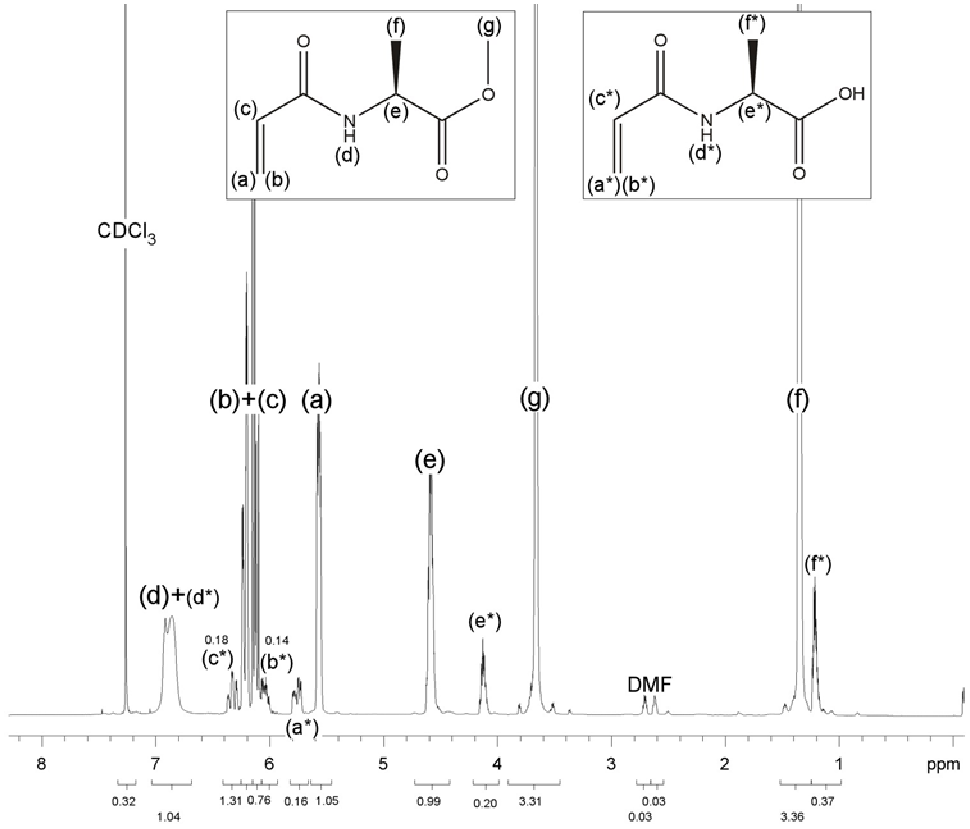

Figure 5-5. 1H NMR of *N*-methyl-L-alanine methyl ester (protons denoted as letters in parentheses) synthesized according to the above procedure. Spectrum collected in $CDCl_3$ solvent. A side product of approximately 15% (mole) *N*-methyl-L-alanine (protons denoted by letters in parentheses with *) remains after extracting and drying the product, which is a viscous oil.

Examination of the shapes of these peaks revealed clear, sharp singlets superimposed on a second, broad peak. The former were due to unreacted monomer, but the latter were due to those substituents in the polymer. Subtracting the intensity of the normalized peaks of the monomers revealed a conversion of approximately 50% after 30 minutes and 66% after 45 minutes.

The synthesis of PLA-PNALAM diblock copolymer followed the scheme of Rzayev and Hillmyer,[13] where PLA-CTA (0.5 g, Figure 5-6) was dissolved in DMF (0.5 mL), and NALAM monomer (1 mL) was added with AIBN (5 mg). The solution was sealed, degassed by three freeze-pump-thaw cycles, and stirred at 60 ºC for 45 minutes. The monomer was diluted with

CH_2Cl_2 and precipitated in pentane, producing a yellow-white powder. After drying in a vacuum oven at 45 ºC overnight, the powder was analyzed by 1H NMR and SEC. The NMR spectra revealed the presence of trace amounts of NALAM, but substantial amounts of PNALAM and PLA. The tertiary proton of the PNALAM units was not visible via the NMR, but the methyl ester proton resonances indicated that PNALAM repeat units were present in a 22:200 molar ratio to the PLA units. This corresponded to molecular weights of approximately $M_{n,PLA}$ = 14 g/mol and $M_{n,PNALAM}$ = 5 kg/mol. SEC revealed a monomodal peak with Mn = 10 kg/mol, PDI = 1.19 (Figure 5-7). The molecular weight of this diblock determined from SEC was surprisingly less than that of the PLA-TC (14.7 kg/mol, see Appendix B), possibly due to an unfavorable interaction between PNALAM and chloroform reducing the effective size of the diblock copolymer. The presence of a monomodal peak and the PNALAM resonances in the proton NMR, however, indicate that a PLA-PNALAM diblock copolymer formed (Figure 5-6).

Addition of third block was performed by dissolving PLA-PNALAM in styrene, degassing the solution with three freeze-pump-thaw cycles and cooking the sample for 4.5 hours at 120 ºC (Figure 5-6). Between 4 - 4.5 hours, the solution became very viscous, precluding facile stirring of the solution. After 4.5 hours, the solution was diluted with CH_2Cl_2 and precipitated into pentane, affording a white powder. This powder was dried in a vacuum oven at 45 ºC overnight. NMR revealed the addition of polystyrene to the diblock copolymer (Figure 5-8), with $M_{n,PS}$ = 53 kg/mol, SEC analysis revealed a monomodal peak with $M_{n,Total}$ = 79 kg/mol and PDI = 1.47 (Figure 5-7). The final triblock, PLA-PNALAM-PS, possessed component degree of polymerizations – N_{PLA}:N_{PNALAM}:N_{PS} – of 200:22:515, corresponding to molecular weights of 14k:5k:53k g/mol.

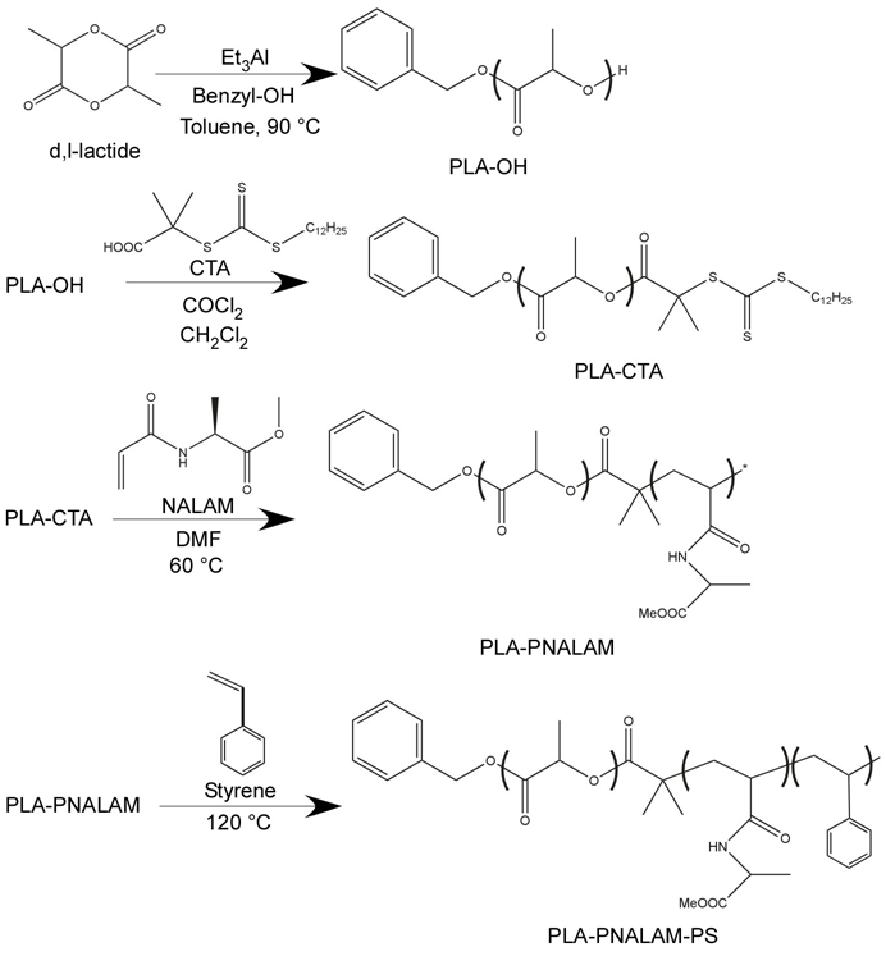

Figure 5-6. Synthesis scheme for PLA-PNALAM-PS triblock copolymers.

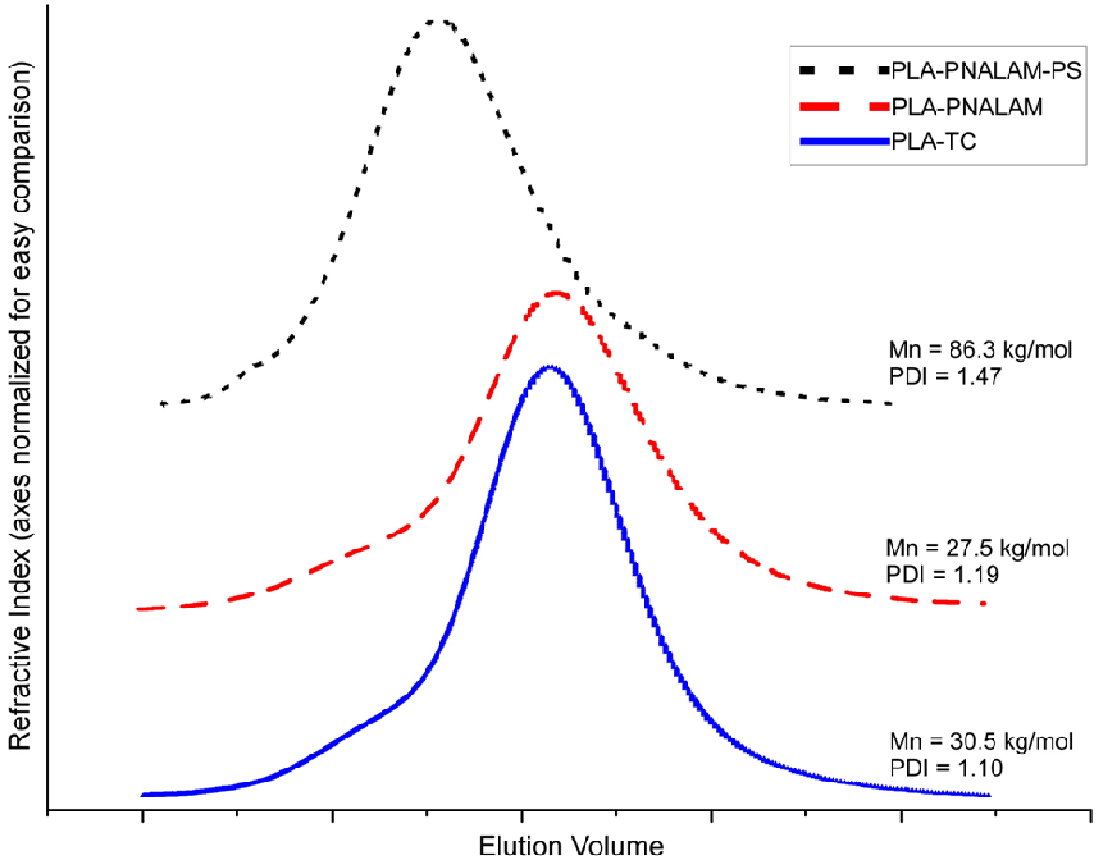

Figure 5.7. Size Exclusion Chromatography traces of PLA-PNALAM-PS (top, black, small dashes) triblock terpolymer as it is being synthesized from (middle, red, long dashes) PLA-PNALAM diblock copolymer. (bottom, blue, solid line) SEC trace of PLA-TC macroinitiator used to prepare PLA-PNALAM and PLA-PNALAM-PS. Notably, the addition of the PNALAM block to the PLA-TC compound caused peak broadening and a slight decrease in Mn compared to PLA-TC. In contrast 1H NMR data suggested that ~5 kg/mol of PNALAM was added to PLA. The broadening at this step was significant considering the small amount of PNALAM added, and this should be addressed in any subsequent studies on this synthesis. The addition of the PS block to PLA-PNALAM resulted in peak broadening and an increase in Mn, which was corroborated by ^{1}H NMR spectra. Again the substantial broadening upon addition of the PS block was unexpectedly large. Anecdotally, this broadening was greater than any peak broadening observed by this author when adding PS to PLA-PDMA to produce PLA-PDMA-PS.

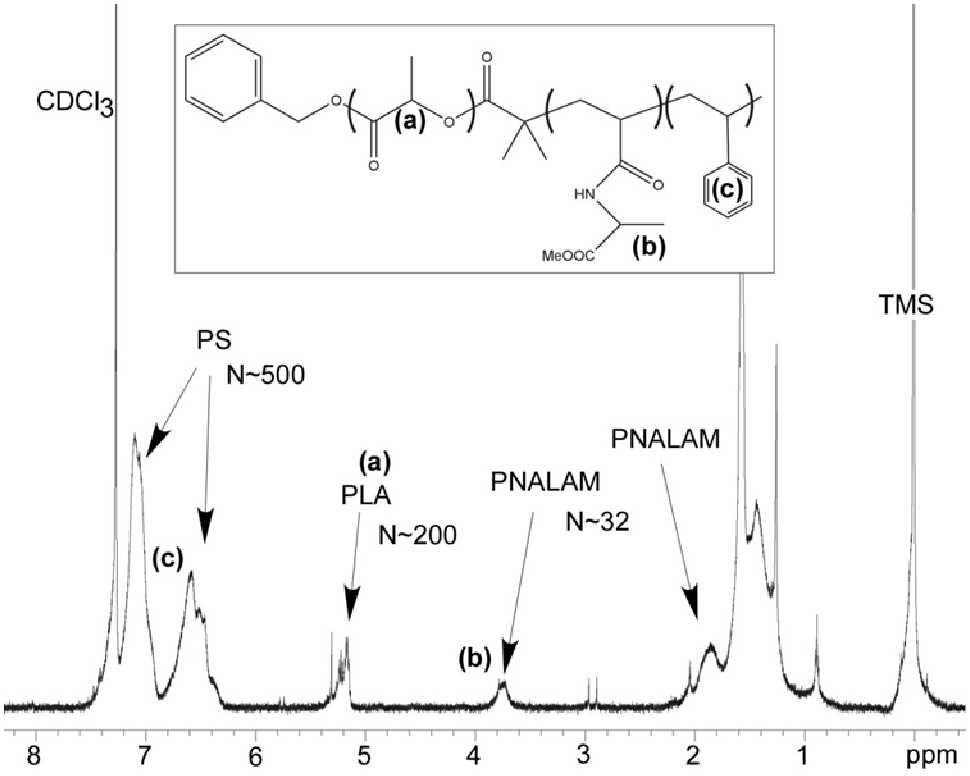

Figure 5-8. 1H NMR (in $CDCl_3$) of PLA-PNALAM-PS triblock terpolymer. The identity of the resonances was determined by comparison with the resonances for each individual homopolymer in the same solvent. This NMR exhibits small traces of pentane (δ ~ 0.9) and DMF (δ ~ 2.9), which remain after the reaction and precipitation procedure.

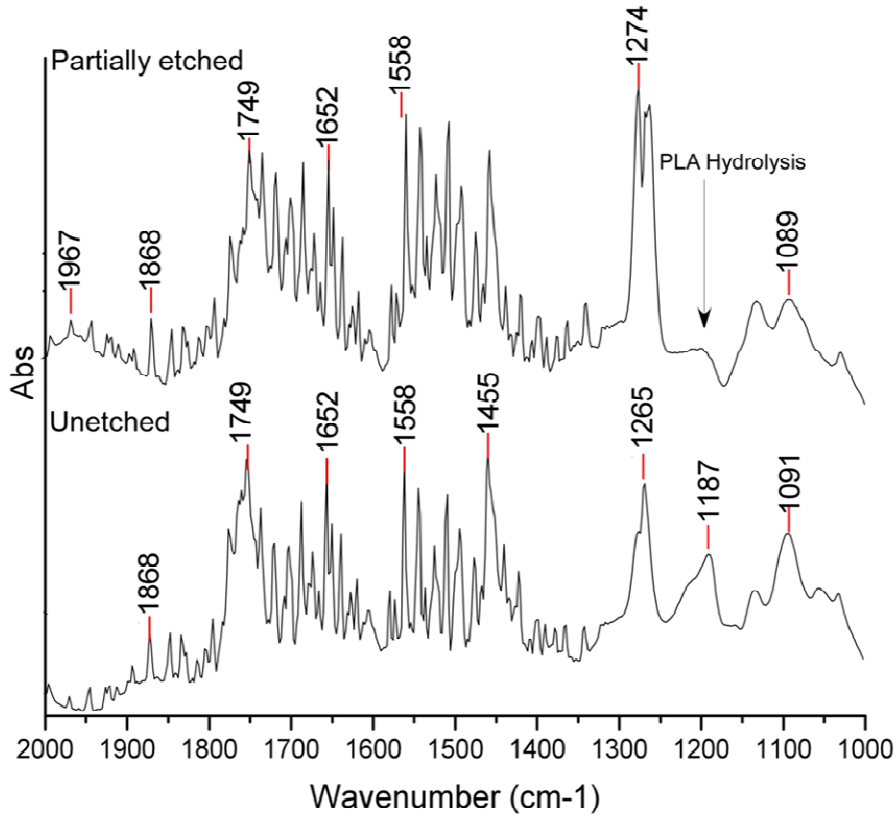

Figure 5.9. IR Spectra collected for (bottom) PLA-PNALAM-PS and (top) aligned, partially etched PLA-PNALAM-PS. The etching was performed in 60 ℃ 0.5 M NaOH in 50/50 MeOH/H2O solution for 7 days, and 1H NMR revealed that this resulted in 60% removal of the PLA but insignificant hydrolysis of the methyl ester of PNALAM (which was desired to form PNALA). The primary differences between the IR spectra collected for the unetched and partially etched triblocks was in the C-O resonance region between 1000-1200 cm^{-1}). This region showed a notable decrease in absorbance for partially etched samples compared with unetched samples, and is expected to be the area where hydrolysis of PLA and the methyl ester of PNALAM would be most visible. When etching PLA from aligned PLA-PDMA-PS, >99% removal of PLA is achieved after 5-7 days. The etching of the PLA with these new triblocks were not as successful, which could be due to poor alignment of the monoliths (F_2 measured between 0.70-0.80 from SAXS, but PLA-PDMA-PS monoliths with these F_2 values still etched completely) or hydrophobic interactions between the PNALAM and the hydrolysis solution. Recommendations for etching in the future include adding SDS to the hydrolysis solution to improve penetration of the hydrolysis solution into the pores, and possibly increasing the NaOH concentration in the solution to cause faster hydrolysis.

5-1.2: Future Work with PLA-PNALAM-PS

The results in the previous section are promising for the development of a porous polymer monolith with chiral pore walls. Those results are only preliminary, however, and additional details such as robust NALAM, PNALAM, and PLA-PNALAM purification techniques need to be pursued. The pressing and etching conditions of the monoliths must also be explored. Initial presses of the triblock terpolymer described above have produced continuous, transparent monoliths which exhibited F_2 values of 0.70-0.80 when their alignment was interogated by SAXS.

After a robust procedure for monolith fabrication has been developed, several opportunities exist for studying confined crystallization in the pores. The crystallization of glycine in the presence of chiral auxiliaries resulted in polymorph and enantiomorph selectivity. Presumably, the enantiomorphic selectivity observed for bulk β-glycine grown in the presence of chiral auxiliaries[5] occurred for the glycine nanocrystals grown with similar auxiliaries in the pores of p-PS-PDMA monoliths. This was not interrogated as part of the studies discussed in Chapter 4, however. This effect could be explored, however, as could the effect of chiral pore walls on the enantioselectivity of β-glycine embedded in p-PS-PNALAM monoliths. The results of such studies could contribute to understanding of the origins of homochirality in the solar system. The crystallization of racemic mixtures of chiral molecules within the monoliths could also produce notable results. Particularly, the crystallization of true racemates within nanoconfinement may produce new polymorphs of racemic crystals or separation of the enantiomorphs into conglomerates. The crystallization of conglomerates might produce new enantiomorphs or true

racemates. The possibility of conglomerate systems or true racemates adopting the same crystal structures in nanoconfinement would also provide insight into crystallization phenomenon.

5-2: Controlling Pore Size and Functionality via Polyelectrolyte Layer-by-Layer Deposition

We initiated studies in controlling the pore size of p-PS-PDMA monoliths by polyelectrolyte Layer-by-Layer (LbL) deposition. This technique, which involves depositing successive layers of oppositely charged polymer electrolytes onto a surface, has been employed to produce fine control over thin film thickness. A wealth of literature exists on this topic.[18] A recent study explored the application of LbL in nanopores,[19] but those works were for nucleopore membranes with low porosity compared with our monoliths and much larger pores (50-850 nm). Our work in this area was limited, owing to interests in other studies that precluded us from pursuing this further. The facile hydrolysis of PDMA to polyacrylic acid, the latter of which is a weak polyelectrolyte widely studied in LbL, suggests that the polymer monoliths developed by Rzayev and Hillmyer may permit LbL within the pores. Most LbL is performed with large polymers that have lengths (~50 nm) much larger than our pore size range (~10 nm). The LbL deposition of low molecular weight polymers, however, could provide a unique way of tailoring membranes based on our monoliths to specific size-related and functionality-related applications.

5-3: Dependence of the δ-Breadth of Diffraction Peaks on Pore Size

In Chapter 4, we discussed the preferred orientation behavior of nanocrystals embedded within porous polymer monoliths. One of the key results extracted from the orientation studies was that the azimuthal breadth (δ-breadth) of the Bragg reflections in the 2D X-ray diffraction patterns indicated a distribution of orientations about a preferred mean orientation. The orientation

distribution, we argued, is a consequence of crystals in or near the preferred alignment being able to grow in excess of their critical sizes. In contrast, crystals far outside of the alignment grow into the pore walls, where they possibly have their sizes limited such that they are unstable. These unstable crystals then vanish because either an amorphous phase is preferred or because they nanocrystals undergo Ostwald Ripening within the pores. These posits have an interesting consequence; namely, if the stabilities of the crystals are limited by the lengths they achieve before growing into the pore walls, then it is reasonable to expect that nanocrystals in wider pores would exhibit a broader distribution of orientations compared with those embedded in small pores. Within large pores, crystals can have a greater deviation from the preferred orientation and still achieve the minimum length necessary for stability (Figure 5-10).

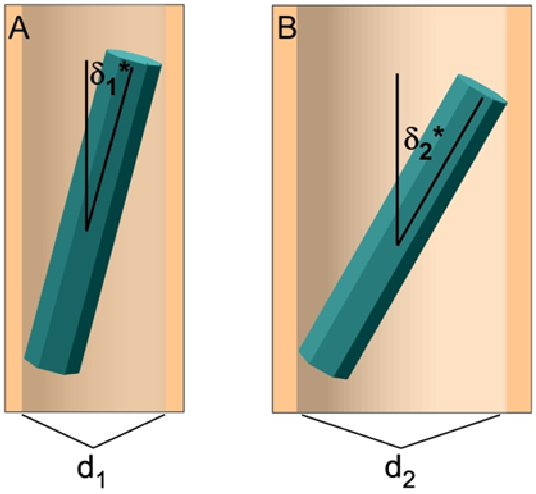

Figure 5-10. Illustration of a crystal that has grown into the pore walls in cylindrical pores of different diameters. (A) Within pores of diameters d_1, a crystal that grows with angle δ_1* relative to the pore direction has its growth limited by the walls. (B) A crystal in larger pores ($d_2 > d_1$) can adopt a larger angle δ_2* with the pore walls and still grow to the same length as the crystal in the smaller pores. If the length of these crystals represents the minimum length required for the crystal to remain stable, δ_1* and δ_2* would manifest as the limits of the azimuthal breadth of Bragg reflections collected for polymer monoliths loaded with crystals of varying orientations. Consequentially, well aligned monoliths with large pores should produce crystals exhibiting broader distribution of orientations compared with monoliths with small pores.

The degree of alignment of the polymer monoliths was a limiting factor in our orientation studies. Poorly aligned monoliths precluded determination of crystal alignment, and all monoliths obtained had varying degrees of disorder. As a result, the δ-breadths measured from the XRD data were a convolution of the distribution of crystal orientations with the pore orientations. This complexity prevents the absolute determination of the δ-spread owing solely to the crystals, however, monoliths with good alignment ($F_2 \sim 0.95$) should permit qualitative determination of whether the above hypothesis is true.

Attempts to determine the effect of pore size on δ-breadth for glycine crystals embedded within p-PS-PDMA were precluded because monoliths with large (>30 nm) and small (10 nm) pore sizes and high degrees of order were not prepared successfully (Appendix B). Examination of the δ-breath for diffraction data of several samples of α-C9 (azelaic acid), α-C11 (undecanoic acid) and α-C13 (brassaylic acid) embedded in 30 nm and 40 nm p-PCHE revealed a wide range of orientation distributions (Tabe 5-1).[ii] The δ-breadths were averaged for each compound in each pore size, however, the errors (corresponding to one standard deviation of the δ-breadth measurements) for each average overlapped. As a result, the δ-breadths of crystals in 30 nm and 40 nm pores could not be statistically discriminated. No clear size dependence on δ-breadth was observed. Attempts to corroborate the δ-breadth measurements with the F_2 values of the monolith employed for each sample was unsuccessful, because the F_2 values were not calculated for each individual piece of the monolith. These crystallization studies were performed without regard for the F_2 value of individual monolith pieces, an oversight that was addressed for the analysis of

ii. This author thanks Dr. Jeong-Myeong Ha for determining the azimuthal breadths of these samples upon request. The δ-breadths for C5 (malonic) and C7 (pimelic) acid were not examined because their polymorphic behavior precluded δ-breadth measurements for one polymorph in a range of pore sizes. Contrarily, the preferred orientation of glycine was only examined in one pore size of p-PS-PDMA monoliths, thus the effect of size on δ-breadth could not be examined for those.

Table 5-1. Azimuthal breadths of the (002) Bragg reflections for the C9, C11, and C13 dicarboxylic acids in 30 nm and 40 nm p-PCHE.

Crystal and Peak	Pore Size	δ-breadth[a] (deg.)	Avg. (deg.)	Std. Dev.
α-C9; (002)	30 nm	25, 29, 30, 46, 47, 42, 49, 41, 42, 35	36	8
	40 nm	25, 23, 27, 25, 18, 24, 26, 33, 35, 33	27	5
α-C11; (002)	30 nm	28, 25, 31, 28, 29, 44, 46	33	9
	40 nm	50, 51, 39, 31, 46, 45, 44, 39, 39, 39	42	6
α-C13; (002)	30 nm	50, 42, 40	44	5
	40 nm	35, 33, 32	33	1

[a]The δ-breadths provided are symmetric about the detector horizon (see Chapter 4 for details) and correspond to 2δ* (Figure 5-10).

glycine orientation within p-PS-PDMA. Without the F_2 values, it is impossible to ascertain whether the variations in δ-breadths could be due to variations in monoliths alignment or on the crystals themselves. Therefore, the effect of pore size on orientation distribution cannot be determined from these data, and additional experiments with monoliths of known, high F_2 values are recommended.

We note in conclusion that monoliths of substantially different pore sizes should be employed for any subsequent orientation studies. Based upon simple geometric considerations, such as those illustrated in Figure 5-10, one can estimate the relationship between the pore diameters d_1 and d_2 and the angles δ_1* and δ_2* values for a crystal of fixed "critical length" (Equation 5.1).

$$\frac{d_1}{\sin \delta_1^*} = \frac{d_2}{\sin \delta_2^*} \qquad 5.1$$

The ratio between δ_1* and δ_2* for d_1 = 30 nm and d_2 = 40 nm varies from .75 for δ_2* = 10° to .73 for δ_2* = 30°. In contrast, if d_1 = 20 nm and d_2 = 40 nm the ratios are closer to 0.50, which should permit clear interpretation of the δ-breadths measured from the diffraction data.

5-4: Predicting Crystal Structures of Newly Discovered Polymorphs

Glycine crystallization in p-PS-PDMA and CPG (Chapter 3) revealed that the highly metastable β form grew preferentially in small pores, and exhibited slow transitions to α-glycine in 55 nm pores. The formation of β-glycine for the smallest crystals and subsequent conversion to α for increasing large crystals suggested that glycine crystals nucleating from bulk solutions likely adopt β first and then transform to stable α-nuclei. The ready conversion of β- to α-glycine for bulk crystals may be due in part to the similar stacked plane molecular architectures of the crystals (Chapter 1). Notably, Ostwald's Rule of Stages suggests that kinetically preferred polymorph transitions occur between forms with the lowest activation, that is, forms that exhibit similar structural features.

The influence of size confinement on crystallization has resulted in the observation of previously unreported polymorphs embedded within nanoporous matrices, such as β-coumarin and δ-pimelic acid (see Chapter 2).[20,21] These forms are typically identified by the positions of their Bragg reflections on X-ray powder diffraction patterns, however unlike the example of glycine, their crystal structures can not be determined by crystallography because suitable bulk crystals can not be obtained. As the pore size of the nanoporous matrices increases, these forms give way to the polymorph preferred in the bulk. We posit that the unidentified polymorphs exhibit crystal packing that has some structural similarity to the corresponding bulk polymorphs, and that this can be used to assist in the prediction of the unknown crystal structures. The predicted structures could then be used to simulate powder diffraction patterns (a straightforward procedure) to determine which structure corresponds to the experimental pattern.

A number of techniques exist that permit structure prediction. Most examples are ab initio methods, such as Monte Carlo methods, that rely on intense calculations.[22,23,24] These calculations

frequently neglect polarization effects in molecules, and are ineffective for molecules such as salts and zwitterions, and solvates. Furthermore, different structures predicted by ab initio methods frequently have very similar lattice energies, precluding the prediction of experimentally observed polymorphs. These methods can also result in a large number of hypothetical structures. Thus, ab initio methods may not be the best route for modeling polymorphs. A practical approach to predicting crystal structures, called crystal engineering, exploits synthons composed of molecules linked by specific interactions as supramolecular building blocks for generating crystal structures.[25] In contrast to the ab initio methods, which predict precise molecular packing, crystal engineering predicts network properties, such as the self-assembly of synthons, for families of related materials.[26] While novel and powerful for predicting these properties, this method is also not suited for polymorph prediction.

A hybrid of these two approaches has been developed by Gervais and Coquerel.[27] Known as the "Derived Crystal Packing" model (DCP), this method of structure prediction consists of two primary steps. First, the mother phase - which would correspond to the known bulk polymorph - is analyzed to extract a number of one- or two-dimensional periodic fragments (Figure 5-11; e.g. a planar structure such as that observed in α-glycine, or a chain of hydrogen bonded molecules such as that observed in α- and β-pimelic acid.). These fragments need not necessarily correspond to a single molecule or unit cell, and are generally chosen to include strong hydrogen bonding directions or pi-pi interactions within the fragment. Second, these fragments are rationally organized into new crystal structures by adding symmetry operators in the additional dimensions (two for a 1D fragment, one for a 2D fragment). The resulting new crystal structures, known as daughter phases, are assembled to comprise one of the 230 space groups. These structures then have their energies minimized computationally and their stabilities compared with the mother phase.

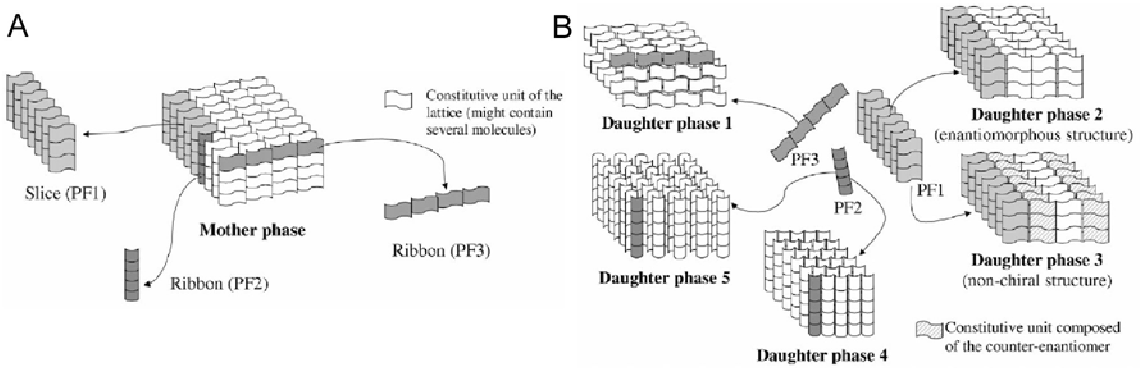

Figure 5-11. Illustration of the DCP process. (A) the crystal structure of the mother phase is analyzed, and periodic fragments - denoted PFs - are extracted to be used as building blocks for the daughter phases (B). Adapted from Ref. 27, with permission. Copyright 2002 IUoC.

The utility of DCP is that it builds upon the structural features of a known polymorph to predict the structure of a related but unknown polymorph. The predictions themselves remain a trial-and-error process, but the rational design of potential polymorph structures from the mother phase fragments may reduce the number of simulations required to determine the structure of the unknown polymorph. DCP may provide a new protocol for polymorph identification, as well as new insights into the structure-property relationships of crystals embedded within nanoporous matrices. The Polymorph Predictor™ in Accelrys' Materials Design Studio™ simulates polymorphs in a method similar to DCP, and may afford a route to determining the unknown crystal structures.

5-5: Exploring the Kauzmann Paradox in CPG

As a supercooled liquid approaches its glass transition temperature, the entropy of the liquid rapidly decreases. Kauzmann[28] noted that if the glass transition was suppressed far enough, the entropy of the liquid would eventually reach and drop below the entropy of the crystalline phase that should nucleate from the supercooled liquid. The temperature at which this would occur is

called the Kauzmann temperature, typically denoted T_K, and presents a limit for supercooling – a liquid that is supercooled below T_K would violate the third law of thermodynamics. This violation is known as the Kauzmann Paradox. Several good reviews exist discussing the Kauzmann Paradox.[29,30,31,32] The limit suggests that a supercooled material must undergo some form of thermodynamically mandated transition. Kauzmann speculated that the kinetic glass transition prior to T_K prevents equilibration of the supercooled liquid at T_K. Another related view speculates that the supercooled compound undergoes a second order thermodynamic transition to a so-called ideal glass at T_K, but that this thermodynamic transition is masked by the kinetic glass transition at $T_g > T_K$. Direct interrogation of T_K for compounds is prevented due to kinetic glassification, thus, T_K is typically estimated by extrapolation of the entropy of the supercooled compound below the observed T_g.

The apparent dependence of both T_g and T_m on 1/r, discussed in chapter 2, suggests a series of experiments that may provide insight into the Kauzmann Paradox. Classic nucleation theory suggests that compounds confined below a particular size thermodynamically prefer an amorphous phase over a crystalline phase (Chapter 1-7). We are curious whether size confinement at this length scale can offer another method of predicting the Kauzmann temperature. Extrapolating the linear dependences of T_g and T_m on 1/r until they intersect would mark a crystal size, denoted r_x, and corresponding temperature, T_x, for which the crystalline and supercooled amorphous state would have equivalent free energy (Figure 5-12). Crystals smaller than this size would thermodynamically prefer the amorphous state. The question arises whether T_x is equivalent to T_K. If so, these experiments would validate the thermodynamic resolution to the Kauzmann Paradox in a previously unreported manner. The possibility of $T_x = T_K$ would also suggest a physical significance for r_x in the determination of the Kauzmann temperature.

Two compounds that may be useful for these studies are As_2Se_3 and As_2S_3. The bulk glassification and melting behavior of these two compounds is well characterized, and their Kauzmann temperatures have been predicted by the temperature dependence of entropies.[33] The suggested Kauzmann temperatures (min. = 97 °C for As_2S_3) and observed bulk melting temperatures, (max = 382 °C for As_2Se_3) are well within temperature limits of modern DSC instruments and the stability limits of CPG. Both compounds are easy to synthesize according to previous work, and they both express experimentally attainable crystallization and glass transition behavior. Therefore, they would be excellent candidates for DSC studies of T_g and T_m vs. 1/r if they were embedded in CPG.

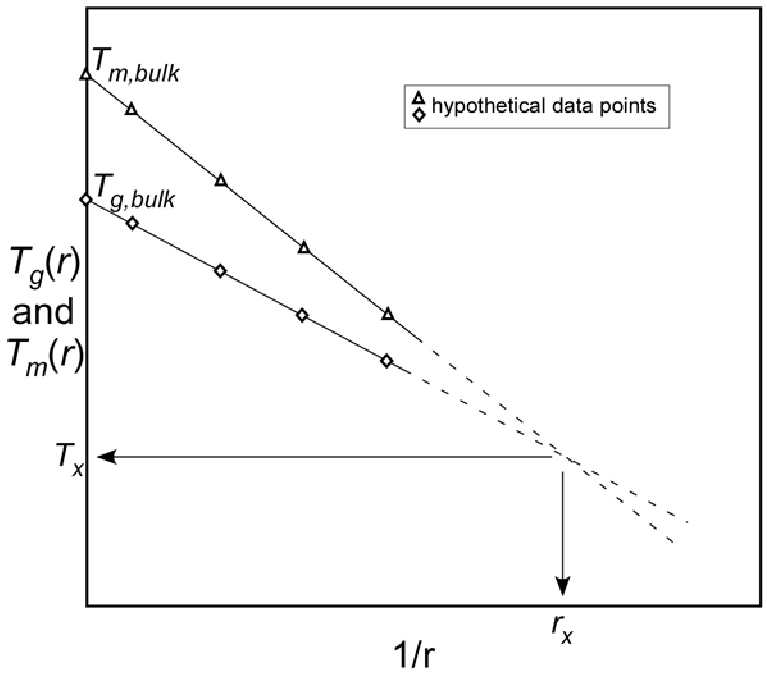

Figure 5-12. Illustration of the determination of T_x and r_x from T_g(r) and T_m(r).

5-6: Concluding Remarks

This thesis has described the evolution of crystallization in nanoconfinement, pursued with the intention of understanding crystal nucleation and growth phenomenon on length scales corresponding to their critical sizes. As part of the original contributions of this thesis, we explored the polymorphism and orientation of glycine under nanoconfinement. Therein we observed polymorph selectivity and stabilization, and demonstrated that manipulating the fast-growth axis of glycine nanocrystals with chiral auxiliaries changed the preferred orientation of the crystals in the pores. We attributed these effects to the delicate balance between surface and volume energies for ultrasmall crystals. In this chapter, we discussed the possibilities of extending our studies to new monoliths, pore wall functionalities, thermotropic properties, and polymorph discovery. Exploration of these areas should provide additional insight into the properties of ultrasmall crystals, and may lead to work in fields such as membrane separations, drug delivery, and polymorph identification.

5-7: References

1. Jaques, J. Collet, A.; Wilen, S. H. *Enantiomers, Racemates, and Resolutions*; John Wiley: New York, 1981.
2. Brittain, H. G. Structural Aspects of Molecular Dissymetry; in *Polymorphism in Pharmaceutical Solids*; Brittain, H.G., Ed.; Marcel Dekker, Inc.: New York, 1999; pp. 363-393.
3. Collet, A.; Brienne, M.-J.; Jacques, J. Optical Resolution by Direct Crystallization of Enantiomer Mixtures. *Chem. Rev.* **1980**, *80*, 215-230.
4. Berfeld, M.; Zbaida, D.; Leiserowitz, L.; Lahav, M. 'Tailor-made' Polymers for the Removal of Lamellar Twinning: Resolution of a-Amino Acids by Entrainment. *Adv. Mater.* **1999**, *11*, 328-331.
5. Torbeev, V. Yu.; Shavit, E.; Weissbuch, I.; Leiserowitz, L.; Lahav, M. Control of Crystal Polymorphism by Tuning the Structure of Auxiliary Molecules as Nucleation Inhibitors. The β-Polymorph of Glycine Grown in Aqueous Solutions. *Cryst. Growth. Des.* **2005**, *5*, 2190-2196.
6. Bernstein, J. *Polymorphism in Molecular Crystals*; Oxford: New York, 2002.

7. (a) Kitaigorodsky, A. I. *Molecular Crystals and Molecules*; Academic Press: New York, 1973. (b) Yu, L. Inferring Thermodynamic Stability Relationship of Polymorphs from Melting Data. *J. Pharm. Sci.* **1995**, *84*, 966-974.
8. (a) Davankov, V. A. The Nature of Chiral Recognition: Is it a Three-Point Interaction? *Chirality* **1997**, *9*, 99-102. (b) Booth, T. D.; Wahnon, D.; Wainer, I. W. Is Chiral Recognition a Three-Point Process? *Chirality* **1997**, 96-98.
9. Hyun, M. H.; Cho, Y. J. Chiral Separation by HPLC With Pirkle-Type Chiral Stationary Phases in *Chiral Separations, Methods and Protocols;* Gubitz, G.; Schmid, M. G. Eds.; Humana Press, 2004.
10. Frostman Thesis
11. Banno, N.; Nakanishi, T.; Matsunaga, M.; Asahi, T.; Osaka, T. Enantioselective Crystal Growth of Leucine on a Self-Assembled Monolayer with Covalently Attached Leucine Molecules. *J. Am. Chem. Soc.* **2004**, *126*, 428-429.
12. Jackson, C. L.; McKenna, G. B. The melting behavior of organic materials confined in porous solids. *J. Chem. Phys.* **1990**, *93*, 9002-9011.
13. Rzayev, J.; Hillmyer, M. A. Nanochannel Array Plastics with Tailored Surface Chemistry. *J. Am. Chem. Soc.* **2005**, *127*, 13373-13379.
14. Mori, H.; Matsuyama, M. Endo, T. Assembled Structures and Chiroptical Properties of Amphiphilic Block Copolmers Synthesized by RAFT Polymerization of *N*-Acryloyl-L-alanine. *Macromol. Chem. Phys.* **2008**, *209*, 210-2112.
15. Bueno, M. P.; Cativiela, C. A.; Mayoral, J. A.; Avenoza, A. Models for the use of a-amino acids as chiral auxiliaries in asymmetric Diels-Alder reactions. *J. Org. Chem.* **1991**, *56*, 6551-6555.
16. Lai, J. T.; Filla, D.; Shea, R. Functional Polymers from Novel Carboxyl-Terminated Trithiocarbonates as Highly Efficient RAFT Agents. *Macromolecules* **2002**, *35*, 6754-6756.
17. Bueno, M. P.; Cativiela, C. A.; Mayoral, J. A.; Avenoza, A. Models for the use of a-amino acids as chiral auxiliaries in asymmetric Diels-Alder reactions. *J. Org. Chem.* **1991**, *56*, 6551-6555.
18. (a) Zhang, X.; Chen, H.; Zhang, H. Layer-by-layer assembly: from conventional to unconventional methods. *Chem. Comm.* **2007**, *14*, 1395-1405. (b) Lynn, D. M. Peeling Back the Layers: Controlled Erosion and Triggered Disassembly of Multilayered Polyelectrolyte Thin Films. *Adv. Mater.* **2007**, *19*, 4118-4130. (c) Sukhishvili, S. A.; Kharlampieva, E.; Izumrodov, V. Where Polyelectrolyte Multilayers and Polyelectrolyte Complexes Meet. *Macromolecules* **2006**, *39*, 8873-8881.
19. Alem, H.; Blondeau, F.; Glinel, K. Demoustier-Champagne, S.; Jonas, A. M. Layer-by-Layer Assembly of Polyelectrolytes in Nanopores. *Macromolecules* **2007**, *40*, 3366-3372.
20. Ha, J.-M. Crystallization and Thermotropic Properties of Organic Solids in Nanoscopic Reactors. Ph.D. Thesis, University of Minnesota, 2006.

21. Ha, J.-M.; Hamilton, B. D.; Hillmyer, M. A.; Ward, M. D. Phase Behavior and Polymorphism of Organic Crystals Confined within Ultrasmall Chambers. *Manuscript in preparation* **2009**.
22. Gdanitz, R. J. Chapter 6 in *Theoretical Aspects and Computer Moledelling*; Gavezzotti, A., Ed. New York: John Wiley and Sons Ltd., 1997. pp. 185-201.
23. (a) Perlstein, J. Molecular self-assemblies: Monte Carlo predictions for the structure of the one-dimensional translation aggregate. *J. Am. Chem. Soc.* **1992**, *114*, 1955-1963. (b) Perlstein, J. Molecular self-assemblies. 2. A computational method for the prediction of the structure of one-dimensional screw, glide, and inversion molecular aggregates and implications for the packing of molecules in monolayers and crystals. *J. Am. Chem. Soc.* **1994**, *116*, 11420-11432.
24. Gavezzotti, A. Are Crystal Structures Predictable? *Acc. Chem. Res.* **1994**, *27*, 309-314.
25. Desiraju, G. R. Supramolecular Snythons in Crystal Engineering - A New Organic Synthesis. *Angew. Chem. Int. Ed. Engl.* **1995**, *34*, 2311-2327.
26. Moulton, B.; Zaworotko, M. J. From Molecules to Crystal Engineering: Supramolecular Isomerism and Polymorphism in Network Solids. *Chem. Rev.* **2001**, *101*, 1629-1658.
27. Gervais, C.; Coquerel, G. Simple model designed to generate new crystal structures derived from a mother phase; application to molecular compounds. *Acta Cryst.* **2002**, *B58*, 662-672.
28. Kauzmann, W. The Nature of the Glassy State and the Behavior of Liquids at Low Temperatures. *Chem. Rev.* **1948**, *43*, 219-256.
29. Stillinger, F.H. Supercooled liquids, glass transitions, and the Kauzmann paradox. *J. Phys. Chem.* **1988**, *88*, 7818-7825.
30. Debenedetti, P. G.; Stillinger, F. H. Supercooled liquids and the glass transition. *Nature*, **2001**, *410*, 259-267.
31. Speedy, R. J. Kauzmann's paradox and the glass transition. *Biophys. Chem.* **2003**, *105*, 411-420.
32. Stillinger, F. S.; Debenedeetti, P. G. Phase transitions, Kauzmann curves, and inverse melting. *Biophys. Chem.* **2003**, *105*, 211-220.
33. Černošek, Z.; Holubová, J.; Černošková, E. Kauzmann Temperature and the Glass Transition. *J. Optoelec. Adv. Mat.* **2005**, *7*, 2941--2944.

Bibliography

Adamski, T. Commination of crystal nucleation by a precipitation method. *Nature* **1963**, *197*, 894.

Ajayan, P. M.; Iijima, S. Capillarity-induced filling of carbon nanotubes. *Nature* **1993**, *361*, 333–334.

Alba-Simionesco, C. Dosseh, G.; Dumont, E.; Frick, B.; Geil, B.; Morineau, D.; Teboul, V.; Xia, Y. Confinement of molecular liquids: consequences on thermodynamic, static, and dynamical properties of benzene and toluene. *Eur. Phys. J. E* **2003**, *12*, 19-28.

Albrecht, G.; Corey, R. B. The crystal structure of glycine. *J. Am. Chem. Soc.* **1939**, *61*, 1087– 1103.

Alcoutlabi, M.; McKenna, G. B. Effects of confinement on material behavior at the nanometer size scale. *J. Phys.: Condens. Matter* **2005**, *17*, R461-R524.

Alem, H.; Blondeau, F.; Glinel, K. Demoustier-Champagne, S.; Jonas, A. M. Layer-by-Layer Assembly of Polyelectrolytes in Nanopores. *Macromolecules* **2007**, *40*, 3366-3372.

Antoniou, A. A. Phase Transformations of Water in Porous Glass. *J. Phys. Chem.* **1964**, *68*, 2754-2763.

Awschalom, D. D.; Warnock, J. Supercooled liquids and solids in porous glass. *Phys. Rev. B* **1987**, *35*, 6779-6785.

Banno, N.; Nakanishi, T.; Matsunaga, M.; Asahi, T.; Osaka, T. Enantioselective Crystal Growth of Leucine on a Self-Assembled Monolayer with Covalently Attached Leucine Molecules. *J. Am. Chem. Soc.* **2004**, *126*, 428-429.

Beck, J.S.; Vartuli, J. C.; Roth, W. J., Leonowicz, M. E.; Kresge, C. T.; Schmitt, K. D.; Chu, C. T.-W.; Olson, D. H.; Sheppard, E. W.; McCullen, S. B.; Higgins, J. B.; Schlenker, J. L. A new family of mesoporous molecular-sieves prepared with liquid crystal templates. *J. Am. Chem. Soc.* **1992**, *114*, 10834-10843.

Beiner, M.; Rengarajan, G. T.; Pankaj, S.; Enke, D.; Steinhart, M. Manipulating the Crystalline State of Pharmaceuticals by Nanoconfinement. *Nano Lett.* **2007**, *7*, 1381-1385.

Beiner, M.; Rengarajan, G. T.; Pankaj, S.; Enke, D.; Steinhart, M. Manipulating the Crystalline State of Pharmaceuticals by Nanoconfinement. *Nano Lett.* **2007**, *7*, 1381–1385.

Berfeld, M.; Zbaida, D.; Leiserowitz, L.; Lahav, M. 'Tailor-made' Polymers for the Removal of Lamellar Twinning: Resolution of a-Amino Acids by Entrainment. *Adv. Mater.* **1999**, *11*, 328-331.

Berkovitch-Yellin, Z.; Addadi, L.; Idelson, M. Lahav, M.; Leiserowitz, L. Controlled modification of crystal habit by 'tailor made' impurities: application to benzamide. *Angewandt Chemie Supplement* **1982**, 1336-1345.

Bernstein, J. Crystal growth, polymorphism and structure-property relationships in organic crystals. *J. Phys. D.* **1993**, *26*, B66-B76.

Bernstein, J. *Polymorphism in Molecular Crystals*; Clarendon Press: Oxford, 2002.

Bernstein, J.; Davey, R. J.; Henck, J.-O. Concomitant polymorphs. *Angew. Chem. Int. Ed.* **1999**, *38*, 3440-3461.

Bilgram, J. H. Dynamics at the solid-liquid transition. *Phys. Rep.* **153**, 1-89.

Boldyreva, E. V.; Drebushchak, T. N.; Shutova, E. S. *Z. Kristallogr.* **2003**, *218*, 366–376.

Boldyreva, E. V.; Drebushchak, V. A.; Drebushchak, T. N.; Paukov, I. E.; Kovalevskava, Y. A.; Shutova, E. S. Poylmorphism of Glycine. Thermodynamic Aspects. Part I. Relative stability of the polymorphs. *J. Therm. Anal. Calorim.* **2003**, *73*, 409–418.

Boldyreva, E. V.; Drebushchak, V. A.; Drebushchak, T. N.; Paukov, I. E.; Kovalevskava, Y. A.; Shutova, E. S. Polymorphism of Glycine. Thermodynamic Aspects. Part II. Polymorphic Transitions. *J. Therm. Anal. Calorim.* **2003**, *73*, 419–428.

Bonafede, S. J.; Ward, M. D. Selective Nucleation and Growth of an Organic Polymorph by Ledge-Directed Epitaxy on a Molecular Crystal Substrate. *J. Am. Chem. Soc.* **1995**, *117*, 7853-7861.

Boomdevi, S.; Dhanasekaran, R.; Ramasamy, P. Investigations on Nucleation and Growth Kinetics of Urea Crystals from Methanol. *Cryst. Res. Technol.* **2002**, *37*, 159-168.

Booth, T. D.; Wahnon, D.; Wainer, I. W. Is Chiral Recognition a Three-Point Process? *Chirality* **1997**, 96-98.

Borisov, B. F.; Charnaya, E. V.; Hoffmann, W. D.; Michel, D.; Shelyapin, A. V.; Kumzerov, Yu. A. Nuclear magnetic resonanoce and acoustic investigations of the melting-freezing phase transition of gallium in a porous glass. *J. Phys.: Condens. Matter* **1997**, *9*, 3377-3386.

Bouchard, A.; Hofland, G. W.; Witkamp, G.-J. Solubility of Glycine Polymorphs and Recrystallization of β-Glycine. *J. Chem. Eng. Data* **2007**, *52*, 1626–1629.

Brandrup, J.; Immergut E. H.; Grulke E. A. ; Abe A.; Bloch R. *Polymer Handbook*, 4th ed.; John Wiley & Sons: New York, 1999.

Brett, T. J.; Alexander, J. M.; Clark, J. L.; Ross II, C. R.; Harbison, G. S.; Stezowsk, J. J. Chemical insight from crystallographic disorder: structural studies of a supramolecular β-cyclodextrin/coumarin photochemical system. *Chem. Commun.* **1999**, 1275-1276.

Brinker, C. J.; Scherer, G. W. *Sol-Gel Science - The Physics and Chemistry of Sol-Gel Processing;* New York, Academic Press, 1990.

Brittain, H.G. *Polymorphism in Pharmaceutical Solids*; New York: Marcel Decker, 1999.

Bucar, D.-K.; MacGillivray L. R. Preparation and Reactivity of Nanocrystalline Cocrystals Formed via Sonocrystallization. *J. Am. Chem. Soc.* **2007**, *129*, 32-33.

Bueno, M. P.; Cativiela, C. A.; Mayoral, J. A.; Avenoza, A. Models for the use of a-amino acids as chiral auxiliaries in asymmetric Diels-Alder reactions. *J. Org. Chem.* **1991**, *56*, 6551-6555.

Buerger, M. J.; Bloom, M. C. Crystal polymorphism. *Z. Kristallogr.* **1937**, *96*, 182-200.

Buffat, Ph.; Borel, J.-P. Size effect on the melting temperature of gold particles. *Phys. Rev. A.* **1976**, *13*, 2287-2298.

Bush, L.; Webb, C.; Bartlett, L.; Burnett, B. The formulation of recombinant factor IX. Stability, robustness and convenience. *Semin. Hematol.* **1998**, *35*, 18–21.

Byrn, S. R.; Pfeiffer, R.; Ganey, M.; Hoiberg, C.; Poochikian, G. Pharmaceutical Solids: A Strategic Apporach to Regulatory Considerations. *Pharm. Res.* **1995**, *12*, 945–954.

Carter, P. W.; Ward, M. D. Directing Polymorph Selectivity During Nucleation of Anthranilic Acid on Molecular Substrates. *J. Am. Chem. Soc.* **1994**, *116*, 769-770.

Castro-Puyana, M.; Salgado, A.; Hazen, R. M.; Crego, A. L.; Alegre, M. L. M. The first contribution of capillary electrophoresis to the study of abiotic origins of homochirality: Investigation of the

enantioselective adsorption of 3-carboxy adipic acid on minerals. *Electrophoresis* **2008**, *29*, 1548-1555.

Černošek, Z.; Holubová, J.; Černošková, E. Kauzmann Temperature and the Glass Transition. *J. Optoelec. Adv. Mat.* **2005**, *7*, 2941--2944.

Chang, B. S.; Reeder, G.; Carpenter, J. F. Development of a Stable Freeze-dried Formulation Recombinant Human Interleukin-1 Receptor Antagonist. *Pharm. Res.* **1996**, *13*, 243–249.

Chattopadhyay, S.; Erdemir, D.; Evans, J. M. B.; Ilavsky, J.; Amenitsch, H.; Segre, C. U.; Myerson, A. S. SAXS Study of the Nucleation of Glycine Crystals from a Supersaturated Solution. *Cryst. Growth Des.* **2005**, *5*, 523–527.

Chemburkar, S. R.; Bauer, J.; Deming, K.; Spiwek, H.; Patel, K.; Morris, J.; Henry, R.; Spanton, S.; Dziki, W.; Porter, W.; Quick, J.; Bauer, P.; Donaubauer, J.; Narayanan, B. A.; Soldani, M.; Riley, D.; McFarland, K. Dealing with the impact of ritonavir polymorphs on the late stages of bulk drug process development. *Org. Process Res. Dev.* **2000**, *4*, 413–417.

Chen, S.; Guzei, I. A.; Yu, L. New Polymorphs of ROY and New Record for Coexisting Polymorphs of Solved Structures. *J. Am. Chem. Soc.* **2005**, *127*, 9881-9885.

Chen, S.; Xi, H.; Yu, L. Cross-Nucleation between ROY Polymorphs. *J. Am. Chem. Soc.* **2005**, *127*, 17439-17444.

Chiarella, R. A.; Gillon, A. L.; Burton, R. C.; Davey, R. J.; Sadiq, G.; Auffret, A.; Cioffi, M.; Hunter, C. A. The nucleation of inosine: the impact of solution chemistry on the appearance of polymorphic and hydrated crystal forms.

Chongprasert, S.; Knopp, S. A.; Nail, S. L. *J. Pharm. Sci.* **2001**, *90*, 1720–1728.

Christenson, H. K. Confinement effects on freezing and melting. *J. Phys.: Condens. Matter* **2001**, *13*, R95-R133.

Ciechanowicz, M.; Skapski, A. C.; Troughton, P. G. H. The crystal structure of the orthorhombic form of hydridodicarbonylbis(triphenylphosphine)-iridium(I): successful location of the hydride hydrogen atom from x-ray data. *Acta Crystallgr.* B **1976**, *32*, 1673-1680.

Cingolani, A.; Berchiesi, G. A DSC Study of phase transitions in aliphatic dicarboxylic acids. *J. Thermal Anal.* **1974**, *6*, 87-91.

Collet, A.; Brienn, M.-J.; Jacques, J. Optical Resolution by Direct Crystallization of Enantiomer Mixtures. *Chem. Rev.* **1980**, *80*, 215-230.

Davankov, V. A. The Nature of Chiral Recognition: Is it a Three-Point Interaction? *Chirality* **1997**, *9*, 99-102.

Davey, R. J. General discussion. *Faraday Discuss.* **1993**, *95*, 160-162.

Davey, R. J.; Allen, K.; Blagden, N.; Cross, W. I.; Lieberman, H. F.; Quayle, M. J.; Righini, S.; Seton, L.; Tiddy, G. J. T. Crystal engineering – nucleation, the key step. *CrystEngComm* **2002**, *4*, 257-264.

Davey, R. J.; Blagden, N.; Potts, G. D.; Docherty, R. Polymorphism in Molecular Crystals: Stabilization of a Metastable Form by Conformational Mimicry. *J. Am. Chem. Soc.* **1997**, *119*, 1767–1772.

Dawson, A.; Allan, D. R.; Belmonte, S. A.; Clark, S. J.; David, W. I. F.; McGregor, P. A.; Parsons, S.; Pulham, C. R.; Sawyer, L. Effect of High Pressure on the Crystal Structures of Polymorphs of Glycine. *Cryst. Growth Des.* **2005**, *5*, 1415–1427.

Debenedetti, P. G.; Stillinger, F. H. Supercooled liquids and the glass transition. *Nature*, **2001**, *410*, 259-267.

Defay, R.; Prigogine, I. *Surface Tension and Adsoption*; Longmans: London, 1966.

deGennes, P. G.; Prost, J. *The Physics of Liquid Crystals*; Oxford University Press: New York, 1993.

deKruif, C. G.; Voogd, J.; Offringa, J. C. Enthalpies of sublimation and vapour pressures of 14 amino acids and peptides. A. *J. Chem. Thermodyn.* **1979**, *11*, 651–656.

Desiraju, G. R. Supramolecular Snythons in Crystal Engineering - A New Organic Synthesis. *Angew. Chem. Int. Ed. Engl.* **1995**, *34*, 2311-2327.

Destro, R.; Roversi, P.; Barzaghi, M.; Marsh, R. E. Experimental Charge Density of [alpha]-Glycine at 23 K. *J. Phys. Chem. A* **2000**, *104*, 1047–1054.

Dinghas, A. Über einen geometrischen Satzs von Wulff für die Gleichgewichtsform von Kristallen. *Z. Krist.* **1944**, *105*, 304-314.

Drebushchak, T. N.; Boldyreva, E. V.; Seryotkin; Yu, V.; Shutova, E. S. Crystal Structure Study of the Metastable β-Modification of Glycine and its Transformation into the α-Modification. *J. Struct. Chem.* **2002**, *43*, 835–842.

Drebushchak, T. N.; Boldyreva, E. V.; Shutova, E. S. β-Glycine. *Acta Crystallogr.* **2002** *E58* o634–o636.

Dunitz, J. D.; Bernstein, J. Disappearing Polymorphs. *Acc. Chem. Res.* **1995**, *28*, 193-200.

Dupre La Tour, F. *Compt. Rend.* **1932**, *194*, 622.

Elsila, J. E.; Dworkin, J. P.; Bernstein, M. P.; Martin, M. P.; Sandford, S. A. Mechanisms of Amino Acid Formation in Interstellar Ice Analogs. *Astrophys. J.* **2007**, *660*, 911–918.

Etter, M. C. Hydrogen bonds as design elements in organic chemistry. *J. Phys. Chem.* **1991**, *95*, 4601-4610.

Ferrari, E. S.; Davey, R. J.; Cross, W. I.; Gillon, A. L.; Towler, C. S. Crystallization in Polymorphic Systems: The Solution-Mediated Transformation of β to α Glycine. *Cryst. Growth Des.* **2003**, *3*, 53-60.

Frenkel, D.; Cacciuto, A. Stresses Inside Critical Nuclei. *J. Phys. Chem. B* **2005**, *109*, 6587-6594.

Frostman, L. Ph.D. Thesis, University of Minnesota.

Gao, Q.; Weber, H.-P.; Craven, B. M.; McMullan, R. K. Structure of suberic acid at 18.4, 75, and 123 K from neutron diffraction data. *Acta Cryst.* **1994**, *B50*, 695-703.

Garten, V. A.; Head, R. B. Crystalloluminescence and the nature of the critical nucleus. *Phil. Mag.* **1966**, *14*, 1243-1253.

Gavezzotti, A. Are Crystal Structures Predictable? *Acc. Chem. Res.* **1994**, *27*, 309-314.

Gavuzzo, E.; Mazza, F. Determination of the molecular packing in the crystal of coumarin by means of potential-energy calculations. *Acta Cryst.* **1974**, *B30*, 1351-1357.

Gdanitz, R. J. Chapter 6 in *Theoretical Aspects and Computer Moledelling*; Gavezzotti, A., Ed. New York: John Wiley and Sons Ltd., 1997. pp. 185-201.

Gervais, C.; Coquerel, G. Simple model designed to generate new crystal structures derived from a mother phase; application to molecular compounds. *Acta Cryst.* **2002**, *B58*, 662-672.

Gibbs, J. W. *Collected Works, Vol. 1, Thermodynamics*; Yale University Press: New Haven, 1948.

Grandeury, A.; Condamine, E.; Hilfert, L.; Gouhier, G.; Petit, S.; Coquerel, G. Chiral Discrimination in Host-Guest Supramolecular Complexes. Understanding Enantioselectivty and Solid Solution Behaviors by Using Spectroscopic Methods and Chemical Sensors. *J. Phys. Chem. B* **2007**, *111*, 7017-7026.

Guillory, J. K. Generation of Polymorphs, Hydrates, Solvates, and Amorphous Solids, in *Polymorphism in Pharmaceutical Solids*; Brittain, H. G., Ed.; New York: Marcel Dekker, 1999. p. 183-226.

Ha, J.-M. Crystallization and Thermotropic Properties of Organic Solids in Nanoscopic Reactors. Ph.D. Thesis, University of Minnesota, September 2006.

Ha, J.-M.; Hamilton, B. D.; Hillmyer, M. A.; Ward, M. D. Phase Behavior and Polymorphism of Organic Crystals Confined within Ultrasmall Chambers. *Manuscript in preparation* **2009**.

Ha, J.-M.; Hillmyer, M. A.; Ward, M. D. Thermotropic Properties of Organic Nanocrystals Embedded in Ultrasmall Chambers. *J. Phys. Chem. B* **2005**, *109*, 1392-1399.

Ha, J.-M.; Wolf, J. H.; Hillmyer, M. A.; Ward, M. D. Polymorph Selectivity under Nanoscopic Confinement. *J. Am. Chem. Soc.* **2004**, *126*, 3382-3383.

Haller, W. Rearrangement Kinetics of the Liquid-Liquid Immiscible Microphases in Alkali Borosilicate Melts. *J. Chem. Phys.* **1965**, *42*, 686-693.

Hamilton, B. D.; Weissbuch, I.; Lahav, M.; Hillmyer, M. A.; Ward, M. D. Manipulating Crystal Orientation in Nanoscale Cylindrical Pores by Stereochemical Inhibition. *J. Am. Chem. Soc.* **2009**, *131*, 2588–2596.

Harbury, L. Solubility and Melting Point as Functions of Particle Size. 1. *J. Phys. Chem.* **1946**, *50*, 190-199.

Haydon, S. C. Dye-Laser Fluorescence of 4-Methylumbelliferone and Related Coumarins. *Spectrosc. Lett.* **1975**, *8*, 815-892.

Hazen, R. M.; Filley, T. R.; Goodfriend, G. A. Selective adsorption of l- and d-amino acids on calcite: Implications for biochemical homochirality. *Proc. Nat. Acad. Sci.* **2001**, *98*, 5487-5490.

Hazen, R. M.; Sholl, D. S. Chiral selection on inorganic crystalline surfaces. *Nature Mat.* **2003**, *2*, 367-374.

Hillier, A. C.; Maxson, J. B.; Ward, M. D. *Electrocrystallization of an Ordered Organic Monolayer: Selective Epitaxial Growth of b-$(ET)_2I_3$ on Graphite. Chem. Mater.* **1994**, *6*, 2222-2226.

Hooks, D. E.; Yip, C. M.; Ward, M. D. Nanoconfined Electrochemical Nucleation of Crystalline Molecular Monolayers on Graphite Substrates. *J. Phys. Chem. B* **1998**, *102*, 9958-9965.

Huang, J.; Stringfellow, T. C.; Yu, L. Glycine Exists Mainly as Monomers, Not Dimers, in Superstaturated Aqueous Solutions: Implications for Understanding Its Crystallization and Polymorphism. *J. Am. Chem. Soc.* **2008**, *130*, 13973-13980.

Hyun, M. H.; Cho, Y. J. Chiral Separation by HPLC With Pirkle-Type Chiral Stationary Phases in *Chiral Separations, Methods and Protocols;* Gubitz, G.; Schmid, M. G. Eds.; Humana Press, 2004.

Iitaka, Y. The crystal structure of β-glycine. *Acta Crystallogr.* **1960**, *13*, 35–45.

Iitaka, Y. The crystal structure of γ-glycine. *Acta Crystallogr.* **1961**, *14*, 1–10.

Jackson, C. L.; McKenna, G. B. The melting behavior of organic materials confined in porous solids. *J. Chem. Phys.***1990**, *93*, 9002-9011.

Jackson, C. L.; McKenna, G. B. Vitrification and Crystallization of Organic Liquids Confined to Nanoscale Pores. *Chem. Mater.* **1996**, *8*, 2128–2137.

Jackson, K. A.; Chalmers, B. Freezing of liquids in porous media with special reference to frost heave in soils. *J. Appl. Phys.* **1958**, *29*, 1178-1181.

Jacques, J. Collet, A.; Wilen, S. H. *Enantiomers, Racemates, and Resolutions*; John Wiley: New York, 1981.

Johnson, B. J. S.; Wolf, J. H.; Zalusky, A. S.; Hillmyer, M. A. Template Syntheses of Polypyrrole Nanowires and CdS Nanoparticles in Porous Polymer Monoliths. *Chem. Mater.* **2004**, *16*, 2909-2917.

Johnson, C. A.; Chakerian, G. D. On the Proof and Uniqueness of Wulff's Construction of the Shape of Minimum Surface Free Energy. *J. Math. Phys.* **1965**, *6*, 1403-1404.

Jonsson, P.-G.; Kvick, Structure of protein and nucleic acid components. III Å. *Acta Crystallogr. B* **1972**, *28*, 1827–1833.

Kang, J. F.; Zaccaro, J.; Ulman, A.; Myerson, A. Nucleation and growth of glycine crystal on self-assembled monolayers on gold. *Langmuir* **2000**, *16*, 3791–3796.

Kauzmann, W. The Nature of the Glassy State and the Behavior of Liquids at Low Temperatures. *Chem. Rev.* **1948**, *43*, 219-256.

Kay, M. I.; Katz, L. The Crystal Structure of α-Pimelic Acid. *Acta Cryst.* **1958**, *11*, 289-294.

Khoshkhoo, S.; Anwar, J. Crystallization of polymorphs: the effects of solvent. *J. Phys. D: Appl. Phys.* **1993**, *26*, B90–B93.

Kitaigorodsky, A. I. *Molecular Crystals and Molecules*; Academic Press: New York, 1973.

Kitamura, M. Controlling factor of polymorphism in crystallization. *J. Cryst. Growth* **2002**, *237-239*, 2205–2214.

Kuan, Y.-J.; Charnley, S. B.; Huang, H.-C.; Tseng, W.-L.; Kisiel, Z. Interstellar Glycine. *Astrophys. J.* **2003**, *593*, 848–867.

Kubelka-Prag, P. *Z. Elektrochem.* **1932**, *38*, 611.

Lai, J. T.; Filla, D.; Shea, R. Functional Polymers from Novel Carboxyl-Terminated Trithiocarbonates as Highly Efficient RAFT Agents. *Macromolecules* **2002**, *35*, 6754-6756.

Lan, C.W. Recent progress of crystal growth modeling and growth control. *Chem. Eng. Sci.* **2004**, *59*, 1437-1457.

Landau, E.; Meir; Grayer. Wolf, S.; Levanon, M.; Leiserowitz, L.; Lahav, M.; Sagiv, J. Stereochemcial studies in crystal nucleation. Oriented crystal growth of glycine at interfaces covered with Langmuir and Langmuir-Blodgett films of resolved α-amino acids. *J. Am. Chem. Soc.* **1989**, *111*, 1436–1445.

Lang, M.; Grzesiak, A. L.; Matzger, A. J. The use of Polymer Heteronuclei for Crystalline Polymorph Selection. *J. Am. Chem. Soc.* **2002**, *124*, 14834-14835.

Laplace, P. S. Traité de Mécanique Céleste; Supplement au Dixième Livre, Sur l'Action Capillaire. Courcier: Paris, 1806.

Last, J. A.; Hillier, A. C.; Hooks, D. E.; Maxson, J. B. Epitaxially-Driven Assembly of Crystalline Molecular Films on Ordered Substrates. *Chem. Mater.* **1998**, *10*, 422-437.

Last, J. A.; Hooks, D. E.; Hillier, A. C.; Ward, M. D. The Physiochemical Origins of Coincident Epitaxy in Molecular Overlayers: Lattice Modeling vs Potential Energy Calculations. *J. Phys. Chem. B* **1999**, *103*, 6723–6733.

Lee, A. Y.; Lee, I. S.; Dette, S. S.; Boerner, J.; Myerson, A. S. Crystallization on Confined Engineered Surfaces: A Method to Control Crystal Size and Generate Different Polymorphs. *J. Am. Chem. Soc.* **2005**, *127*, 14982–14983.

Lee, I. S.; Kim, K. T.; Lee, A. Y.; Myerson, A. S. Concomitant Crystallization of Glycine on Patterned Substrates: The Effect of pH on the Polymorphic Outcome. *Cryst. Growth Des.* **2008**, *8*, 108–113.

Legros, J.-P.; Kvick, Å. Deformation electron density of glycine at 120 K. *Acta Crystallogr. B* **1980**, *36*, 3052–3059.

Li, J.; Wang, Z.; Yan, X.; Hu, L.; Liu, Y.; Wang, C. Evaluate the pyrolysis pathway of glycine and glycylglycine by TG-FTIR. *J. Anal. Appl. Pyrolysis* **2007**, *80*, 247–253.

Lilly Industries Limited, Kingsclere Road, Basingstoke Hants RG21 2XA, U.K. Eur. Pat. 0 454 436 A1, Bulletin 91/44, Oct 30, 1991.

Litvan, G. G. Phase Transitions of Adsorbates. 1. Specific Heat and Dimensional Changes of the Porous Glass-Water System. *Can. J. Chem.* **1966**, *44*, 2617-2622.

Litvan, G. G.; McIntosh, R. Phase Transitions of Water and Xenon Adsorbed In Porous Vycor Glass. *Can. J. Chem.* **1963**, *41*, 3095-3107.

Loisel, C.; Keller, G.; Lecq, G.; Bourgaux, C.; Ollivon, M. Phase transitions and polymorphism of cocoa butter. *J. Am. Oil Chem. Soc.* **1998**, *75*, 425–439.

Lynn, D. M. Peeling Back the Layers: Controlled Erosion and Triggered Disassembly of Multilayered Polyelectrolyte Thin Films. *Adv. Mater.* **2007**, *19*, 4118-4130.

Mao, H.; Hillmyer, M. A. Nanoporous Polystyrene by Chemical Etching of Poly(ethylene oxide) from Ordered Block Copolymers. *Macromolecules* **2005**, *38*, 4038-4039.

Markov, I. V. *Crystal Growth for Beginners*; World Scientific: London, 2003.

Marsh, R. E. A refinement of the crystal structure of glycine. *Acta Crystallogr.* **1958**, *11*, 654–663.

Matsumoto, M.; Saito, S.; Ohmine, I. Molecular dynamics simulation of the ice nucleation and growth process leading to water freezing. *Nature*, **2002**, *416*, 409-413.

McCrone, W. C. Polymorphism. In *Physics and chemistry of the organic solid state;* Fox, D.; Labes, M. M.; Weissberger, A. Eds.; Wiley Interscience: New York, 1965. Vol. 2.

Meng, J.; Fu, D.; Yao, X.-K.; Wang, R.-J.; Matsuura, T. Solid-state photodimerization of coumarin in the presence of crystal lattice-controlling substance. *Tetrahedron* **1989**, *45*, 6979-6986.

Mitchell, C. A.; Yu, L.; Ward, M. D. Selective Nucleation and Discovery of Organic Polymorphs through Epitaxy with Single Crystal Substrates. *J. Am. Chem. Soc.* **2001**, *123*, 19830-10839.

Moorthy, J. N.; Venkatesan, K.; Weiss, R. G. Photodimerization of coumarins in solid cyclodextrin inclusion complexes. *J. Org. Chem.* **1992**, *57*, 3292-3297.

Mori, H.; Matsuyama, M. Endo, T. Assembled Structures and Chiroptical Properties of Amphiphilic Block Copolmers Synthesized by RAFT Polymerization of *N*-Acryloyl-L-alanine. *Macromol. Chem. Phys.* **2008**, *209*, 210-2112.

Moulton, B.; Zaworotko, M. J. From Molecules to Crystal Engineering: Supramolecular Isomerism and Polymorphism in Network Solids. *Chem. Rev.* **2001**, *101*, 1629-1658.

Mullin, J.W. *Crystallization*; Elsevier Butterworth-Heinemann: London, 2001.

Myasnikova, R. M.; Davydova, T. S.; Simonov, V. I. *Sov. Phys. Crystallogr.* **1974**, *18*, 454-456.

Nail, S. L.; Shan, J. *Pharm. Biotech.* **2002**, *14*, 281–360.

Näther, C.; Bock, H.; Claridge, R. F. C. Solvent-shared radical ion pairs [pyrene^{-}Na^{+}O(C_2H_5)$_2$]inf: ESR evidence for two different aggregates in solution, room temperature crystallization, and structural proof of another polymorphic modification. *Helv. Chim. Acta* **1996**, *79*, 84-91.

Näther, C.; Nagel, N.; Bock, H.; Seitz, W.; Halvas, Z. Structural, kinetic and thermodynamic aspects of the conformational dimorphism of diethyl 3,6-dibromo-2,5-dihydroxyterephthalate. *Acta Crystallogr. B* **1996**, *52*, 697-706.

Nielsen, A. E. *Kinetics of Precipitation*; Pergamon Press: New York, 1964.

Nyvlt, J.; Sohnel, O. Matuchova, M. Broul, M. *The Kinetics of Industrial Crystallization*; Academia: Prague, 1985.

Ostwald, W. F. Studies on formation and transformation of solid materials. *Z. Phys. Chem.* **1897**, *22*, 289-330.

Ostwald, W. *Lehrbuch der Allgemeinen Chemie*; Leipzig, Germany, 1896. Vol. 8, Part 1.

Otpushchennikov, N. F. Determination of the size of the elementary crystal nucleus from acoustic measurement. *Soviet Phys. Cryst.***1962**, *7*, 237-240.

Oxtoby, D. W. Nucleation of First-Order Phase Transitions. *Acc. Chem. Res.***1998**, *31*, 91-97.

Patrick, W. A.; Kemper, W. A. Melting Temperatures of Compounds Adsorbed on Silica Gel. *J. Phys. Chem.* **1938**, *42*, 369-380.

Patrick, W. A; Land, W. E. A Study of the Influence of Capillarity on the Melting Point of Iodine. *J. Phys. Chem.* **1934**, *38*, 1201-1210.

Pawlow, P. The dependency of melting point on the surface energy of a solid body. *Z. Phys. Chem.* **1909**, *65*, 545-548.

Perlstein, J. Molecular self-assemblies. 2. A computational method for the prediction of the structure of one-dimensional screw, glide, and inversion molecular aggregates and implications for the packing of molecules in monolayers and crystals. *J. Am. Chem. Soc.* **1994**, *116*, 11420-11432.

Perlstein, J. Molecular self-assemblies: Monte Carlo predictions for the structure of the one-dimensional translation aggregate. *J. Am. Chem. Soc.* **1992**, *114*, 1955-1963.

Pervolich, G. L.; Hansen, L. K.; Bauer.Brandl, A. The Polymorphism of Glycine. Thermochemical and structural aspects. *J. Therm. Anal. Calorim.* **2001**, *66*, 699–715.

Petit, S.; Coquerel, G.; Hartman, P. Nucleation and crystal growth of molecular solvates with several conformations both in solution and in solid state; application to some hydrated copper(II) sulfoxinates. *J. Cryst. Growth* **1994**, *137*, 585-594.

Petropavlov, N. N.; Tsygankova, I. G.; Teslenko, L. A. Microcalorimetric investigation of polymorphic transitions in organic crystals. *Sov. Phys. Crystallogr.* **1988**, *33*, 853-855.

Polymorphism in Pharmaceutical Solids; Brittain, J. G. , Ed.; Marcel Dekker: New York, 1999.

Power, L. F.; Turner, K. E.; Moore, F. H. The crystal and molecular structure of glycine by neutron diffraction – a comparison. *Acta Crystallogr. B* **1976**, *32*, 11–16.

Prasad, R.; Lele, S. Stabilization of the amorphous phase inside carbon nanotubes: solidification in a constrained geometry. *Phil. Mag. Lett.* **1994**, *70*, 357-361.

Price, C. P.; Grzesiak, A. L.; Matzger, A. J. Crystalline Polymorph Selection and Discovery with Polymer Heteronuclei. *J. Am. Chem. Soc.* **2005**, *127*, 5512–5517.

Raabe, G. *Z.* The Use of Quantum Chemical Semiempirical Methods to Calculate the Lattice Energies of Organic Molecular Crystals. Part I: The Three Polymorphs of Glycine. *Naturforsch.* **2000**, *55a*, 609–615.ro

Radhakrishnan, R.; Gubbins, K. E.; Sliwinska-Bartkowiak, M. Effect of the fluid-wall interaction on freezing of confined fluids: Towad the development of a global phase diagram. *J. Chem. Phys.* **2000**, *112*, 11048 – 11057.

Rault, J.; Neffati, R.; Judeinstein, P. Melting of ice in porous glass: why water and solvents confined in small pores do not crystallize? *Eur. Phys. J. B* **2003**, *36*, 627-637.

Reinnie, G. K.; Clifford, J. Melting of Ice in Porous Solids. *J.Chem. Soc., Faraday Trans. 1* **1977**, *73*, 680–689.

Rengarajan, G. T.; Enke, D.; Beiner, M.; Steinhart, M. Stabilization of the amorphous state of pharmaceuticals in nanopores. *J. Mat. Chem.* **2008**, *18*, 2537–2539.

Rennie, G. K.; Clifford, J. Melting of Ice in Porous Solids. *J. Chem. Soc. Faraday Trans. 1* **1997**, *73*, 680-689.

Ring, T. A. Nano-sized cluster nucleation. *Adv. Coll. Int. Sci.* **2001**, *91*, 473-499.

Rodante, F.; Marrosu, G.; Catalani, G. Thermal analysis of some α-amino acids with similar structures. *Thermochim. Acta* **1992**, *194*, 197–203.

Rodrigeuz-Hornedo, N.; Murphy, D. Significance of Controlling Crystallization Mechanisms and Kinetics in Pharmaceutical Systems. *J. Pharm. Sci.* **1999**, *88*, 651–660.

Rzayev, J.; Hillmyer, M. A. Nanochannel Array Plastics with Tailored Surface Chemistry. *J. Am. Chem. Soc*. **2005**, *127*, 13373-13379.

Rzayev, J.; Hillmyer, M. A. Nanoporous Polystyrene Containing Hydrophilic Pores from an ABC Triblock Copolymer Precursor. *Macromolecules* **2005**, *38*, 3-5.

Sahin, O.; Dolas, H.; Demir, H. Determination of nucleation kinetics of potassium tetraborate tetrahydrate. *Cryst. Res. Technol.***2007**, *42*, 766-772.

Sakurai, S.; Aida, S.; Okamoto, S.; Ono, T.; Imaizumi, K.; Nomura, S. Preferential Orientation of Lamellar Microdomains Induced by Uniaxial Stretching of Cross-Linked Polystyrene-block-polybutadiene-block-polystyrene Triblock Copolymer. *Macromolecules* **2001**, *34*, 3672-3678.

Sands, B. W.; Kim, Y. S.; Bass, J. L. Characterization of bonded-phase silica gels with different pore diameters. *J. Chromatogr.* **1986**, *360*, 353-369.

Schreiber, A.; Ketelsen, I.; Findenegg, G. H. Melting and freezing of water in ordered mesoporous silica materials. *Phys. Chem. Chem. Phys.* **2001**, *3*, 1185-1195.

Selvaraju, K.; Kirubavathi, K.; Vijayan, N.; Kumararaman, S. Investigations on the nucleation kinetics of bis glycine sodium nitrate. *J Cryst. Growth* **2008**, *310*, 2859-2862.

Sheng, H. W.; Ren, G. Peng, L. M.; Hu, Z. Q.; Lu, K. Superheating and melting-point depression of Pb nanoparticles embedded in Al matrices. *Phil. Mag. Lett.* **1996**, *73*, 179-186.

Sheng, H. W.; Ren, G.; Peng, L. M.; Hu, Z. Q.; Lu, K. Epitaxial dependence of the melting behavior of In nanoparticles embedded in Al matrices. *J. Mater. Res.* **1997**, *12*, 119-123.

Snyder, L. E.; Lovas, F. J.; Hollis, J. M.; Friedel, D. N.; Jewell, P. R.; Remijan, A.; Ilyushin, V. V.; Alekseev, E. A.; Dyubko, S. F. A Rigorous Attempt to Verify Interstellar Glycine. *Astrophys. J.* **2005**, *619*, 914– 930.

Speedy, R. J. Kauzmann's paradox and the glass transition. *Biophys. Chem.* **2003**, *105*, 411-420.

Steele, W. V.; Chirico, R. D.; Cowell, A. B.; Knipmeyer, S. E.; Nguyen, A. Thermodynamic Properties and Ideal-Gas Enthalpies of Formation for 1,4-Diisopropylbenzene, 1,2,4,5-Tetraisopropylbenzene, Cyclohexanone Oxime, Dimethyl Malonate, Glutaric Acid, and Pimelic Acid. *J. Chem. Eng. Data*, **2002**, *47*, 725-739.

Steinhart, M.; Göring, P.; Dernaika, H.; Prabhukara, M.; Gösele, U.; Hempel, Thurn-Albrecht, T. Coherent Kinetic Control over Crystal Orientation in Macroscopic Ensembles of Polymer Nanorods and Nanotubes. *Phys. Rev. Lett*. **2006**, *97*¸ 027801.

Steinhart, M.; Stephan S.; Wehrspohn, R.B.; Gosele, U.; Wendorff, J. H. Curvature-Directed Crystallization of Poly(vinylidene difluoride) in Nanotube Walls. *Macromolecules* **2003**, *36*, 3646-3651.

Stillinger, F. S.; Debenedeetti, P. G. Phase transitions, Kauzmann curves, and inverse melting. *Biophys. Chem.* **2003**, *105*, 211-220.

Stillinger, F.H. Supercooled liquids, glass transitions, and the Kauzmann paradox. *J. Phys. Chem.* **1988**, *88*, 7818-7825.

Sukhishvili, S. A.; Kharlampieva, E.; Izumrodov, V. Where Polyelectrolyte Multilayers and Polyelectrolyte Complexes Meet. *Macromolecules* **2006**, *39*, 8873-8881.

Sun, X.; Garetz, B. A.; Myerson, A. S. Supersaturation and Polarization Dependence of Polymorph Control in the Nonphotochemical Laser-Induced Nucleation (NPLIN) of Aqueous Glycine Solutions. *Cryst. Growth Des.* **2006**, *6*, 684–689.

Takagi, M. Electron-Diffractionstudy of Liquid-Solid Transition. *J. Phys. Soc. Jpn.* **1954**, *9*, 359-363. (in English)

Takagi, S.; Chihara, H.; Seki, S. Vapor Pressure of Molecular Crystals. XIII. Vapor Pressure of α-Glycine Crystal. The Energy of Proton Transfer. *Bull. Chem. Soc. Jpn.* **1959**, *32*, 84–88.

Takahashi, S.; Miura, H.; Kasai, H.; Okada, S.; Oikawa, H.; Nakanishi, H. Single-Crystal-to-Single-Crystal Transformation of Diolefin Derivatives in Nanocrystals. *J. Am. Chem. Soc.* **2002**, *124*, 10944-10945.

Tanaka, H. Possible resolution of the Kauzmann paradox in supercooled liquids. *Phys. Rev. E* **2003**, 011505, 1-8.

ten Wolde, P. R.; Ruiz-Montero, M. J.; Frenkel, D. Numerical calculation of the rate of crystal nucleation in a Lennard-Jones system at moderate undercooling. *J. Chem. Phys.* **1996**, *104*, 9932-9947.

Thalladi, V. R.; Nisse, M.; Boese, R. The Melting Point Alteration in α,ω-Alkanedicarboxylic Acids. *J. Am. Chem. Soc.* **2000**, *122*, 9227-9236.

Thomson, W. On the equilibrium of vapour at a curved surface of liquid. *Phil. Mag.* **1871**, *42*, 448-452.

Threlfall, T. L. Analysis of Organic Polymorphs – A Review. *Analyst* **1995**, *120*, 2435-2460.

Torbeev, V. Yu.; Shavit, E.; Weissbuch, I.; Leiserowitz, L.; Lahav, M. Control of Crystal Polymorphism by Tuning the Structure of Auxiliary Molecules as Nucleation Inhibitors. The β-Polymorph of Glycine Grown in Aqueous Solutions. *Cryst. Growth Des.* **2005**, *5*, 2190-2196.

Unruh, K. M.; Huber, T. E.; Huber, C. A. Melting and freezing behavior of indium metal in porous glasses. *Phys. Rev. B* **1993**, *48*, 9021-9027.

Vippagunta, S. R.; Brittain, H. G.; Grant, D. J. W. Crystalline solids. *Adv. Drug Delivery Rev.* **2001**, *48*, 3-26.

Vlieg, E.; Deij, M.; Kaminski, D.; Meekes, H.; van Knckevort, W. Towards an atomic-scale understanding of crystal growth in solution. *Faraday Disc.* **2007**, *136*, 57-69.

Volmer, M. *Kinetic Der Phasenbildung*; Steinkoff: Dresden, 1939.

Weissbuch, I., Leiserowitz, L.; Lahav, M. Direct assignment of the absolute configuration of molecules from crystal morphology. *Chirality* **2008**, *20*, 736-748.

Weissbuch, I.; Addadi, L.; Lahav, M.; Leiserowitz, L. Molecular recognition at crystal interfaces. *Science* **1991**, *253*, 637-645.

Weissbuch, I.; Lahav, M.; Leiserowitz, L. Toward Stereochemical Control, Monitoring, and Understanding Crystal Nucleation. *Cryst. Growth Des.* **2003**, *3*, 125-150.

Weissbuch, I.; Leiserowitz L.; Lahav M. Tailor-Made and charge-transfer auxiliaries for the control of the crystal polymorphism of glycine. *Adv. Mater.* **1994** *6*, 952-956.

Weissbuch, I.; Leiserowitz, L.; Lahav, M. Stochastic "Mirror Symmetry Breaking" via Self-Assembly Reactivity and Amplification of Chirality: Relevance to Abiotic Conditions. *Top. Curr. Chem.* **2005**, *259*, 123-165.

Weissbuch, I.; Torbeev, V. Yu.; Leiserowitz, L.; Lahav, M. Solvent Effect on Crystal Polymorphism: Why Addition of Methanol or Ethanol to Aqueous Solutions Induces the Precipitation of the Least Stable b-Form of Glycine. *Ange. Chem. Int. Ed.* **2005**, *44*, 3226-3229.

Wesolowski, M.; Erecinska, J. Relation Between Chemical Structure of Amino Acids and their Thermal Decomposition. Analysis of the data by principal component analysis. *J. Therm. Anal. Calorm.* **2005**, *82*, 307–313.

Wolf, J. H.; Hillmyer, M. A. Ordered Nanoporous Poly(cyclohexylethylene). *Langmuir* **2003**, *19*, 6553-6560.

Wulff, G. Zur Frage der Geschwindigkeit des Wachstums unter Auflosung der Kristallfiachen. *Z. Krist.* **1901**, *34*, 449-530.

Yau, S.-T.; Vekilov, P. G. Quasi-planar nucleus structure in apoferritin crystallization. *Nature* **2000**, *466*, 494-497.

Young, T. Essay on the Cohesion of Fluids. *Phil. Trans.* **1805**, *xx*, 65-87.

Yu, L. Color Changes Caused by Conformation Polymorphism: Optical-Crystallography, Single-Crystal Spectroscopy, and Computation Chemistry. *J. Phys. Chem. A* **2002**, *106*,544-550.

Yu, L. Inferring Thermodynamic Stability Relationship of Polymorphs from Melting Data. *J. Pharm. Sci.* **1995**, *84*, 966-974.

Yu, L. Survival of the fittest polymorph: how fast nucleater can lose to fast grower. *Cryst. Eng. Comm.* **2007**, *9*, 847-851.

Yu, L.; Stephenson, G. A.; Mitchell, C. A.; Bunnel, C. A.; Snorek, S. V.; Bowyer, J. J.; Borchardt, T. B.; Stowell, J. G.; Byrn, S. R. Thermochemistry and Conformational Polymorphism of a Hexamorphic Crystal System. *J. Am. Chem. Soc.* **2000**, *122*, 585-591.

Zaccaro, J.; Matic, J.; Myerson, A. S.; Garetz, B. A. Nonphotochemical, Laser-Induced Nucleation of Supersaturated Aqueous Glycine Produces Unexpected γ-Polymorph. *Cryst. Growth Des.* **2001**, *1*, 5–8.

Zalusky, A. S. Olayo-Valles, R.; Taylor, C. J.; Hillmyer, M. A. Mesoporous Polystyrene Monoliths. *J. Am. Chem. Soc.* **2001**, *123*, 1519-1520.

Zalusky, A. S. Olayo-Valles, R.; Wolf, J. H.; Hillmyer, M. A. Ordered Nanoporous Polymers from Polystyrene-Polylactide Block Copolymers. *J. Am. Chem. Soc.* **2002**, *124*, 12761-12773.

Zhang, X.; Chen, H.; Zhang, H. Layer-by-layer assembly: from conventional to unconventional methods. *Chem. Comm.* **2007**, *14*, 1395-1405.

Zhao, D.; Feng, J.; Huo, Q.; Melosh, N.; Fredrickson, G. H.; Chmelka, B. F.; Stucky, G. D. Triblock Copolymer Synthesies of Mesoporous Silica with Periodic 50 to 300 Angstrom Pores. *Science*, **1998**, *279*, 548-552.

Appendix A: Thermodynamic Derivation of Classic Nucleation Theory

---

The derivation of classic nucleation is included in this thesis to fill an apparent void in modern literature. In our experience, recent discussions of classic nucleation neglect explanations of the underlying assumptions or choice of system,[1,2,3,4] whereas classic discussions are turgid to the point of inaccessibility.[5] The derivation discussed here is provided in an attempt to give a clear glimpse at the ideas behind classic nucleation theory. This particular derivation is for a solid nucleating from a solution, but analogous results can be derived for nucleation from the melts and from vapors. All fundamental thermodynamic principles employed herein were taken from Sandler.[6]

A-1: Thermodynamic Derivation of Critical Size and Energy

Consider a closed system filled with a solution and held at constant T and p. This system can be described by the Gibbs Free Energy, G (Equation A.1), which is defined for constant T and p. H is enthalpy, S is entropy.

$$G = H - TS \quad \text{A.1}$$

The driving force for the nucleation of a solid phase, denoted phase II, from the solute is determined by the thermodynamic favorability of the new phase. If a differential element of the solution were to solidify, the total Gibbs free energy of the system would change by a differential amount (Equation A.2) corresponding to the sum of the changes in free energy of the two phases, less the amount of work required to form an interface between them. dG is the change in Gibbs energy of the system, dG_I is the change in Gibbs energy of phase I, dG_{II} is the change in Gibbs energy of phase II, and $dW_{I\text{-}II}$ is the work required to form an interface.

$$dG = dG_I + dG_{II} + dW_{I-II} \quad \text{A.2}$$

The system remains closed, thus moles of material, N, remains constant; however, the formation of a solid phase decreases the amount of material in the liquid phase (Equation A.3, Figure A-1A). The presence of the work term, $dW_{I\text{-}II}$, in Equation A.2 is required because the interactions between Phase I and II may not be equivalent to the interactions of Phase I and Phase II with themselves. The work is equivalent to the energy required to split areas dA of Phase I from itself (i.e. interaction cleaving) and of Phase II from itself, plus the energy gained from combining the cleaved surfaces (Figure A-1B). These energies are denoted dW_1, dW_2, and $-dW_3$, respectively. Cleaving a surface dA of a homogeneous phase generates $2dA$ worth of surface after the split - one for each half of the cleaved phase. Therefore, the effects of dW_1 and dW_2 are halved when compared with $-dW_3$. The result is the definition of γ, the surface energy of the interface, in terms of those works and the differential area (Equation A.4). The surface energy is equivalent to the change in free energy with respect to the change in surface area of the solid (Equation A.5).

$$dN = dN_I + dN_{II} = 0 \quad \text{A.3}$$

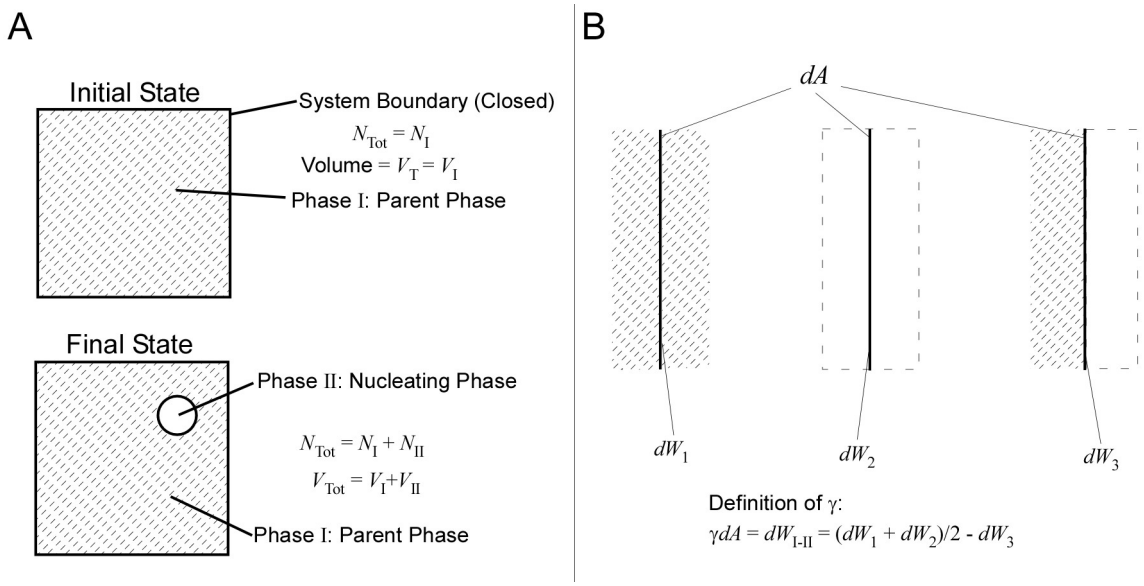

Figure A-1. (A) Illustration of the initial and final states of a closed system in which nucleation occurs. (B) Scheme illustrating the definition of the surface energy, γ, based upon the work required to separate molecules of phase I (dW_1), molecules of phase II (dW_2), and molecules of phase I from molecules of phase II (dW_3) for a differential area dA.

$$\gamma dA = dW_{I-II} = (dW_1 + dW_2)/2 - dW_3 \qquad \text{A.4}$$

$$\gamma = \frac{dG}{dA} \qquad \text{A.5}$$

The energy required to perform γdA, i.e. generate the interface between phases I and II, is obtained from the Gibbs energy of the formation of phase II from phase. The changes in Gibbs energy of each phase owing to the transfer of molecules between phases to the next written as (Equation A.6, A.7):

$$dG_I = \sum_i \underline{G}_{I,i} dN_{I,i} \qquad \text{A.6}$$

$$dG_{II} = \sum_i \underline{G}_{II,i} dN_{II,i} \qquad \text{A.7}$$

The subscript *i* denotes a component species, such as a solvent or solute molecule. The terms $\underline{G}_{I,i}$ and $\underline{G}_{II,i}$ correspond to the molar Gibbs energy of species *i* in phases I and II, respectively. The $dN_{I,i}$ and $dN_{II,i}$ terms correspond to the moles of species *i* joining phase I or II, respectively. The sum of these terms (Equation A.8) can be rewritten in terms of the amount of material moving phase II (Equation A.9) after employing the mass balance, $dN_{II,i} = -dN_{I,i}$ (Equation A.3).

$$dG_I + dG_{II} = \sum_i \underline{G}_{I,i} dN_{I,i} + \sum_i \underline{G}_{II,i} dN_{II,i} \qquad \text{A.8}$$

$$dG_I + dG_{II} = \sum_i (\underline{G}_{II,i} - \underline{G}_{I,i}) dN_{II,i} \qquad \text{A.9}$$

By definition, the molar Gibbs energy of species *i* in phase *M* is the derivative of the Gibbs energy of phase *M* with respect to the amount of *i*. This definition allows the molar Gibbs energy term in Equation A.9 to be rewritten as Equation A.10. The relationship can be simplified by employing the mass balance, $dN_{I,i} = -dN_{II,i}$ and combining similar terms (Equations A.11). This result defines the chemical potential of species *i*, $\Delta\mu_i$ (Equation A.12).

$$\underline{G}_{II,i} - \underline{G}_{I,i} = \frac{dG_{II}}{dN_{II,i}} - \frac{dG_I}{dN_{I,i}} \qquad \text{A.10}$$

$$\underline{G}_{II,i} - \underline{G}_{I,i} = \frac{dG_{II}}{dN_{II,i}} + \frac{dG_I}{dN_{II,i}} \qquad \text{A.11}$$

$$\underline{G}_{II,i} - \underline{G}_{I,i} = \frac{d(G_{II,i} + G_{I,i})}{dN_{II,i}} = \frac{dG}{dN_{II,i}} = -\Delta\mu_i \qquad \text{A.12}$$

Equation A.9 may now be rewritten (Equation A.13) and substituted along with Equation A.4 into A.2 (Equation A.14). This result is valid for a system of multiple components, but does not account for anisotropy in the nucleating phase, wherein $\Delta\mu dN$ and γdA depend on the location of addition of a particle of species *i* to phase II. Also, this model does not account for rotational and translational contributions to the free energy.

$$dG_I + dG_{II} = -\sum_i \Delta\mu_i dN_{II,i} \quad \text{A.13}$$

$$dG = -\sum_i \Delta\mu_i dN_{II,i} + \gamma dA \quad \text{A.14}$$

For a one component system, such as a solution where the solvent does not crystallize, crystallization from the melt, or a solvate (where the molar proportions between solute and solvent molecules in the crystal is constant and can thus be treated as one component) we obtain the relation described in chapter 1 (Equation A.15, A.16):

$$dG_{system} = -\Delta\mu dN_{II} + \gamma dA \quad \text{A.15}$$

$$\Delta G_{cryst} = -\Delta\mu N + \gamma A \quad \text{A.16}$$

Now, assuming that the Phase II adopts a spherical geometry, the *N* particles of the spherical nucleus can be described in terms of the volume of the sphere, with radius *r,* and the molecular volume, *v*. Likewise, the Gibbs energy associated with the interface formation can be described in terms of the surface area of the sphere (Equation A.17, Figure A-2). The change in chemical potential of the particles that join the nucleus may be rewritten according to the definition of activity (Equation A.18), where *a* describes the activity of the particle prior to escaping the supersaturated solution (or supercooled melt) and *a** describes the activity of a particle in a

saturated solution (or melt at the melting temperature) (Equation A.19). T is absolute temperature and **k** is the Boltzmann constant. In the limit of near infinite dilution the activities a and a^* can be approximated respectively by the concentrations c and c^*, the ratio of which is the supersaturation, S (Equation A.20). Alternate definitions for $\Delta\mu$ are employed when discussing other nucleation phenomenon (Table A-1).

$$\Delta G_{cryst} = -\frac{4/3\pi r^3}{v}\Delta\mu + 4\pi r^2\gamma \qquad \text{A.17}$$

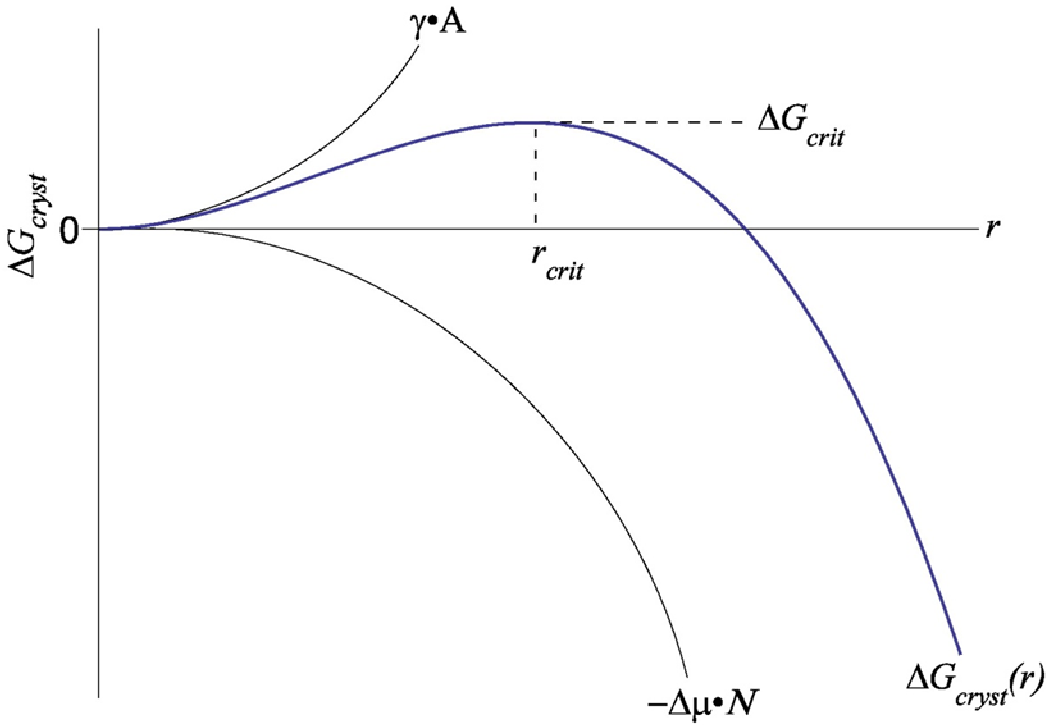

Figure A-2. Illustration of the free energy (ΔG_{cryst}) profile of a growing crystal nucleus as a function of crystal radius, r. The energy profile results from the sum of the energetic benefit associated with a species changing phases, $-\Delta\mu \bullet N$, and the penalty associated with forming an interface between the original and crystalline phase, $\gamma \bullet A$. The profile goes through a maximum, ΔG_{crit}, for crystals of size r_{crit}. Crystals smaller than r_{crit} are expected to dissolve spontaneously, however, crystals larger than r_{crit} are expected to grow spontaneously. The formation of these crystals is discussed in the text.

$$a = \exp\left(\frac{\Delta\mu}{RT}\right) \quad \text{A.18}$$

$$\Delta G_{cryst} = -\frac{4/3\pi r^3}{v}\mathbf{k}T\ln\left(a/a_*\right) + 4\pi r^2\gamma \quad \text{A.19}$$

$$\Delta G_{cryst} = -\frac{4/3\pi r^3}{v}\mathbf{k}T\ln\left(S\right) + 4\pi r^2\gamma \quad \text{A.20}$$

Equation A.20 describes a competition between the energetic benefit gained for particles forming a new phase (e.g. a crystal) when they are driven by supersaturation and the energetic penalty paid for forming an interface (e.g. the surface of the crystal) between the new and old phase. The energetic profile of a growing crystal nucleus is a function of crystal size, and is parameterized by the radius, *r*. Notably, this size-dependent profile passes through a maximum free energy, which can be determined along with the corresponding size when $d\Delta G_{cryst}/dr = 0$

Table A-1. Expressions for $\Delta\mu$, Equation A.17, for different nucleation events. All of these expressions are contingent on the assumptions that the systems are ideal and that the entropies and enthalpies of transitions are independent of temperature. The temperatures T_i (i = transition type) are the bulk thermodynamic transition temperatures, while T are the size-dependent transition temperatures. The ΔH_i are the enthalpies of the transitions, written as positive numbers.

Nucleation Event	$\Delta\mu$	**Alternate** $\Delta\mu$
Vapor condensation into a liquid (vap) or solid (sub)	$\mathbf{k}T\ln\left(p/p_0\right)$	$\frac{\Delta H_{vap/sub}\left(T_{vap/sub}-T\right)}{T_{vap/sub}}$
Crystallization from solution	$\mathbf{k}T\ln\left(c/c_0\right)$	$\frac{\Delta H_{sol}\left(T_{sol}-T\right)}{T_{sol}}$
Bubble nucleation in liquid	$-\mathbf{k}T\ln\left(p/p_0\right)$	$-\frac{\Delta H_{vap}\left(T_b-T\right)}{T_b}$
Crystallization from melt	-	$\frac{\Delta H^{fus}\left(T_m-T\right)}{T_m}$

(Equation A.21). Nuclei smaller than the size corresponding to this maximum dissolve spontaneously, owing to increasing crystal free energy with increasing crystal size, however, nuclei larger than this size grow spontaneously. For these reasons, the size and corresponding maximum free energy are known as the critical radius, r_{crit} (Equation A.22), and the critical energy, ΔG_{crit} (Equation A.23), respectively. The free energy maximum, ΔG_{crit}, is tantamount to the energetic barrier that must be surpassed to achieve spontaneous crystal growth.

$$\frac{d\Delta G_{cryst}}{dr} = 0 = -\frac{4\pi r_{crit}^2}{v}\mathbf{k}T\ln(S) + 8\pi r_{crit}\gamma \qquad \text{A.21}$$

$$r_{crit} = \frac{2v\gamma}{\mathbf{k}T\ln(S)} \qquad \text{A.22}$$

$$\Delta G_{crit} = \frac{4\pi\gamma r_{crit}^2}{3} \qquad \text{A.23}$$

Additional discussion on classic nucleation theory can be found in Chapter 1.

A-2: References

1. Nyvlt, J.; Sohnel, O. Matuchova, M. Broul, M. *The Kinetics of Industrial Crystallization*; Academia: Prague, 1985
2. *Polymorphism in Pharmaceutical Solids*; Brittain, H. G., Ed.; New York: Marcel Dekker, 1999.
3. Mullin, J.W. *Crystallization*; Elsevier Butterworth-Heinemann: London, 2001.
4. *Handbook of Industrial Crystallization*; Myerson, A. S., Ed.; Butterworth-Heinemann: London, 1993.
5. Gibbs, J. W. *Collected Works, Vol. 1, Thermodynamics*; Yale University Press: New Haven, 1948.
6. Sandler, S. I. *Chemical and Engineering Thermodynamics*; John Wiley & Sons: New York, 1999. 3rd Ed.

Appendix B: Fabrication of p-PS-PDMA Monoliths

B-1: Synthesis of p-PS-PDMA Monoliths

The synthesis of the polylactide-poly(dimethyl acrylamide)-polystyrene (PLA-PDMA-PS) triblock copolymers follow the procedure previously reported by Rzayev and Hillmyer.[1,2] Three batches of PS-PDMA-PLA triblock terpolymers were synthesized in order to generate monoliths with three different pore sizes. For all syntheses, toluene was passed through an activated alumina column and copper catalyst column prior to use. methylene chloride was dried in an M-Braun solvent purification system. D,L-lactide was purified by recrystallization from ethyl acetate. Dimethyl acrylamide and styrene were purified by passing the liquids through a short basic alumina column prior to use. The

chain transfer agent, *S*-1-Dodecyl-*S*'-(α,α'-dimethyl-α''-acetic acid)trithiocarbonate (CTA) was synthesized according to the original procedure.[3] All other reagents were used as received.

B-1.1: PS-PDMA-PLA, 14k-5k-23k

The first PS-PDMA-PLA triblock was synthesized as follows: An air free flask with a screw-on, Teflon top, and a Teflon stir bar were baked in an oven overnight to remove residual water from the glass. In an air-free glove box, benzyl alcohol (0.036 mL, 3.5×10^{-4} mol) and triethyl aluminum (1.0 M in heptanes, 0.175 mL, 1.5×10^{-4} mol) were added with 35 mL of toluene into the flask. The solution was stirred overnight to allow the initiator to activate (appx. 16 hours). The next day, D,L-lactide (5 g, 3.5×10^{-2} mol) was added to the toluene solution in the glove box. The amount of D,L-lactide was chosen such that a target molecular weight (~7 kg/mol) would be achieved at ~50% D,L-lactide conversion. The flask was sealed and removed to ambient conditions, and then stirred at 90 ºC for 2 hours and 55 minutes. After this time the flask was opened and 1M HCl (5 mL) was added to quench the reaction. The mixture was precipitated in methanol, redissolved in methylene chloride, and precipitated twice in pentane. The resulting white powder was dried in a vacuum oven at 40 ºC overnight. The yield was 2.8 g (56%). ^{1}H NMR data collected for the powder in $CDCl_3$ exhibited resonances at δ(ppm) = 1.55 (3 lactide methyl protons, relative integration ≈ 565), 4.35 (1 hydroxyl end group proton, rel int. ≈ 0.95) 5.2 (1 lactide tertiary proton, rel. int. ≈ 188), and 7.35 (5 Benzyl end group

protons, rel. int. = 5). The resonances at 1.55 and 5.2 were smeared over approximately 0.2 ppm, signifying that the functional groups observed were components of a polymer chain. End group analysis revealed M_n = 13.5 kg/mol, which was significantly higher than the targeted molecular weight. The M_n, which is almost twice the expected value for ~50% conversion, suggests that much of the benzyl alcohol either did not activate or deactivated before the polymerization. As a result, the propagating chains of PLA were able to grow longer than expected. Size exclusion chromatography ($CHCl_3$ eluent) revealed a monomodal size distribution with M_n = 14.7 kg/mol and PDI = 1.05, which indicates the formation of PLA-OH.

The PLA-OH (2.5 g, 1.8×10^{-4} mol) was dried under vacuum at 40 ºC overnight to ensure that any residual methanol and pentane had been removed from the polymer. The polymer was then dissolved in dichloromethane (100 mL) in a nitrogen-filled, flame-dried flask. Meanwhile, in a different flame-dried and nitrogen-filled flask, oxalyl chloride (1 mL, molar excess) and CTA (molar excess) were mixed with dichloromethane (5 mL) and stirred for 2 hours. Gas bubbles evolved as the oxalyl chloride reacted with the carboxyl end of the CTA to form an acid chloride. After the bubbles stopped, the flask was evacuated and the volatiles were removed, leaving behind a yellow residue. The PLA-OH in CH_2Cl_2 was cannula transferred to the flask with the residue and stirred for 48 hours. We note that diluting the PLA-OH in 100 mL CH_2Cl_2

facilitated the cannula transfer of the polymer, but slowed the reaction of the polymer with the CTA compared with the original procedure.[1,i] The solution was precipitated in methanol chilled by an ice bath. The precipitate was collected, dissolved in CH_2Cl_2, and reprecipitated in pentane twice. The resulting off-white powder (yield = 2.4 g, 95%) was dried overnight at 40 ºC in a vacuum oven. ^{1}H NMR of the powder (in $CDCl_3$) revealed that the hydroxyl resonance at δ(ppm) = 4.35 was absent, whereas resonances corresponding to the presence of CTA (two alkane protons, closest to the trithio group, on the dodecane chain: δ = 3.27 ppm; rel. int.= 2; benzyl alcohol = 5) were now visible. This indicated >99% conversion of PLA-OH to the macromolecular chain transfer reagent, PLA-CTA.

The PLA-CTA was mixed with AIBN (2 mL of 56 mg AIBN dissolved into 10 mL DMF), PLA-CTA (2 g), and *N*,*N*-DMA (0.56 mL) in a pressure vessel with DMF (4 mL total). After the PLA-CTA dissolved, the vessel was sealed and degassed by three freeze-pump-thaw cycles. The mixture was stirred at 60 ºC for 45 minutes, after which it was diluted with 4 mL CH_2Cl_2 and precipitated in pentane three times. The resulting powder (Yield = 1.4 g) was characterized after drying overnight at 40 ºC in a vacuum oven. ^{1}H

---

i. We also note that other instances of this reaction that did not achieve >99% conversion of the hydroxyl end of PLA-OH to PLA-CTA, due to either contaminants in the vessel (such as residual water or methanol) or lack of reaction time. In these cases, we were able to reprecipitated the mixture of PLA-OH and PLA-CTA, and rerun the reaction to achieve complete conversion.

NMR: $M_{n,PDMA}$ = 4.8 kg/mol. SEC: M_n = 19.0 kg/mol, PDI = 1.06. The characteristic resonances for the six dimethyl protons of PDMA were located at δ = 2.9 ppm (rel int. ≈ 290 to benzyl alcohol's 5, corresponding to $N_{PDMA} \approx 48$) however, the backbone hydrogen resonances were buried in the PLA methyl proton resonances. Notably, the CTA resonance originally at 3.27 ppm remained (rel. int. = 1.6 to benzyl alcohol 5.0; expected int: 2.0), though it shifted to 3.35 ppm in this spectra. This indicated that approximately 80% of the PLA-PDMA chains still possess the CTA end group. Collectively, these data indicate the formation of a diblock copolymer, PLA-PDMA-CTA, with component molecular weights of 14k-5k g/mol.

The last block was added by dissolving PLA-PDMA-CTA (1.4 g) in bulk styrene (6 g), degassing with three freeze-pump-thaw cycles, and stirring the mixture at 120 ºC for 4 hours. The resulting solution was extremely viscous and was no longer be stirred by the stirbar, so it was diluted in CH_2Cl_2 and precipitated in pentane. A white powder was obtained after two more precipitations in pentane, and was subsequently dried overnight at at 70 ºC in a vacuum oven (yield = 2.2 g). ^{1}H NMR: $M_{n,PS}$ = 23.4 kg/mol, determined from the integrations of resonances at 6.6 ppm and 7.1 ppm, which corresponded to two and three aromatic protons per styrene repeat unit, respectively. SEC: M_n = 45.6 kg/mol, PDI = 1.19. Total molecular weights: 14k-5k-23k PLA/PDMA/PS.

The PLA-PDMA-PS copolymer was compressed in a flat die mold at 130 °C and 1000 psi for 10 minutes in preparation for channel-die alignment. The compressed polymer was then pressed in a channel die (Figure B-1) at 130 °C and 1000 psi over one hour to

allow for shear alignment of the phase domains.[4,5] After alignment, the monoliths were

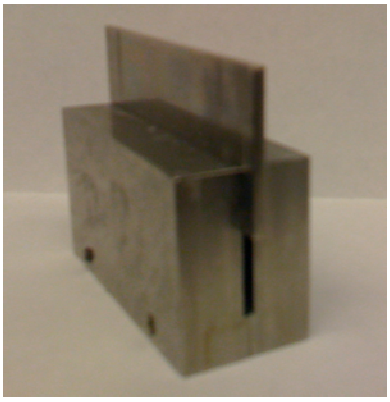

Figure B-1. A channel die, such as the one used to press the PLA-PDMA-PS triblocks into monoliths. Photograph provided by Ms. Elizabeth Jackson. Used with permission.

generally transparent. This quality was characteristic of monoliths with well-aligned cylindrical PLA domains, and opaque monoliths tended to exhibit poor alignment.

Prior to etching the PLA component from the monolith, small-angle X-ray scattering (SAXS) of the aligned triblocks revealed Bragg peaks consistent with hexagonally-packed PLA cylinders with diameters of 22 nm ± 2 nm, where the error corresponds to the pore diameters expected at $q^* \pm \sigma$ (σ = one standard deviation of the intensity distribution about q*). These cylinders are surrounded by a PDMA lining (approximately 1.7 nm thick, based on the PDMA volume fraction) and a PS matrix. The extent of cylinder orientation in the triblock monoliths, as given by the second order orientation factor F_2 (Equation B.1), was determined from the 2-D SAXS data using the normalized orientation distribution function $P(\phi)$ (Equation B.3), where ϕ is the azimuthal angle around a circle of constant q and $I(q^*,\phi)$ is the scattering intensity at the primary Bragg

peak, q^*.[6] Early samples, such as those used to study the polymorphism of glycine (Chapter 3), exhibited $F_2 \approx 0.8$, but after studies were initiated to optimize the alignment of these monoliths, $F_2 \approx 0.94$ were achieved (see below). The samples were then etched for 5 days in a 65 °C solution of 0.5 M NaOH in 50/50 MeOH:H_2O, after which ^{1}H NMR confirmed complete removal of the PLA. SAXS measurements of the p-PS-PDMA monoliths obtained after chemical etching of the PLA block confirmed retention of the alignments of the monoliths. The cylinder diameter inferred from the SAXS data is equivalent, within error, to the 20 nm diameter measured by SEM (Figure B-2), which is reduced from the actual value by the platinum coating.

$$F_2 = 1 - 3\left\langle (\cos\phi)^2 \right\rangle \qquad \text{B.1}$$

$$\left\langle (\cos\phi)^2 \right\rangle = \int_0^{\pi} (\cos\phi)^2 P(\phi) \sin\phi d\phi \qquad \text{B.2}$$

$$P(\phi) = \frac{I(q^*, \phi) q^{*2}}{\int_0^{\pi} I(q^*, \phi) q^{*2} \sin\phi d\phi} \qquad \text{B.3}$$

B-1.2: PS-PDMA-PLA, 9k-2k-20k

The synthesis of the second PS-PDMA-PLA triblock followed the same procedure as the first, but with a lower target molecular weight. Triethyl aluminum (240 μL) and benzyl alcohol (50 μL) were mixed in 35 mL toluene and stirred overnight. 5g of D,L-lactide was added, and the reaction was stirred at 90 ºC for two hours and twenty

minutes. After this time, 5 mL of 1M HCl was added to quench the reaction, and the

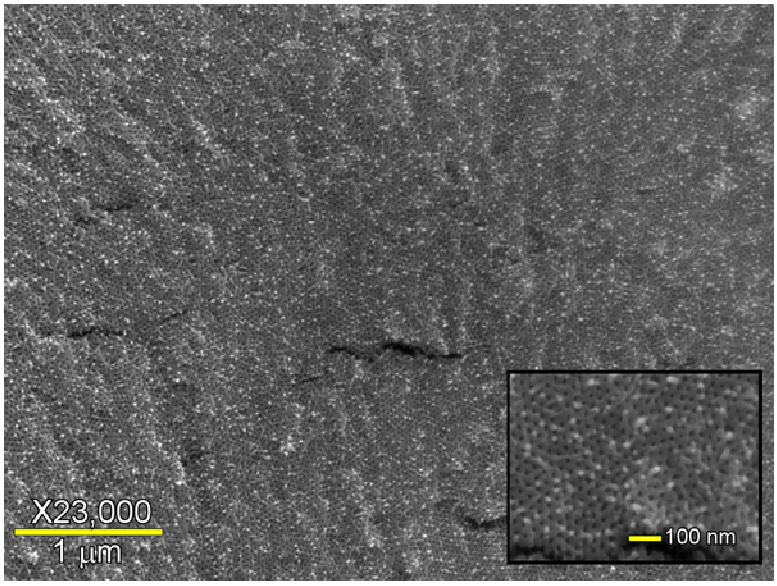

Figure B-2. Illustrative SEM image of an aligned, etched monolith prepared from 14k-5k-23k PLA-PDMA-PS. Inset: Monolith at higher magnification. The light portions of the SEM image are portions of the PS matrix that were plastically deformed when the monolith was cleaved with a razorblade. This deformation can be avoided by cooling the monolith in liquid nitrogen before cleaving.

product was precipitated in cold methanol. The precipitate was redissolved in CH_2Cl_2 and precipitated in pentane. The white powder that resulted was dried overnight at 50 ºC in a vacuum oven, and yielded 2.5 g. Analysis of ^{1}H NMR spectra collected for the powder (in $CDCl_3$) indicated the formation of PLA-OH with ^{1}H NMR: 8.5 kg/mol. SEC (THF Eluent) produced M_n = 9 kg/mol and PDI = 1.06.

The entirety of the PLA-OH was reacted with excess CTA according to the procedure described above. ^{1}H NMR spectra collected after precipitation and drying indicated >99% conversion of PLA-OH to PLA-TC (Yield = 1.7 g, 68%).

The target molecular weight for PDMA was 2 kg/mol, which corresponded to 1.7 g of *N*,*N*-DMA assuming 25% conversion. *N*,*N*-DMA (1.8 mL, 1.73g) and 0.017 g AIBN were mixed in 8 mL DMF, degassed by three freeze-pump-thaw cycles, and stirred for 15 minutes at 60 ºC. After precipitation and drying, 1.52 g of white PLA-PDMA-CTA powder was obtained. ^{1}H NMR: $M_{n,PDMA}$ = 2.0 kg/mol, and SEC: $M_{n,Total}$ = 9.3 kg/mol, PDI = 1.08. Total molecular weights were PLA-PDMA: 9k-2k g/mol.

The entirety of the PLA-PDMA-CTA powder was dissolved in bulk styrene (7.3 g). The target molecular weight for PS was 25 kg/mol at 50% styrene conversion. After three freeze-pump-thaw cycles, the reaction mixture was stirred at 120 ºC for 4 hours. Subsequent precipitation yielded 2.74 g of solid, and ^{1}H NMR indicated that M_n = 14 kg/mol. We suspected this polystyrene block might be too small to induce cylindrical morphology, so the entirety of the material (2.74 g) was added to 11 mL styrene, degassed, and stirred at 120 ºC for 3 hours and 45 minutes. After this time, the solution was diluted with CH_2Cl_2 and precipitated in cold methanol. Subsequent precipitations in pentane produced a white powder (Yield: 3.4 g after drying). ^{1}H NMR: $M_{n,PS}$ = 19.7 kg/mol, and SEC: PDI = 1.26. A small shoulder on the SEC trace suggested the presence of styrene homopolymer. The total molecular weights for this triblock were PLA-PDMA-PS: 9k-2k-20k g/mol.

The PLA-PDMA-PS copolymer was pressed in a flat die mold at 130 °C and 1000 psi for 10 minutes in preparation for channel-die alignment. The pressed polymer was then shear aligned in a channel die at 120 °C over one hour to allow for phase domain

alignment. ^{1}H NMR indicated complete removal of PLA after etching. SEM indicated large domains of well-ordered hexagonally packed cylinders with approximately 10 nm diameters (Figure B-3). The pore diameter and quality of orientation were corroborated by SAXS data, with F_2 = 0.80. SAXS also suggested an average pore size of approximately 10 nm. Notably, alignment of these triblocks did not produce orientations of the quality observed for the 18k-5k-23k triblock. This could be attributed to the lower press temperature not providing enough mobility to the polymer, or the lower molecular weights not generating enough driving force for highly ordered phase separation. Nevertheless, these monoliths exhibited uniform pore size suitable for the study of crystallization under nanoconfinement; however, their degree of alignment did not permit for reliable measurement of the orientation of nanocrystals embedded within them.

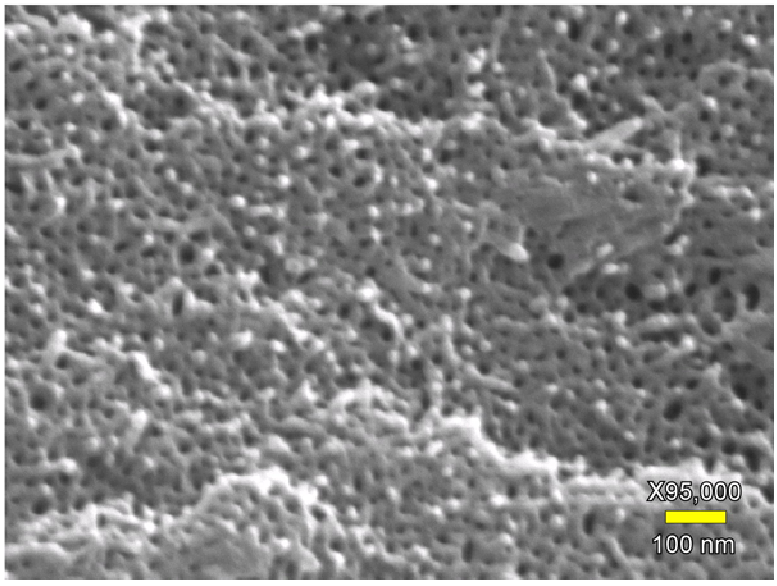

Figure B-3. SEM image of the porous surface of an etched p-PS-PDMA monolith with ~10 nm pore diameters, prepared from 9k-2k-20k PLA-PDMA-PS.

B-1.3: PS-PDMA-PLA 30k-18k-125k

The synthesis of the third PS-PDMA-PLA triblock followed a similar procedure as the first two, but with a higher target molecular weight. Triethyl aluminum (0.175 mL, 1.5×10^{-4} mol) and benzyl alcohol (3.5×10^{-4} mol) were stirred in toluene (35 mL) overnight. The following day, D,L-lactide (10 g, double the concentration of triblock #1) was added, the reaction vessel was sealed, and the solution was stirred at 90 ºC for 4.5 hours. The reaction was quenched with 1M HCl and precipitated in cold methanol. The reaction yielded 6 g of white PLA-OH powder after drying. 1H NMR: M_n = 30 kg/mol. SEC: M_n = 32 kg/mol (THF eluent), PDI = 1.07.

The entirety of the PLA-OH was reacted with excess CTA according to the procedure described above. ^{1}H NMR spectra collected after precipitation and drying indicated >99% conversion of PLA-OH to PLA-TC (Yield = 3.5 g, 58%).

The target molecular weight for PDMA was 10 kg/mol, which required 3.7 g of *N*,*N*-DMA assuming 25% conversion. *N*,*N*-DMA (3.8 mL, 3.7 g) and 0.010 g AIBN were mixed in 20 mL DMF, degassed by three freeze-pump-thaw cycles, and stirred for 70 minutes at 60 ºC. After precipitation and drying, 5.6 g of chunky white PLA-PDMA-CTA solid was obtained. ^{1}H NMR: $M_{n,PDMA}$ = 18.0 kg/mol, and SEC: $M_{n,Total}$ = 36 kg/mol, PDI = 1.11. Total molecular weights were PLA-PDMA: 30k-18k g/mol.

In order to achieve cylindrical morphology in the final triblock, a PS volume fraction of ~0.6-0.75 was desired. This corresponded to a target M_n of >100 kg/mol. Due to the gelation of bulk styrene reactions at molecular weights far below 100 kg/mol (such as in

the reactions described above), we opted to add PS to 30k-18k PLA-PDMA-CTA by reaction in solution. 5.6 g of PLA-PDMA-CTA was dissolved in 56 mL of DMF. AIBN (0.010 g) and styrene (25.5 mL) were added, and the vessel was sealed and degassed by three freeze-pump-thaw cycles. Subsequently, the solution was stirred at 120 ºC for 46.5 hours. The reaction was diluted with 20 mL CH_2Cl_2 and precipitated in methanol, and then the collected product – a hard, white solid – was dried overnight at 75 ºC (11 g yield). ^{1}H NMR: $M_{n,PS}$ = 125 kg/mol, and SEC: PDI = 1.80. The total molecular weights for this triblock were PLA-PDMA-PS, 30k-18k-120k g/mol.

The PLA-PDMA-PS copolymer was pressed in a flat die mold at 170 °C and 1000 psi for 10 minutes in preparation for channel-die alignment. The pressed polymer was then shear aligned in a channel die at 170 °C over one hour to allow for phase domain alignment. Temperatures lower than this, such as those used to press the 20 nm and 10 nm p-PS-PDMA samples described above, did not grant the triblock enough mobility for pressing. ^{1}H NMR indicated complete removal of PLA after etching. SEM indicated domains of poorly-ordered, irregular pores (Figure B-4). SAXS data revealed $F_2 < 0.6$. The alignment of this triblock was attempted at 150 ºC and 190 ºC, and neither temperature afforded better monolith alignment. Notably, all of the monoliths produced from this triblock were completely opaque, whereas well-aligned monoliths are semi-transparent. Due to the poor alignment of this monolith, which most likely owed to the high molecular weight (and hence, poor mobility) of the constituent polymer blocks, this monolith was not used for crystallization studies.

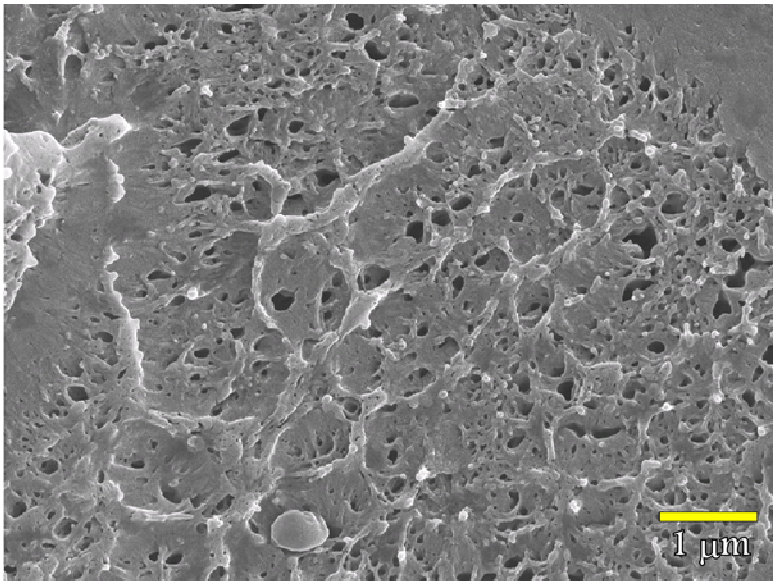

Figure B-4. Illustrative SEM image of a pressed and etched p-PS-PDMA monolith prepared from 30k-18k-125k PLA-PDMA-PS.

B-2: Domain Alignment from Channel Die Pressing of PS-PDMA-PLA[ii]

We undertook a study to determine the best pressing conditions for the channel-die alignment of PS-PDMA-PLA monoliths, using the 20 nm-pore triblock (PLA-PDMA-PS: 14k-5k-23k) described above. Samples were pressed at 120 ºC, and every 10 ºC hotter, up to 180 ºC. Greater temperatures resulted in discoloration of the monolith (they turned from yellow to brown), probably due to decomposition of the PLA component. Pressing was performed by allowing the channel die to warm in the hydraulic hot press for 20 minutes, then slowly closing a hydraulic press by 2-3 mm every 10 minutes until the

[ii] This work was performed jointly by the author and Dr. Eric Todd.

monolith protruded from the sides of the die. The pressing process generally took one hour. Alignments corresponding to $F_2 \approx 0.8$ were achieved at most of the temperatures examined. Notably, at 160 ºC, the triblock was pressed slowly by the weight of the channel die alone – the hydraulic press was not needed to exert pressure, although it was still used to keep the die level. This slow, steady flow was found to be optimal for alignment, and so subsequent studies were performed by pressing at this temperature. The monolith could be aligned in this manner at higher temperatures, but the best alignments were observed for samples pressed at 160 ºC. We note that this temperature is dependent on both molecular weight and polymer composition.

Some samples were annealed in the channel die for 1 - 2 days by storing the sample in a vacuum oven at ~170 ºC. We suspected that annealing improved the alignment of the monoliths, but comparisons between monolith alignments before and after annealing were impossible because the samples had to be removed from the channel die for the SAXS experiments required to determine F_2. The monolith pieces with the highest degree of alignment ($F_2 > 0.90$), however, came exclusively from annealed samples, consequentially, annealing the samples was performed regularly as part of the alignment process.

In addition to examinations of the effect of press temperature and annealing on domain alignment, we also examined the distribution of F_2 factors for a monolith throughout the length of the channel die. We expected that the ends of the pressed monolith, which underwent the greatest degree of extensional flow, would exhibit noticeably higher F_2

values than the middle of the monolith. Our examination revealed that the best-aligned portions of the monolith were located at the end (Figure B-5), however, the degree of variability in the alignment of the samples across the length of the channel die appeared random.

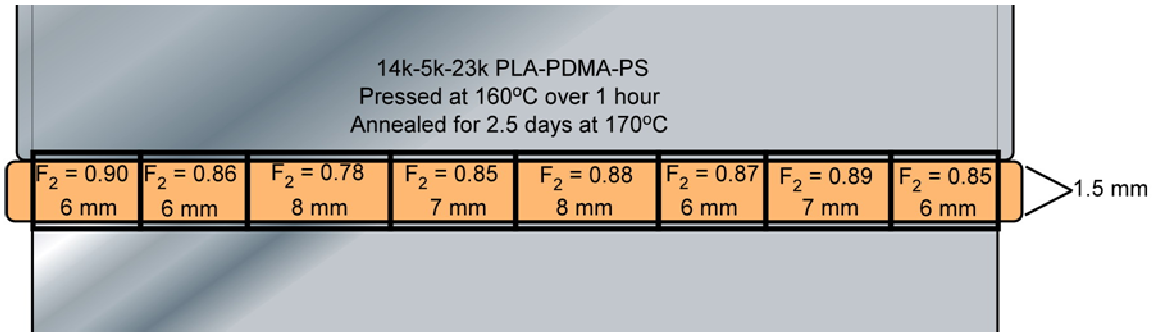

Figure B-5. Schematic illustrating F_2 values obtained as a function of channel die position for p-PS-PDMA monoliths prepared from 14k-5k-23k PLA-PDMA-PS.

One possible cause of the random alignment quality in the monoliths might be drag caused by the channel die during the polymer extensional flow. Consequentially, we examined the effects of applying various lubricants to the channel die on monolith alignment. The two main lubricants examined were silicon oil and aerosol Teflon spray. Each of these lubricants was applied to the channel die as a thin layer, and wiped off with a paper towel to leave a slight residue. The monoliths were then pressed as normal. Notably, the use of either lubricant greatly improved the quality and regularity of the orientation over the length of the channel die (Figure B-6). Furthermore, the orientations were superior for portions of the monolith that were not at the center.

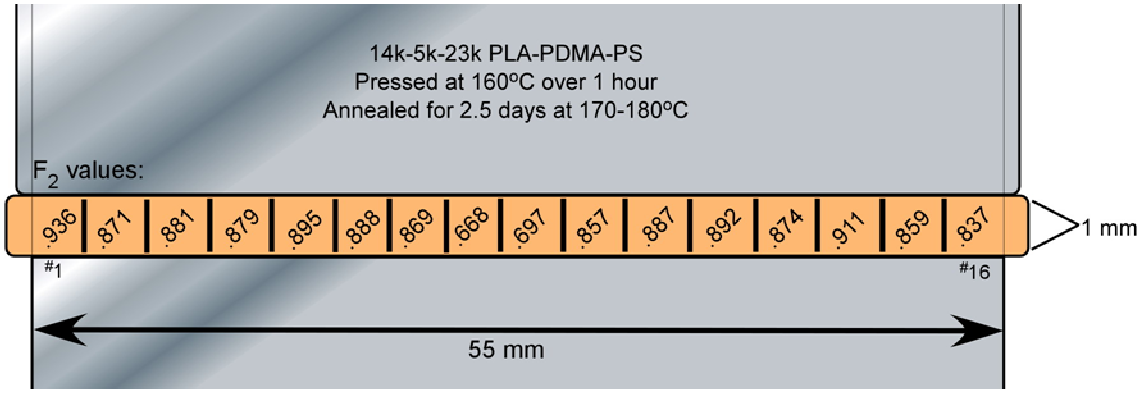

Figure B-6. Schematic illustrating F2 values obtained as a function of channel die position for p-PS-PDMA monoliths prepared from 14k-5k-23k PLA-PDMA-PS, using a small amount of silicon oil as a lubricant.

B-3: Characterization Methods

Nuclear magnetic resonance (NMR) analysis was performed on a Varian Inova VI-500 spectrometer (Varian Inc., Palo Alto, California) in deuterated chloroform at concentrations of approximately 1%. Size-exclusion chromatography (SEC) data were obtained using a Hewlett-Packard 1100 series liquid chromatograph (Hewlett-Packard, Inc., Palo Alto, California) equipped with Jordi polydivinylbenzene columns with pore sizes of 10000, 1000, and 500 angstrom as well as a Hewlett-Packard 1047A refractive index detector (Hewlett-Packard, Inc., Palo Alto, California). Chloroform was used as a mobile phase, at 35 °C with a flow rate of 1 mL/min, unless otherwise noted. The instrument was calibrated with polystyrene standards. SAXS experiments were run on a home-built beam line at the University of Minnesota Characterization Facility, and SEM

was performed on a JEOL 6500 SEM at the University of Minnesota Characterization Facility.

B-4: Concluding Remarks

This appendix has been dedicated to the study of the monoliths used to perform the bulk of the work discussed in this thesis. The synthesis of PLA-PDMA-PS triblock terpolymers and their subsequent fabrication into porous monoliths are straightforward, however, obtaining porous monoliths with a high degree of pore alignment is as much art as science. The syntheses described above reveal that not all triblock compositions conducive to forming cylinders result in well-aligned cylinders. Furthermore, the technique used to press the sample plays as much of a role in determining the final orientation as the triblock composition. It is our hope that future researchers find this information useful in their own work.

B-5: References

1. Rzayev, J.; Hillmyer, M. A. Nanoporous Polystyrene Containing Hydrophilic Pores from an ABC Triblock Copolymer Precursor. *Macromolecules* **2005**, *38*, 3-5.
2. Rzayev, J.; Hillmyer, M. A. Nanochannel Array Plastics with Tailored Surface Chemistry. *J. Am. Chem. Soc.* **2005**, *127*, 13373-13379.
3. Lai, J. T.; Filla, D.; Shea, R. Functional Polymers from Novel Carboxyl-Terminated Trithiocarbonates as Highly Efficient RAFT Agents. *Macromolecules* **2002**, *35*, 6754-6756.
4. Zalusky, A. S.; Olayo-Valles, R.; Wolf, J. H.; Hillmyer, M. A. *J. Am. Chem. Soc.* **2002**, *124*, 12761-12773.

5. Wolf, J. H.; Hillmyer, M. A. *Langmuir* **2003**, *19*, 6553-6560.
6. Sakurai, S; Aida, S.; Okamoto, S.; Ono, T.; Imaizumi, K.; Nomura S. Preferential Orientation of Lamellar Microdomains Induced by Uniaxial Stretching of Cross-Linked Polystyrene-block-polybutadiene-block-polystyrene Triblock Copolymer. *Macromolecules* **2001**, *34*, 3672-3678.